UNIVERSITY OF
BIRMINGHAM

Microstructural Characterisation of Pearlitic and Complex Phase Steels Using Image Analysis Methods

by

Xi Liu

A thesis submitted to

The University of Birmingham

For the degree of

DOCTOR OF PHILOSOPHY

Metallurgy and Materials Science

School of Engineering

The University of Birmingham

January 2014

Acknowledgements

A big thank you must go to my supervisors Dr R. M. Ward and Dr M. Strangwood, for all their guidance, encouragement, kind support and help throughout this project.

I would like to thank Professor P. Bowen for the provision of research facilities within the School of Metallurgy and Materials. Thanks are also given to all the staff and students that helped me during my time in the department.

Thanks to all the colleagues in the research group and my friends at the university. You make me really enjoy my 4 year time in Birmingham.

Finally, I want to thank my parents for their patience and support in every situation.

Abstract

The properties of materials are a primary factor to determine their applications, which makes the measurement of properties very important for both material design and quality control. As materials' properties are determined by the microstructure of the materials such as grain size or the volume fraction of the present phases, microstructural characterisation is a powerful tool for property prediction.

Unfortunately, microstructural characterisation has not been widely applied with all steels such as pearlitic steels or complex multi-phase steels due to their complex microstructures. These microstructures may contain features that cannot be resolved by optical microscopy, and in which important information is contained in their texture rather than simply their grey level. These microstructures were investigated in this study using image texture analysis.

Fourier transform-based analysis was applied to pearlitic microstructures to extract the image orientation information. The orientation information as well as the grey value of low pass filtered image was used as predicates in a split-merge algorithm to segment the pearlitic colonies.

A supervised classification method based on various statistical measures including a number of 2-point statistics (Grey Level Co-occurrence Matrix measures) was developed to distinguish the bainite (upper bainite and lower bainite), martensite and ferrite phases in steels. The influence of etching on the analysis results was also investigated.

The pearlite colony segmentation was fairly accurate on a synthetic image that contains idealised pearlitic structures, but it was also found that there are fundamental difficulties with estimating colony boundaries from a real single 2-D pearlitic image. The multi-phase analysis was found to be fairly accurate for overall phase fraction under the conditions investigated here.

The investigation of etching effect on image analysis show that the method used in this study is not very sensitive to the etching degree.

Table of Contents

Chapter 1. General Introduction

Steel has been one of the most important materials used by humans for up to 4000 years due to its good mix of properties and low cost. It has been found that the mechanical properties of steel are extremely dependent upon its internal structure at scales of nanometres up to microns or even millimetres (its 'microstructure'). We can adjust the internal structure of steels through composition changes, heat treatments or mechanical deformation, and through this we can design them to fulfil various requirements in a range of applications.

There are multiple ways in which the atoms within steel can be arranged and bonded, called phases. Different phases have different properties, which may be suitable for different applications, either singly or in combinations. For instance pearlitic steels have high strength, good wear resistance and good delamination resistance (Krauss, 2005), so they are widely used as rail steels (Stone and Knupp, 1978, Bramfit et al., 1995) and steel wire (Krauss, 2005). The steels with more than one phase including dual phase steels, transformation induced plasticity steels and complex steels usually have good combination of strength and toughness, thus they are well suited for applications requiring strength and formability typically as in the automotive industry (Romero et al., 2010, Sodjit and Uthaisangsuk, 2012).

Whether a material is appropriate for a particular application is determined by the properties of the material. The properties can be measured using a range of mechanical tests, e.g. hardness, tensile, compressive and fatigue testing; chemical and physical tests. Some of the tests are readily accessible such as hardness. Others are difficult to measure such as yield or tensile strength as special samples have to be machined. Properties such as toughness and the fatigue strength are even more difficult to determine since the testing needs several samples for each condition and

the testing process is time-consuming.

Apart from by the above direct mechanical or physical tests, the properties of materials can also usually be predicted by characterising the microstructure of the materials, as the properties are determined by the microstructure. There are a number of microstructural characterisation techniques including optical microscopy, Scanning Electron Microscopy (SEM), Transmission Electron Microscopy (TEM), x-Ray Diffraction (XRD), Electron Backscattered Diffraction (EBSD), Magnetic-based methods and Ultrasonic sound based methods. Among these techniques, electron microscopy and optical microscopy are able to reveal the morphology of the microstructural features in a prepared sample surface. Electron microscopy is widely used due to its high resolution down to the nanometre scale. However optical microscopy also has its own advantages such as low cost, easy use on large sample areas and easy operability.

Specifically for the pearlitic steels, interlamellar spacing, colony size and prior austenite size are the factors that predominantly determine the strength and toughness properties (Gladman et al., 1972). For the interlamellar spacing measurement, a SEM or TEM is adequate. However to measure the colony size and especially the prior-austenite grain size is very difficult and requires a skilled metallographer using the light microscope or SEM and special procedures (Bramfitt, 1998). For the steels with multiple phases, the fraction, size, shape and distribution of the phase constituents determine the properties. XRD is an efficient technique to measure the fraction of the present phases, but the size, shape and distribution are not accessible. Image analysis methods are also applied for this application. Unlike the XRD technique, which is a crystallographic analysis of the bulk microstructure, image analysis method is extracting information directly from the micrograph of the sample surface. So once the present features in the sample images are classified into phases, the fraction, size, shape and distribution of these phases are easily obtained. Most of

the current image analysis based characterisation uses the histogram of the brightness (intensity) of the individual pixels that make up the image, and relies on all the pixels in one phase having intensities in a different range from all of those in another phase. This makes it extremely simple to distinguish the phases just using thresholding, and has been shown to work for some dual phase steels that have a high inter-phase contrast (Krebs et al., 2011, Burikova and Rosenberg, 2009). However for many other steels with more complex microstructures the different phases overlap in brightness levels. In this case, intensity thresholding is no longer able to distinguish the phases, and instead some analysis of the spatial patterns of intensity within the phases, the 'texture', is needed.

The aim of this PhD is to explore what is possible using texture-based optical image analysis methods for the two examples of: (1) colony characterisation of pearlitic steels and (2) phase classification of multi-phase steels.

(1) The difficulty that lies in the first task is that a pearlite colony contains two phases (ferrite and cementite) so it is not directly characterisable by the contrast of the phases; instead the orientation (and other features) of the lamellae determines a colony. This study needs to solve several problems: the measurement of the orientation of image pixels, the determination of appropriate features that characterise colonies and the segmentation of colonies using these features. A FFT based technique was used here to measure the orientation. A split and merge algorithm was applied for the image segmentation based on three features: orientation within a region, Kernel Average Misorientation along the interface between two adjacent regions and smoothed grey level within a region. The algorithm showed high accuracy on a synthetic image containing idealised lamellar structures. For images with real pearlitic structures, the results were less accurate because of the complexity of real pearlitic lamellae and the imperfections contained in the pearlitic structure apart from lamellae. However, no published literature could be found in this field, and so the work in this PhD shows

what is possible using an FFT-based technique.

(2) A quantitative analysis of some simple dual-phase steel microstructures, such as ferrite and martensite alone, can be carried out using conventional image analysis methods based on grey scale segmentation (characterising phases by the brightness of their individual pixels in an optical image). However for multi-phase steels with mixed microstructures containing small features and low inter-phase contrast, grey-scale segmentation is typically not applicable. Instead, image texture analysis can make use of the *local patterns* of variation in intensity between a pixel and its neighbours. Among a number of image texture analysis methods, those based on Grey Level Occurrence Matrix (GLCM) are widely used due to their general good performance in similar studies (refer to section 3.4.3). It was also applied in this study. The texture analysis method used here was 'trained' on regions of known phases that were manually selected from given images: firstly the neighbourhood size and other GLCM parameters were determined; then the best combination of 2-order statistical features, from a library of over 20, was determined using a Sequential Backward Selection algorithm. Finally those parameters were used to classify the images. Manual classification was also carried out as an evaluation of the automatic method. For a complex microstructure containing ferrite, martensite, upper and lower bainite, the manual classification results by different people varied greatly, which indicated the difficulty of the problem. The automatic classification result was mostly within the range of manual results. The algorithm was also used on a series of samples that have similar microstructures containing bainite and martensite. It showed high accuracy with those microstructures. Also the results indicated that the same set of features can be applied to similar microstructures without re-applying the feature selection procedure.

Image quality is a crucial factor in image analysis. In the particular application of material science, sample preparation is a primary influencing process to image quality.

Therefore it is important to study external influencing factors to image analysis results such as the degree of etching. For example if the only way to obtain accurate results from image analysis is by extremely careful etching, then it limits the broad application of the technique. If the results are fairly insensitive to the degree of etching, however, then the method can be widely used with confidence. The effects of etching were studied in this work, and found to be acceptable within practical limits.

Chapter 2. Literature Review on Steel Metallurgy, Microstructure and Properties

2.1 Brief Background of Steel

Steel is an iron-based material containing low amounts of carbon and various additional alloying elements. It can be made into a great number of compositions with exactingly designed properties to meet a wide range of needs.

The earliest iron artefacts, from the 5th millennium BC in Iran and 2nd millennium BC in China, were made from meteoritic iron-nickel (Photos, 1989). The earliest known production of steel is a piece of ironware excavated from an archaeological site in Anatolia (Kaman-Kalehoyuk) and is about 4,000 years old. Although steel had been produced by various inefficient methods long before the Renaissance (roughly from the 14th century to the 17th century), it became a more common and inexpensive mass-produced material after more-efficient production methods were devised in the past few centuries, such as the Bessemer process and basic oxygen steelmaking, which lowered the cost of production while increasing the quality of the metal. Today, steel is one of the most common materials in the world (and iron is one of Earth's most abundant elements), with more than 1.5 billion tons produced annually (WordsteelAssociation, 2012). It is a major component in buildings, infrastructure, tools, ships, automobiles, machines, appliances and weapons.

Nowadays, high and ultra-high strength steels are on the market with a tensile strength of up to 5500 MPa (Bhadeshia and Honeycombe, 2006). Other properties such as fracture toughness, weldability and ductility are specified for different applications.

The strength requirements may be met by adjustment of the chemical composition, mechanical processing and heat treatment through (i) work hardening, (ii) grain refinement, (iii) solid solution strengthening by interstitial and/or substitutional atoms, (iv) precipitation hardening (Bhadeshia and Honeycombe, 2006) and (v) transformation hardening.

2.2 Strengthening Mechanisms

2.2.1 Work Hardening

Work hardening, also known as strain hardening or cold working, is the phenomenon whereby a metal becomes harder and stronger as it is plastically deformed at temperatures lower than one third (typically) of the absolute melting temperature of the metal (Callister, 2007). Due to the increase of dislocation density (resulting from dislocation multiplication or the formation of new dislocations) with cold deformation, the average distance of separation between dislocations decreases, which means the resistance to dislocation movement by other dislocations becomes more significant. Thus the imposed stress necessary to continue plastic deformation of a metal increases with increasing cold work. However, work hardening is usually accompanied by a decrease in ductility.

2.2.2 Grain Refinement

Most materials for structural components are in the polycrystalline state, in which the grain size or the grain boundary density influences the mechanical properties significantly. Two main reasons cause grain boundaries to act as a barrier to dislocation motion (Callister, 2007):

a) A moving dislocation needs to change its direction to pass from one grain into another if the boundary between these two grains is low angle or a twin boundary; it

becomes more difficult as the misorientation between grains increases.

b) It is nearly impossible for a dislocation to move directly across high-angle grain boundaries due to a high misalignment of the boundaries. Stress at the end of dislocations piled-up at a grain boundary may trigger dislocations in adjacent grains, to move / from which will lead to a discontinuity of slip planes across the grains.

The grain boundary area to hinder dislocation motion is greater for smaller grains than for bigger grains. The grain size-strength relationship was firstly proposed by Hall (1951) and Petch (1953) as the following equation:

$$\sigma_y = \sigma_0 + k_y d^{-1/2} \quad \text{(Eq2.1)}$$ (Hall, 1951, Petch, 1953)

Here d is the average grain diameter, and σ_0 and k are constants for a particular material, σ_y is the yield stress.

However, the Hall-Petch relation is not valid any longer when grain boundaries make contributions to deformation by sliding and/or diffusive flow along the boundaries, which are independent of dislocation glide (Blum et al., 2006). A critical grain size (d_c), below which the Hall-Petch relationship is no longer possible, is suggested as:

$$d_c = Gb/\{(1-v)H_v\} \quad \text{(Eq2.2)}$$ (Nieh and Wadsworth, 1991)

Where G is the shear modulus, b is the Burgers vector, v is the Poisson's ratio and H_v is the material hardness.

2.2.3 Solid Solution Strengthening

This hardening technique is to alloy with impurity atoms that dissolve into the parent metal either substitutionally or interstitially. For iron only a few of elements such as carbon, hydrogen and nitrogen have atoms that are small enough to go into solution interstitially. The atoms of size and electronic structure close to those of iron, that do not combine to form carbides, nitrides, or other compounds, will substitute for iron atoms in iron crystals and form a substitutional solid solution.

The size and electronic structure differences between host iron atoms and either interstitial or substitutional alloying atoms impose lattice strains or stress fields that restrict the movement of dislocations. In the substitutional case, the stress fields are spherically symmetric, meaning that they have no shear stress component. Conversely, solute atoms in interstitial positions cause a tetragonal distortion, producing a shear field that can interact with edge, screw and mixed dislocations. A larger stress is needed to propagate the dislocation in any direction, which means a greater strengthening effect compared with the substitutional case (Krauss, 2005).

2.2.4 Precipitation Hardening and Dispersion Hardening

The hardening using second phase particles is commonly used for steels which normally have more than one phase present. For steels this would usually be carbo-nitrides or intermetallics (maraging steels) precipitated from solid solution.

When dislocations are moving through a matrix, which is precipitation hardened there are two main interactions. The dislocation can either cut through the particles or bend around and bypass them. The cutting of particles is possible only when the slip plane is continuous from the matrix through the precipitate particle.

A stress increase is needed to move the dislocations through a lattice containing

precipitate particles in either cutting or bypassing cases. Orowan et al. (1954) proposed that in the bypassing case the dislocation is assumed to bend between two particles; yielding occurs when the bowed-out dislocation becomes semi-circular in shape; after yielding, the dislocation leaves Orowan loops around the particles, the formation of which makes the dislocation motion more and more difficult (Figure 2-1).

The strength increase depends not only on the volume fraction of precipitates but also on their diameter and therefore the spacing or number density respectively. For a constant volume fraction of precipitates the material strength increases as the size of precipitates decreases.

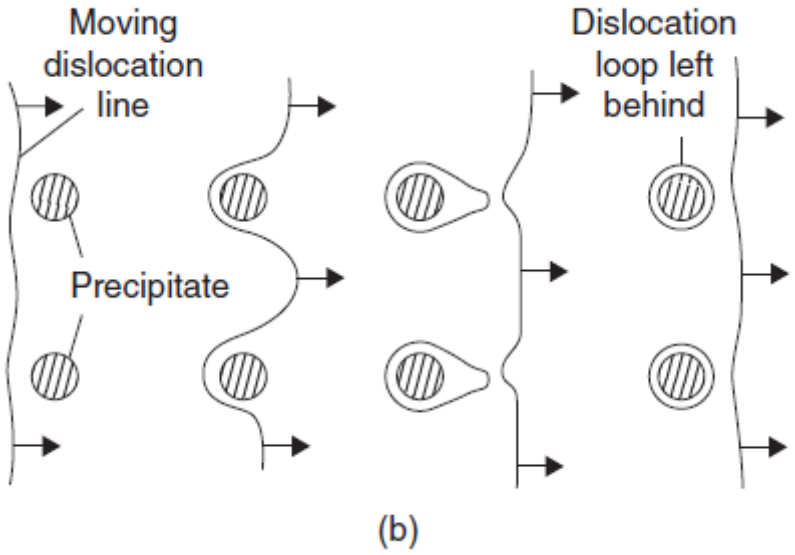

Figure 2- 1 A schematic representation of Orowan mechanism for dispersion hardening (R.E.Smallman and A.H.W.Ngan, 2007)

2.2.5 Transformation Hardening

One of the significant advantages of iron is its allotropy, i.e. the prevailing crystal structure depends on composition, temperature and external pressure (Callister, 2007). At atmospheric pressure, there are three allotropic forms of iron: alpha iron (ferrite), gamma iron (austenite) and delta iron. The vast majority of steels rely on just two

allotropes, alpha and gamma. The crystal structure of pure iron changes from the body-centred cubic (bcc) to face-centred cubic (fcc) form during heating up at 910 ℃ (Ae3 point) (Bhadeshia and Honeycombe, 2006).

One of the reasons why there is a great variety of microstructures in steels is that the same allotropic transition can occur in a variety of ways depending on the manner in which the atoms move to achieve the change in crystal structure. The transformation can occur either by breaking of bonds and rearranging the atoms into an alternative pattern (reconstructive or diffusional transformation), or by inhomogeneously deforming the original pattern into a new crystal structure (displacive or shear transformation) (Bhadeshia and Honeycombe, 2006).

The diffusion of atoms leads to the new crystal structure during a reconstructive transformation. The flow of matter is sufficient to avoid shear components of the shape deformation. Displacive transformations occur at temperatures where diffusion is incompatible with the rate of transformation.

The allotropic property of iron makes the transformation hardening or phase balancing an important strengthening method for steel. Phase balance hardened steels use predominately higher levels of alloying elements, such as C and Mn, along with heat treatment to increase strength. Manganese increases hardenability and tensile strength of steel, but to a lesser extent than carbon. Mn is also able to decrease the critical cooling rate during hardening, thus increasing the steel's hardenability much more efficiently.

Transformation-hardened steels can have a dual or triple microstructure of ferrite with varying levels of pearlite, bainite or martensite, which allows for varying levels of strength. Three basic types of transformation-hardened steels are dual-phase steels (DP), transformation-induced plasticity steels (TRIP) and martensitic steels.

The dual phase steels (ferrite and martensite) are often cast into slabs and hot rolled. Hot rolled coils are cold reduced and then further processed using continuously annealing technology.

TRIP steels consist of three phases: ferrite, bainite and retained austenite. It has been shown, that during the deformation process of an austenitic steel at ambient temperature the austenite steadily transforms into martensite, resulting in an increased elongation value (Kim, 1988). This combination of microstructures has the benefits of higher strength and great improvements in formability over other high-strength steels. Thermal processing for TRIP steels involves annealing the steel in the alpha + gamma region for some time and then quenching it to a point above the martensite start temperature, which allows the formation of bainite.

Martensitic steels are fully quenched to martensite during processing. The martensite structure is then tempered back to the appropriate strength level in order for adding toughness to the steel.

2.2.6 Effects of Carbon

Differences in the ability of ferrite and austenite to accommodate carbon result in important characteristics of the Fe-C diagram. The maximum solubility of carbon in austenite reaches 2.11wt% at 1148 ℃. Ferrite has a much lower ability to dissolve carbon than austenite: the solubility reaches a maximum of only 0.02 wt% at 727 ℃. The difference in solubility results from larger interstices in austenite. When the solubility limit for carbon in austenite or ferrite is exceeded, a new phase – iron carbide or cementite – forms in iron-carbon alloys and steels. Cementite crystals assume many shapes, arrangements, and sizes that together with ferrite contribute to the great variety of microstructures found in steels (Krauss, 2005).

2.3 Phases in Steel

2.3.1 Pearlite

Pearlite, as a lamellar mixture of ferrite and iron carbide, is a very common constituent of a wide variety of steels, where it provides a substantial contribution to strength.

When austenite is cooled, pearlite forms below the eutectoid temperature by the coordinated transform:

$$\gamma(0.77\ \text{wt\% C}) \rightarrow \alpha(0.022\ \text{wt\% C}) + Fe_3C(6.7\ \text{wt\% C}) \qquad \text{(Eq2.3)}$$

(Callister, 2007)

For carbon atoms to selectively partition to the cementite phase, diffusion is necessary (Figure 2- 2). The layered pearlite forms without long-range atomic diffusion but only with short range interfacial redistribution.

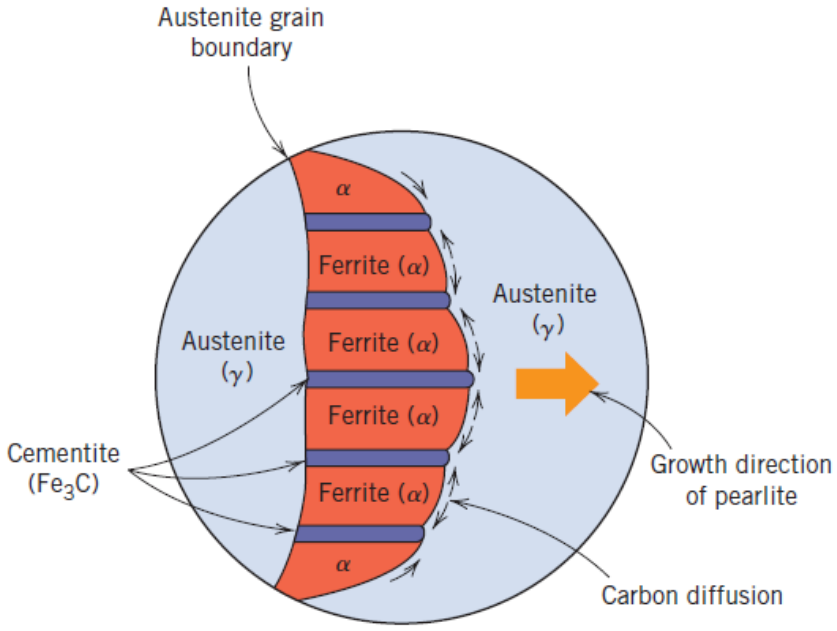

Figure 2- 2 Schematic representation of the formation of pearlite from austenite; direction of carbon diffusion indicated by arrows (Callister, 2007)

The true morphology of pearlite is sometimes not evident in two-dimensional sections. In three-dimensions, pearlite consists of an interpenetrating bi-crystal of cementite and ferrite, which when sectioned gives the lamellar appearance as can be seen in Figure 2- 3 (Bhadeshia and Honeycombe, 2006).

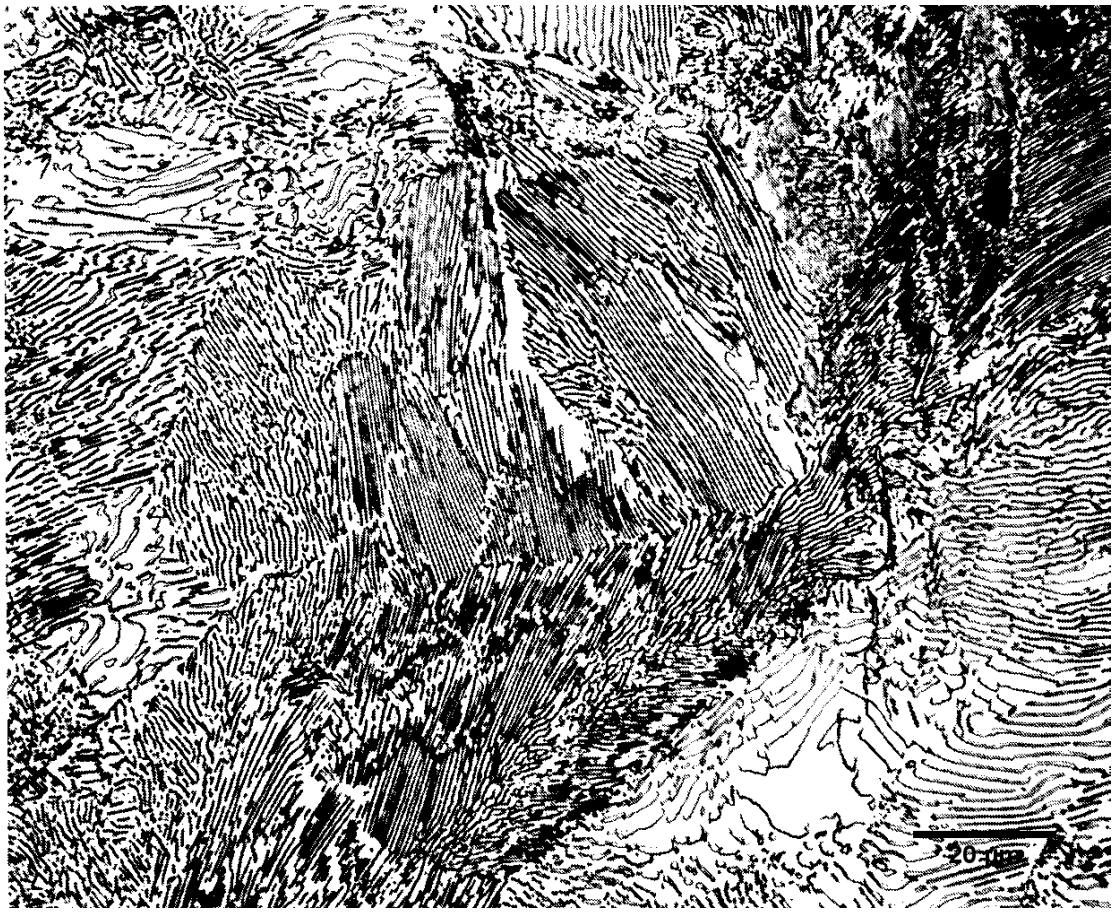

Figure 2- 3 Pearlite in a furnace-cooled Fe-0.75C alloy. Picral etch. Original magnification at 500x (Krauss, 2005)

Figure 2- 4 schematically illustrates the individual constituents of pearlite (however there is a mistake in the diagram: the colonies are not likely to cross prior austenite boundaries). A nodule nucleates at a grain boundary, triple point, grain corner, or surface inhomogeneity such as an inclusion and grows radially until impingement occurs with surrounding nodules (Bramfitt and Marder, 1973a). The basic structural

unit of pearlite is the colony. A nodule usually consists of an aggregate of more than one colony. Ideally pearlitic colonies are composed of parallel lamellae of cementite and intergrown ferrite (Garbarz and Pickering, 1988). Hull and Mehl's work (1942) showed that all the ferrite lamellae had the same crystallographic orientation, and so did all the cementite lamellae. The joint growth of neighbouring colonies leads to a rounded nodule of pearlite (Guy and Hren, 1974).

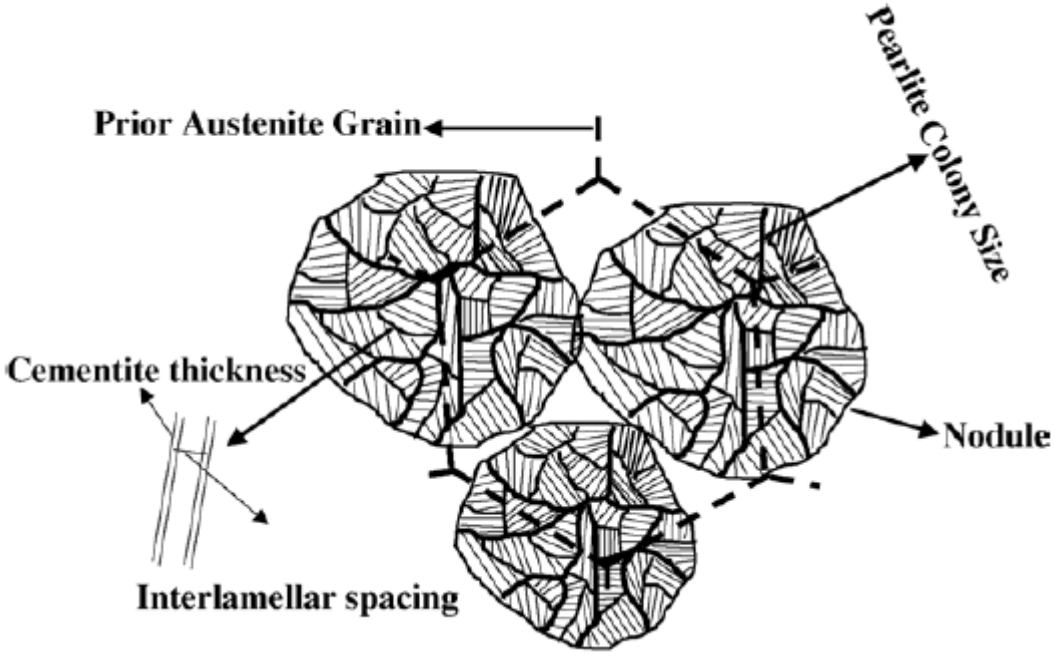

Figure 2- 4 Schematic diagram illustrating the various constituents in the pearlitic microstructure (Elwazri et al., 2005)

Then a colony can be defined as a structural unit in which cementite lamellae are aligned nearly parallel to each other and pearlite nodule can be defined as a structural unit in which the ferrite matrix has nearly the same crystallographic orientation everywhere (Garbarz and Pickering, 1988). It was also found that in most cases a misorientation of the order of several degrees exists between pearlite colonies within one nodule (Walentek et al., 2006). Also, growth faults such as linear discontinuities in the cementite lamellae, deviations in the lamellae' orientation, and low angle boundaries in the pearlitic ferrite usually occur in real pearlitic colonies (Bramfitt and

Marder, 1973b).

Colonies of lamellae of various orientations and spacings characterise the microstructure. However, the observed spacing on the optical micrograph is generally greater than the true lamellar spacing because the sectioning angle varies with respect to the lamellae plane (Samuel, 1999, Krauss, 2005), as is illustrated in Figure 2- 5.

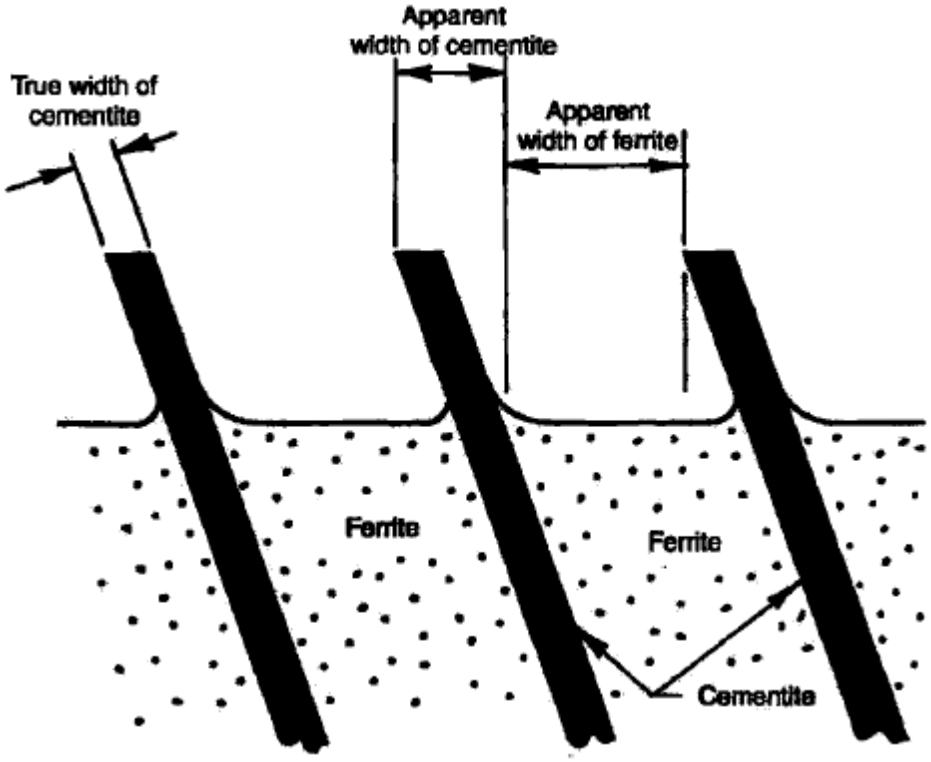

Figure 2- 5 Surface topography of pearlite after etching (Samuel, 1999)

The true lamellar spacing has been studied by researchers and it is found that the spacing varies over wide ranges from 140 nm to 1900 nm (Mehl and Hagel, 1956, Ridley, 1984). The spacing is determined by a number of factors within which the subcritical temperature at which a colony is nucleated is prominent (Samuel, 1999).

Apart from the interlamellar spacing (in mm) of ferrite and cementite lamellae in pearlite, *S*, the prior austenite grain size (in mm), *d*, and pearlite colony size (in mm),

P, are also important influencing factors to the properties (Gladman et al., 1972). The Yield Strength (*YS*) of fully pearlitic steels can be expressed as:

$$YS\ (MPa) = 2.18\left(S^{-\frac{1}{2}}\right) - 0.40\left(P^{-\frac{1}{2}}\right) - 2.88\left(d^{-\frac{1}{2}}\right) + 52.3 \quad \text{(Eq2.4) (Hyzak and Bernstein, 1976, Gladman et al., 1972)}$$

The ductile-brittle Transition Temperature (TT) can be approximated from the following relationship:

$$TT = 217.84 - 0.83\left(P^{-\frac{1}{2}}\right) - 2.98\left(d^{-\frac{1}{2}}\right) \quad \text{(Eq2.5) (Hyzak and Bernstein, 1976, Park and Bernstein, 1978)}$$

From Eq2.4 and 2.5, it can be seen that for pearlite, strength is controlled by interlamellar spacing, colony size and prior-austenite grain size, and toughness is controlled by colony size and prior-austenite grain size. Unfortunately, all of these factors are difficult to measure. For the interlamellar spacing, a SEM or a TEM with a magnification of 10,000x is adequate. The colony size and especially the prior-austenite grain size are very difficult to measure and require a skilled metallographer using the light microscope or SEM and special procedures (Bramfitt, 1998).

Due to its high carbon content and other strengthening mechanisms including microalloying or cold work, pearlitic steels can achieve tensile strengths up to 4000MPa (Lesuer et al., 1996). Pearlite exhibits a good resistance to wear because of the hard carbide and some degree of toughness as a result of the ferrite's ability to flow in an plastic manner (Li et al., 2005). Due to the excellent wear resistance along with good weldability, strength, and fracture resistance, pearlitic steels have been widely applied in industrial applications such as high-strength wires (Tarui et al., 1996,

Lesuer et al., 1996), structural applications (Lee et al., 2010), and especially the rail industry (Bolton and Clayton, 1984, Nakkalil et al., 1991, Garnham and Davis, 2011).

2.3.2 Bainite

Similar to pearlite in constitution, bainite also consists of ferrite and carbide (Borgenstam and Hillert, 1996). Often the transformation of austenite to bainite occurs in two stages, beginning with a displacive reaction which stops prematurely, to be followed by precipitation of carbides from the supersaturated ferrite or austenite at a slower rate (Bhadeshia, 2001).

Mainly depending on the transformation temperature and alloy composition (Mehl, 1939), there are two types of bainite formed: upper bainite, which is normally generated between 550 ℃ and 400 ℃, and the other one is lower bainite, with a transition temperature range of 400 — 250 ℃.

Lower bainite (lath bainite or plate bainite (Kutsov et al., 1999)), which is obtained by transformation at relatively low temperatures just above the martensite start temperature, consists of ferrite in a lath or plate and contains an intra-ferritic distribution of carbide particles (see Figure 2- 6) because of the slower diffusion rate associated with the reduced transformation temperature. Upper bainite (feathery bainite) forms at a higher temperatures and comprises a series of parallel ferrite laths separated by continuous or semi-continuous carbide layers or carbide-particle arrays (Figure 2- 6) (Bhadeshia, 2001, Yang and Fang, 2005).

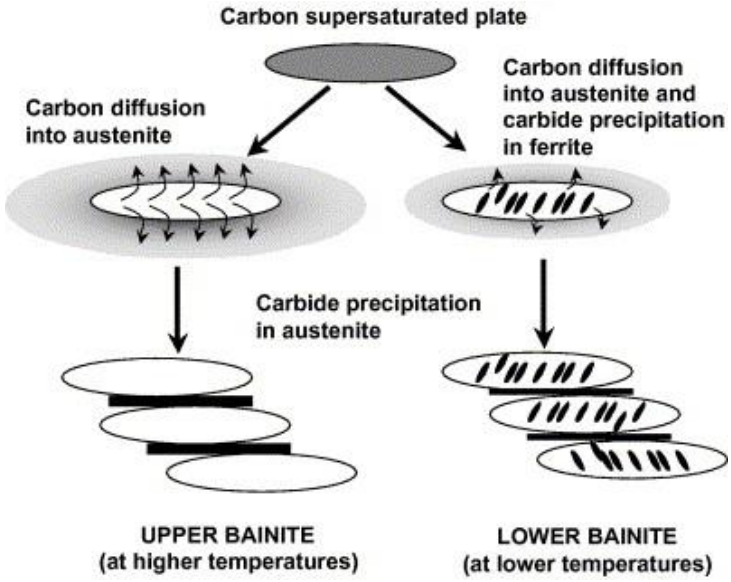

Figure 2- 6 Schematic representation of the transition from austenite to upper or lower bainite (Bhadeshia, 2001)

Both of these consist of aggregates of ferrite plates, which are called sheaves, separated by cementite, martensite or untransformed austenite. The plates within each sheaf are called sub-units (Figure 2- 7).

Many observations showed that the shape of a sheaf is that of a wedge-shaped plate (Srinivasan and Wayman, 1968). The thicker end of the wedge usually begins at an austenite grain boundary. The sub-units within sheaves have a lenticular plate or lath morphology.

The thickness of bainite plates is determined by the austenite strength, phase transformation driving force and transformation temperature (only a small effect) as shown in Figure 2- 8 (Bhadeshia, 2001). Strong austenite and high driving force lead to thicker bainite plates. Statistics show that the value of thickness can range from 50 nanometres to 340 nanometres (Singh and Bhadeshia, 1998, Bhadeshia, 2001).

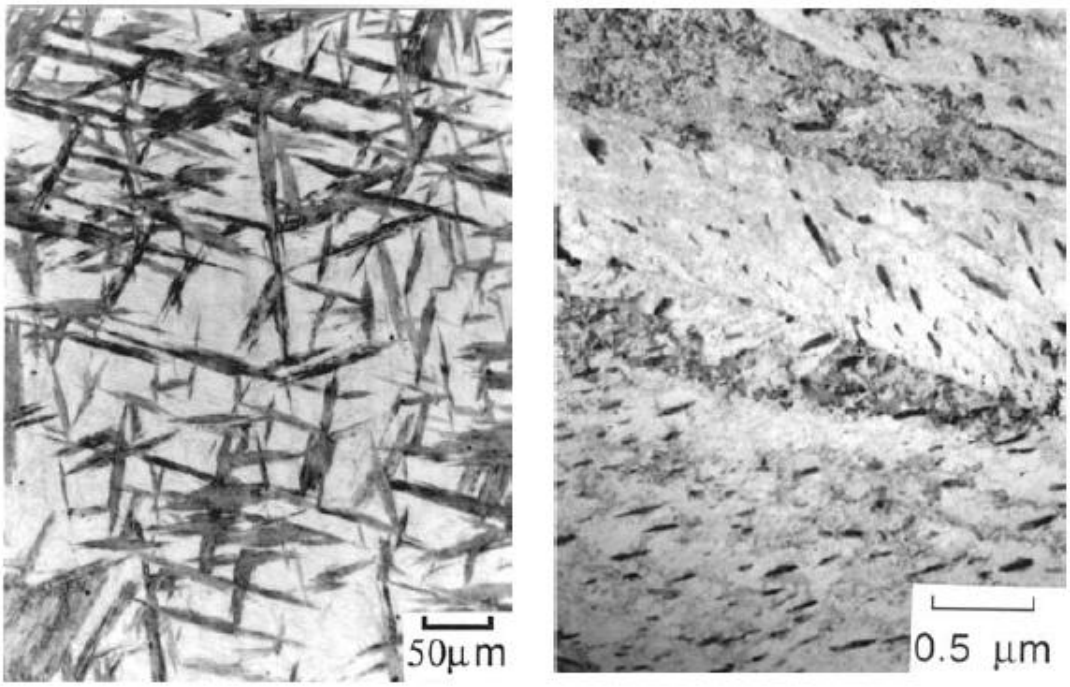

Figure 2- 7 (a) Light micrograph illustrating sheaves of lower bainite in a partially transformed (395°C) Fe- 0.3C- 4Cr wt% alloy. The light etching matrix is martensite. (b) Corresponding transmission electron micrograph illustrating sub-units of lower bainite (Bhadeshia, 2001)

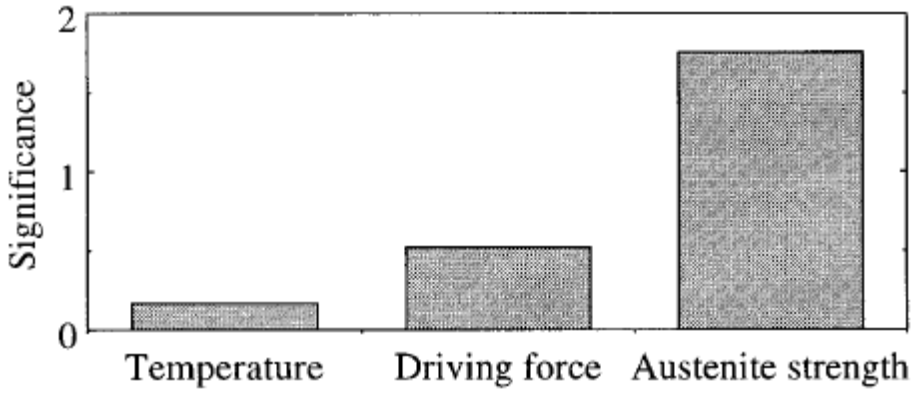

Figure 2- 8 The significance of each of the variables plotted on the horizontal axis (temperature, driving force and austenite strength), in influencing the thickness of bainite plates (Bhadeshia, 2001)

Generally bainitic steels are stronger and harder than pearlitic steels because of their finer structure (Figure 2- 9). The mechanical properties also vary with the

morphology of bainite. The tensile strength is higher for bainite obtained at lower transformation temperatures than for higher transformation temperatures due to the finer plate size and higher dislocation density (Bhadeshia, 2001).

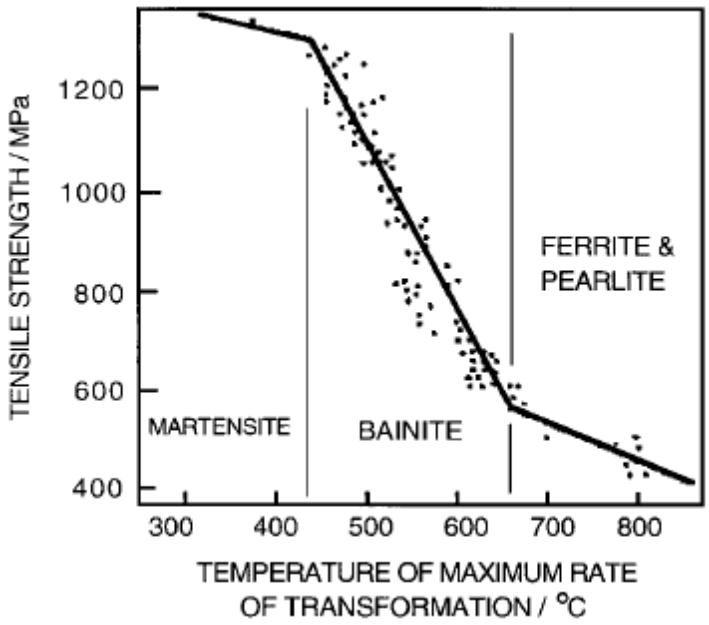

Figure 2- 9 Variation in the tensile strength of structural steels as a function of the temperature at which the rate of transformation is greatest during continuous cooling heat treatment (Irvine et al., 1957)

The property-microstructure relationship becomes more complicated when the toughness of bainitic steels is considered. The spacing of high angle boundaries in the bainitic structure is particularly important in this case, as the high-angle boundaries impede the propagation of cleavage cracks. Thus, that is the coarsest carbides in the microstructure which control toughness of the steel. The presence of comparatively large carbides in bainite, especially upper bainite, leads to a decrease in toughness (Barbacki, 1995).

2.3.3 Martensite

Another phase, called martensite, is formed when austenite is rapidly cooled (or

quenched) to a relatively low temperature. At the martensite formation temperature, diffusion, even of interstitial atoms, is usually not conceivable over the time of the experiment. Therefore the chemical composition of the martensite is identical to that of the parent austenite.

During the displacive lattice transformation from FCC of austenite to BCT of martensite, the interstitial space for the accommodation of carbon atoms (diameter: 0.154 nm) decreases from 0.1044 nm to 0.0346 nm, which produces a big distortion in the BCC lattice (Pan et al., 1998). The deformation of the austenite lattice causes a change in the shape of the transformed region, consisting of a large shear and a volume expansion (Bhadeshia and Honeycombe, 2006). The displacive transformation can be described as two successive shear displacements - first by a homogeneous shear throughout the plate which occurs parallel to a specific plane in the parent phase known as the habit plane. The second displacement is inhomogeneous by one of two mechanisms: slip as in Fe-C martensite or twinning as in Fe-Ni martensite (Figure 2- 10).

Mainly dependent on the carbon content, three types of martensite can be formed during quenching. The morphology of low carbon (up to 0.5 wt%) martensite is lath-like. For lath martensite the laths have an average thickness about 200 nm (Lee et al., 2009), and a length ranging from several to dozens of microns (Kotrechko et al., 2006). Lath martensite has a fuzzy and nondistinct appearance, as shown in Figure 2-11. The medium carbon martensite, with characteristic morphology is that of lenticular plates (Figure 2- 12), first start to form in steels with about 0.5 wt% carbon. Unlike the laths, the lenticular plates form in isolation rather than in packets. When the carbon content is higher than 1.4 wt%, the orientation relationship and the habit plane of martensite changes but the morphology is still lenticular plates (Bhadeshia and Honeycombe, 2006). In plate martensite, it is possible to see the individual plates.

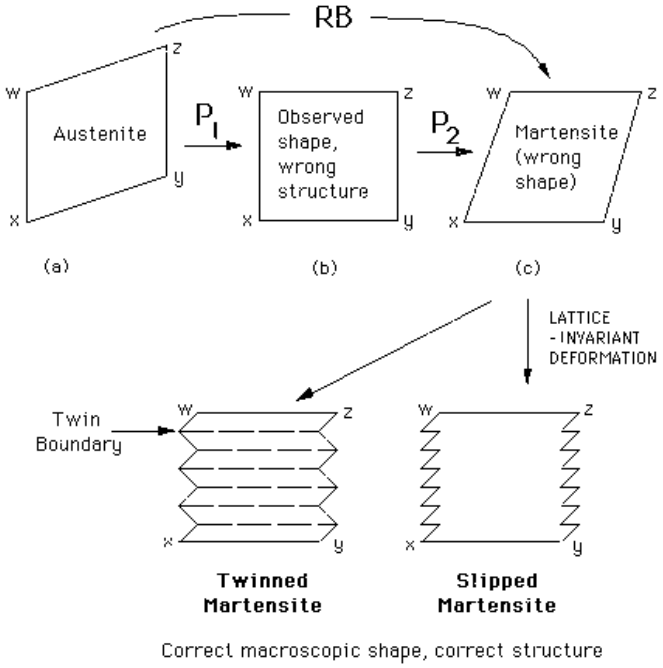

Figure 2- 10 The phenomenological theory of martensite crystallography RB: the combination of Bain strain B and rigid body rotation R, is a invariant-line strain, P1 and P2 are invariant-plane strain (Bhadeshia and Honeycombe, 2006)

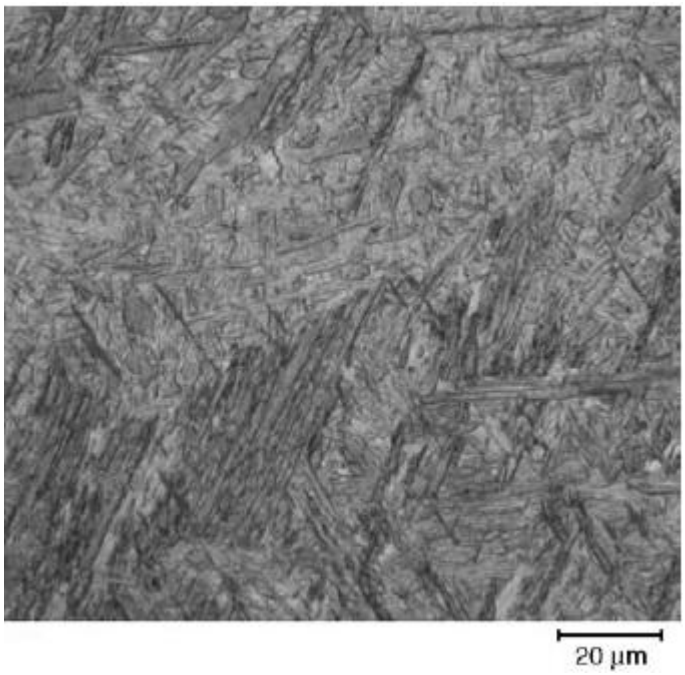

Figure 2- 11 Optical micrograph of lath martensite from a 0.18 C wt% steel (Verhoeven, 2007)

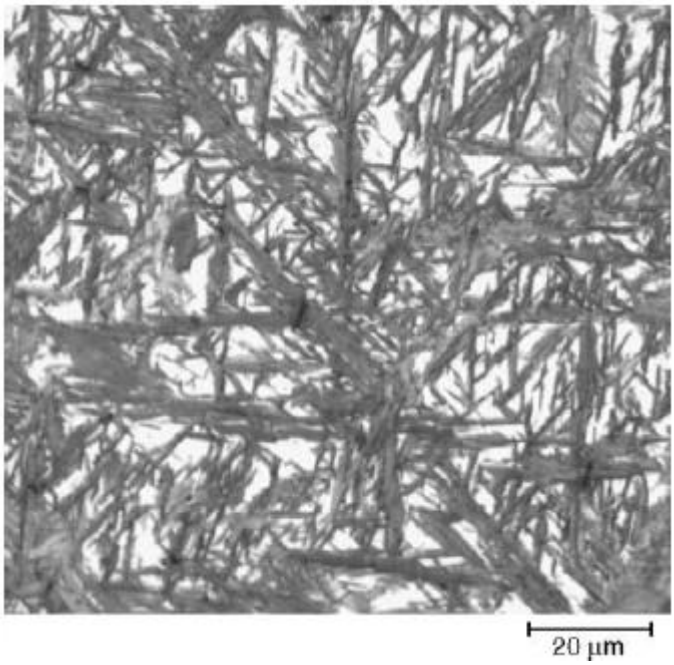

Figure 2- 12 Optical micrograph of plate martensite from a 1.4% C steel (Verhoeven, 2007)

It appears that there are two main contributions to the high strength of martensite (Cohen, 1962). One comes from the structures of twin plates or high dislocation density (Kelley and Nutting, 1961); the other one is that the carbon atoms strain the ferrite lattice, due to the increase of distortion during quenching as mentioned above (Dieter, 1988).

The microstructures of martensite and bainite at first seem quite similar like thin plates (Sandvik, 1982, Swallow and Bhadeshia, 1996, Dunne and Wayman, 1971); this is a consequence of the two microstructures sharing many aspects of their transformation mechanisms. Under a simple light microscope, the microstructure of bainite appears darker than martensite since there is a larger phase contrast effect with the ferrite/carbide interfaces in bainite than that with the lath boundaries in martensite (Bowen et al., 1986). Also, the particle size in bainite is much coarser than that in martensite (Tarpani et al., 2002, Wei et al., 2004), as is shown in the example in Figure 2- 13 and Table 2- 1.

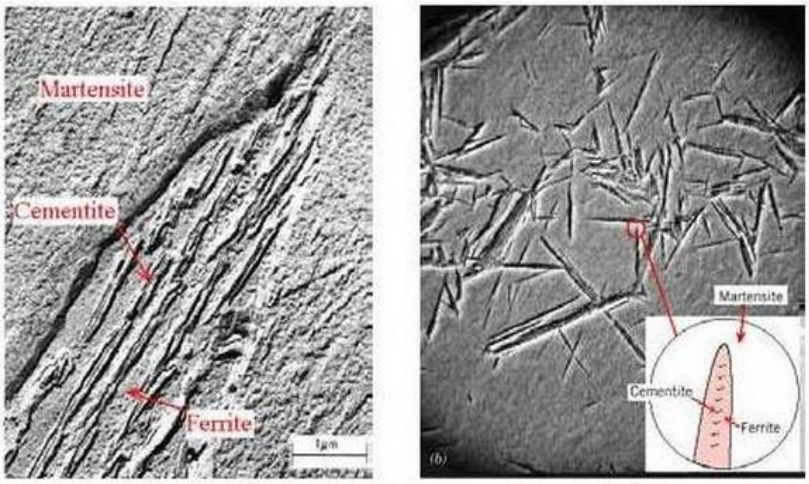

Figure 2- 13 Microstructure of the bainite/martensite double-phase steel (Shah, 2013)

Table 2- 1 Some microstructural characterisations of martensite and bainite (Bowen et al., 1986)

Microstructure	Mean cementite size/nm	Coarsest particle/nm
Tempered martensite (tempering: usually performed by reheating and cooling after hardening process)	38	110
Auto-tempered martensite (the tempering of the first-formed martensite, i. e. the martensite formed near Ms, during the reminder of the quench)	14	36
Upper bainite	220	1000
Mixed upper and lower bainite	230	720

Of the various microstructures that may be produced for a given steel alloy, martensite is the hardest and strongest and the most brittle. Its hardness is dependent on the carbon content as demonstrated in Figure 2- 14. In contrast to pearlitic steels, strength and hardness of martensite are attributed to the effectiveness of the interstitial carbon atoms in hindering dislocation motion (as a solid-solution effect) and to the relatively few slip systems rather than to the microstructure.

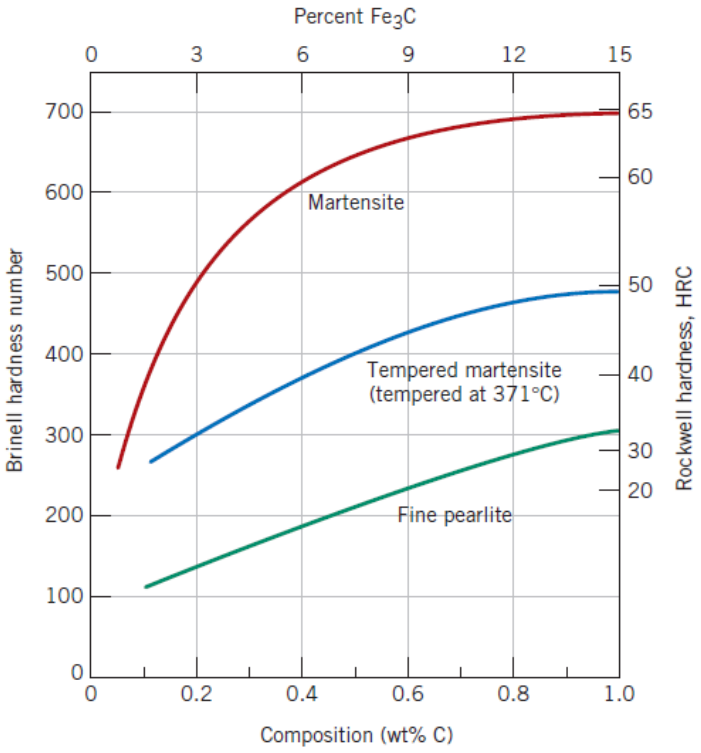

Figure 2- 14 Hardness (at room temperature) as a function of carbon concentration for plain carbon martensitic, tempered martensitic, and pearlitic steels (Bain, 1939, Grange et al., 1977, Callister, 2007)

2.4 Effects of Mixed Microstructures on Properties

Conventional high strength steels are manufactured by adding alloying elements such as Nb, Ti, V, and/or P in low carbon or IF (interstitial free) steels. These steels have widely been applied. However, as the demands for weight reduction are further increased, new families of high strength steels including DP (dual phase), TRIP (transformation induced plasticity), FB (ferrite-bainite), CP (complex phase) and TWIP (twin induced plasticity) steels have been developed (Zrnik et al., 2006).

Due to an excellent combination of strength and ductility and relative ease of manufacture, dual phase steels having two phases namely ferrite and martensite are gaining the widest industrial usage especially in the automotive industry (Romero et al., 2010, Sodjit and Uthaisangsuk, 2012). The hard second phase of martensite is

present in the form of islands in a matrix of ferrite. The property of good ductility to this steel is imparted by the soft ferrite phase, which is generally continuous.

The microstructure of transformation-induced plasticity steels (TRIP steel), consists of ferrite, bainite and metastable austenite (Jacques et al., 2001). During deformation, whether in forming or during operation, the retained austenite transforms into a harder phase – martensite – providing this material with enhanced work-hardening characteristics (Jingyi et al., 2011). The TRIP effect is also thought to be the main phenomenon responsible for the improved balance of strength and ductility exhibited by the new and so-called "TRIP-assisted multiphase steels" (Stringfellow et al., 1992).

Complex phase steels belong to a group of steels with very high tensile strength of 800 MPa or even greater. The chemical composition of CP steels, and also their microstructure, is very similar to that of TRIP steels. Typically, CP steels have no retained austenite in the microstructure, but contain harder phases such as martensite and bainite (Kuziak et al., 2008).

High strength structural steels with mixed microstructure of martensite, bainite and ferrite have been found to have better strength and toughness than single phase microstructures of low temperature products. Generally speaking, the strength and hardness of steel increase with increasing martensite volume fraction; while the ductility decreases. This is valid for both triple phase steels (ferrite, bainite and martensite) (Zare and Ekrami, 2011) and dual phase steels (ferrite and martensite) (Erdogan and Tekeli, 2002). At the same martensite volume fraction values, fine microstructures demonstrated a better combination of strength and ductility and higher hardness than coarse ones (Erdogan and Tekeli, 2002). The presence of bainite (typically lower bainite) in steels contributes to the improvement of toughness. However, there is not a monotonic relationship between them. Bohlooli and Nakhaei

(2013) compared the strength and ductility of three bainite-ferrite steels containing 49%, 54% and 63% bainite respectively. The results showed the sample with 63% bainite had the highest strength and best ductility. However, when the bainite fraction increased to 100%, its toughness and ductility decreased greatly (Saeidi and Ekrami, 2009).

Tomita and Okabayashi (1985) concluded that the mechanical properties, especially toughness, of high strength steels having a mixed microstructure of martensite and bainite are affected more by the size, shape, and distribution of bainite rather than the difference in martensite and bainite strength, and/or the type of mixture present. In the steel with a multiple phase microstructure they tested, the occurrence of upper bainite resulted in poor toughness (Tomita and Okabayashi, 1985, Tomita and Okabayashi, 1983). Also they found that for that steel a mixed microstructure containing tempered martensite with 25% lower bainite provided the best combination of strength and ductility. These findings were confirmed by Abbaszadeh et al. (2012) and Young and Bhadeshia (1994) using martensite-bainite dual phase steels. They also observed a maximum point (at about 28% bainite) in the curve of strength as a function of lower bainite fraction. They explained this phenomenon (strength increase first as increasing the lower bainite fraction from a fully martensitic structure) on the basis of two factors: a) the partitioning of the prior austenite grains by the lower bainite resulting in the refinement of martensite substructures (Tomita and Okabayashi, 1983); b) the strengthening of the lower bainite by the surrounding relatively rigid martensite because of a plastic constraint effect. Abbaszadeh et al. also found that the increasing of the upper bainite volume fraction in the mixed upper bainite-martensite microstructures resulted in the decreasing of properties such as yield strength, ultimate tensile strength, elongation and Charpy V-notch impact energy.

Therefore, it is important to measure the fraction of phase constituents in a mixed microstructure (including distinguishing upper and lower bainite), in order to

predicate the properties of the material.

2.5 Quantitative Characterisation of Microstructure

The determination of the properties of samples is essential for the development of new materials with specifically tailored properties, the design of their thermomechanical treatments and the quality control of existing fabrication processes.

Some mechanical properties are readily accessible, such as hardness. Others are difficult to measure such as yield or tensile strength, as special samples have to be machined from the material. Properties such as toughness and the fatigue strength are far more difficult to determine since the testing needs several samples for each condition and the testing process is time-consuming.

In many systems, relationships between properties and microstructure have been established, e.g. the Hall-Petch relationship (Hall, 1951), as microstructures have been more readily obtained than mechanical data and contain a large amount of information about the materials and their processing history. Quantitative analysis of microstructural images not only allows the possibility of performing a quality control check of the processing route, but also gives the possibility of further establishing correlations between microstructural features and related properties (Figure 2- 15).

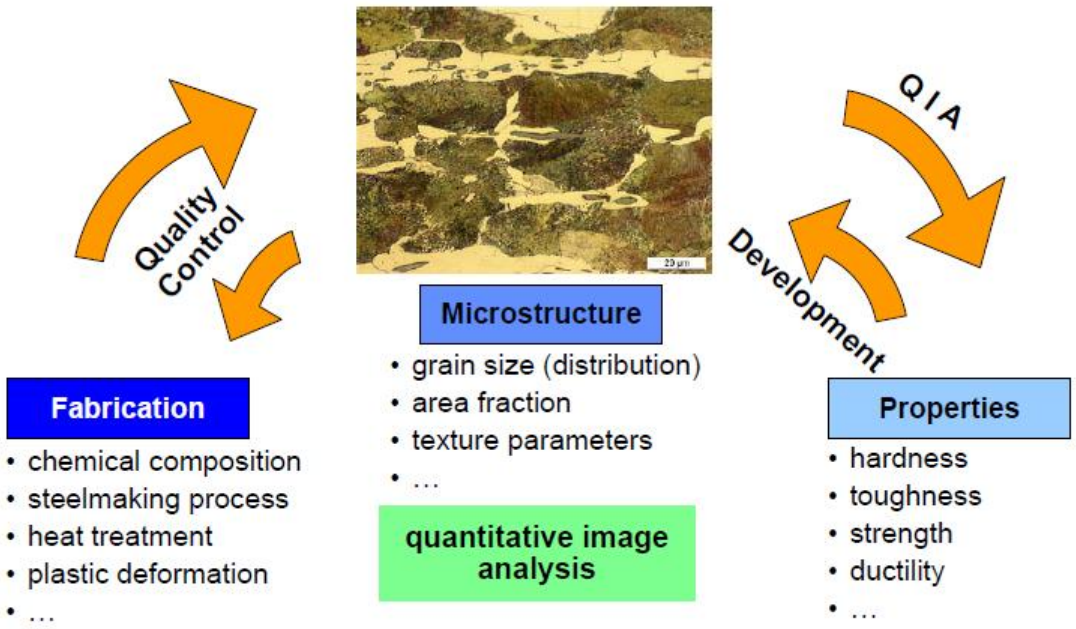

Figure 2- 15 Microstructure as a connection between the fabrication of components and their properties (Fuchs, 2005)

However, particularly for strengthening mechanisms, the relevant microstructural features have various scales and techniques for being quantitatively analysed. The grain size of steels or the morphological units of phases (e.g. bainitic laths) have a scale of micrometres, so they can be characterised with optical microscopy or scanning electron microscopy; the strengthening precipitates or second phases can range from nanometres (e.g. nitrides or intermetallic compounds) to micrometres (e.g. carbides), so can also be characterised with SEM or possibly optical microscopy; the solid solution strengthening is to dissolve alloying elements in to parent atoms substitutionally or interstitially, while work hardening is to produce more dislocations with the material, both of which are only observable with TEM and hard to characterise. Therefore, among the strength influencing factors, only the grain size and phase balance can be characterised optically.

Chapter 3. Literature Review on Image Analysis

3.1 Background of Digital Image Analysis

3.1.1 Microscopy and Image Acquisition

The material structures as reviewed in Chapter 2 have to be magnified for viewing and analysis due to their size. Traditionally, optical microscopy is commonly used in this field of characterisation. The resolution of an optical microscope is dependent on the wavelength of light used to image the sample surface and can be calculated according to

$$d_{gr} = \frac{0.61*\lambda}{n*sin\sigma} = \frac{0.61*\lambda}{N.A.} \quad \text{(Eq3.1)}$$

(Hecht, 2002, Jonkman et al., 2003)

Where d_{gr} represents the resolution limit, λ denotes the wavelength of the light, n the refractive index of the medium between object and objective and σ the angle between the illuminating beam and the optical axis of the microscope. N.A. is also referred to as numerical aperture.

For the medium air n has a value of about 1. This means that the resolution of an optical microscope is limited to about 476 nm for red light with a wavelength of about 780 nm. The spatial resolution of an optical microscope is often given an approximate value of 0.35 μm. Compared to the typical sizes of the features of the phases (martensite, bainite) that reviewed in section 2.3.3, it can be found that the martensite laths are not resolvable under optical microscope, while lower and upper bainite may be resolvable.

To resolve the very fine structures of hardened steels a higher resolution would be

necessary. This can be achieved using electron microscopy. Thanks to the very small wavelength of the electron (around 0.5 nm for an accelerating voltage of 60 kV) compared to the wavelength of the optical light, 100000 times the resolution of the optical microscope should be achievable theoretically (Fuchs, 2005).

Nevertheless optical microscopy plays an important role in quantitative image analysis due to its advantages over electron microscopes:

- lower price
- greater availability in both scientific and industrial environments
- comparatively simple usability
- additional information from colour images
- possibility of high automation
- lower requirements for sample preparation

Thanks to these strengths, optical microscopy is still widely used in both scientific and industrial environments in spite of its disadvantage of limited resolution. However as some aspects of the microstructure which would allow phases too be simply characterised cannot be resolved optically, alternative methods have to be found to characterise the optical images of the complex microstructures of modern steels.

3.1.2 Types of Digital Image Analysis

Image representation can be roughly divided into four levels (Figure 3- 1), or alternatively two even simpler ways are often distinguished: low-level image processing (transform of an image to another including image compression, pre-processing methods for noise filtering, edge extraction and image sharpening) and high-level image interpretation (Sonka et al., 1998). E.g. the inputs are images, but the outputs are a set of characteristics or parameters (e.g. detecting the owner of a face or

finger print) extracted from those images (Gonzalez and Woods, 2007).

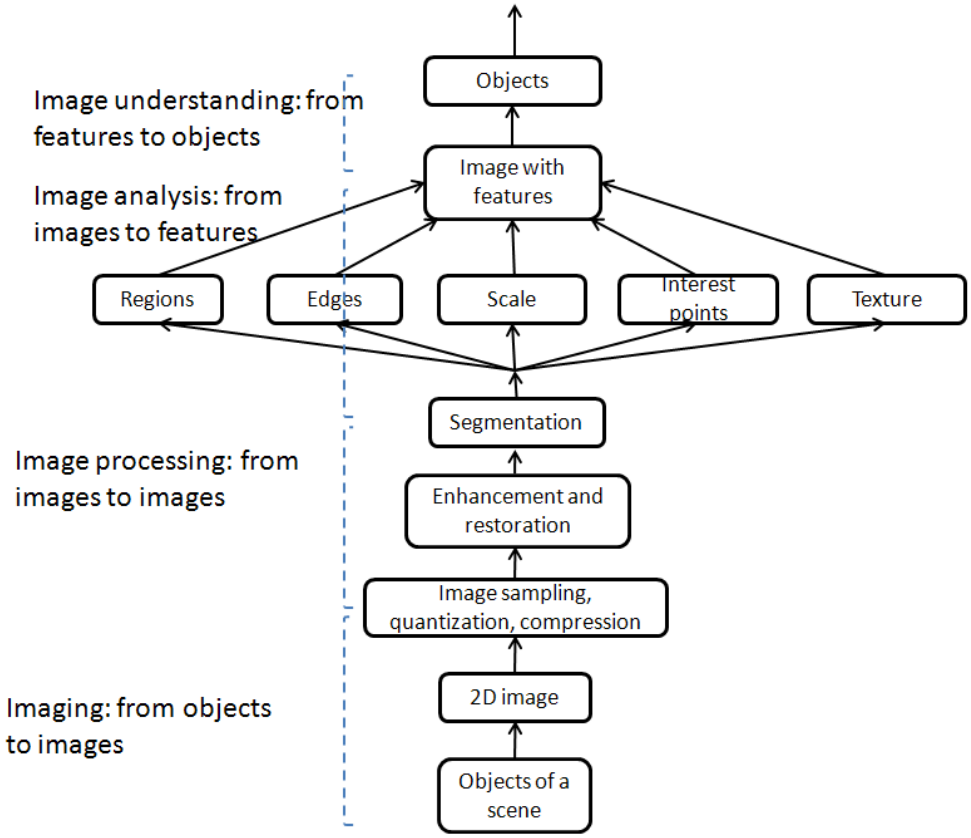

Figure 3- 1 Four possible levels of image representation suitable for image analysis problems (Sonka et al., 1998)

3.2 Image Shade Correction

3.2.1 Shading Problem in Image Acquisition

Optical microscope images are produced by the interaction between objects in real space, the illumination, and the camera. In the optical imaging system, the images frequently exhibit significant variation in intensity (shading) across the field-of-view. In some cases, the image may be brighter in the centre and darker in the edge; in other cases the brightness of the pixels on one side may be higher than those on the other. The shading might be attributed to multiple factors from non-uniform illumination, non-uniform camera sensitivity, the design of the light path between the camera and the microscope or even dirt and dust on glass (lens) surfaces (Rochow and Tucker,

1994). This shading effect is of great harm for subsequent image processing and especially quantitative image analysis, therefore eliminating it is frequently necessary.

Imaging system

The shading correction issue was studied and discussed by Young (2000). He theoretically described this problem. The illumination over the microscope field-of-view $I_{ill}(x,y)$ interacts with the object $a(x,y)$ in a multiplicative way to produce the image $b(x,y)$:

$$b(x,y) = a(x,y) \cdot I_{ill}(x,y) \quad \text{(Eq3.2)}$$

(Young, 2000)

The object represents various microscope imaging modalities:

$$a(x,y) = \begin{cases} r(x,y) & reflectance\ model \\ 10^{-OD(x,y)} & absorption\ model \\ c(x,y) & fluorescence\ model \end{cases} \quad \text{(Eq3.3)}$$

(Young, 2000)

where *OD(x,y)* is the optical density, *c(x,y)* is proportional to the concentration of fluorescent material, and *r(x,y)* is the reflectance, which is applicable in this case. The camera also often contributes *gain* and *offset* terms, so that:

$$\begin{aligned} c[m,n] &= gain[m,n] \cdot b[m,n] + offset[m,n] \\ &= gain[m,n] \cdot I_{ill}[m,n] \cdot a[m,n] + offset[m,n] \end{aligned} \quad \text{(Eq3.4)}$$

(Young, 2000)

both the camera *gain* and *offset* can vary as a function of position, thereby

contributing to the problem of shading.

3.2.2 Shading Correction Method

Two calibration images are needed through the imaging system – *BLACK[m,n]* and *WHITE[m,n]*. The *BLACK* image is generated by covering the lens leading to *b(x,y)* in shading model (Eq3.4) equal 0, which in turn leads to *BLACK[m,n]=offset[m,n]*. The *WHITE* image is generated by using *a[m,n]=0* which gives $WHITE[m,n] = gain[m,n] \cdot I_{ill}[m,n] + offset[m,n]$. The correction then becomes:

$$\hat{a}[m,n] = constant \cdot \frac{c[m,n]-BLACK[m,n]}{WHITE[m,n]-BLACK[m,n]} \quad \text{(Eq3.5)}$$

(Young, 2000)

The constant term is chosen to produce the desired dynamic range. The same equation was also given by van den Doel et al. (1998) and a textbook written by Murphy (2001).

In the shading correction process of this study, the white image was taken from an as-polished sample and the black image was simply to set '0' everywhere in the image.

3.3 Conventional Intensity Based Image Analysis

The intensity of image pixels, regardless of location, often carries much of the information about features (feature: a quantitative measure of a certain texture characteristic) in an image and so is most important for images analysis. Furthermore, intensity based approaches such as image thresholding and subsequent edge detection are effective and fast for the analysis of simple images.

The simplest thresholding technique is to partition the image histogram by a single

global threshold. Then segmentation can be carried out by labelling each pixel as object or background depending on its intensity value compared with the threshold value.

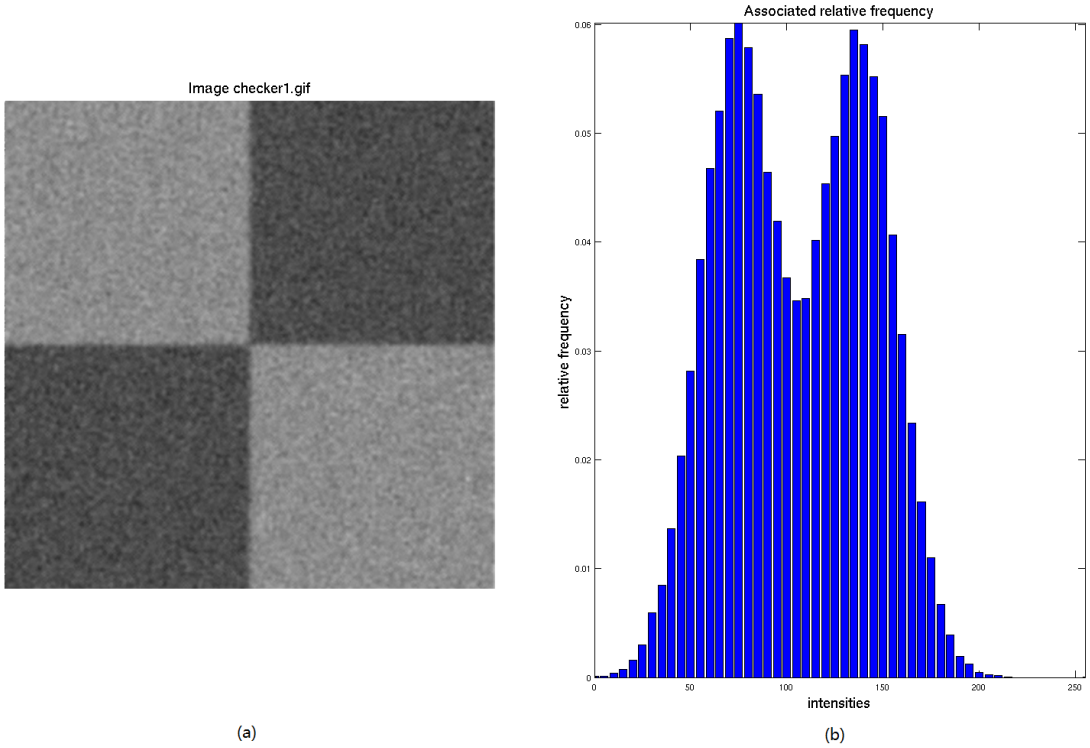

Figure 3- 2 (a) Original image; (b) image histogram (Coste, 2012)

Figure 3- 2 (a) shows a simple image; Figure 3- 2 (b) shows its histogram. By simply applying a threshold as the local minimum value between two intensity peaks in Figure 3- 2(b), a segmented image can be obtained as Figure 3- 3.

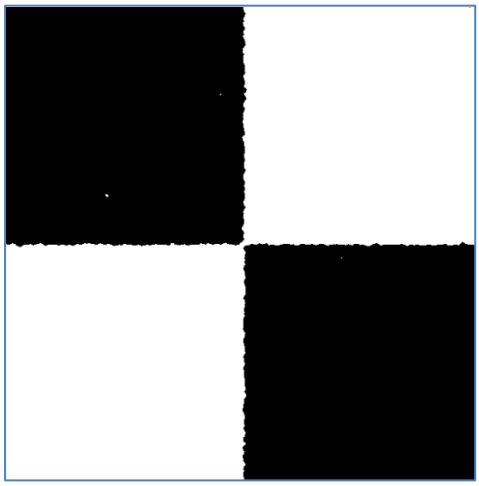

Figure 3- 3 Segmented image of Figure 3- 2(a)

This technique is suitable for images that consist of objects with homogeneous intensities and definite contrast. However, many images are more complicated, so image texture analysis is induced and more widely applied nowadays.

3.4 Image Texture Analysis

All natural and artificial images have texture in common, which gives information not just about the colour or grey level of a point in an image, but also about the spatial arrangement of colour or intensities in an image or selected region of an image (Shapiro and Stockman, 2001). Figure 3- 4 gives an example of different textures: dog fur, grass, river pebbles, cork, checkered textile, and knitted fabric (Sonka et al., 1998).

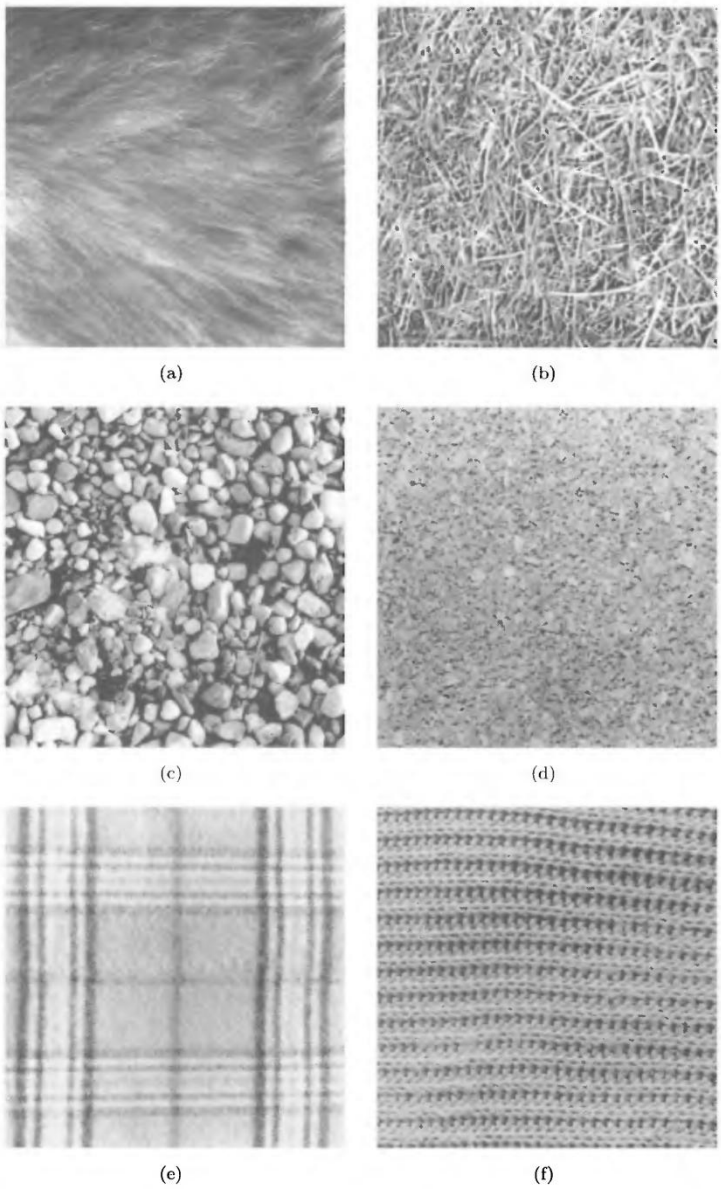

Figure 3- 4 Textures: (a) dog fur; (b) grass; (c) river pebbles; (d) cork; (e) checkered textile; (f) knitted fabric (Sonka et al., 1998)

The main aim of texture analysis is texture recognition and texture-based shape analysis. Some more precise features in the tone and structure of a texture, rather than simply being described as fine, coarse, grained, smooth, etc, are needed to be found to make machine recognition possible (Sonka et al., 1998). For this four different approaches have been established (Materka and Strzelecki, 1998):

- geometrical (or structural)
- statistical

- model-based
- signal processing (or transform) methods

For the structural approach texture is represented by well-defined primitives (the simplest geometric objects or shapes such as a point, a straight line or a cube) and a hierarchy of spatial arrangements of these primitives (Materka and Strzelecki, 1998). A structural description of a texture includes a set of identifiable primitives and a specification of their placement patterns (the probability of the chosen primitive being placed at a particular location (Materka and Strzelecki, 1998)), which needs to be efficiently computable. As the structural approaches are based on the theory that textures are made up of primitives appearing in a near-regular repetitive arrangement (Cun Lu and Yan Qiu, 2004), it can work well for man-made, regular patterns.

In contrast to structural methods, statistical approaches do not attempt to describe the exact structure of the texture (Cun Lu and Yan Qiu, 2004). They represent the texture indirectly by computing at each point in the image non-deterministic properties (or local features) that govern the distributions and relationships between the grey levels (Materka and Strzelecki, 1998) and deriving a set of statistics from the distributions of the local features (Ardizzoni et al., 1999). The autocorrelation (ACF) method (Haralick, 1979), edge frequency (EF) method (Haralick, 1979) and the well-known Grey Level Co-occurrence Matrix (GLCM) (Haralick et al., 1973) are classical statistical approaches to texture analysis.

Model-based texture analysis (Derin and Elliott, 1987, Manjunath and Chellappa, 1991) such as fractal dimension (Chaudhuri and Sarkar, 1995) and Markov Random Field (MRF) (Krishnamachari and Chellappa, 1997), using fractal and stochastic models, attempt to interpret an image texture by use of generative image and stochastic models respectively. It has been shown to be useful for texture analysis and discrimination (Kaplan and Kuo, 1995, Chaudhuri and Sarkar, 1995); however, it lacks orientation selectivity and is not suitable for describing local image structures

(Materka and Strzelecki, 1998). In addition, the computational complexity arising in the estimation of stochastic model parameters is another big problem.

Transform methods of texture analysis, such as Fourier (Chi-Ho and Pang, 2000), Gabor (Idrissa and Acheroy, 2002) and wavelet transforms (Arivazhagan and Ganesan, 2003), represent an image in a space whose co-ordinate system has an interpretation that is closely related to the characteristics of a texture (such as frequency or size). The usefulness of Gabor filters is limited in practice because there is usually no single filter resolution at which one can localise a spatial structure in natural textures (Osicka, 2008). The wavelet transforms feature several advantages over Gabor transform (Materka and Strzelecki, 1998):

- varying the spatial resolution allows it to represent textures at the most suitable scale,
- there is a wide range of choices for the wavelet function.

They make wavelet transforms attractive for texture segmentation, however the problem of being not translation-invariant still exists (Lam and Li, 1997).

3.4.1 Approaches of Estimating the Local Orientation of Images

Numerous techniques for estimating the local orientation or anisotropy of images have been developed so far. Rao (1990) introduced an approach to determine the principal orientation field of an image using the direction of local grey-level gradients. The Principal Component Analysis (PCA) (for explanation see (Pearson, 1901)) of local grey level gradient based method is also popular (Bazen et al., 2000). The 2-dimensional probability density function of the gradient vectors can be obtained by performing the PCA to the auto-covariance matrix of them. And the main direction of gradient can be measured from the auto-covariance matrix. This technique has been applied for fingerprint segmentation (Bazen and Gerez, 2002) in which the researchers used PCA to estimate the directional field from the gradients of grey level, and measure the orientation of the fingerprint by extracting the singular points where

the directional field is discontinuous. This method provided same results as the traditional method but it was not capable of detecting low-quality areas in a fingerprint.

Gu et al. (2004) improved the technique for the orientation field of fingerprints using a combination of two models including a polynomial model to approximate the orientation field globally and a point-charge model at each discontinuous or singular point. The two models were combined smoothly through a weight function. Experimental results showed that the method was more accurate and robust compared with the previous work.

However, most of the established methods including the methods shown above rely on the strong hypothesis that the gradients are well-defined, which make them very sensitive to noise (Bergonnier et al., 2007). The Fourier transform introduced below is also a powerful tool in measuring the local orientation of image. It is less sensitive to noise because the Fourier transform based methods do not measure the orientation directly by the location gray value gradients and also a noise removal operation can be easily performed based on the Fourier transform.

3.4.2 Fourier Transform (FT)

The Fourier transform is named in the honour of Joseph Fourier. Its basic concept is that any function of time or space that periodically repeats itself, or even functions that are not periodic (but whose area under the curve is finite), can be expressed as the sum of sine and/or cosine waves of different frequencies, each multiplied by a different coefficient (Gonzalez and Woods, 2007). Fourier transform has enormous applications in physics, engineering and chemistry, including communication (Gregory and Gallagher, 2002), image processing and data analysis.

3.4.2.1 Domains of Image

In image analysis, the domain is the set of "input" or argument values for which the image is defined. That is, the image provides an "output" or value for each member of the domain. Images can be represented in quite a few domains such as spatial domain; frequency domain (Zheng, 2005); Hough domain (Engelbrecht and Wahl, 1988); and Radon domain (Martinst and Rangayyan, 1997).

The spatial domain is the normal image space and most used in human life. The positions in spatial domain (pixels) directly correspond to real positions in the scene. Pixel value and location in this space is usually referred to by column *(x)*, row *(y)* and intensity value *(z)* (in the situation of 2 dimensions).

The image spatial frequency refers to the periodicity with which the image intensity values change. Therefore, the frequency domain is a space in which each image value at image position *(x,y)* represents the amount that the intensity values vary over a specific distance in the spatial domain image. The processing in the frequency domain is widely used in the image analysis field. (And our ears effectively perform a Fourier transform in hardware; we perceive frequencies rather than individual variations in air pressure).

The image information in the Hough domain shows the pixels of the original (spatial) image as sinusoidal curves. The corresponding curves to the points on a straight line in the original image (spatial domain) will intersect in the Hough domain. Similarly with the Hough domain, the information within the Radon domain shows a line through the original image as a point. Therefore, the Hough transform and Radon transform are efficient in detecting lines.

3.4.2.2 Spatial Frequency

Microscopy images are 2D functions $f(x,y)$ in spatial coordinates *(x,y)*. Each function gives the colours or grey intensities of positions in space.

Before looking at 2D image spatial frequency, a simple 1D periodic situation such as the sine function $\varphi(x) = \sin(x)$ is introduced.

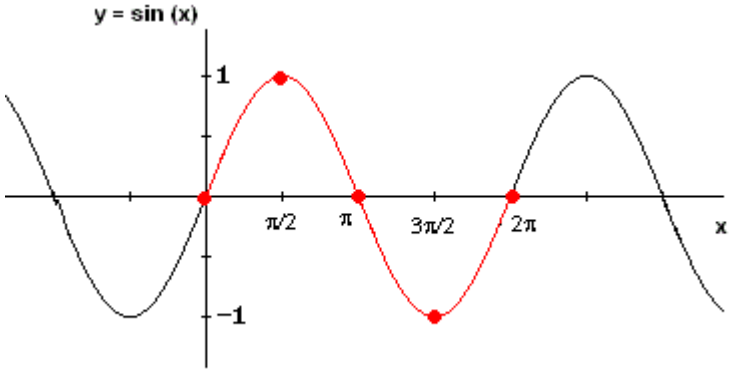

Figure 3- 5 The representation of a periodic function $\varphi(x) = \sin(x)$

The function in Figure 3- 5 consists of a fixed pattern that repeats endlessly in both directions. The length L or period of one cycle (shown in red) is 2π, and the frequency of the function is the reciprocal of the period. Depending on the units in which L or x-coordinate is measured, the term of frequency has different physical significance. If *x* coordinate is in the time domain, then the frequency is temporal frequency – a number of occurrences of a repeating event per unit time. If *x* coordinate is the measures of distance, then the frequency is spatial frequency, which is the number of complete cycles of the sinusoid per the image width *N* measured in the number of pixels. For the example in Figure 3- 5, every cycle has a length of 2π, which means every length unit represent $\frac{1}{2\pi}$ cycles, so the spatial frequency of the function ω is $\frac{1}{2\pi}$.

Besides the frequency, two other parameters are also important to the sinusoidal function – amplitude *A*, which is the peak deviation of the function from zero, and phase θ, which specifies (in radians) where in its cycle the oscillation is at *t=0*. These three parameters can determine any sinusoidal function in the form of $f = A \cdot \sin(\omega x + \theta)$.

3.4.2.3 Fourier Transform (FT)

However, most of the functions being used in scientific research are not sinusoidal. Any function of time or space, that satisfies some certain conditions (Dirichlet conditions, see (Sneddon, 1995)), can be expressed as the sum of sine and/or cosine waves of different frequencies, each multiplied by a different coefficient.

1-D Fourier Transform pair

The Fourier transform, *F(u)*, of a single variable, continuous function, *f(x)*, is defined by the equation (Gonzalez and Woods, 2007)

$$F(u) = \int_{-\infty}^{\infty} f(x) e^{-j2\pi ux} dx \qquad \text{(Eq3.6)}$$

The summation of sine and cosine waves might not be apparent in (Eq3.6), but, by applying Euler's equation (Eq3.7), gives Eq3.8:

Euler's equation: $e^{i\theta} = cos\theta + isin\theta$ (Eq3.7)

Where e = 2.71828…, and θ is an angle which can be any real number.

$$F(u) = \int_{-\infty}^{\infty} f(x)(cos2\pi ux - isin2\pi ux) dx \qquad \text{(Eq3.8)}$$

2-D Fourier Transform pair

The equation (Eq3.6) can be easily extended to two variables:

$$F(u,v) = \int_{-\infty}^{\infty}\int_{-\infty}^{\infty} f(x,y)e^{-j2\pi(ux+vy)}\,dxdy \qquad \text{(Eq3.9)}$$

Where $j = \sqrt{-1}$, *u*, *v* are the frequency variables, *x*, *y* are the spatial/time variables. If *f(x)* is continuous and integrable, and *F(u)* is integrable, which means that it exists for almost all real life signals, *f* can be reconstructed from its Fourier transform using the *inverse Fourier transform*

$$f(x) = \frac{1}{\sqrt{2\pi}}\int_{-\infty}^{\infty} F(u)e^{j2\pi ux}du \qquad \text{(Eq3.10)}$$

or

$$f(x,y) = \int_{-\infty}^{\infty}\int_{-\infty}^{\infty} F(u,v)e^{j2\pi(ux+vy)}\,dudv \qquad \text{(Eq3.11)}$$

The only difference between the forward and inverse Fourier transform is the sign above e, which makes it easy to go back and forth between spatial and frequency domains; it is one of the characteristics that makes Fourier transform useful (Abdellah, 2012).

Discrete Fourier Transform

As the task in image analysis is to deal with the information given by pixels, which are never continuous, the Discrete Fourier Transform (DFT) is used here rather than the equations mentioned above for the continuous functions.

Given *M* discrete samples of $f(x)$, sampled in uniform steps, *x = 0, 1, 2, …, M-1*,

$$F(u) = \frac{1}{M}\sum_{x=0}^{M-1} f(x)e^{-j2\pi ux/M} \quad \text{for u = 0, 1, 2, …, M-1} \qquad \text{(Eq3.12)}$$

Similarly, given *F(u)*, we can obtain the original function back using the inverse DFT:

$$f(x) = \sum_{x=0}^{M-1} F(u)e^{j2\pi ux/M} \quad \text{for x = 0, 1, 2, …, M-1} \qquad \text{(Eq3.13)}$$

Extension of the one-dimensional discrete Fourier transform and its inverse to two dimensions is straightforward, which is shown below:

$$F(u,v) = \frac{1}{MN}\sum_{x=0}^{M-1}\sum_{y=0}^{N-1} f(x,y)\, e^{-j2\pi(\frac{ux}{M}+\frac{vy}{N})} \qquad \text{for u = 0, 1, 2, …,}$$

M-1, and v = 0, 1, 2, …, N-1, (Eq3.14)

$$f(x,y) = \sum_{x=0}^{M-1}\sum_{y=0}^{N-1} F(u,v)\, e^{j2\pi(\frac{ux}{M}+\frac{vy}{N})} \qquad \text{for x = 0, 1, 2, …, M-1,}$$

and y = 0, 1, 2, …, N-1, (Eq3.15)

the variables *u* and *v* are the *transform* or the *frequency* variables, and *x* and *y* are the *spatial* and *image* variables.

Fast Fourier Transform

One of the main reasons that the DFT has become an essential tool in signal processing was the development of the fast Fourier transform (FFT) (Gonzalez and Woods, 2007). Computing the 1-D Fourier transform of *M* points using Eq3.14 directly requires on the order of M^2 multiplication/addition operations, while an FFT can compute the same result in only *MlogM* operations. The bigger the problem, the greater the computational advantage becomes.

There are many distinct FFT algorithms involving a wide range of mathematics, from

simple complex-number arithmetic to group theory and number theory. The most commonly used FFT is the Cooley-Tukey algorithm, which is based on the factorization of M.

3.4.2.4 Applications of Fourier Transform in Texture Analysis

There are many situations in graphics and vision, especially in image processing (Su and Chen, 2001, Fessler and Sutton, 2003) and filtering (Xia et al., 1995), where the use of a Fourier transform is beneficial.

Frequency filter (noise reduction, image smoothing and image sharpening)

The FFT transform has a property that adding together the transforms of two original images or functions produces the same result as the transform of the sum of the originals. This property is the basis to use subtraction to remove unwanted parts of images, mostly periodic noise or normal high frequency noise. The reverse operation of removing low frequency part of image is image sharpening.

Figure 3- 6 shows an image with its Fourier transform power spectrum. There is a gradual reduction in amplitude at higher frequencies of the image. Keeping the low frequencies and removing the high frequencies (image smoothing) can be accomplished by setting the amplitude of all sinusoids above a selected frequency to zero (Figure 3- 6 (c)). Conversely keeping the high frequencies and removing the low frequencies is to set the amplitude below a selected frequency to zero. The smoothed and sharpened images are shown in Figure 3- 6 (d) and (f) respectively.

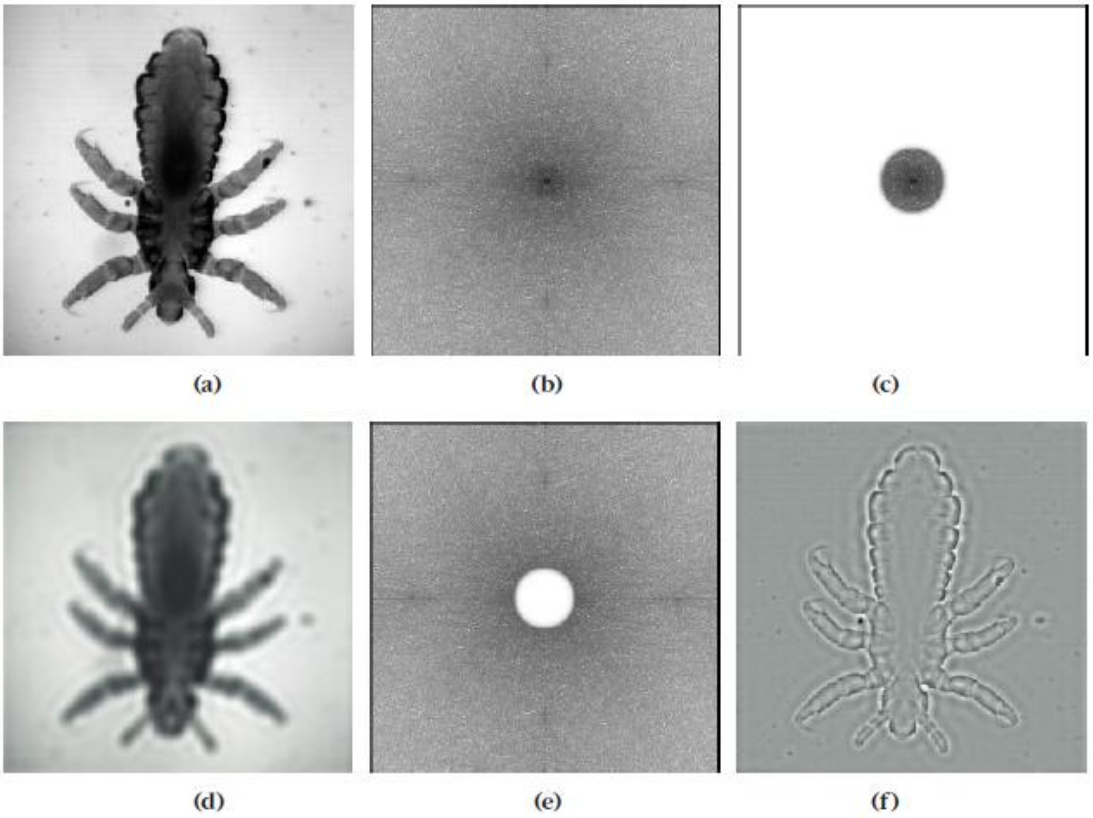

Figure 3- 6 Frequency filtering using the Fourier transform: (a) original image; (b) Fourier transform power spectrum; (c) reducing to zero the amplitude of all frequencies above a chosen value; (d) retransforming just the low frequencies (a low-pass filter); (e) reducing to zero the amplitude of all frequencies below a chosen value; (f) retransforming just the high frequencies (a high-pass filter) (Russ, 2011)

Wang and Liu (2010) used 2-D FFT for periodic noise (artefacts) removal on ultrasonic strain images. Firstly the 2-D FFT was performed to the initial images. The peaks on the spectrum domain were detected by comparing the pixel value in the domain to a predefined threshold. Then the selected impulses determined by the detected peaks were removed and the spatial domain was obtained by an inverse 2-D FFT. The results were promising with reduced artefacts but preserved useful details. Similar techniques were also performed by a number of researchers (Kaur et al., 2011, Lee and Han, 2012, Pellequer et al., 2012, Xia et al., 1995).

Pattern/Texture recognition

The Fourier theory is also a significant tool for pattern/texture features using its ability to discriminate frequencies. Its application in texture recognition can be roughly divided into two categories: texture similarity evaluation and texture orientation measurement.

Texture characterisation or texture similarity evaluation

The texture characterisation or texture similarity evaluation is normally performed by deriving a property measure such as energy from the Fourier domain of structures. The similarity of an unknown structure with a prototype structure is determined by how close their property measures are.

The method that Gibson and Gaydecki (1995) used for histological image segmentation was to compute a cost function, by which the difference of two Fourier moduli can be measured (definition see (Bergman et al., 2011)). The cost function can indicate how close two textures were. The results suggested that the method had a comparable performance to Haralick measures based technique with a greater speed.

El Oirrak et al. (2002) used Fourier Series to produce normalised descriptors for shape. In this study, they proposed the pseudo affine arc length instead of the normally used arc length in order to extract affine invariant descriptors using the Fourier Series coefficients. The obtained experimental results from synthetic and real shapes in binary images demonstrated the validity and applicability of their approach. Based on this study, the authors complemented colour information into the descriptors, making the technique able to discriminate two objects with the same shape but different colours (El Oirrak et al., 2003).

This method has two characteristics: it needs to be trained so it is only appropriate for the data having limited classes; it is not capable of providing a value of orientation.

Texture orientation descriptor

The output of Fourier Transform in general is orientation dependent. by applying a 2-D FFT onto an image with oriented pattern, the output image will show a clustering around a specific orientation (Yau et al., 1999). This is the basis of texture orientation measurement by FFT.

Zhou et al. (2001) proposed a texture feature extraction method based on Local Fourier Transform (LFT), which can describe the spatial distribution of pixel neighbourhood. As good classification accuracy as the Gabor (detailed explanation refer to (Feichtinger and Strohmer, 1998)) based features was obtained using the LFT-based features. However, the LFT just takes 8 adjacent pixels into account, which might not be suitable for large-scale spatial relationships.

The Gabor filters, which are also Fourier domain based operators, characterise the anisotropy of patterns by comparing their directional response in the frequency domain. It was shown to have beneficial properties in detecting the directional structures in image analysis, but their computational complexity has prevented their use in practice (Ilonen et al., 2005). Moreover, for the Gabor filter, the spectral resolution and spatial resolution are restricted by each other. The number of selected orientations is normally limited to 4 to 8 (Table 3- 1). Chen et al. (2004) proposed that for filter mask size 9*9, 33*33 and 61*61, four selected orientations (0°, 45°, 90°, 135°) were found to be the best choice. This orientation resolution might be enough for distinguishing oriented microstructures, but too low to measure the precise or approximate value of the orientation angle. The reason that the Gabor filter does not have high spectral resolution may lie in the usage of Gaussian functions, which causes

the blurring of input-signal in the mid-frequency space (Yu et al., 2004). However, the concept of measuring the orientation of a structure by detecting its response to a directional mask in the frequency domain is applicable to this study.

Table 3- 1 Review of the number of used orientations of Gabor filter in some literatures

Literatures	Number of used orientations
Turner (1986)	4
Jain and Farrokhnia (1990)	4
Manjunath and Ma (1996)	6
Jain et al. (1997)	4
Kruizinga and Petkov (1999)	8
Li and Shawe-Taylor (2005)	4-6
Yan et al. (2011)	4
Raheja et al. (2013)	8
Clausi and Deng (2005)	4

In Bergonnier's local anisotropy analysis study (2007), he compared three methods including auto-correlation method, polar mapping and anisotropy tensor. Both of the latter two methods are Fourier domain based, and the difference of them was the computation method of L2-norm (a norm defined for a complex vector, sometimes also called Euclidean Norm). In testing the local orientation of a texture, both of the two Fourier domain based methods provided a reasonable estimate over the auto-correlation method, and the anisotropy tensor method performed better than the other in terms of computation time. The research indicated again that the Fourier domain based technique has advantages over other methods in estimating the anisotropic or orientated textures.

As the FT based methods have been proved to be generally advantageous over other methods in detecting texture patterns with different orientations, frequencies, sizes,

and positions (Meyer and Coifman, 1997), it is used in the pearlitic colony characterisation in this study.

3.4.3 Grey Level Co-occurrence Matrix (GLCM) – Based Methods

3.4.3.1 Definition of GLCM

The GLCM, which was proposed by Haralick et al. (1973), is a technique that allows the extraction of second order statistical information from an image, regarding the spatial distribution of pairs of pixels as a matrix. This matrix contains the relative frequencies with which two neighbouring pixels (separated by distance *d* with angle *a*) occur in the image, one with grey tone *i* and the other with grey tone *j* (Marceau et al., 1990), or in other words, the matrix is an estimate of the joint probability of an "*i*" GL (grey level) pixel and of a "*j*" GL pixel, for a given pixel spacing and direction (Anys and Dong-Chen, 1995).

For a rectangular image consisting of N_x and N_y pixels in the horizontal and vertical spatial domains respectively, let $L_x = \{1,2, \dots, N_x\}$ and $L_y = \{1,2, \dots, N_y\}$, so the set $L_y \times L_x$ is the set of resolution cells of the image. The grey values of every pixel are quantized to N_g levels (Haralick et al., 1973). Then the initial image can be represented as a function of the coordinates in the new grey value system ranging from 1 to N_g.

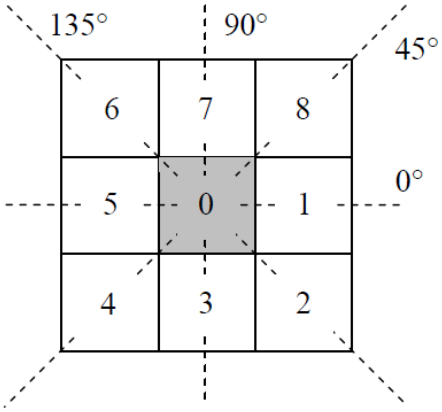

Figure 3- 7 Spatial relationship of pixels adjacent to pixel 0 in horizontal (0°), vertical (90°) and two diagonal directions (45° and 135°) (Fuchs, 2005)

The spatial relationship of the grey values is computed in order to determine the textural measures. Each pixel, excluding those on the periphery of the image, is defined to have 8 nearest neighbours (Figure 3- 7).

It is assumed that the texture-context information is specified by the matrix of relative frequencies P_{ij} with which two neighbouring resolution cells separated by distance d occur on the image, one with grey tone i and the other with grey tone$j$. Such matrices of grey-level spatial-dependence frequencies are also a function of the angular relationship between the neighbouring resolution cells, and the angles are formally quantized to 45° intervals. The unnormalised frequencies are defined by (Haralick et al., 1973)

$$P(i,j,d,0^{\circ}) = \#\begin{Bmatrix}((k,l),(m,n) \in (L_y \times L_x | k-m=0, |l-n|=d) \\ I(k,l)=i, I(m,n)=j\end{Bmatrix} \quad \text{(Eq3.16)}$$

$$P(i,j,d,45^{\circ}) = \#\begin{Bmatrix}((k,l),(m,n) \in (L_y \times L_x | (k-m=d, l-n=-d) or \\ (k-m=-d, l-n=d), I(k,l)=i, I(m,n)=j\end{Bmatrix} \quad \text{(Eq3.17)}$$

$$P(i,j,d,90^{\circ}) = \#\begin{Bmatrix}((k,l),(m,n) \in (L_y \times L_x || k-m|=d, l-n=0) \\ I(k,l)=i, I(m,n)=j\end{Bmatrix} \quad \text{(Eq3.18)}$$

$$P(i,j,d,135^{\circ}) = \#\begin{Bmatrix}((k,l),(m,n) \in (L_y \times L_x | (k-m=d, l-n=d) or \\ (k-m=-d, l-n=-d), I(k,l)=i, I(m,n)=j\end{Bmatrix} \quad \text{(Eq3.19)}$$

Where # denotes the number of elements in the set (Haralick et al., 1973), (k,l) the coordinate with grey value i and (m,n) the coordinate with grey value j (Al-Janobi, 2001). In order to compare results from different images, all the elements are normalised by dividing the total number of pixel pairs occurring in the image with distance d and angle $\propto$.

As an example for such a GLCM an image showing 16 pixels with four different grey levels labelled with the numbers 0 to 3 is presented in Figure 3- 8.

0 0 1 1
0 0 1 1
0 2 2 2
2 2 3 3

Figure 3- 8 The grey image (left) and its corresponding grey values (right) (Beyer, 2000)

The respective GLCM for the direct horizontal neighbour ($\alpha = 0^{\circ}$) with 1 pixel distance is used in this example.

neighbour pixel value -> ref pixel value:	0	1	2	3
0	0,0	0,1	0,2	0,3
1	1,0	1,1	1,2	1,3
2	2,0	2,1	2,2	2,3
3	3,0	3,1	3,2	3,3

Figure 3- 9 The combinations of the grey level occurrence that are possible for the test image, and their position in the GLCM (Beyer, 2000)

2	2	1	0
0	2	0	0
0	0	3	1
0	0	0	1

Figure 3- 10 Filled co-occurrence matrix for the test image (Beyer, 2000)

The possible combinations of grey level co-occurrence and the corresponding GLCM are shown respectively in Figure 3- 9 and Figure 3- 10. The top left cell in the GLCM indicates that within the image area there are two examples of a pixel with grey value 0 appearing to the right of another pixel with grey level 0 (reference pixel).

3.4.3.2 Second Order Statistics Based on GLCM

The extraction of the texture information contained in the image can be done using different texture parameters based on the normalised GLCM. In various papers, a set of 22 parameters has been proposed (Haralick et al., 1973, Soh and Tsatsoulis, 1999, Clausi, 2002), which extracts the textual features from the GLCM and characterises the corresponding image quantitatively. The mathematical description of these texture parameters is as follows:

1) Texture parameter 1 = Autocorrelation (Soh and Tsatsoulis, 1999)

$$f_1 = \sum_i \sum_j (ij) p(i,j) \qquad \text{(Eq3.20)}$$

2) Texture parameter 2 = Contrast (Soh and Tsatsoulis, 1999, Haralick et al., 1973)

$$f_2 = \sum_{n=0}^{N_g-1} n^2 \left[\sum_{i=1}^{N_g} \sum_{j=1}^{N_g} p(i,j) \right]_{|i-j|=n} \qquad \text{(Eq3.21)}$$

3) Texture parameter 3 = Correlation (Matlab, 2012)

$$f_3 = \frac{\sum_i \sum_j (i-\mu_x)\cdot(j-\mu_y)\cdot p(i,j)}{\sigma_x \cdot \sigma_y} \quad \text{(Eq3.22)}$$

4) Texture parameter 4 = Correlation (Haralick et al., 1973, Soh and Tsatsoulis, 1999)

$$f_4 = \frac{\sum_i \sum_j (i\cdot j)\cdot p(i,j) - \mu_x \cdot \mu_y}{\sigma_x \cdot \sigma_y} \quad \text{(Eq3.23)}$$

5) Texture parameter 5 = Cluster Prominence (Soh and Tsatsoulis, 1999)

$$f_5 = \sum_i \sum_j \left(i + j - \mu_x - \mu_y\right)^4 p(i,j) \quad \text{(Eq3.24)}$$

6) Texture parameter 6 = Cluster Shade (Soh and Tsatsoulis, 1999)

$$f_6 = \sum_i \sum_j \left(i + j - \mu_x - \mu_y\right)^3 p(i,j) \quad \text{(Eq3.25)}$$

7) Texture parameter 7 = Dissimilarity (Soh and Tsatsoulis, 1999)

$$f_7 = \sum_i \sum_j |i - j| \cdot p(i,j) \quad \text{(Eq3.26)}$$

8) Texture parameter 8 = Energy (Haralick et al., 1973, Soh and Tsatsoulis, 1999)

$$f_8 = \sum_i \sum_j p(i,j)^2 \quad \text{(Eq3.27)}$$

9) Texture parameter 9 = Entropy (Soh and Tsatsoulis, 1999)

$$f_9 = -\sum_i \sum_j p(i,j) \cdot log\ (p(i,j)) \quad \text{(Eq3.28)}$$

10) Texture parameter 10 = Homogeneity (Matlab, 2012)

$$f_{10} = \sum_i \sum_j \frac{p(i,j)}{1+|i-j|} \quad \text{(Eq3.29)}$$

11) Texture parameter 11 = Homogeneity (Soh and Tsatsoulis, 1999)

$$f_{11} = \sum_i \sum_j \frac{1}{1+(i-j)^2} p(i,j) \quad \text{(Eq3.30)}$$

12) Texture parameter 12 = Maximum Probability (Soh and Tsatsoulis, 1999)

$$f_{12} = \overset{MAX}{i,j} p(i,j) \quad \text{(Eq3.31)}$$

13) Texture parameter 13 = Sum of Squares (Haralick et al., 1973)

$$f_{13} = \sum_i \sum_j (i-u)^2 \cdot p(i,j) \quad \text{(Eq3.32)}$$

14) Texture parameter 14 = Sum Average (Haralick et al., 1973)

$$f_{14} = \sum_{i=2}^{2N_g} i \cdot p_{x+y}(i) \quad \text{(Eq3.33)}$$

15) Texture parameter 15 = Sum Variance (Haralick et al., 1973)

$$f_{15} = \sum_{i=2}^{2N_g} (i-f_{16})^2 \cdot p_{x+y}(i) \quad \text{(Eq3.34)}$$

16) Texture parameter 16 = Sum Entropy (Haralick et al., 1973)

$$f_{16} = -\sum_{i=2}^{2N_g} p_{x+y}(i) \cdot log\ [p_{x+y}(i)] \quad \text{(Eq3.35)}$$

17) Texture parameter 17 = Difference Variance (Haralick et al., 1973)

$$f_{17} = variance\ of\ p_{x-y} \quad \text{(Eq3.36)}$$

18) Texture parameter 18 = Difference Entropy (Haralick et al., 1973)

$$f_{18} = -\sum_{i=0}^{N_g-1} p_{x-y}(i) \cdot log\ [p_{x-y}(i)] \quad \text{(Eq3.37)}$$

19) Texture parameter 19 = Information Measure of Correlation 1 (Haralick et al., 1973)

$$f_{19} = \frac{HXY-HXY1}{max\ (HX,HY)} \quad \text{(Eq3.38)}$$

20) Texture parameter 20 = Information Measure of Correlation 2 (Haralick et al., 1973)

$$f_{20} = (1 - exp\ [-2 \cdot (HXY2 - HXY)])^{0.5} \quad \text{(Eq3.39)}$$

21) Texture parameter 21 = Inverse Difference Normalised (IDN) (Clausi, 2002)

$$f_{21} = \sum_i \sum_j \frac{p(i,j)}{1+|i-j|/{N_g}^2} \quad \text{(Eq3.40)}$$

22) Texture parameter 22 = Inverse Difference Moment Normalised (IDMN) (Clausi, 2002)

$$f_{22} = \sum_i \sum_j \frac{p(i,j)}{1+(i-j)^2/{N_g}^2} \quad \text{(Eq3.41)}$$

The following abbreviations are used:

$p(i,j)$	$(i,j)^{th}$ entry in a normalised GLCM with distance d under angle α, $= P(i,j)/R$
$p_x(i)$	sum of the i^{th} column of the GLCM with $p_x(i) = \sum_{j=1}^{N_g} p(i,j)$
$p_{x+y}(k)$	$p_{x+y}(k) = \sum_{i=1}^{N_g} \sum_{j=1}^{N_g} p(i,j) \quad i+j=k, \quad k=2,3,\dots,2N_g$
$p_{x-y}(k)$	$p_{x-y}(k) = \sum_{i=1}^{N_g} \sum_{j=1}^{N_g} p(i,j) \quad \lvert i-j \rvert = k, \quad k=0,1,\dots,N_g-1$
$\mu_x, \mu_y, \sigma_x, \sigma_y$	means and standard deviations of p_x and p_y
$\sum_i$ and $\sum_j$	$\sum_{i=1}^{N_g}$ and $\sum_{j=1}^{N_g}$ respectively
HX	entropy of p_x
HY	entropy of p_y
HXY	$HXY = -\sum_i \sum_j p(i,j) \cdot \log(p(i,j))$
HXY1	$HXY1 = -\sum_i \sum_j p(i,j) \cdot \log(p_x(i) \cdot p_y(j))$
HXY2	$HXY2 = -\sum_i \sum_j p_x(i) \cdot p_y(j) \cdot \log(p_x(i) \cdot p_y(j))$

(note: the IDN was given as $\sum_i \sum_j \frac{p(i,j)}{1+|i-j|^2/{N_g}^2}$ in the original paper. However, according to the context it is believed that there is a mistake here and the expression should be Eq3.40.)

A few parameters with identical name may have different equations due to their different sources. But they represent similar property of images.

The GLCM based features are commonly used as statistical parameters in image texture analysis. A classifier or a combination of classifiers is usually applied together to group these features to categories. Xian (2010) used the GLCM texture features

with a fuzzy support vector machine to identify malignant and benign liver tumors from ultrasonography and achieved high accuracy. Manivannan et al. (2012) presented an efficient and highly reliable automatic selection of optimal segmentation algorithm for characterising particulate matter based on the GLCM features of image and a new self-regulating SVM classifier. The performance of the new technique is drastically improved over the previous histogram-based SVM. However, the conventional SVMs are only valid for data with two categories. Sharma et al. (2008) used first- (mean, standard deviation and entropy) and second- order (14 GLCM features) statistical features for a segmentation based on artificial neural networks. The algorithm needed to be supervised for selecting texture primitives. On the medical images (soft tissue images) that were used in this study, the algorithm performed well. Arebey et al. (2012) applied the GLCM texture features with the multi-layer perceptron (MLP) (a feedforward artificial neural networks model) and the K-nearest neighbour (KNN) classifier for bin image classification and grading. In their work the KNN classifier outperformed MLP, which supports the use of the KNN classifier as a general starting point for image classification task. They also reduced the number of features used to four using the feature analysis, and found that that did not significantly affect classification accuracy compared to the use of ten features.

3.4.3.3 Comparative Studies and Reviews

Besides GLCM, there are a large number of texture extraction methods as mentioned before. Therefore the selection of appropriate features is important. Sharma and Singh (2001) compared 5 feature extraction methods including auto-correlation, edge frequency, primitive-length, Law's method, and co-occurrence matrices. By changing the positional difference in the horizontal and vertical direction between 0 and 9, a total of 100 features were given by the autocorrelation technique. The averaged feature values in all four directions were used in the GLCM-based measurements. 70 and 125 features were computed using the edge-frequency based method and Law's method respectively. The leave-one-out method was used to select the most

appropriate features for all feature extraction methods. These methods were applied with Meastex database containing examples of artificial and natural textures. Finally a total of 944 images containing 4 classes (asphalt, concrete, grass and rock) were obtained. The data for these classes is overlapping no matter what feature extraction method was employed. The classification was performed by k-nearest neighbour classifier and Linear Discriminant Analysis. It was found that the GLCM and Law's method performed better than other techniques. It was also found that there was difference in results between different classifiers (the linear analysis and nearest neighbour). The best overall result using nearest neighbour methods was obtained with co-occurrence matrices, whereas the best using linear analysis was obtained using combined set of features.

Ohanian and Dubes (1992) carried out a performance evaluation for four popular classes of textural features including GLCM features, Gabor filters, Markov Random Field parameters and fractal based features. Classification was performed and assessed with a KNN classifier and the Leave-one-out selection method (refer to section 6.3.3 in the thesis). Four classes of images which included synthetic images (fractal surface and Gaussian Markov Random Field images) as well as natural images (leather samples and painted surfaces) were used in the evaluation. The GLCM features generally had a better performance than the other three feature extraction methods and it was suggested they should be always considered with small window sizes. This conclusion has a high reference value to the phase classification study since small window sizes are assumed to be more suitable than large window sizes because of the small scale of the characteristics of the phases. This literature also provides evidence supporting the use of the KNN classifier and the leave-one-out selection method, which will be used in this PhD.

du Buf et al. (1990) presented a comparative study of texture features in unsupervised image segmentation. Co-occurrence method, fractal dimension, Laws, Hadamard

masks, spectral decomposition and grey-level extrema method were used for feature extraction. A quadtree smoothing-based method developed by Spann and Wilson (1985) was applied for segmentation. The tests were performed on a set of 20 texture images, and evaluated by the mean boundary error. The results obtained showed that the co-occurrence method, Laws masks and Hadamard masks gave best overall results. Another conclusion from the authors was that the combination of features from different extraction methods does not always guarantee an improvement of the segmentation result.

From the above literatures and the listed ones in Table 3- 2 that have been reviewed on image texture analysis, it can be concluded that (1) there is no universally best feature for all image analysis issues. Different texture patterns can be characterised using different feature extraction methods according to some certain characteristics of the patterns such as size, shape, brightness etc. These features are more distinguishable in characterising the patterns than other features; (2) the co-occurrence method has an overall good performance in the texture analysis research with either synthetic images or natural images, and hence is worthy to be tried first when working on texture analysis. Also, the following point needs to be clarified: most of the studies aim at classifying a whole image with a certain size (ranging from 8x8 to 512x512) to a known category, while my study is aiming at classifying individual pixels.

Table 3- 2 Some of the reviewed literatures on the image texture analysis

researchers	Testing images	Texture feature extraction methods	Classification or segmentation methods	Feature selection methods	performances	Other notes
Weszka et al. (1976)	9 terrain classes (urban, suburb, lake, woods, scrub, railroad, swamp, marsh, orchard) with 6 images in each class	Fourier power spectrum, second order grey level statistics, grey level difference statistics and grey level run length statistics		Linear discriminate technique	Features based on 2-order and difference statistics do about equally well (2-order statistics did best for single features, and the difference statistics perform best for feature pairs)	Higher-order classifier than the Fisher linear discriminant and leave-one-out testing scheme were not used because of the smallness of the data.
Parikh (1977)	245 Cloud images belonging to 4 type (low, mix, cirrus and cumulonimbus)	45 spectral features including mean, standard deviation and cumulative based features; The textural features used are based on those proposed by Weszka et al. (1976)	Maximum likelihood , multiclass voting, and multiclass one-against-the-rest classifier	Linear discriminate technique	91% classification accuracy on the 4 class problem and 98% on the three class problem. The spectral features were more important than the textural features.	The classifiers tested were similar in performance.
Conners and Harlow (1980)	Synthetic textures (128x64 pixels) which can be represented by random fields generated using Markov chains.	Co-occurrence methods (SGLDM(also called GLCM)); the grey level run length method; the gray level difference method and the power spectral method	Performance evaluated by the number of visually distinct texture pairs that each method can discriminate (detail please refer to original paper)		The co-occurrence method is the most powerful algorithm of the four considered. For other three methods, they cannot discriminate between a Markov texture from its 180 degree rotated version. GRLM is also very sensitive to noise.	

Augusteijn et al. (1995)	A TM image of size 1907 x 1784 pixels showing 14 categories of a land cover region. The ground truth map of this image was obtained from Huber and Casler (1990). 9 categories in the total 14 which were available in sufficiently large segments (8x8 in this study) were used in the study.	Co-occurrence matrices, grey level differences, texture-tone analysis, Fourier transform based features and Gabor filters	Neural network classifier		No universally best feature is found. The best feature sets depend on the data. Roughly 90% recognition results was obtained using Fourier based features and 86% was obtained with the co-occurrence features.	When Fourier features and Gabor filters are carefully chosen, these measures can be just as effective or possibly more effective than co-occurrence measures for certain sets of data. The co-occurrence method was considered to be slow because the calculations involve 256 grey levels and the effect of the reduction of the number of grey levels was not investigated.
Reuze et al. (1994)	MR muscle tissue images with 3 classes: man, woman, patient	Fractal, co-occurrence, higher order statistics and mathematical morphology		Linear discriminant analysis	Morphological methods (49 correct in 67) and co-occurrence features (47 in 65) gave the best performance.	
Tuceyran and Jain (1998)	Survey of the various texture analysis applications in the area of materials, medical image analysis, document processing and remote sensing	Statistical methods, geometrical methods and model based methods of signal processing			The co-occurrence features are better suited for texture analysis rather than image segmentation. The autocorrelation features can be used to assess the amount of regularity, fineness or coarseness.	

Backes et al. (2013)	Three image databases were used. 1) brodatz texture album (1776 images; 111 classes); 2) VisTex colour textures; 3) the suite Outex_TC_00013.	First-order histogram (Materka and Strzelecki, 1998); Fourier descriptor (Azencott et al., 1997); Gabor filters (Jain and Farrokhnia, 1990); GLCM; Discrete Cosine Transform(Ng et al., 1992); Grey level difference matrix (Weszka et al., 1976); Wavelet descriptors (Randen and Husoy, 1999); Local Binary Pattern Variance (Guo et al., 2010); Complete Local Binary Pattern (Guo and Zhang, 2010); Local Ternary Pattern (Suruliandi et al., 2011, Tan and Triggs, 2010).		Linear discriminant analysis and leave-one-out algorithm	Different features have different performance with different datasets and different situation of noise as well. Generally the GLCM features performed well. One of its advantages is its small number of features (32 features). For instance, it performed generally (except for the rotated textures) better than the Local Ternary Pattern based features which are using 32786 features.	

3.4.4 Texture Classification

After texture features are extracted, they need to be classified into several categories. The four best-known approaches for texture classification are: 1) template matching, 2) statistical classification, 3) syntactic or structural matching, and 4) neural networks. These methods are not necessarily independent.

Template matching is one of the simplest and earliest approaches. In this method, a template or a prototype of the pattern to be recognized is available. The pattern of the new data is determined by computing the similarity between the stored template and the new data. One of the disadvantages of this approach is that it would fail if the patterns are distorted due to the imaging process, viewpoint change, or large intra-class variations among the patterns (Jain et al., 2000).

Statistical approach is a method of representing each pattern in terms of d features or measurements which are placed into a vector. A d-dimensional space can be generated. The goal is to choose those features that allow pattern vectors belonging to different classes to occupy compact and disjoint regions in the d-dimensional space. To compare patterns, this approach uses measures by observing distances between points in the multi-dimensional space.

Syntactic approach, also called structural pattern recognition system, is based on the relation between features. In this approach, patterns are represented by structures which can take into account more complex relations between features than numerical feature vectors used in the statistical approach. Patterns are described in a hierarchical structure composed of smaller sub-structures. Unfortunately, the syntactic pattern recognition approach is generally very difficult to handle (Parasher et al., 2011).

Neural network approach is a self-adaptive trainable process which is able to learn to

resolve complex problems based on available knowledge. An artificial neural network (ANN) based system simulates how the biological brain works. It consists of an extremely large number of simple processors with many interconnections. Each processing element can pass information to another by those interconnections. The approach attempts to use some organizational principles (such as learning, generalization, adaptivity, fault tolerance, distributed representation and computation) in a network of weighted directed graphs in which the nodes are processors and directed edges (with weights) are connections between processors. Neural network approaches have the ability to learn complex nonlinear input-output relationships, use sequential training procedures, and adapt themselves to the data (Jain et al., 2000). Most of the well-known neural network models are based on or similar to classical statistical pattern recognition methods (Jain et al., 2000, Ripley, 1993, Anderson et al., 1990).

Among these pattern recognition methodologies the statistical approach is most intensively used in practice because it is the simplest to handle. Therefore, this method is applied in this study. The recognition system is operated in two modes: training (learning) and classification (testing) (Figure 3- 11).

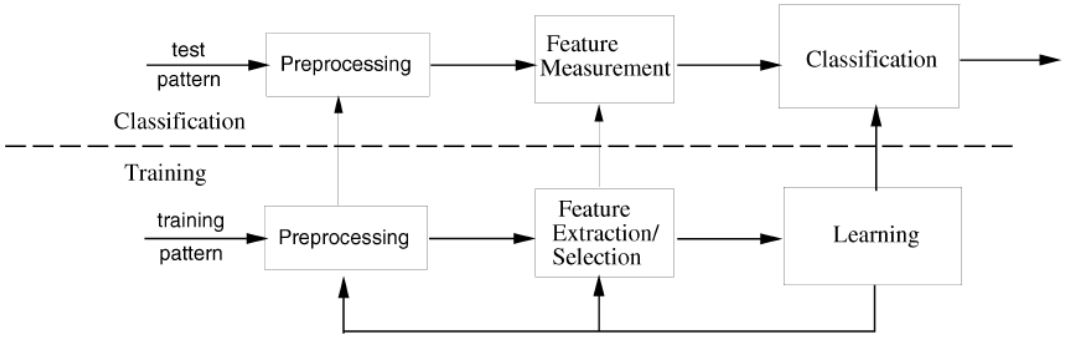

Figure 3- 11 Model for supervised pattern recognition (Jain et al., 2000)

3.5 Image Segmentation Techniques

3.5.1 Types of Segmentation Techniques

In computer vision, segmentation is the process of partitioning an image into several disjoint regions whose characteristics such as intensity, colour and texture, are similar (Raviraj et al., 2011). More precisely, image segmentation is the process of assigning a label to every pixel in an image such that pixels with the same label share certain visual characteristics (Singh and Singh, 2010). Reed and Dubuf (1993) regarded the image segmentation as a combination of independent subprocesses of texture feature extraction, feature selection or reduction, followed by a segmentation algorithm. As the texture feature extraction methods have been reviewed in previous section (section 3.4) and the feature selection method will be briefly described in section 6.3.3, this section will focus on the segmentation algorithm. Based on the features that segmentations used, the algorithms can be grouped into two categories: grey level based algorithms and textural feature based algorithms (Sharma et al., 2008, Wu et al., 2009). Based on what objects that the technique can detect, the segmentations can be divided into three groups in another way — pixel-based, edge-based and region-based.

Pixel-based segmentation: In the conventional pixel-based segmentation technique, each pixel is segmented based on grey level values (histogram) rather than contextual information. This is the key point: a pixel is classified by its individual brightness, regardless of those of its immediate neighbours. Usually a histogram is computed from all of the pixels in an image, and the peaks and valleys in the histogram are used to locate the clusters in the image (Shapiro and Stockman, 2001). Beyond the grey level thresholding method, pixel-based segmentation also consists of other complicated techniques such as grey level clustering (Kavitha and Chellamuthu, 2010, Fan-Chei et al., 2009, Chen et al., 2011), multivariate classifiers and iterative

contextual pixel classification. In grey level clustering technique a K-means algorithm (aiming to partition *n* observations into *k* clusters in which each observation belongs to the cluster with the nearest mean (Xin et al., 2011)) is used to partition all pixels in an image into *K* clusters. Multivariate classification uses more spectral information apart from grey level such as colour. It is usually used with hyperspectral imaging method (Nanyam et al., 2012, Rajkumar et al., 2012). Iterative contextual classification is also focusing on the relationship of the nearby pixels. A probability model is usually built in this technique to describe the relationship between a pixel and its neighbours. Therefore the parameters of the model need to be estimated and it affects the classification performance. Another difficulty of this technique is in propagating contextual information through the image although the computation is still kept in small neighbourhoods.

Edge-based segmentation: Region boundaries and edges are closely related, since there is often a sharp adjustment in intensity at the region boundaries. In this technique, an edge filter is applied to the image; pixels are classified as *edge* or *non-edge* depending on the filter output (Glasbey and Horgan, 2000). Most of the edge-based methods can be grouped into two categories, search-based and zero-crossing based. The search-based methods detect edges by first computing a measure of edge strength, usually a first-order derivative expression such as the gradient magnitude, and then searching for local directional maxima of the gradient. There are several types of first-order derivative operators including Roberts operator (Roberts, 1963), Prewitt operator (Prewitt, 1970), Sobel operator (Kanopoulos et al., 1988). Canny (1986) proposed a method with generally better performance using two criteria with a multiple response measure. The zero-crossing-based methods search for the zero crossings in a second-order derivative expression computed from the image in order to detect edges. Laplacian filters are mostly applied in this approach.

Edge detection is a common approach for detecting meaningful discontinuities in grey

level, but the detection quality of this method is highly dependent on lighting conditions, the presence of objects of similar intensities, density of edges in the scene, and noise (Nadernejad et al., 2008), and discontinuous and even false edges are often given because of that (Kumar and Sahoo, 2010, Davis, 1975), which will make the subsequent segmentation work difficult.

Non-linear edge detectors that generally use neighbourhoods of many sizes at every point were also developed (Rosenfeld et al., 1969, Rosenfeld, 1972). The "SUSAN" edge detector is a popular non-linear edge detection method. It introduced a concept of a Univalue Segment Assimilating Nucleus (USAN) to represent a local area having similar brightness within a certain size of neighbourhood. The USAN area is at a maximum when the nucleus lies in a flat region of the image. It falls to half of the maximum mask area near a straight edge, and falls even further when inside a corner (Figure 3- 12). This property is the main determinant of the presence of edges. Rezai-Rad compared SUSAN and Sobel edge detection methods on Magnetic Resonance Imaging (MRI) images, and found that the SUSAN provided better edge localization and connectivity, and was less affected by the noise than Sobel detector.

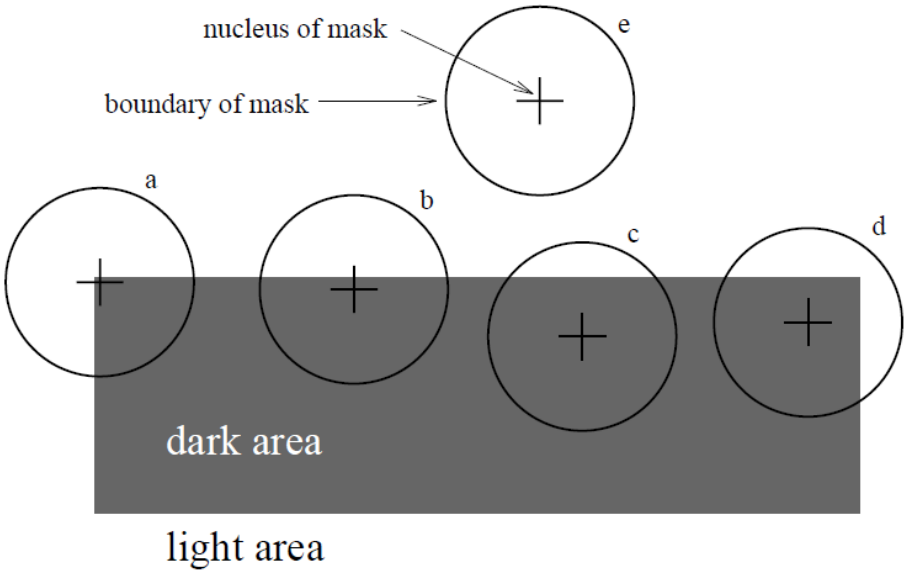

Figure 3- 12 Four circular masks showing the USAN areas at different places on a simple image; USANs are shown as the dark parts of the masks (Smith and Brady, 1997).

However, all edge detectors have a big weakness, which is the creation of incomplete or unneeded edges as shown in Figure 3- 13. The two regions (region A and B) in Figure 3- 13 are separated by a sharp edge and a smooth transition region. The grey level gradient in the vertical direction between the transition region and region A and B is much bigger than that in the horizontal direction, which leads to the generation of incomplete and unneeded edges by the edge-based method (shown in Figure 3- 13 (a)). The region-based methods, which are going to be reviewed in next part, segment regions using the properties of regions other than the properties of edges, therefore the incomplete edges are avoided.

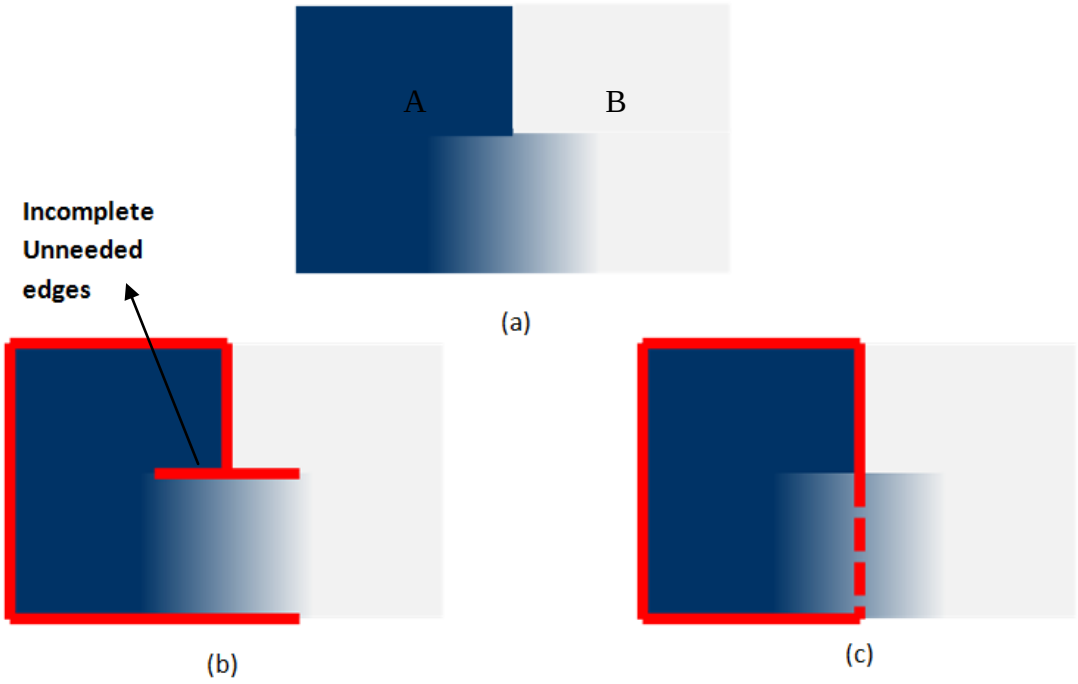

Figure 3- 13 A diagram showing the incomplete or unneeded edges that the edge-based segmentation generates with comparison segmentation by region-based method: (a) the initial image containing two regions; (b) the detected edges by edge-based method; (c) the detected edges by region-based method

Region-based segmentation: region-based segmentation methods attempt to determine or partition the region directly according to common image properties by

grouping together pixels which are neighbours and have similar properties while splitting groups of pixels which are dissimilar in properties. A significant advantage of the region-based segmentation is that it guarantees to produce coherent regions. Linking edges, gaps produced by missing edge pixels, etc. are not an issue. Several methods are commonly used for region-based segmentation: region growing, region merging, region splitting, and region split-merge.

Region growing is the process of joining neighbouring points or collection of points into larger regions based on specific homogeneity measures such as grey level, colour, texture, etc (Zucker, 1976). Arbitrary seeds should be selected in the image first as starting positions for growing. Region merging is similar to region growing but it does not require seed selection. In region merging, an image is divided into an initial set of regions such as one region per pixel, or 2x2, 4x4, etc. Then similar regions are merged. Region splitting is a reverse process of region merging. Its basic idea is to break the image into a set of disjoint regions which are coherent within themselves. It initially takes the whole image to be the area of interest then whether the region splits depends on whether all pixels contained in the region satisfy some similarity constraint. The split and merge algorithm is to perform a merging process after each split or all splits.

Deng and Manjunath (2001) used a region growing approach for the segmentation of colour-texture regions in images and video. A variance or homogeneity measure was used in this study to determine the initial seed points in the image (the first step of the region growing method is to select some seed points based on user defined criteria. Then the regions are grown from the seed points based on one criterion or a group of criteria which define a region). The algorithm had a good performance with an example flower garden picture. However, the suitable selection of seed points is important for the segmentation and affects the results greatly.

The image merging process can either start from small blocks that have been divided

from the whole image (with same size such as 1x1, 2x2, etc), or it can also start with oversegmented results obtained by low-level segmentation algorithms. In the novel region merging algorithm for automatic object extraction proposed by Zha et al. (2013), the mean shift algorithm (Comaniciu and Meer, 2002) was chosen to perform initial segmentation. In the region merging process, the regional histogram based similarity measure was used as the criterion. The order of merging was basically determined by the similarity and size of the adjacent regions. 10 natural images with different scenes were used to test the algorithm and comparison was made between the algorithm and dynamic region merging (DRM). It showed that this algorithm performed better than the DRM on 9 images.

Region growing/merging is a classical segmentation method. KumarV and Sumithra (2012) compared the performance of different medical image segmentation algorithms including thresholding, clustering and image growing. In the segmentation of normal and abnormal brain MRIs, the region growing method gave better output than the other two methods, but it required manual interaction to select the seed point in their research.

The region splitting approach is hardly used alone because its final segmentation would probably contain many neighbouring regions that have identical or similar properties. Lemkin (1979) studied this technique and proposed that it could be applied for a particular class of images in which central parts of the desired regions are known and additional information about the edge pixel regions is known. So the use of region splitting is much limited.

Region split-merge is a combinative technique of splitting and merging. Laprade (1988) used the split-and-merge for the segmentation of aerial photographs. The least square fits of the intensity surface were computed as a predicate for both splitting and merging. This method of segmentation appeared promising. However, the least square

fits based predicate is only suitable for regions with uniform intensities. In our case of pearlite colony segmentation, the main feature to separate colonies would be the misorientation between colonies rather than the homogeneity of each colony due to the presence of the bending and fragmented cementite lamellae. Liu and Sclaroff (2004) introduced a deformable template to guide the splitting and merging operations (Lifeng and Sclaroff, 1999). In this technique, a shape model is specified in terms of functions applied to a closed polygon. During the segmentation process, the image is firstly oversegmented. Then the algorithm tests various combinations of candidate region grouping by recovering the model alignment and deformations to match the specified shape model. The algorithm performed well with images containing objects with similar shape such as bananas or leaves. Although it is not suitable for the pearlite colony segmentation because the pearlite colonies have a range of different shapes, it showed the good performance of the split-and-merge algorithm.

Comparison of Region Growing and Split-Merge

The performance of region growing and split-merge algorithms was compared in previous research. Sharma (2001) performed a performance evaluation of image segmentation methods in scene analysis. She compared four segmentation algorithms including fuzzy c-means (FCM) clustering based algorithm, histogram thresholding based segmentation, region growing segmentation and split-merge segmentation. The segmentation methods were evaluated by comparing the object recognition accuracy after the segmentation process. Four image data sets (MeasTex, VisTex, PANN Vegetation, PANN Natural Object) were used in her study and split-merge based algorithm showed the highest recognition rate. It was also found that the use of nearest neighbour classifier improved the quality of results than the linear classification in general.

Szenasi (2013) also compared the split-merge algorithm with the original region

growing method for medical image segmentation. He did the comparison with 39 sample images. The results showed that 19 images were better segmented with split-merge, while 17 images were better with region growing. And it was also found that the run time of split-merge algorithm was insignificant compared to the runtime of the region growing with small dimensional images.

Region growing/merging and split-merge algorithm both have strengths and disadvantages; none of them can be universally appropriate for all image segmentation problems. The region growing/splitting algorithm normally starts from small blocks even individual pixels, which makes these algorithms sensitive to noise. Moreover, in the pearlite colony segmentation in this study, the Kernel Average Misorientation value along the edge between two adjacent regions and the difference of average grey level between the regions will be used as the criteria to determine whether these two regions can form a colony. If the regions are too small, the features would be easily affected by noise or discontinuities in the image and thus affect the segmentation. The split-merge algorithm can avoid this by starting the merging process from relatively large blocks that the splitting process generates. Thus split-merge process is used in this study for segmentation.

3.5.2 Measures for Image Segmentation Evaluation

Unnikrishnan et al. (2005) presented the following broad methods for assessing the performance of segmentation methods as follows:

1. Region differencing: measures by computing the degree of overlap between clusters or the cluster associated with each pixel in one segmentation and its "closest" approximation in the other segmentation (Huang and Dom, 1995).
2. Boundary matching: measures by matching boundaries between segmentations, and computing some summary statistics of match quality (Freixenet et al., 2002, Huang and Dom, 1995).

3. Information theory: in each segmentation compute a measure of information content, which is related to the conditional entropies between the class label distribution of the segmentations, and compute how much this information one segmentation gives about the other (Meilă, 2003).
4. Non-parametric tests: Cohen's Kappa (Cohen, 1960), Jaccard's index, Fowlkes and Mallow's index (Fowlkes and Mallows, 1983) are popular non-parametric measures in literatures. The latter two work by counting pairs of pixels that have compatible label relationships between two segmentations.

The region based evaluation method (method 1) was applied in this work because it relates most directly to the correct segmentation of regions (colonies) and hence the average colony size, which is the parameter that is to be characterised in this work.

Chapter 4. Literature Review on the Applications of Image Analysis to Steel and Metallurgy

When a material is fabricated, its properties will depend on the morphology of its microstructure, which in turn depends on the process used (Hall, 1951, Spychalski et al., 2002). Almost all materials have a microstructure, and the condition of this microstructure can often tell why a component fails or behaves in an unpredictable way. In general, microscopy and imaging strive to link the macroscopic properties of a material to its underlying microstructural features in an effort to predict a materials performance (O'Flaherty and Edwards, 2011).

4.1 Non-image-based Microstructural Characterisation Methods

There are a large number of techniques available to characterise the microstructure of steels. Specifically, on the phase characterisation and quantification issue in steel, electron microscopy techniques and especially XRD quantitative analysis methods are widely used, but magnetic and ultrasonic approaches have also been attempted.

Wang et al. (2006) carried out phase identification (ferrite, bainite, retained austenite and martensite) by measuring the height of various phases by means of atomic-force microscopy (AFM) after etching. The identification was verified by use of optical microscopy (OM), scanning electron microscopy and transmission electron microscopy. However, it is difficult to automatically measure the phase fractions using the surface micrographs that are obtained by these techniques. The quantitative analysis was carried out with X-ray diffraction (XRD) and thermodynamic calculation. The accuracy of the quantitative analysis methods was not assessed in this paper. Wang et al. (2010) also carried out a similar microstructure characterisation study with martensitic steel having initial martensite, fresh martensite after quenching and partitioning and retained austenite present. The identification of phases was performed by means of SEM, TEM and EBSD. The fraction of each phase was

measured by XRD and by a computational model. It was found that the XRD measured phase volume fraction was roughly in agreement with the model-based predicated value. However, its usage is limited due to the cost and low popularity of the XRD instrument.

Moorthy et al. (1997) used magnetic Barkhausen noise (MBN) analysis to carry out the microstructural characterization of quenched and tempered carbon steel. When a ferromagnetic material is subjected to a varying magnetic field, the flux density changes during magnetization induce voltage in the pick-up coil. The phenomenon is called MBN and it is sensitive to microstructural variation such as grain size, precipitation of second phase particles (size, morphology and number), dislocation density and strain in the material. The MBN has started to be used for the evaluation of the proportion of phases in the materials that have different MBN sensitivities. In Kleber et al's research (2008), they used the MBN to characterise different grade of commercial dual-phase steels. It showed that the amplitude field position of the Barkhausen noise peak is linearly dependent on the ferrite proportion for this series of steel when other influencing factors keep constant. That makes the evaluation of steels with varying proportion of ferrite phases achievable with the help of calibration curves. However, the change in peak position is far more complicated. Its evolution is no long linear when the phases have different magnetic properties. Due to the high sensitivity of the MBN signal to other parameters such as the residual stress or the dislocation density, samples with similar thermomechanical treatments and same experimental conditions for the MBN measurements are necessary, which greatly limits the application of MBN.

Ultrasonic sound can also be used for structure characterisation based on its velocity variation in different microstructures. Freitas et al. (2010) used this property to characterise steel with different microstructures: ferrite, pearlite, ferrite-pearlite and martensite. By measuring the velocity of ultrasonic in the longitudinal and transverse

direction of the steel samples, different microstructure can be correctly identified. It is also capable of detecting the microstructure changes such as the lamellar thickness of the pearlite structure.

Like the magnetic technique, the ultrasonic signals are affected by a number of factors apart from phase constituents. By this method, the microstructure is evaluated with regard to the changes in the velocity of propagation, loss of amplitude and analysis of backscattered signal (Freitas et al., 2010). So it is usually used for discriminating a series of microstructures rather than quantitatively analysing one microstructure.

Even less research has been carried out on the measurement of the pearlitic colony size because it is usually very difficult or impossible by means of both metallographic methods and electron backscattered diffraction measurements (Walentek et al., 2006). Manually drawing the boundaries was the main characterisation method used (Pickering and Garbarz, 1987). Boundaries of a colony can be recognised from the appearance and spatial orientation of the cementite lamellae (Garbarz and Pickering, 1988). However, there is no specified rule or standard such as degree of misorientation to define colony boundaries. And in many cases, the pearlite structure is not perfectly sound, so the colony boundaries are very difficult to find. Hence the manual method is highly dependent on the user's experience. Walentek et al. (2008) attempted the measurement using Electron Backscattered Diffraction (EBSD) method but failed for the following reasons: the pearlitic colonies are not always separated by High Angle Boundaries (HAB) or Low Angle Boundaries (LAB); the changes of the crystallographic orientation of the ferrite matrix does not always coincide with changes in the morphology (Van Boxel et al., 2005). Therefore by now the issue of pearlite colony size remains open because the relationship between metallurgical and optical microtexture and morphology is as yet sometimes unclear and does not allow determining the mean colony size by EBSD.

4.2 Image Analysis Applications in Steel and Other Metallurgical Study

Image analysis based on optical microscopy can be a good complement of these non-image-based techniques due to its low cost and the fairly strong connection between sample microstructure and a 2d image after appropriate preparation. Photons, possibly from controlled angles, interact with surface relief, and/or the specularity and emissivity of the material locally, and are then imaged within the microscope. However, as mentioned in Chapter 2, multiphase steels may contain ferrite, martensite, bainite and retained austenite; these phases can have overlapping grey levels in typical optical images, making identification by pixel grey levels inaccurate or impossible. A further challenge is that pearlitic colonies contain lamellae of ferrite and cementite whose orientation typically characterise them, rather than their grey levels. These microstructural characteristics and the features of optical microscopy combine to make the quantitative characterisation of phases in steel a difficult problem. Nonetheless image analysis has been widely applied in many aspects of steel study for a long period.

Grain size measurement

Grain size measurement in a sample by image analysis is an important tool since it can provide information about the mechanical properties such as strength, strain, ductility and resistance to stress (Peregrina-Barreto et al., 2013). Grain size can be determined by different image analysis methods. Peregrina-Barreto et al. (2013) used the peak value of the grey level histogram to automatically threshold the grey levels in the image of the microstructure of a single phase steel (a commercial carbon steel AISI/NOM 1008 Figure 4- 1 (a)) followed by some post-processing including noise elimination and morphological closing, to prepare a binary image from which individual grains could be identified subsequently (Figure 4- 1 (b)). It can be seen that

the grey level of the grain boundaries is generally lower than those of the matrix in Figure 4- 1 (a), so an appropriate threshold value between the grey level of grain boundaries and the grey level of matrix could easily segment most of the boundaries. The incomplete boundaries generated during the thresholding were reconstructed with a close operation (explained in section 6.2.10). The results had a good agreement with the experimental reference value which was obtained by a combined manual testing method of Heyn Lineal Interception (ASTM, 2004) and Abrams Three-circle Interceptions (ASTM, 2004).

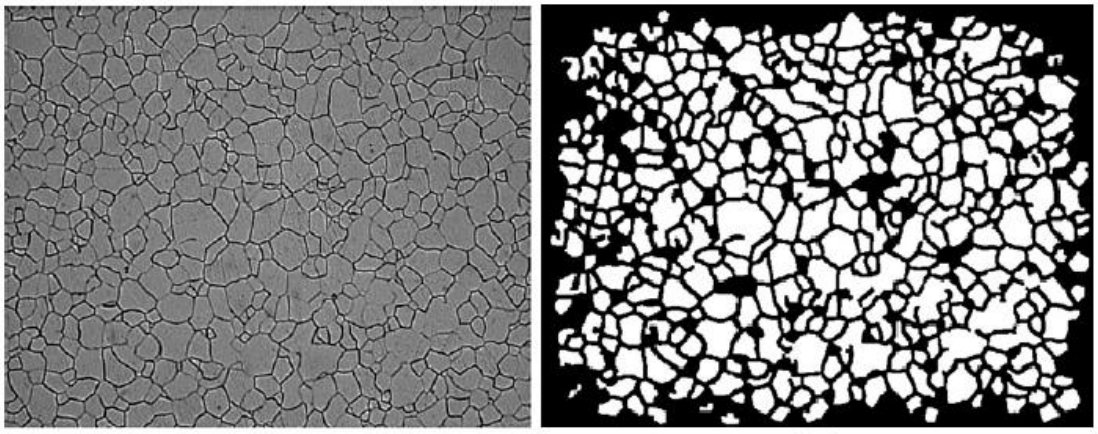

Figure 4- 1 (a) Original image; (b) Final image for grain size measurement (Peregrina-Barreto et al., 2013)

The image thresholding method accomplishes the segmentation of grains using the contrast between steel matrix and grain boundaries. Similarly, grain boundaries can also be detected according to the change in local gradient of the grey level versus position between grains and boundaries. Several algorithms including global thresholding, boundary detection based on local minimum, 1D edge detection (Sobel, Roberts and Prewitt detectors) and 2D edge detection (Laplace operator) respectively were applied by Latala and Wojnar (2001) to reveal the boundaries of a single phase material (austenitic steel in this study). A local function AND was used to obtain a single binary image based on three partial images that the 1D edge detector generated.

The results indicated that although every algorithm had missed or overestimated a few small boundaries, they showed high accuracy and repeatability and much less scatter compared with the manual results. Again, the success here was due to the fact that the grain boundaries could be easily classified by their different grey level to that of the grain interiors.

When images are fuzzy or noisy, the above algorithms are typically not sufficient to accurately detect the boundaries. Some more complicated computational intelligence techniques were developed to try to overcome these difficulties. Dengiz et al. (2005) used the brightness relationship between the pixel of interest and its neighbours, followed by two approaches including a fuzzy logic algorithm and a neural network to detect the boundaries in images of superalloy steel microstructure during sintering. A local square region of 21 x 21 pixels around the classified pixel was used by the algorithm. A relative brightness ratio for the target pixel was calculated by dividing its value to the average brightness value of the local neighbourhood. Three features were computed for the classified pixel from itself and its local neighbourhood. A fuzzy classification algorithm was used. If the output of the algorithm was higher than 0.65, the pixel was classified as a boundary pixel; if it was lower than 0.6, it was classified as a non-boundary pixel; if the value was between 0.6 and 0.65, the classification of this pixel would be dependent on its neighbouring pixels. Both the results of fuzzy logic algorithm and neural networks algorithm are shown in Figure 4- 2. Although neither of them was perfectly good, they were much improved over the conventional thresholding technique. And the neural networks approach performed slightly better than the fuzzy logic method. The disadvantage of the neural networks was that it required the images to be processed be similar to the images used for training.

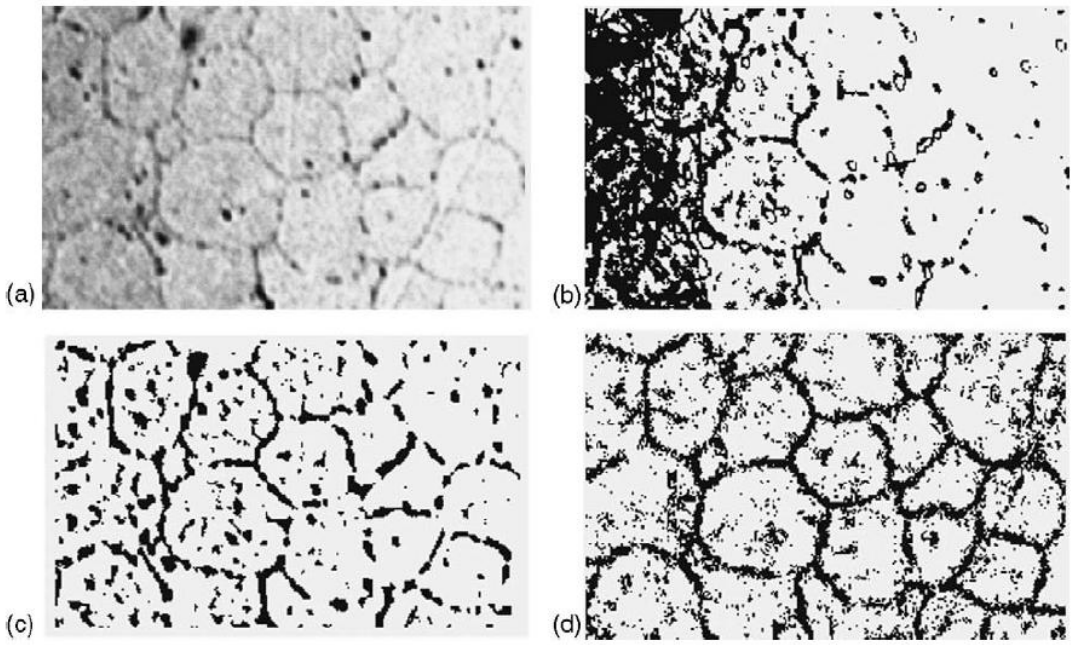

Figure 4- 2 An example taken from (Dengiz et al., 2005) showing the segmentation results using the proposed algorithm: (a) a smoothed and contrast enhanced source image; (b) output of simple thresholding by hand; (c) output of the fuzzy logic algorithm; (d) output of the neural networks algorithm

Characterisation of the Microstructure in a Whole Image

During quality control or property prediction process, it is usually helpful to characterise the microstructure of samples of materials to give some quantitative values, which can be linked with the properties or the quality of the material. Methods based on image texture analysis are often used. Chmiela et al. (2009) used Hurst correlation (for a definition refer to Maruta et al., 2010) as a measure of heterogeneity in a study of multiscale description of the heterogeneity of multiphase materials such as cast iron and banded structures of steel (ferrite and pearlite) based on an analysis of moments of inertia. They computed the Hurst correlation using the gliding-box method (Cheng, 1999) with varying scale sizes and used that as a inhomogeneity measure. The results showed that the proposed method allowed a precise evaluation of the degree of distribution inhomogeneity for any type of model or real structures.

Kim et al. (2011) used a wavelet packet transform (description in Cincotti et al., 2011) to extract quality-related textural information under multi-resolution scale and a sequential floating forward selection method (explanation refer to Webb and Copsey, 2011) was applied to obtain optimal textural features from these texture measures. A k-nearest neighbour classifier was then used to distinguish the quality of the material. A total of 35 images of real industrial steel surfaces from four quality classes were used to validate the automated surface quality determination system, and the classification accuracy could reach at 99.3%. It shows that although the KNN classifier is simple it can also have good performance.

Dutta (Dutta et al., 2012, Dutta et al., 2014) carried out three methods including box counting, grey level co-occurrence matrix technique and run length statistical analysis technique to automatically characterise micrographs and fractographs of steels (AISI 304LN stainless steel and Cu-strengthened high-strength low alloy steel). Ten texture descriptors were extracted from these three techniques for the characterisation and correlated with observed mechanical properties. The results showed that the trend of descriptors have variations in the similarity with the trend of mechanical properties. Some descriptors had the similar trend with a certain property while others might agree with another property better. Generally grey level co-occurrence matrix method is the most efficient method among them in terms of computational speed.

Fuchs (2005) studied the application of texture parameters in characterising diffusional and displacive transformation products in his PhD project. 2-D statistical parameters based on the GLCM (the Haralick parameters) were used to characterise the transformation products of steel. He also tried to correlate these texture features to the processing parameters such as austenitising temperature and the mechanical properties such as micro-hardness. The correlation between texture features and property parameters was improved by incorporation of standard microstructural data

with the use of a full set of Haralick parameters in a neural networks technique, but a correlation between the texture features and processing parameters was not successfully found. Individual Haralick parameters could be related to the characteristics in well-defined model images, but failed to be related to microstructural features in real microstructures in this study, which greatly limited its application.

In the studies listed above (and generally for image texture analysis in steel) it can be seen that most of the current research is focused on characterising the microstructure of a whole sample or image. A considerable region of a sample or the whole sample is studied, and a measure to characterise that region or that sample is extracted using a particular method, in order to characterise the region or sample. Individual microstructural features or regions are not typically identified down to the pixel level, and so the optical resolution of the image often does not need to be sufficient to explicitly resolve them.

Phase Classification

When the characterisation is performed at the pixel level, which is to classify each individual pixel in the microstructure image to a specific category, the task becomes much tougher than the overall microstructure characterisation. The difficulty of phase classification in steel microstructure is dependent on the number of phases present and the inter- and intra-phase grey-level contrast.

An example of a situation where there is sufficient inter-phase contrast for simple grey-level (intensity)-based thresholding to work is the classification of dual phase steel that contains martensite and ferrite, due to the high grey level contrast between these two phases (Burikova and Rosenberg, 2009).

When there are more phases present in the steel microstructure and less contrast between phases, the problem becomes complicated, which has thus limited the application of image analysis method for multiphase microstructure classification. Generally, the grey level range in optical images between upper bainite and lower bainite, and between martensite and ferrite is very close. Moreover, the grey levels between bainite and martensite are sometimes overlapped. This makes the steel phases difficult to classify. Komenda (2001) proposed a supervised classification method to recognise steel mixed microstructures containing lower bainite, phosphorus-rich ferrite, pearlite and martensite. Image features were used, but these consisted only of each pixel and its four surrounding neighbours, which was very likely to miss important information at larger length scales. Probability theory was then used to do the classification in the feature space. However, it was not presented in the paper which features were used to classify the steel phases. The example image and its automatic recognition are shown in Figure 4- 3 and Figure 4- 4 respectively. A classification accuracy analysis was not calculated in the paper, and from the images presented it was difficult to determine the classification performance. However, from Figure 4- 4 it can be seen that lower bainite and martensite were not clearly distinguished from each other. Moreover, quite a few regions (shown in white) were not classified at all, which will reduce the classification accuracy.

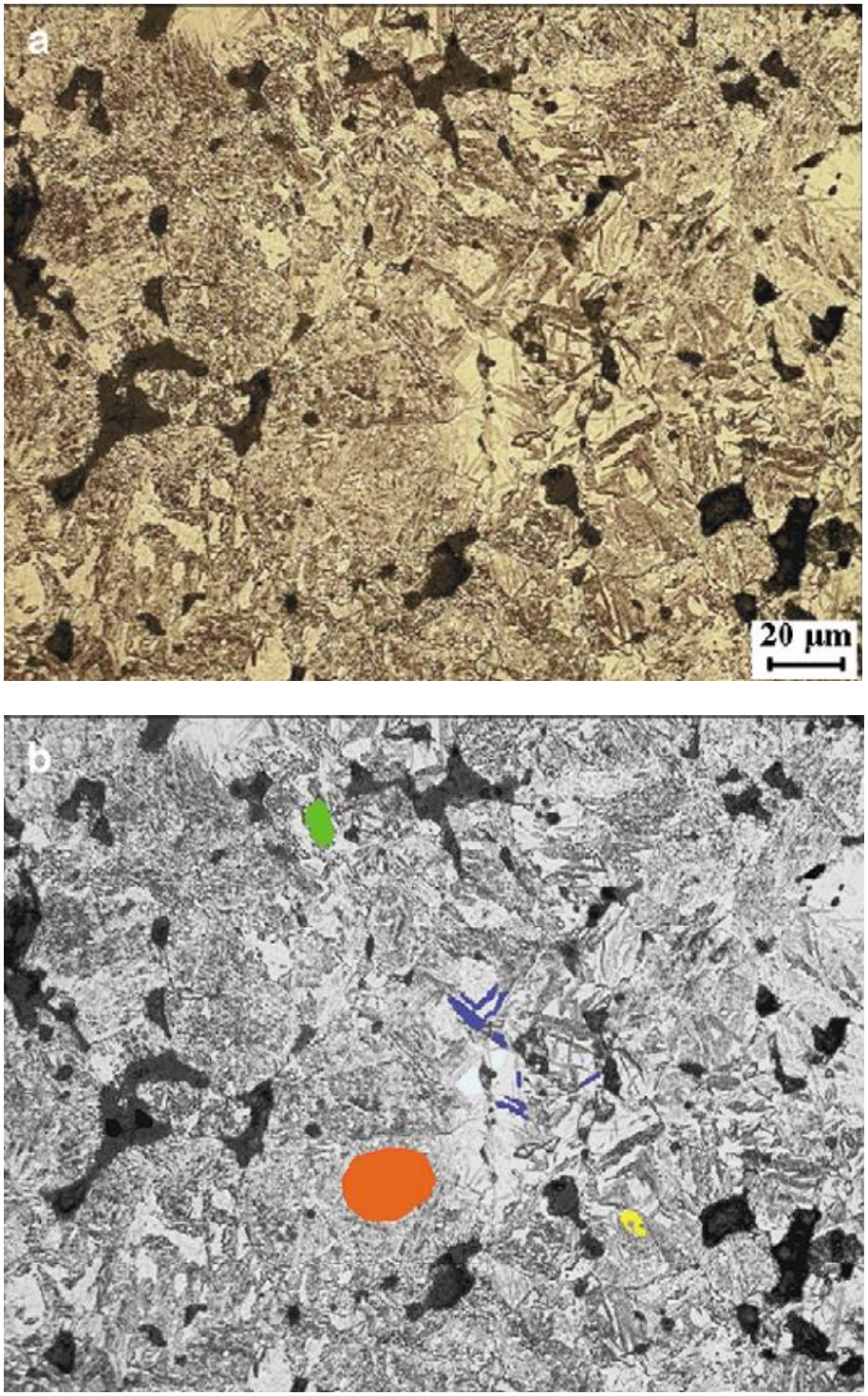

Figure 4- 3 Sintered-steel microstructure (optical microscope, 400 x magnification): (a) original image; (b) training image (Komenda, 2001)

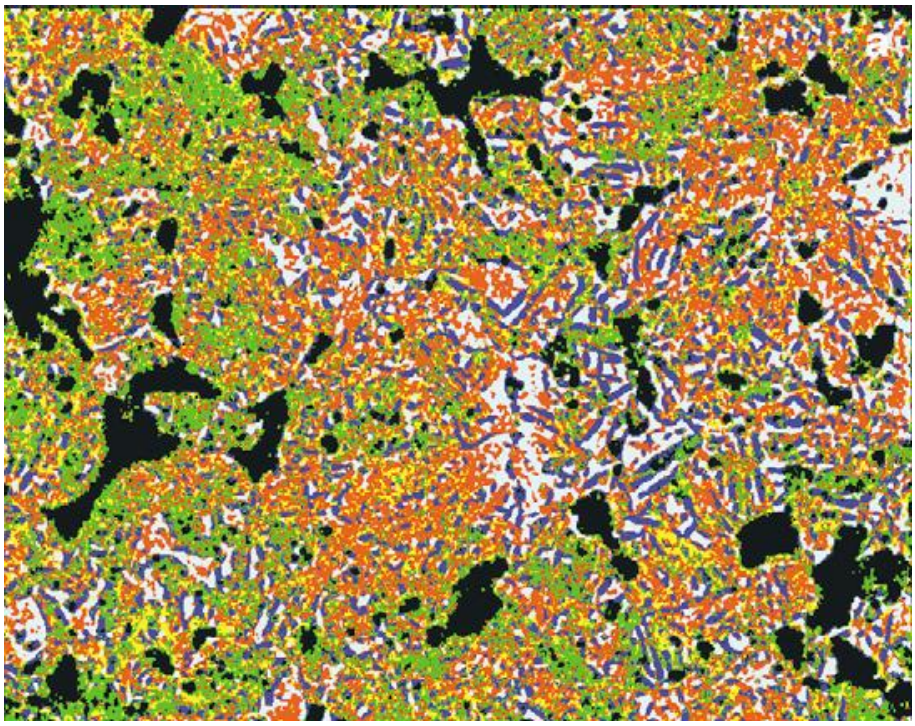

Figure 4- 4 The same structure as in Figure 4- 3 after automatic recognition with phases marked with colours: lower bainite (dark blue), upper bainite (red), phosphorus-rich ferrite (green), fine pearlite (yellow), martensite (light blue), pores (black) (Komenda, 2001)

4.3 Aims and objectives

According to the reviewed literatures, the following issues in steel study remain unsolved: for pearlitic steel, the pearlite colony size is an important factor that determines the strength and toughness of material, however, the measurement of colony size can be only carried out manually by skilled people; for complex steels, the phase fraction and distribution are determinant of the properties of material, but only the phase fraction can be measured by XRD.

Thus the purpose of this PhD is to solve or make some progress the above issues using optical image analysis methods, in order to save some labour work from the manual method of pearlite colony size measurement, and provide an alternative approach to measure the phase fraction and distribution in complex steels.

The PhD was studied in a following way:

- Investigation of the influence of uneven illumination in sample images, and its automatic correction.
- Investigation of a method based on Fourier transforms to characterise the orientation information of micrographs.
- Development of a split-merge segmentation algorithm to separate the pearlitic colonies using orientation and grey scale information.
- To propose appropriate features that can be used in the segmentation algorithm to characterise pearlite colonies.
- To classify different phases in steel microstructure including ferrite, bainite and martensite based on GLCM statistical parameters and feature selection method.
- To study the effect from sample preparation to the image analysis results. The etching degree is the main focus.

Chapter 5. Experimental Methods

5.1 Sample Preparations

5.1.1 Cutting

All the samples were metallographically cut using a Struers Accutom-50 with a diamond cut-off wheel. This wheel was 127 mm in diameter and 0.4 mm thick. To avoid heating of the samples and mechanical deformation during cutting which might influence the microstructure, a low feed speed of up to 0.2 mm/s was chosen along with use of the cooling system to cool the samples during cutting.

5.1.2 Mounting

To increase the handling and improve the quality of the metallographic preparation the samples were mounted. The samples were hot mounted in bakelite using a Struers electro-hydraulic mounting press.

5.1.3 Grinding, Polishing and Etching

The mounted samples were mechanically ground and polished using a Struers LaboForce semi-automatic grinding/polishing machine. The MD-Disc system was used to fix the grinding and polishing discs. The procedures for metallographic preparation are given in Table 5- 1.

Table 5- 1 Procedures for the metallographic preparation of the heat treated steel samples

	Grinding		Polishing			
	1	2	3	5	6	7
Disc	MD-Piano	MD-Piano	MD-Largo	MD-DAC	MD-NAP	MD-Chem
Grit/ grain size (μm)	220	600	9	3	1	OPS
Lubricant / abrasive	water	water	diamond	diamond	diamond	silica
Speed	300 rpm	300 rpm	150 rpm	150 rpm	150 rpm	150 rpm
Pressure	180N	180 N	180 N	180 N	150 N	90 N
Time in min	Until flat	4	4	4	3	1

The etchant used in this work is 5% nital (5 ml nitric acid in 95 ml ethanol), which can reveal the general structure of samples. The criterion for the time of each etching process was the obtention of highest contrast of features.

5.2 Characterisation Methods

5.2.1 Optical Microscopy

The optical microscopical investigations have been made using a Leica DMRX upright microscope in brightfield reflected light. The microscope was attached to a computer using AxioVision 4.6.3 software for the digitisation, acquisition and analysis of micrographs.

5.2.2 Scanning Electron Microscopy (SEM)

The secondary electron imaging was carried out on a JEOL 7000 SEM operating at 20

kV with a field emission gun (FEG) with Oxford INCA imaging software.

5.3 Shading Correction

In order to get test images which are appropriate for histogram-based image analysis, dual-phase steel (300M) containing ferrite and martensite was used. The chemical composition and TTT diagram of 300M are shown in Table 5- 2 and Figure 5- 1 respectively. Two samples were cut off and heat-treated following the temperature route shown in Figure 5- 1. Sample SC1 was polished in order to provide the White calibration images while sample SC2 was etched after polishing to provide the dual phase images.

Table 5- 2 Chemical composition of 300M

Bulk Content for 300M, wt %								
C	Si	Mn	P	S	V	Cr	Mo	Ni
0.42	1.65	0.8	0.005	0.002	0.07	0.82	0.39	1.83
Al	As	Cu	N	Nb	Ti	Sn	Fe	
0.023	0.015	0.12	0.004	0.001	0.006	0.01	Balance	

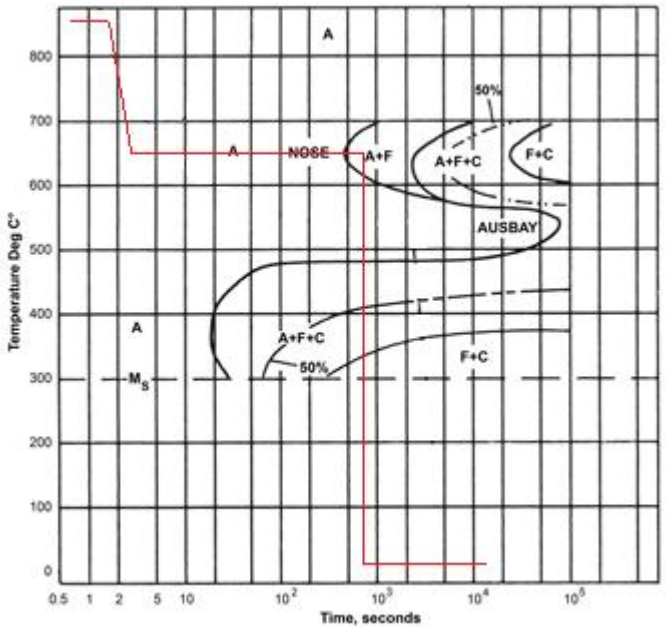

Figure 5- 1 The TTT diagram of 300M (Filice and Pritchard, 1998) and the heat treatment temperature profile for the sample SC2 (red line)

5.4 Pearlite Colony Characterisation

Rail steel R260 was used for the pearlitic structure characterisation investigations. Its chemical composition is given in Table 5- 3. Sample P was taken from the material.

Table 5- 3 Chemical composition of R260 steel (Herian and Aniotek, 2008)

Chemical composition of steel [wt%]							
Grade	C	Mn	Si	P	S	Cr	Al
R260	0.62~ 0.80	0.7~ 1.2	0.15~ 0.58	Max0.025	0.008~ 0.025	0.04	0.003

This steel mainly consists of pearlite and small amount of ferrite if the carbon content is below the eutectoid composition.

5.5 Phase Classification for Complex Steel

Two medium carbon steels — 9260 (material 1) and 300M (material 2), were used in the study. The first material was used to generate a multi-phase microstructure containing upper bainite, lower bainite, ferrite and martensite. The second material was used to generate a set of samples containing less number of microstructures, to test the phase classification algorithm and investigate whether the features selected based on one sample are appropriate for another sample with similar microstructure. The chemical compositions of the two steels are shown in Table 5- 4 and Table 5- 2.

Table 5- 4 Chemical compositions of steel 9260

Bulk content for material 1, wt %					
C	Mn	Si	Cr	P & S	Fe
0.55 – 0.60	0.80 – 1.00	1.80– 2.10	0.15 – 0.30	0.035 max	Balance

Sample A was heat treated to obtain a mixed microstructure of ferrite, martensite, upper bainite, lower bainite. The Time Temperature Transformation (TTT) curve of steel 9260 is shown in Figure 5- 2.

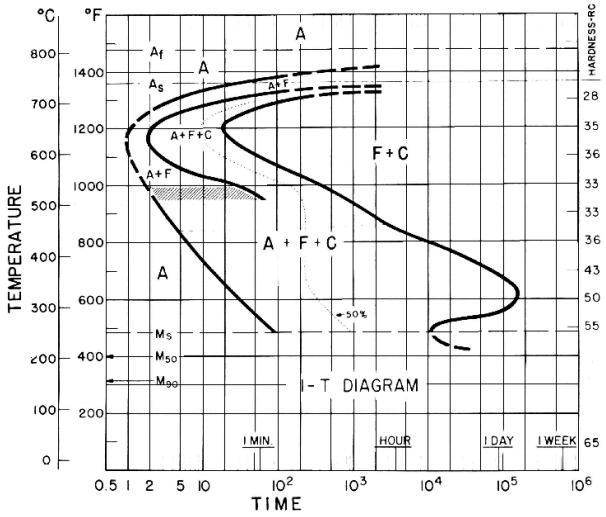

Figure 5- 2 Time Temperature Transformation curve of steel 9260 (ASM, 1977)

Based on the TTT diagram, the following heat treatment (Figure 5- 3) was applied.

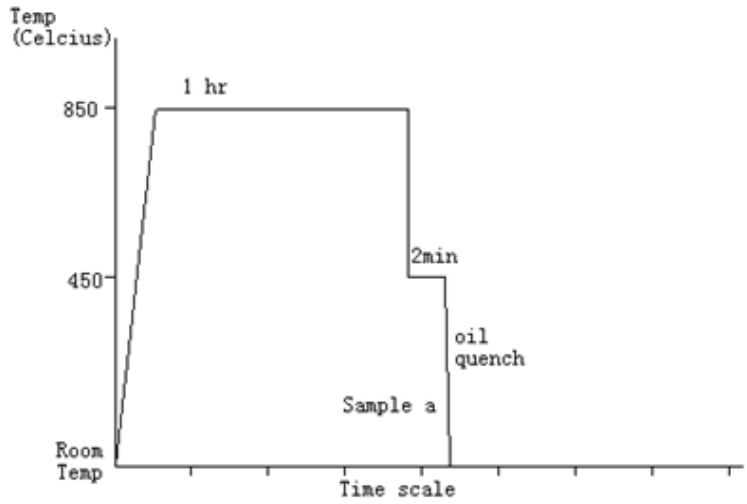

Figure 5- 3 Schematic time-temperature profile for the heat treatment condition for sample A

Five samples (Sample B, C, D, E and F) from material 2 were heat treated to obtain a mixed microstructure of martensite, upper bainite and lower bainite. The TTT curve of steel 300M is shown in Figure 5- 4. A hole was drilled on each sample in order to attach a thermocouple and monitor the temperature of the centre of the sample (Figure 5- 5).

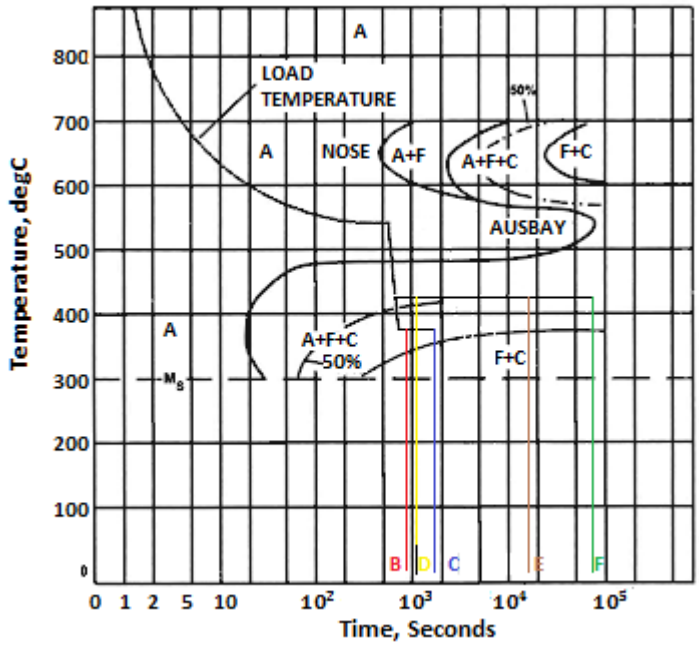

Figure 5- 4 Schematic TTT curve for 300M specification (Filice and Pritchard, 1998); The black line with red, blue, yellow, brown and green ends represent the temperature profiles of the heat treatment of sample B, C, D, E and F, the detail of which is shown in Table 5- 5.

Table 5- 5 Heat treatment profiles for sample B, C, D, E and F

	Stage 1: austenisation and homogenisation (temperature and holding time)	Stage 2: Forced air cooling to 550 ℃ and hold for:	Stage 3: Forced air cooling to a lower temperature and hold for:	Stage 4: Quench to room temperature
Sample B	925 ℃, 1hr	15mins	375 ℃,5mins	Water quench
Sample C	925 ℃, 1hr	15mins	375 ℃,60mins	Water quench
Sample D	925 ℃, 1hr	15mins	425 ℃,10mins	Water quench
Sample E	925 ℃, 1hr	15mins	425 ℃,3hr	Water quench
Sample F	925 ℃, 1hr	15mins	425 ℃,15hr	Water quench

Table 5- 5 shows the temperature and time profile of the heat treatments of sample B,

C, D, E and F. Forced air cooling was applied from stage 1 to stage 2 and from stage 2 to stage 3. The temperature of the sample was monitored by thermal couple during the heat treatment.

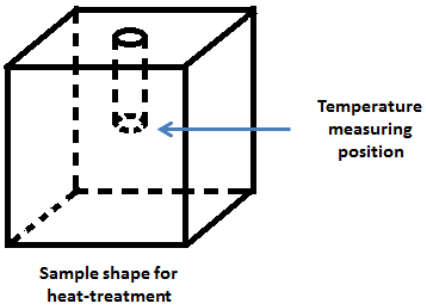

Figure 5- 5 Illustration of the shape of the samples for heat-treatment. The sample is machined to a cube with 10 millimetres on each side. A hole is drilled to the centre to place thermocouple.

5.6 Study of Influence from Etching Degree on Image Analysis

Sample F was used to study the influence from etching degree to the image analysis of the microstructure. 5% nital etchant was applied on the sample surface at room temperature for 5, 10, 15 and 20 seconds respectively. Images of 5 locations were taken from the sample with different etching durations. The influence of etching degree on image analysis was studied with these images.

Chapter 6. Image Analysis Models Used in This Study

6.1 Creation of the White and Black images

In order to verify that there is little influence from the sample SC1 surface on the background brightness, four images were obtained at a same position with the sample horizontally rotated by 0°, 90°, 180°, 270° (see Figure 6- 1). A grey scale line scan was taken at the same location of each image, to show the shading problem.

It is illustrated in Figure 6- 1 that although the sample was rotated by 90 degrees from each other, the general trend of the grey value is similar: it is higher on the left side, lower on the right side. Given that the dominant change from left to right is similar for four orientations indicates the shading effect comes from the microscope rather than the sample. However, there is a slight difference between them: 1) on image (d) the grey scale in the middle left is averagely higher than other positions on the line scan while it is not on other images; 2) the grey levels on image (b) and (f) range between 185 and 220 while that on image (d) and (e) range between 190 and 220. This variation may be caused by the sample itself since the sample is unlikely to be prepared to an ideal state with everywhere having exactly same reflectivity. An averaging process of these four orientations could be helpful in reducing the influence from the sample. However, it will be difficult to completely remove the influence.

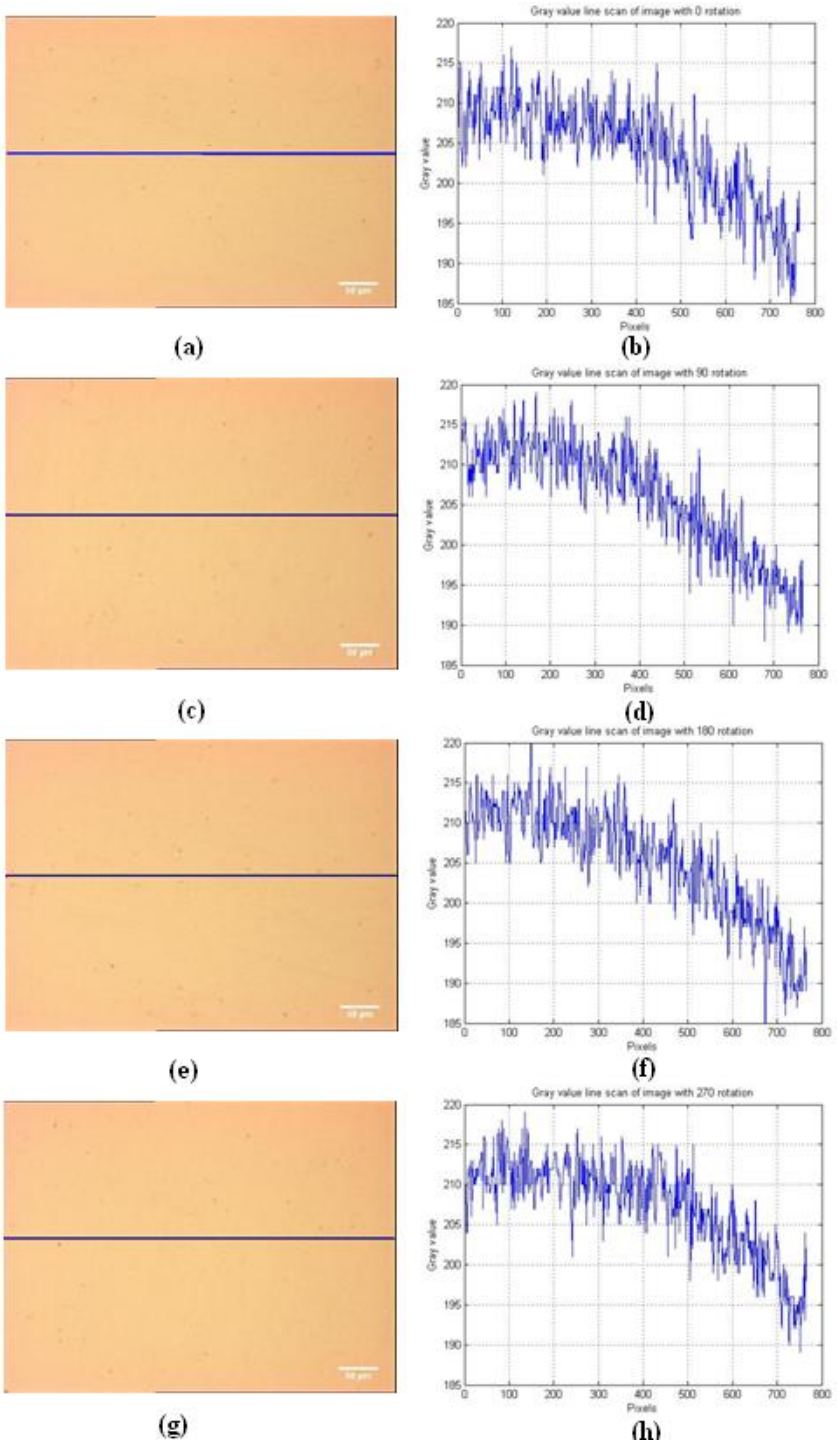

Figure 6- 1 The images with as-polished sample SC1 horizontally rotated by (a) 0°; (c) 90°;(e) 180°;(g) 270° and a grey level line scan of (b) 0°; (d) 90°;(f) 180°;(h) 270°. The scale bars located at the bottom right of each optical micrograph represents 50 μm. A line scan of grey value was performed along the blue line in the left hand side figures. The X-axis of the 4 plots on the right hand side represent the pixel distance of the blue line from left to right; the Y-axis represent the grey levels of the corresponding pixel on that line.

The white image can be extracted from these images after noise removal (process schematically shown in Figure 6- 2).

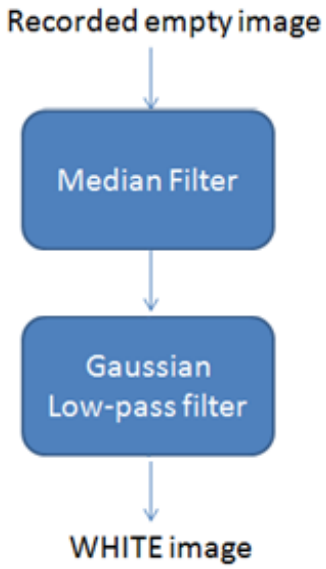

Figure 6- 2 Block diagram of generating the white image. The empty image taken from an as-polished sample was processed by a median filter and a Gaussian low-pass filter to generate the WHITE image.

The noise removing procedure was completed using two filters: median filter and Gaussian low pass filter. Based on the Fourier Transform, low-pass filtering can eliminate most of the high-frequency variations (frequency: the rate of cyclic variation of the luminance in a visual stimulus as a function of length) which are most likely to be noise.

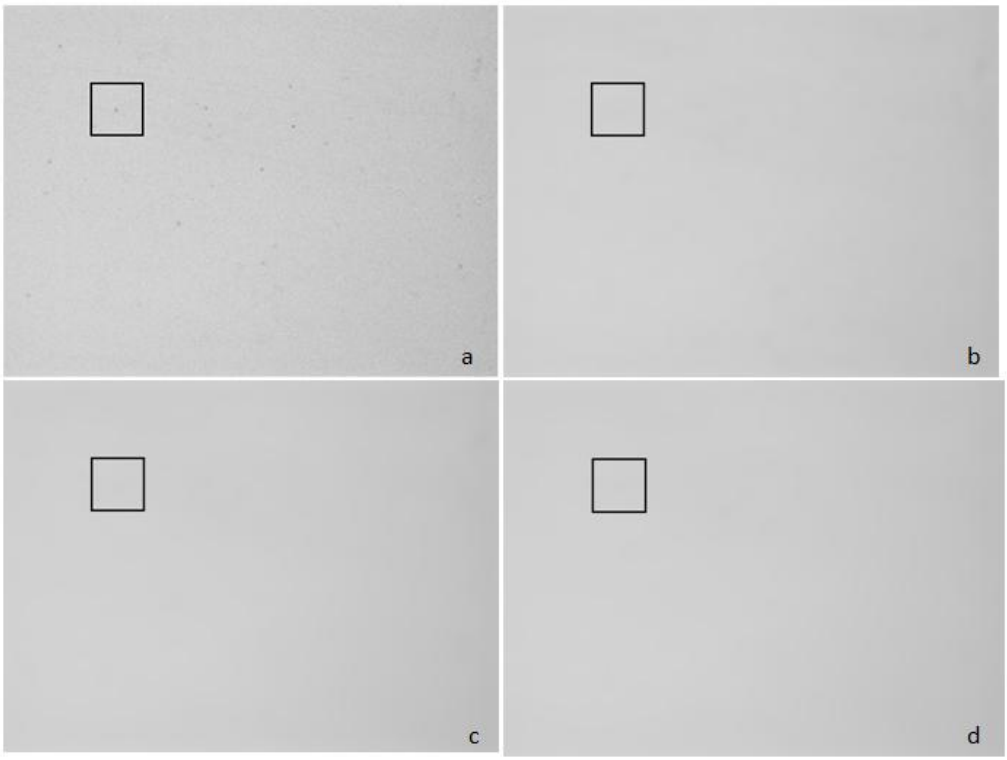

Figure 6- 3 (a) The initial background image; (b) the image after applying a 10x10 median filter; (c) the image after applying a Gaussian low-pass filter (radius = 10); (d) the image after applying a 10 x 10 median filter then followed by a Gaussian low-pass filter (radius = 10). The grey value plot of a sampling area which is highlighted in a black square is shown in Figure 6- 4.

Figure 6- 3 (a) shows the initial background image. Figure 6- 3 (b), (c) and (d) show the image after applying a 10x10 median filter, a Gaussian low-pass filter with 10 pixel radius, and a combination of median filter and Gaussian low-pass filter respectively. Although Figure 6- 3 (b), (c) and (d) have been smoothed from (a), the differences between these three images is hard to be seen visually. Therefore, a small region (black line surrounded) on the images was studied at a higher magnification to show the effect of smoothing (Figure 6- 4).

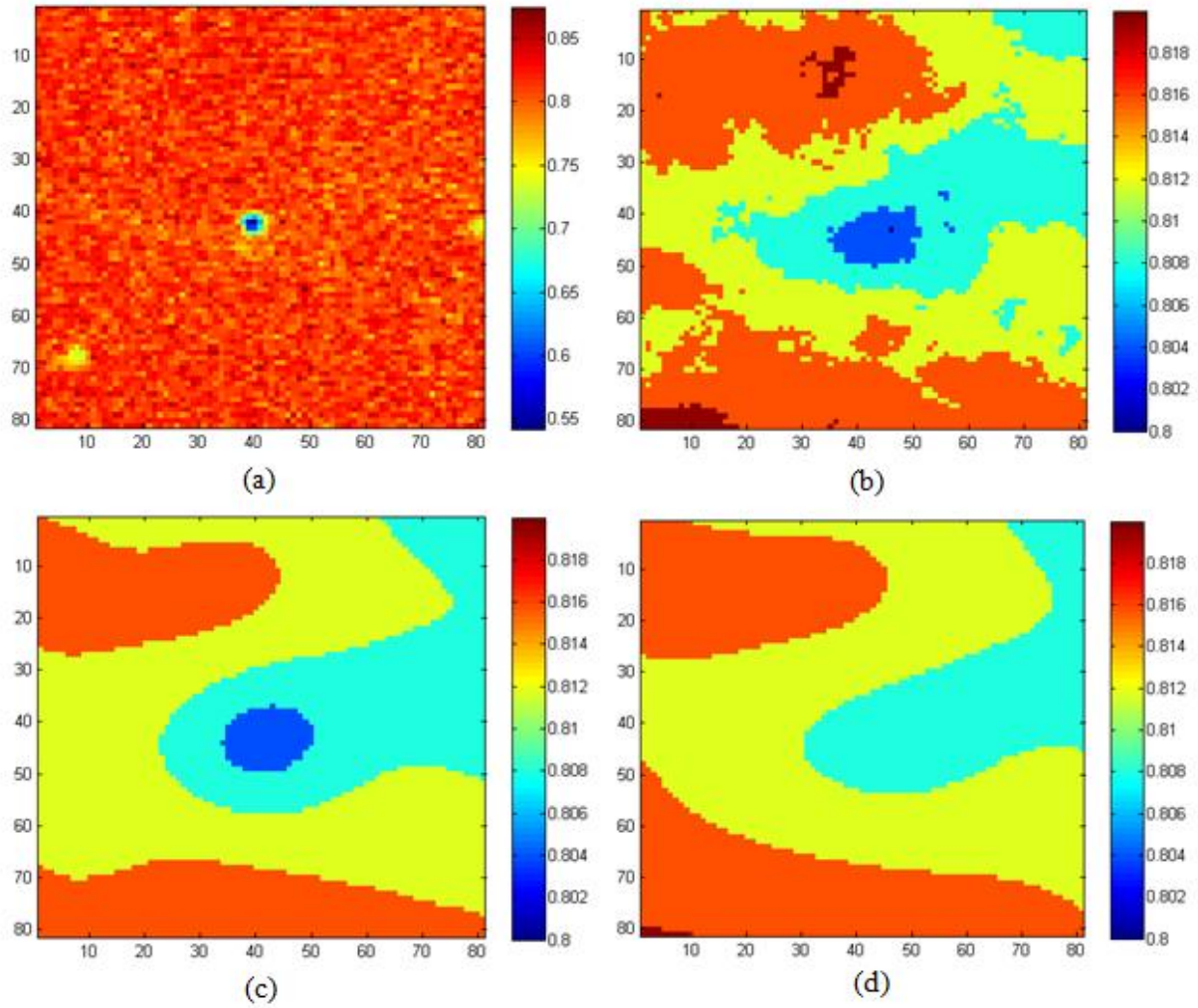

Figure 6- 4 The 2D grey level surface plots of Figure 6- 3 with the colour representing the grey level intensities: (a) the grey value plot of the black square marked region in the initial background image (Figure 6- 3 (a)); (b) the grey value plot of the black square marked region in the median filter processed image (Figure 6- 3 (b)); (c) the grey value plot of the black square marked region in the Gaussian low-pass filter processed image (Figure 6- 3 (c)); (d) the grey value plot of the black square marked region in the image after a median filter and Gaussian low-pass filter (Figure 6- 3 (b)).

Figure 6- 4 (a) shows the 2D grey level surface plots of the selected regions (black line surrounded) in Figure 6- 3. Figure 6- 4 (b) and (c) are the surface plot of median filtered image and Gaussian low-pass filtered image. It can be seen that after the median filtering, there were still a lot of spikes in the image, which showed that the

median filter was not good at dealing with the high frequency noise. The hole in figure (c) showed a weakness of Gaussian filter, which is that it is affected by single unrepresentative values (the biggest spike in figure (a)). The single pixel or a small patch of pixels with unrepresentative value might be caused by the inclusions or particles in the as polished specimen. A combined use of median filter and Gaussian low-pass filter can solve both problems (figure d).

The contour representation of final white image is shown in Figure 6- 5.

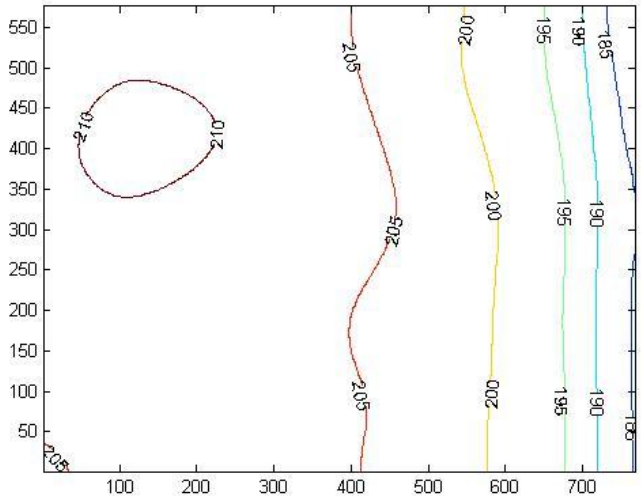

Figure 6- 5 The contour representation of final WHITE image

The BLACK image is simply 0 at every point of the image.

6.2 Model for Pearlite Colony Characterisation

6.2.1 Amplitude Spectral Density

By DFT an image which is a set of brightness values in *x* and *y* spatial coordinates can be represented by orthogonal coordinates *(u,v)* or by polar coordinates (ω, φ) in frequency space, that is two frequency coordinates u, v for the first form or a frequency coordinate ω as well as a directional coordinate φ for the second form.

There are direct relations between the two coordinate forms, which are shown in Eq6.1:

$$\omega = |u^2 + v^2|^{1/2}$$
$$\varphi = tan^{-1}\left[\frac{v}{u}\right] \quad \text{(Eq6.1)}$$

The Amplitude Spectral Density (ASD) can be calculated as the magnitude of the complex Fourier transform and has the property that, if $A(\omega,\varphi)$ denotes the grey level in the ASD image at the coordinates (ω,φ), then the value $A(\omega,\varphi)$ gives the sum of the content of the frequency component ω (in cycles per Fourier Transform neighbourhood size *h*) in the direction φ at all possible positions in the original image.

One of the significant advantages of using the ASD lies in its reordering mechanism. Any periodic variation in the original image at a given frequency and direction is displayed as a high amplitude at a single point in the ASD image, so that it can be easily recognised (From and Sandström, 1998). This is one of the theoretical bases of the study in this chapter.

Figure 6- 6 is a schematic representation of amplitude and angle of Fourier transform. There are two similar structures shown at different positions in the left side figure, but as long as the direction and period (h/15 per cycle) of their variation in grey value are the same, these will correspond to a same position in the amplitude spectrum domain. To be specific, the amplitude of this position in the ASD is the local frequency in the initial image (period is T=h/15, frequency is h/T = 15), and its direction is same as the intensity gradient of the structures in the image. The intensity of this position represents the frequential components (at coordinates (ω,φ)) of the original spatial

image.

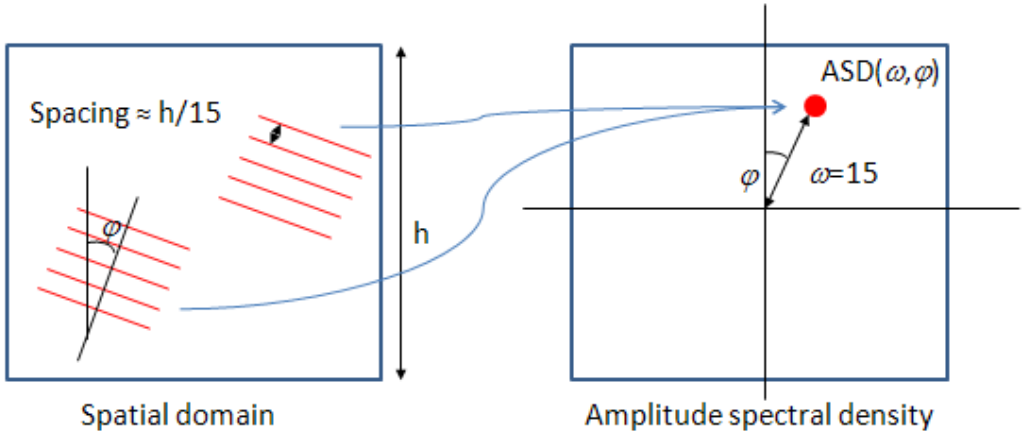

Figure 6- 6 Schematic representation of amplitude and angle of ASD: the frequential representation of a lamellar structure in the spatial domain is a point with its amplitude and angle respectively representing the frequency and orientation of its spatial structure.

6.2.2 Orientation Determination Method for Individual Pixels

After the ASD image of a local image was obtained by DFT, a family of 2-pixel wide straight lines across the central point of the ASD image were generated, with angles in a linear distribution between 0 ° and 180 °. The number of the lines is determined by the resolution requirement of orientation. For example, 60 lines (180 °/3 °) were needed in order to reach a resolution of 3 °.

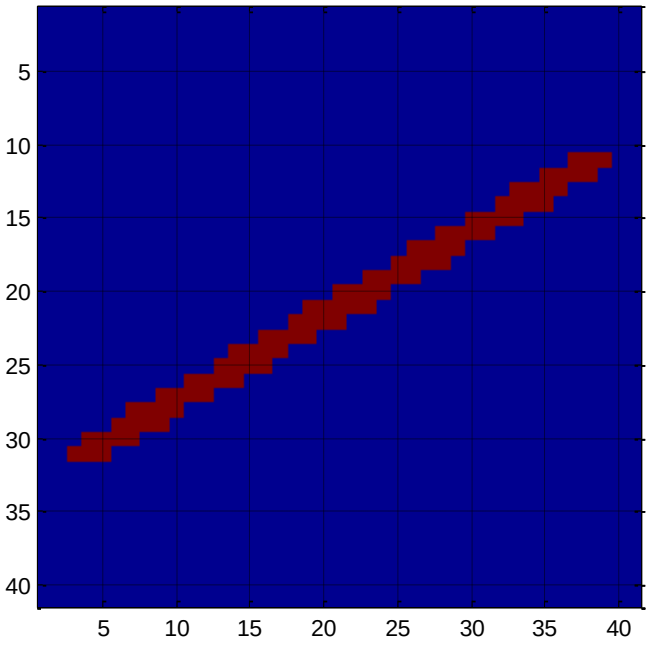

Figure 6- 7 An illustration of a measuring mask with the orientation angle being 30°. The value of the pixels on the red line is 1, and the value of blue background is 0.

A band pass filter was combined with the mask shown in Figure 6- 7 to eliminate unwanted effects at low frequency (from any features with a spatial dimension greater than the expected inter-lamellar spacing) and at high frequency (from noise in the image and the edges of the sample region). So the final mask used to compute the sum of ASD on each direction is shown in Figure 6- 8. Then the orientation of the lamellae in this region of interest was determined to be the direction of the mask whose ASD sum (called energy afterwards) was greatest.

$S_\varphi = \sum A_p$ (φ is the direction angle of the measuring mask, p is any pixels on the measuring mask) (Eq6.2)

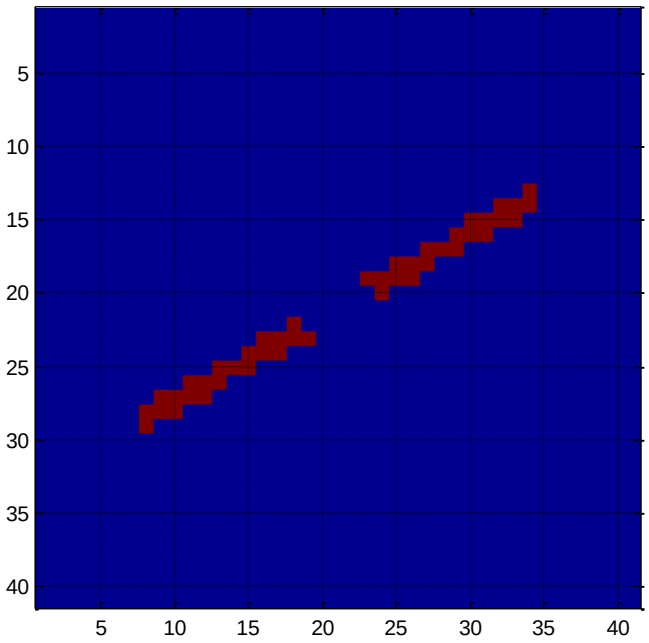

Figure 6- 8 The measuring mask after applying a band pass filter. The value of the pixels on the red line is 1, and the value of blue background is 0.

6.2.3 Orientation Mapping for the Entire image

Most of the image processing procedures in this study including the image orientation measurement in this chapter are based on the neighbourhood operations (that generate an 'output' pixel based on the pixel at the corresponding position in the input image and its certain size region of neighbouring pixels). The principle is shown in Figure 6- 9. The top row of Figure 6- 9 is the initial image. The crossed pixel is the target pixel, and the blue square centred at it is the neighbourhood within which the target pixel's neighbourhood is considered. By the application of different algorithms (Fourier transform to detect orientation in this chapter) different features can be extracted from the selected neighbourhood, and the feature or features will be stored in the same position in the output matrix (red point in the bottom row) as the target pixel in the initial image. Then next target pixel will be studied until all the pixels have been analysed. Since the margin points of image do not have as many neighbouring pixels as those inside the image, those pixels cannot get orientation information under the same conditions (in term of the number of neighbouring pixels) and thus are not

considered in the further processing procedures. The processed images are a number of pixels smaller than the original images. That number is determined by the neighbourhood size.

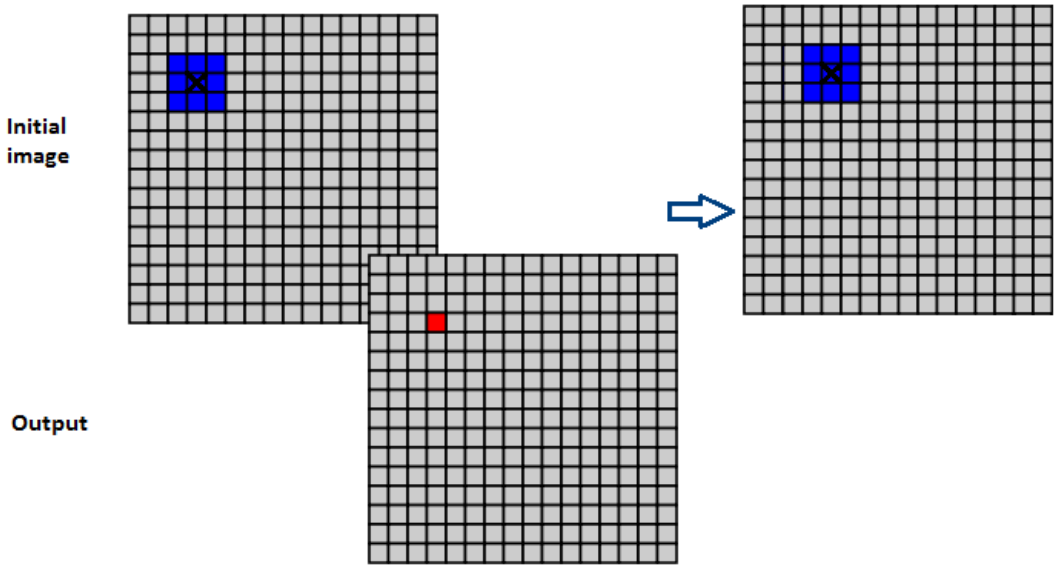

Figure 6- 9 Schematic illustration of the neighbourhood operation. The upper row is initial image and the lower is the output. The pixel with a cross is the target pixel, the blue square is the window within which the target pixel's neighbourhood is considered. The feature value computed from the neighbourhood will be stored at the same position as the target pixel in the output image.

6.2.4 Definition of Directionality

A pearlitic micrograph might contain unoriented areas for some reasons such as spheroidization of the structure, improper specimen preparation or inappropriate imaging. Although an orientation angle can be obtained in these cases by the above algorithm as long as the grey level is not same everywhere within the image, the results are more likely determined by other factors rather than the lamellae and are normally unreliable. Therefore the concept of directionality is introduced here to quantitatively measure the degree or the strength of a structure being orientated and based on that a criterion to discard the less oriented structures can be set up.

The directionality is defined as the ratio of the maximum $S(\varphi)$ to the average of $S(\varphi)$ of all directions, and its value will be at least 1 (unoriented) to N_d (completely oriented, where N_d is the number of angles considered)

$$\text{directionality} = \frac{\text{maximum}(S(\varphi))}{\text{mean}(\sum_{\varphi=0}^{\varphi=\pi} S(\varphi))} \quad \text{(Eq6.3)}$$

6.2.5 Features to Characterise Pearlitic Colonies

As mentioned before, the orientation and interlamellar spacing are two of the most important characteristics for pearlitic colonies. Different lamellar spacings might arise for a number of reasons including physical reasons such as thermal fluctuation and/or recalescence effects, and mechanical reasons such as sectioning angle (Boswell and Chadwick, 1977, Ridley, 1984). The interlamellar spacing can be related to the distance between the maximum value in the ASD image and the centre point. It requires a large neighbourhood size during the FFT to enlarge that distance in order to obtain a higher accuracy, which will reduce the spatial resolution of the algorithm. Thus to accurately measure the numerical value of the interlamellar spacing is realizable but difficult using the FFT method. An indirect method was used in this study, which is to use the average grey levels within a region to detect the difference of the interlamellar spacing because various interlamellar spacings very likely lead to different average grey levels of the colonies (assuming the brightness of the ferrite and cementite respectively are identical between colonies). In this work, the grey value of the smoothed image (by a Gaussian low pass filter) was used as the grey level predicate instead of the raw value of the original image itself, as the cementite and ferrite lamellae in the original images have distinct grey level difference, which might cause the separation of them by the direct use of their grey levels (see the results in section 7.2.9.4).

The colony orientation which is normally referred to is the average orientation angle of all pixels in the colony. However the average orientation angle might not properly characterise the orientation feature of a colony when it contains curved lamellae. Therefore another orientation based feature — Kernel Average Misorientation (KAM) — is used here along with the average colony orientation.

In the KAM approach, the arithmetic mean of the scalar (positive) misorientation between groups of pixels, or kernels (Schwartz et al., 2009), is calculated and mapped. It provides average misorientation between the kernel (data point) and its neighbours at a defined neighbourhood size (Man et al., 2009). Thus KAM has a higher value along colony boundaries where orientations are rapidly changing with position than inside colonies where changes are slower with position.

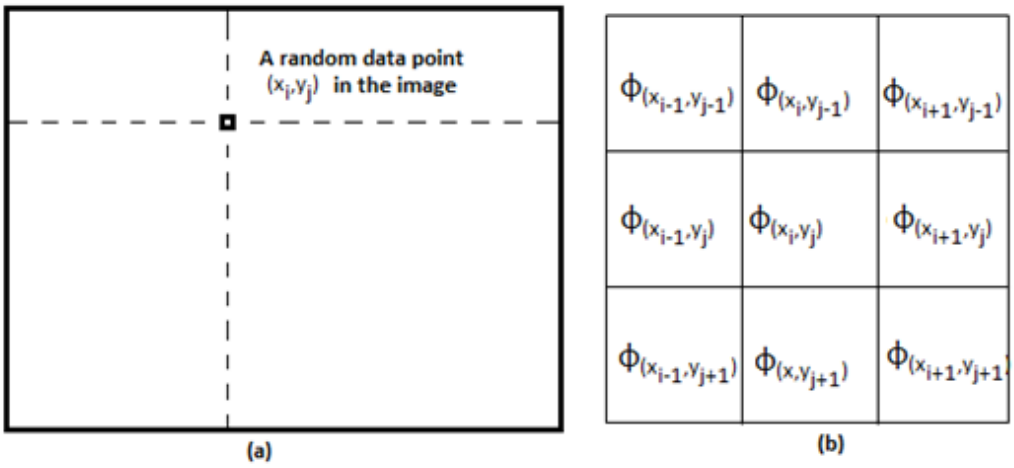

Figure 6- 10 An illustration of local orientation map: (a) a random data point in an image; (b) the shape and size of neighbourhood to compute the KAM is defined, 3x3 in this illustration.

Figure 6- 10 is an illustration of computing KAM based on the orientation map. Given a centre position, a number of neighbouring pixels are selected (3x3 in this example). The KAM of the centre position (x_i, y_i) is computed by averaging the differences

between the orientation value of itself and its neighbours.

$KAM = \frac{\sum_{m=i-1}^{i+1}\sum_{n=j-1}^{j+1}|arc((x_m,y_n),(x_i,y_j))|}{N}$ (N is the number of neighbouring pixels selected, equals 4 here; *arc* is a method to measure the angular difference of two vectors in polar coordinate systems) (Eq6.4)

The periodicity of the measured orientation information is illustrated in Figure 6- 11. The angular difference of two vectors in such polar coordination system was measured with an algorithm as follows (Liu and Singh, 1992, Nikolaidis and Pitas, 1998):

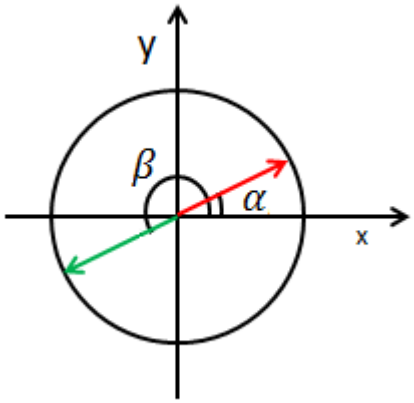

Figure 6- 11 A schematic illustration of the periodicity of angular signal: α and β are on the same line with different direction. In this study, α and β are regarded as same orientation.

$$arc(\theta_1,\theta_2) = \frac{T}{2} - \left|\frac{T}{2} - |\theta_1 - \theta_2|\right| \quad \text{(Eq6.5)}$$

where T is the period of the signal. T equals π in this algorithm (in the polar coordinate system, 1 °and 181 °are regarded as same orientation). In the illustration of Figure 6- 12, the difference between θ_2 and θ_3 is apparently smaller than $\frac{\pi}{2}$, so

$arc(\theta_2, \theta_3) = \frac{\pi}{2} - \left|\frac{\pi}{2} - |\theta_2 - \theta_3|\right| = \theta_3 - \theta_2$; the difference between θ_1 and θ_4 is bigger than $\frac{\pi}{2}$, so $arc(\theta_1, \theta_4) = \frac{\pi}{2} - \left|\frac{\pi}{2} - |\theta_1 - \theta_4|\right| = \pi + \theta_1 - \theta_4$.

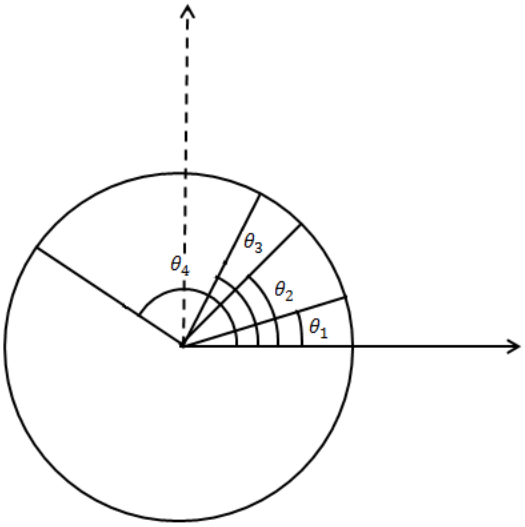

Figure 6- 12 Illustration of four different orientations ($\theta_1, \theta_2, \theta_3and\theta_4$) in the angular coordinate system

Given the orientation map, the arc distances between the angle of a pixel and any of its neighbouring pixels can be computed.

6.2.6 Padding Images to Square

Since the split-and-merge algorithm is quadtree-based, the image from which splitting is started needs to be square and quadratic integer power. Most images including those used in this study do not satisfy the requirement. The problem is solved by padding initial images to required size by repeating the border elements of the image. If other value is used here, an oversegmentation of the initial image would be probably caused in the splitting process, which may be reconstructed by the merging process. After the splitting process is done, the padded part from the previous step would be deleted, in order that the image recovers to its original size for merging.

6.2.7 Split-merge Segmentation Algorithm

The main goal of region splitting and merging is to distinguish the homogeneous regions of the image (Horowitz and Pavlidis, 1976). Its concept is based on quadtrees: each node of the trees has four descendants and the root of the tree corresponds to the entire image.

Let R represent the entire image and P is the homogeneity predicate by which splitting and merging action is determined. If R is a square image, the approach consists of successively subdividing it into smaller and smaller square regions so that, for any region $R_i \subset R, P(R_i) = TRUE,$ which is, if $P(R_i) = FALSE$, R_i has to be newly subdivided and so on. After the process of splitting, merging process is to merge two adjacent regions R_j and R_k if $P(R_j \cup R_k) = TRUE$. The summarized procedure is described as follows:

Step1. Splitting steps: any region R_i in which $P(R_i) = FALSE,$ is split into four disjoint quadrants.

Step2. Merging steps: when no further splitting is possible, merge any adjacent regions R_j and R_k if $P(R_j \cup R_k) = TRUE$.

Step3. Stop only if no further merging is possible.

In the example shown in Figure 6- 13, only R_4 is subdivided further.

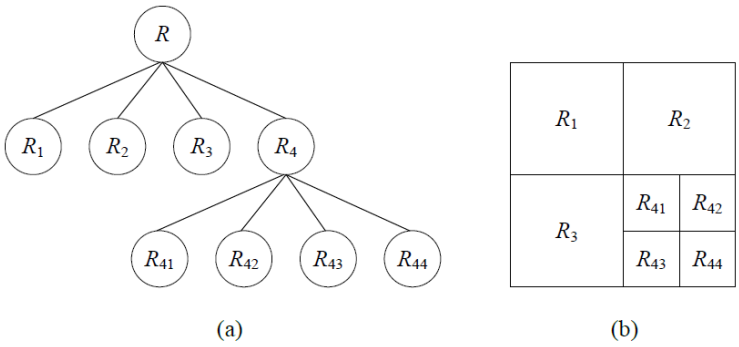

Figure 6- 13 (a) The structure of quadtree, where R represents the entire image; (b) Corresponding partitioned image (Gonzalez and Woods, 2007)

6.2.8 Labelling in Splitting

During the splitting process, every new block is given a unique and systematic code, which is helpful in building block networks with clear spatial relationships and determining the processing order in the following merging process. The labelling method is explained as follows.

Since every split of a block in the algorithm generates 4 sub-blocks, a quaternary labelling algorithm is appropriate. The initial entire image is labelled "1". If a block with label "*xy*" has been split into 4 sub-blocks, then these four sub-blocks is labelled with 0 to 3 added after the code of parent block in an anticlockwise order starting from the top left one. So the code for these four would be: *xy0*, *xy1*, *xy2* and *xy3*. If a block is no longer dividable, it will keep its code regardless the digits of other blocks.

The advantages for this labelling algorithm are listed as follows:

a) It is convenient to find the position of any block in the image by its label;
b) The digit of the label indicates the size of the corresponding block, which is used as an important reference to determine the proceeding order during the merging process.

6.2.9 Predicates Used in the Split and Merge Algorithm

Three predicates are used in the algorithm, including two orientation-based features (average orientation value of region and inter region KAM) and a grey value-based feature (average grey value of region). Since the KAM feature is a measure to show the possibility of a pixel belonging to colony boundaries, it is suitable for determining whether the interface between two adjacent regions is part of a colony boundary or not. It is not applied during the splitting process, which is to generate regions. The schematic illustration of the splitting and merging process including the predicates used in the process are shown in Figure 6- 14 and Figure 6- 15 respectively.

During the splitting process (Figure 6- 14), the absolute differences between the maximum and minimum of orientation and grey level over the parent block are used as predicates instead of the average values. Criteria for checking the homogeneity are defined, which are Φ_c for the range of grey value, and A_c for the range of orientation. The relation between these two predicates is logic "or", which means the parent block will be split either if $P(\Phi_i) = FALSE$ or $P(A_i) = FALSE$.

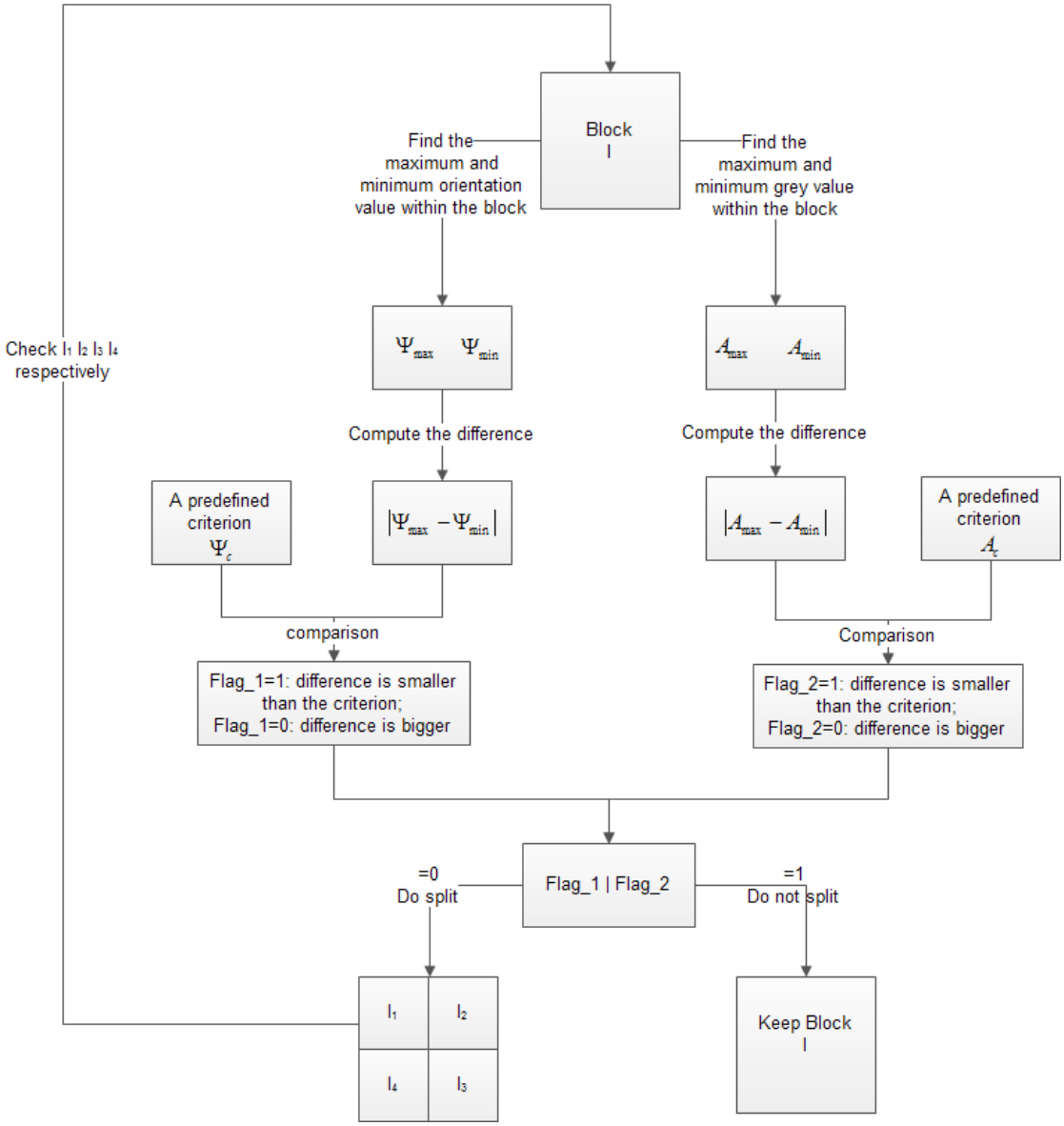

Figure 6- 14 Schematic illustration of the splitting process including the predicates used in the process

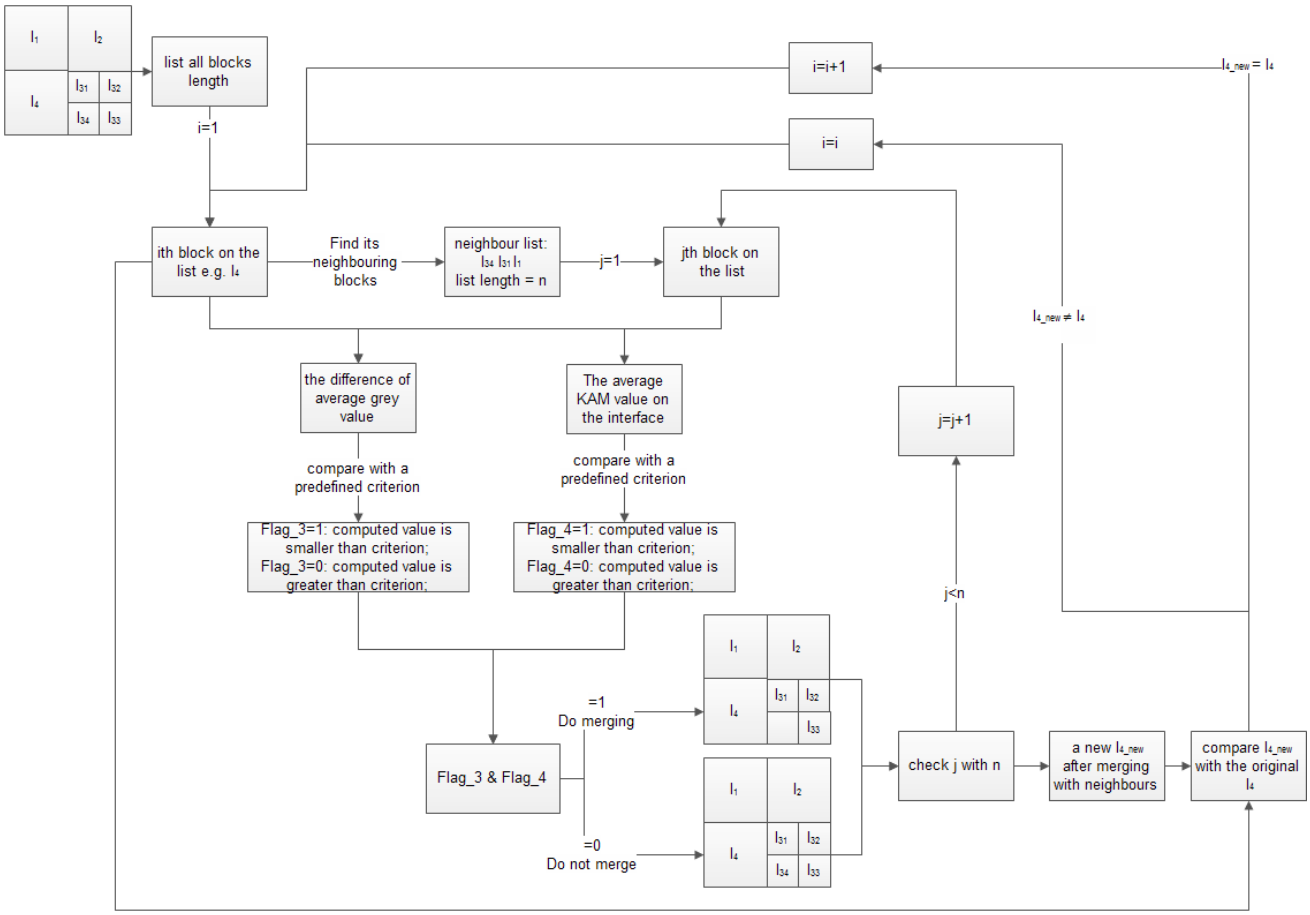

Figure 6- 15 Schematic illustration of the merging process including the predicates used in the process

KAM is introduced as another orientation-based feature in the merging process (Figure 6- 15). The relationship between the KAM predicate and the average orientation predicate is logic OR, while the grey value predicate is a necessary condition to perform the merging process.

6.2.10 Post-processings

Closing operation

In mathematical morphology, the closing of an image A by a structuring element B is the erosion of the dilation of A (Figure 6- 16). Closing tends to enlarge the boundaries of foreground (bright) regions in an image, and shrink background colour holes in

such regions, but it is less destructive of the original boundary shape. Therefore closing is applied here, to smooth the colony boundaries.

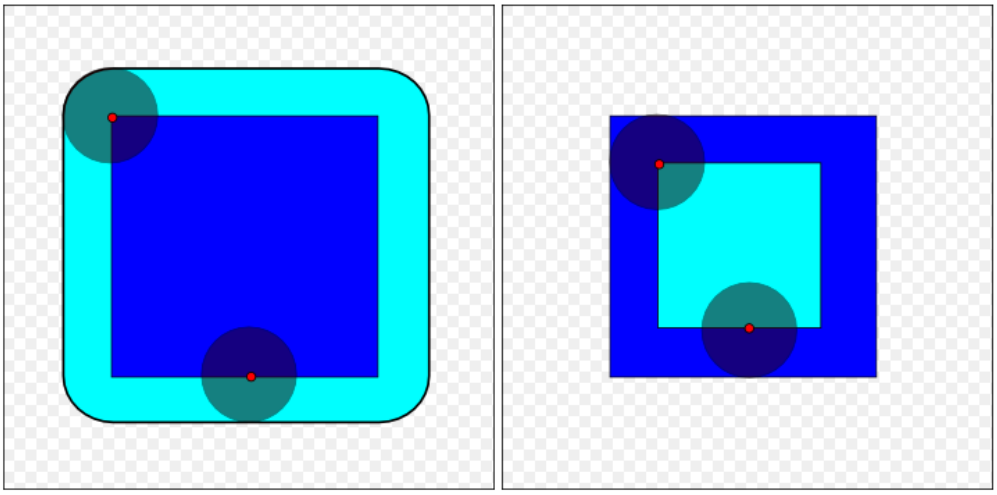

Figure 6- 16 An illustration of dilation (a) and erosion (b). The region in dark blue is an object in image A, the moving circle is the structuring element B. The dilated object in (a) is the light blue region, which is covered by the structuring element pixels while the origin element is probing inside the object. For erosion the new object is the light blue region, in which the origin of the element locates while the structuring element is probing inside the object (Efford, 2000).

Hole-filling and small region merging

There are quite a few small regions generated by the algorithm, especially those surrounded by only one region (holes inside a region), that are highly unlikely to be pearlitic colonies due to their isolation. Small regions which are adjacent to more than one region are also likely to be falsely generated as their size might be smaller than the resolution of the detecting algorithm. Therefore, a program to fill the holes and merge small regions whose sizes are below a particular value is applied. One point needed to be noted is how to determine the critical size.

In the orientation detecting algorithm, a probing window centred at the data point is

used to determine the orientation of that point by Fourier transform method. An appropriate neighbourhood size needs to be selected during this process. In this study, a neighbourhood size which allows 3~4 cycles of bright to dark lines (interlamellar spacing) within the area of interest is used. Meanwhile, if the neighbourhood size is smaller than a cycle length, a low accuracy would result. As a result, the cycle length (interlamellar spacing), based on which the probing window size is determined, can be used as a critical size to do the small colony merging (refer to section 7.2.10.2).

Directionality-based filter

Some areas in pearlitic images might be extremely weakly oriented due to either their real microstructure or bad image quality. The parameter directionality introduced in section 6.2.4 is used to discard these areas. Firstly a relatively big and weakly-oriented region should be selected, and the average directionality value for all the pixels in the region is worked out. This value would be used as the critical directionality value of the filter.

The processed results by the above algorithms contain the segmented colony information and the directionality of each pixel in the colonies. For each colony, the fraction of pixels with a directionality being below the critical value is computed. If this fraction is greater than 50%, that indicates most of this colony is weakly oriented, so this colony would not be counted into the final colony statistics.

6.2.11 Overall Flow Chart of the Algorithm

The overall flow chart of the colony size characterisation algorithm is shown in Figure 6- 17. The parameters used for each procedure are summarised in Table 6- 1.

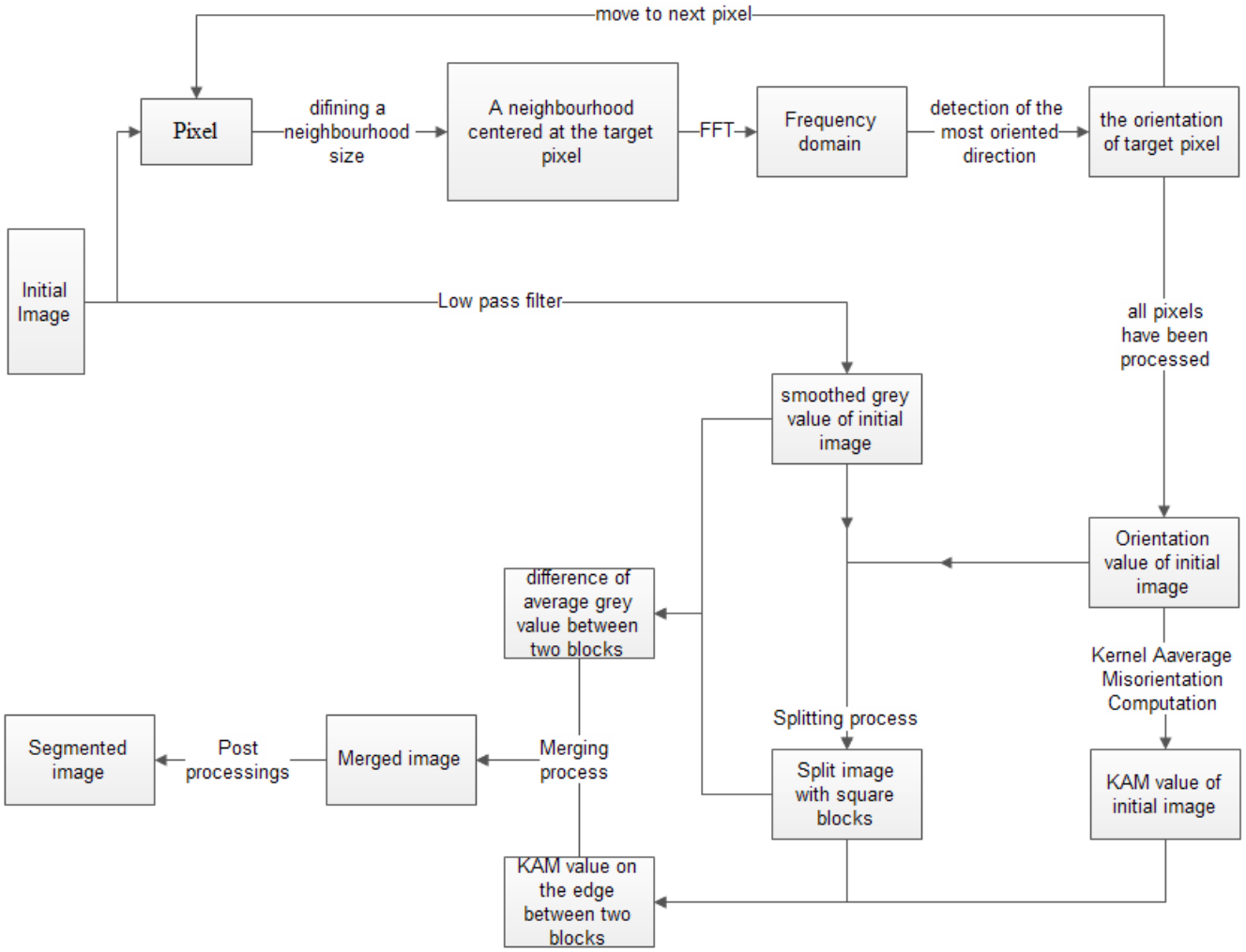

Figure 6- 17 The overall flow chart of the pearlite colony characterisation algorithm starting from pixel level to the segmented image

Table 6- 1 Summary of the main parameters used in the algorithm

Procedures	Parameter used
Neighbourhood size for FFT	35 pixels
Radius of Gaussian low pass filter for smoothing images to provide the grey value predicate	10 pixels
Neighbourhood for KAM computation	4-nearest pixels
Orientation criteria for splitting	10 °
Grey level criteria for splitting and merging	10% of the grey level range
KAM criteria for merging	5 °
Closing operation size (post-processing)	2 pixels
Merging small regions (post-processing)	650 pixels (area)

6.2.12 Synthetic Image

Apart from the micrographs from actual steel samples, a synthetic image (Figure 6- 18) with lamellar structure was also generated for testing the algorithm. In the synthetic image, most of the lamellae are straight. One colony has curved lamellae. Another one colony has very thin lamellae, to represent a relatively larger interlamellar spacing compared with its neighbouring colonies in terms of its response to low pass filtering.

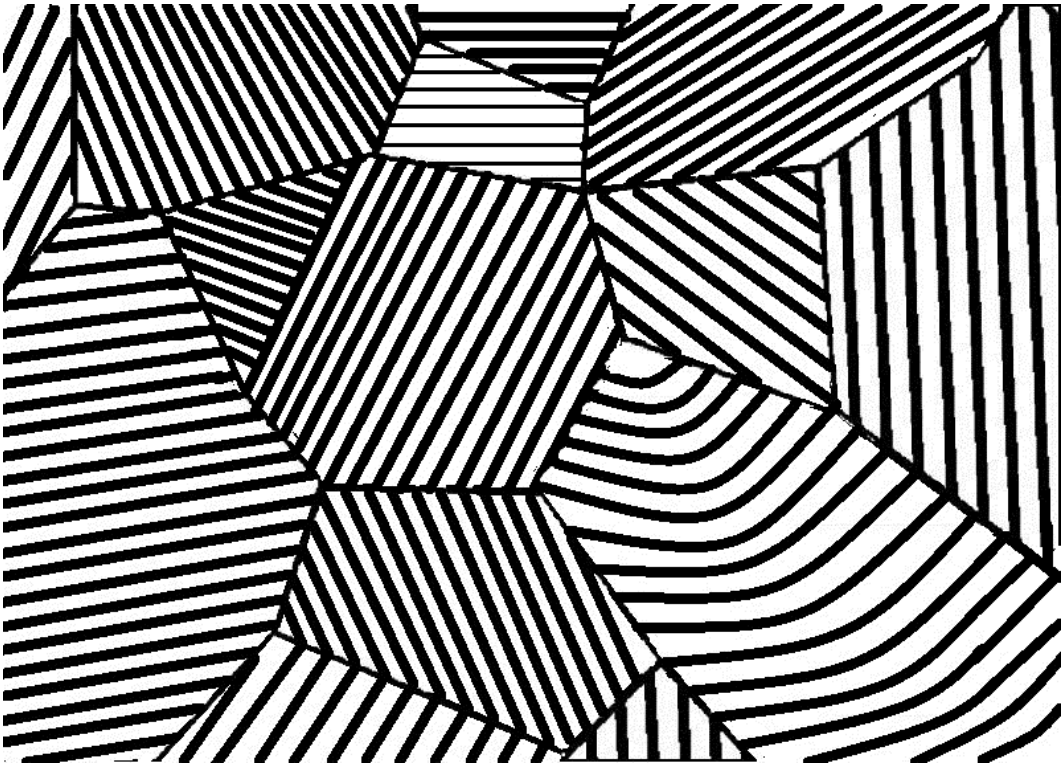

Figure 6- 18 A generated synthetic image having ideal lamellar structures for testing the colony characterisation algorithm (this image was inspired by Schulgasser (1977), Chen and Chen (2011). Some modifications were made to the structure shown in the latter literature.)

6.3 Phase Classification Model for Complex Phase Steels

6.3.1 General Principles of the Modified Algorithm Used in This Study

More than 20 GLCM statistics are used as classifying features in the study. For a particular feature, there are also a few influencing parameters which need to be determined such as the offset and direction angle in the GLCM. Therefore, to select the most representative features with appropriate parameters is an important stage in the training process. The whole algorithm is working as follows:

1) Select a training image, and draw a few typical regions that clearly represent each class (phase) on the image.

2) Generate a random subset with a given percentage (e.g. 60%) of the selected training pixels, to act as the training set; the rest of the pixels will be the testing set. The correct categories of the training set and testing set are known.
3) GLCM parameter determination: using the training set and testing set using the features with varying GLCM parameters, to get an accuracy ratio (the number of pixels classified as the correct class by the total number of the testing set of the class) with that set of GLCM parameters. Then select the best set of GLCM parameters according to their classification accuracy.
4) Feature reduction: sequential backwards selection algorithm was used to find out a few most representative features (n) out of the feature library. These features generated based on the GLCM with the parameters determined in the step (3) will be used in the classification.
5) Training: use all the selected pixels in step (2) to generate the signature for each class, which means an n-dimensional feature space is generated.
6) Predicting: extract the features for all of the unclassified images, and classify these images using a certain classifier.

The flow chart of the algorithm is shown in Figure 6- 19.

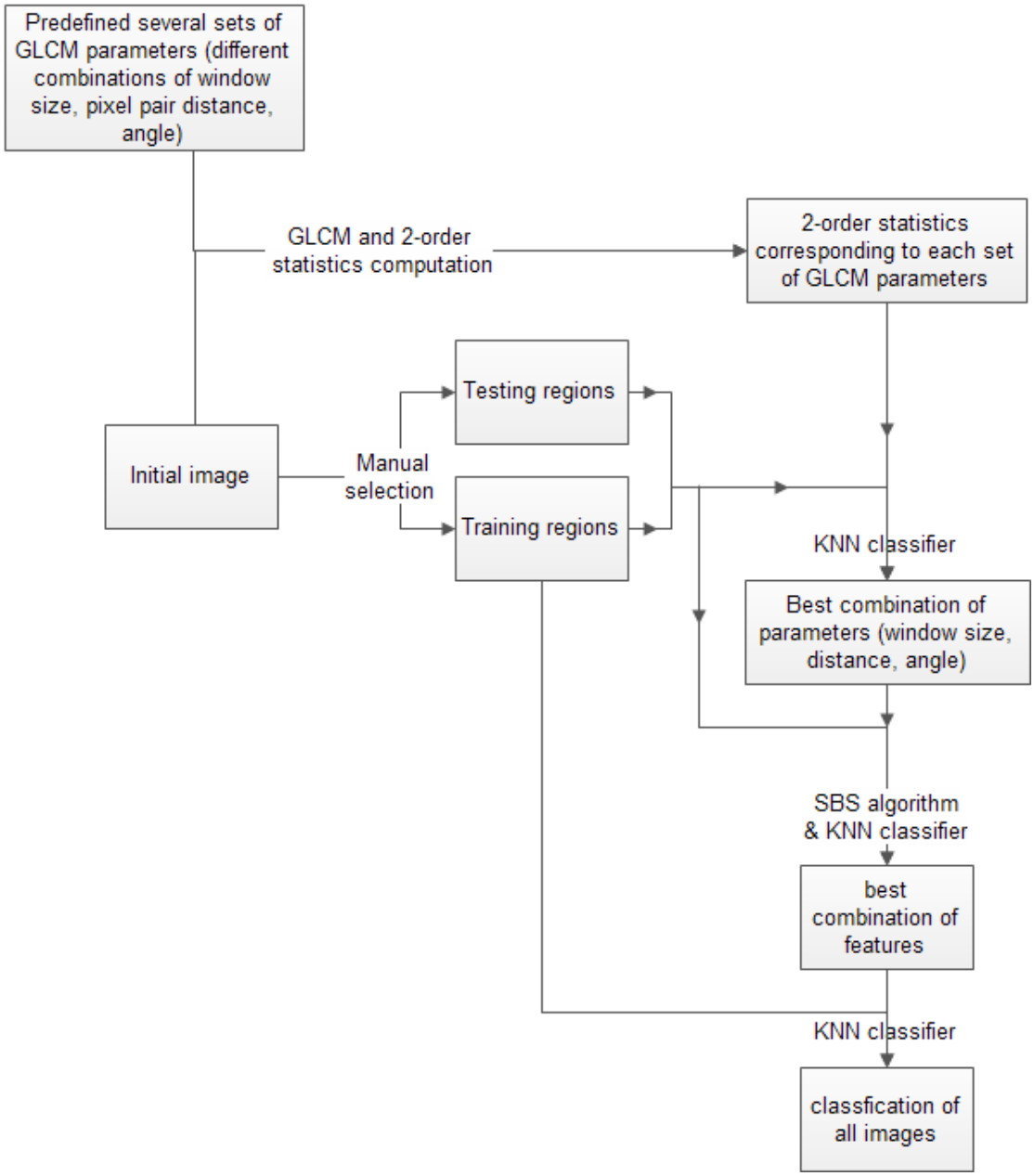

Figure 6- 19 The flow chart showing the procedures of the phase classification algorithm

6.3.2 Region Selection and GLCM Parameter Determination

The first step of the algorithm is to select several regions with representative morphology of each phase to train the classifier. Using the GIMP software (Kimball and Mattis, 1996), the selected regions are painted with different colour so that the selected regions can be located by detecting the colour.

Three influencing parameters need to be defined to determine a GLCM. These parameters are the pixel pair distance *d*, the angle α, and the number of grey level N_g in the new grey level system. In addition, the size of the local neighbourhood *A* is also an unknown parameter and needs to be determined. In the process of determining these parameters, various sets of parameters were applied to classify the testing regions after training and the set with highest classification accuracy was selected.

6.3.3 Feature Selection Algorithm

The next step after the best parameter settings have been determined is to select a combination of a few features that gives the best classification performance. That can reduce the computational complexity. A Sequential Backward Selection (SBS) method was used in the study to determine the best combination among a number of features. This approach is schematically shown in Figure 6- 20. The selection procedure consists of the following steps:

- Compute the classification accuracy for the feature vector $[x_1, x_2, x_3, x_4]^T$.
- Eliminate one feature and for each of the possible resulting combinations ($[x_1, x_2, x_3]^T$, $[x_1, x_2, x_4]^T$, $[x_1, x_3, x_4]^T$, $[x_2, x_3, x_4]^T$), compute the corresponding classification accuracy. Select the combination with the best value, say$[x_1, x_2, x_4]^T$.
- From the selected three-dimensional feature vector eliminate one feature and for each of the resulting combinations ($[x_1, x_2]^T$, $[x_1, x_4]^T$, $[x_2, x_4]^T$), compute the classification accuracy and select the one with the best value.

Thus from *m* features, one feature from the best combination is dropped out at each step until *l* features are left. In the algorithm used in this study, the feature selection process keeps running until only 1 feature is left. Then the best *l* features are determined by the classification accuracy of each step. In each case, the classifier is

trained using the training data and tested using the (different) testing data, as otherwise over-fitting is likely.

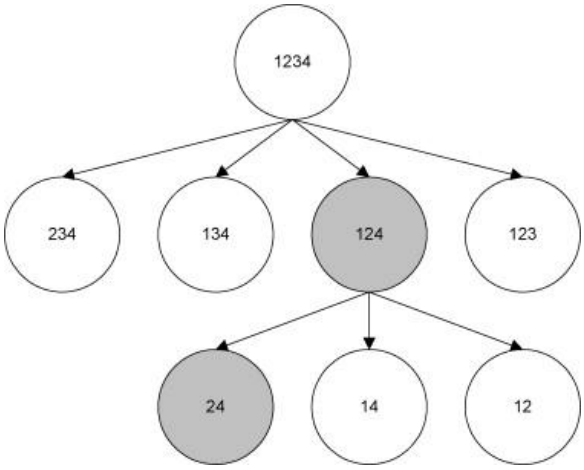

Figure 6- 20 A schematic illustration of the sequential backward selection method (Godavarthy et al., 2008)

6.3.4 Classifier

The classifier used in this study is a K-Nearest Neighbours classifier, which is a method for classifying objects based on the closest training examples in the feature space. The training examples generate vectors in a multidimensional feature space, each with a class label. In the classification stage, an unlabelled vector (test point) is classified by assigning the label which is most frequent among the *k* training samples nearest to that test point. Usually Euclidean distance is used as the distance metric, which is defined as follows:

$$dist(x, y) = \sqrt{\sum_k (x_k - y_k)^2} \qquad \text{(Eq6.6)}$$

Where *x* and *y* are two points in the k-dimensional feature space and x_k and y_k are their corresponding feature values in these dimensions.

There are several prominent advantages with this method such as simple and intuitive learning, flexible decision boundaries and variable-sized hypothesis space. However, some disadvantages still exist (Suguna and Thanushkodi, 2010):

- Features with larger ranges will be treated as more important.
- Irrelevant or correlated features have high impact and need to be eliminated.
- Typically cannot handle high dimensionality.

Therefore, some types of processing are applied to solve these aforementioned problems:

- Feature data normalization. After obtaining the data of the training points, the mean and standard deviation of the population of values of each feature were calculated. These values were used to normalize the training data to have a mean of 0 and a variance of 1. The mean and standard deviation of the training data were also used to normalize the testing sets. This normalization step was included so that all features contributed equally to the Euclidean distance metric used to define nearest neighbours.

  Normalization procedures for training and testing stages:

$$X_k^{nor} = {X_k - \bar{X}_k}/{s_k} \qquad \text{(Eq6.7)}$$

  Where for each feature, *k*, X_{nor} is the normalized training data, X is the initial training data, $\bar{X}$ is the mean value of the training data and s is the standard deviation of the training data.

  And for the testing process:

$$Y_k^{nor} = {Y_k - \bar{X}_k}\Big/{S_k} \quad \text{(Eq6.8)}$$

Where Y_{nor} is the normalized training data, *Y* is the initial training data.

6.4 Parameters Used for Estimating the Influence of Etching Degree on Image Analysis

Etching degree affects image analysis in this study by affecting the grey level of pixels of different phases and thus affecting their separability. Three separability measures from literature (Theodoridis and Koutroumbas, 2009) are used in here to quantify the separability of pixels under each etching condition.

The following matrices are defined:

Within-class scatter matrix:

$$S_\omega = \sum_{i=1}^{M} P_i \sum i \quad \text{(Eq6.9)}$$

Where $\sum i$ is the covariance matrix for class ω_i

$$\sum i = E[(x - \mu_i)^T (x - \mu_i)] \quad \text{(Eq6.10)}$$

And P_i is the priori probability of class ω_i. That is, $P_i \cong \frac{n_i}{N}$, where n_i is the number of samples in class ω_i, out of a total of *N* samples. Trace $\{S_\omega\}$ is a measure of average, over all classes, variance of the features.

Between-class scatter matrix

$$S_b = \sum_{i=1}^{M} P_i(\mu_i - \mu_0)^T(\mu_i - \mu_0) \quad \text{(Eq6.11)}$$

Where μ_0 is the global mean vector

$$\mu_0 = \sum_{i}^{M} P_i\mu_i \quad \text{(Eq6.12)}$$

Trace $\{S_b\}$ is a measure of the average (over all classes) distance of the mean of each individual class from the respective global value.

Mixture scatter matrix

$$S_m = E[(x - \mu_0)^T(x - \mu_0)] \quad \text{(Eq6.13)}$$

That is, S_m is the covariance matrix of the feature vector with respect to the global mean. Then three separability measures can be defined as:

$$\text{J1} = \frac{\text{trace}\{S_m\}}{trace\{S_w\}} \quad \text{(Eq6.14)}$$

$$\text{J2} = \frac{|S_m|}{|S_w|} = |S_\omega^{-1}S_m| \quad \text{(Eq6.15)}$$

$$\text{J3} = \text{trace}\{S_\omega^{-1}S_m\} \quad \text{(Eq6.16)}$$

The separability measures take large values when samples in the *l*-dimensional space are closely clustered around their mean, within each class, and the clusters of the different classes are well separated.

Chapter 7. Results and Discussions

7.1 Shading Correction

7.1.1 Phase Observations and Identification

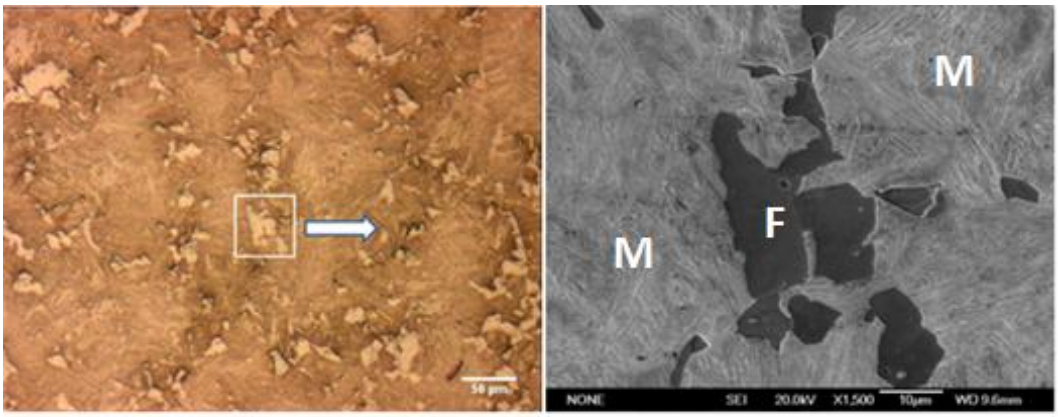

Figure 7- 1 An optical image (a) and SE image (b) showing the microstructure of sample SC2; the white rectangular marked region in image (a) is shown in a higher magnification in image (b). The scale bar length in (a) and (b) is 50μm and 10μm respectively.

Optical and secondary electron (SE) micrographs of the sample SC2 are shown in Figure 7- 1. Two different phases (ferrite and martensite) can be observed. In the SE image (Figure 7- 1b), the uniformly dark regions represent ferrite, while the lath-like structures with inter-distributed bright and dark regions correspond to martensite. In the optical image (Figure 7- 1a), the bright regions represent ferrite. The ferrite is mainly distributed along prior austenite grain boundaries.

It can also be seen that the contrast between martensite and ferrite for optical image and SE image is inverse: the ferrite is bright in optical image but dark in SE image and the martensite is dark optically but bright in SEI. The reason lies in the different imaging principles of electron microscope and optical microscope. Contrast in SEM is defined as the ratio of the change in signal (secondary electron intensity) between two

points on the specimen and the average signal. Secondary electrons can escape from the surface of most materials at depths between 5 ~ 50 nm depending on the accelerating voltage, a greater number of electrons escape from surfaces having a higher angle with the normal incidence of the beam (Rochow and Tucker, 1994), which is due to the increased interactive volume (Figure 7- 2), therefore a rougher surface has a higher brightness.

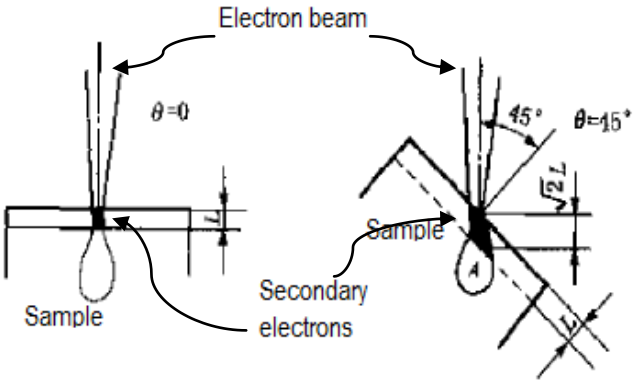

Figure 7- 2 The interaction volume of SE with different θ which show that a tilted surface gives larger volume to provide secondary electrons (Wang, 2006)

For optical microscopes using reflected light, the contrast is related to the reflectivity of the sample surface and the phase shift from varying heights. Compared with ferrite, martensite has a lower reflectivity due to its rougher surface caused by the surface relief phenomenon, which makes it appears darker than ferrite optically.

7.1.2 Shading Correction Results

Effects of shade correction on classification by grey level

A scan of pixel brightness along a line was taken both from the uncorrected image and the shading-corrected image, and the results are shown in Figure 7- 3.

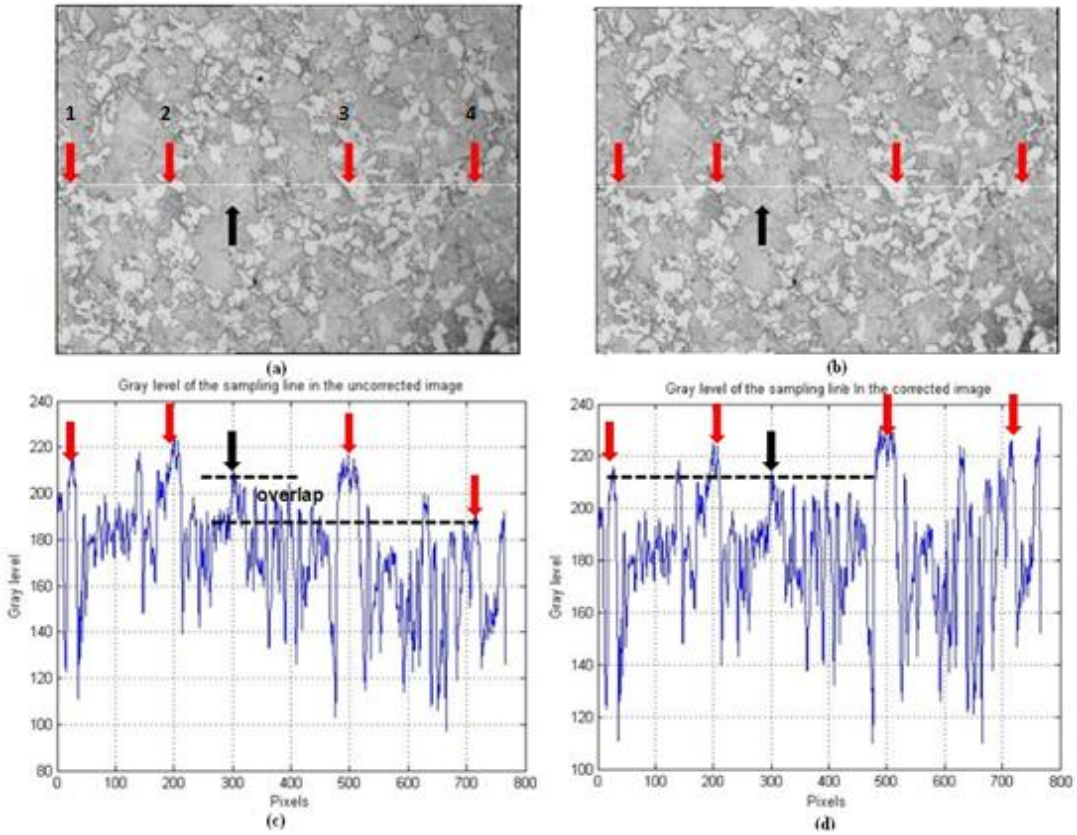

Figure 7- 3 A typical optical image from sample SC2 to show the effect of shade correction: (a) uncorrected image; (b) corrected image; (c) the grey levels of the pixels from a horizontal line scan in the uncorrected image; (d) the grey levels of the pixels from a line scan in the same position in the corrected image. Some sampling ferrite regions were highlighted by red arrows, and some sampling martensite regions were highlighted by black arrows.

The uncorrected and corrected images of sample SC2 are shown in Figure 7- 3(a) and (b). The grey values of a horizontal line scan in the same position of two images are shown in Figure 7- 3(c) and Figure 7- 3(d). Image (c) shows that the grey levels of ferrite cover a wide range (from 190 to 220), which causes a big overlap of grey levels between the ferrite region in the right side and martensite region in the left side. After the shading correction processing, the grey levels of the right hand side area were increased. The grey value of the 2 ferrite regions which are highlighted with red arrows 3 and 4 in Figure 7- 3 have risen to about 230 from original values of 210 and 190 respectively, which are very close to that of region 2 (around 225). However,

there are still a few locations where the shading effect was not well corrected. 4 example ferrite regions were numbered and marked with an arrow on Figure 7- 3. The grey value of location 1 was not changed much after shade correction and is slightly lower than the other 3 locations. Similarly, the grey values of the martensitic regions between location 1 and location 2 were not changed much, which is unlike those area between location 3 and location 4. There are two possible reasons:

The smoothing of the white calibration image is not perfect.
The WHITE calibration image from the as-polished sample does not exactly represent the background of the images from the etched samples.

Although region 1 still has a lower grey level than other ferritic regions, it is still slightly higher than the highest grey level of martensite (highlighted by the black arrow) and can be distinguished. In general the grey values of each phase become approximately constant regardless of their position in the image, and the overlap was removed. As more detailed image analysis relies on absolute grey levels, it is beneficial to do this shade correction first.

Effects of shade correction on classification by image texture

Whether the image texture analysis is improved by shade correction was also studied. The algorithm proposed in section 6.3 was used here. An example image with a two phase structure including upper bainite and martensite was taken from sample F. Figure 7- 4 (a) shows the initial example image and (b) shows the shade corrected image. It can be seen the image brightness in (a) is generally higher on the left and lower on the right. After the shade correction procedure, the brightness throughout the image is roughly even. The training sets for the initial image and corrected image were taken from exactly same locations on the image (see Figure 7- 5), which can eliminate the influence of the training set positions to the classification performance.

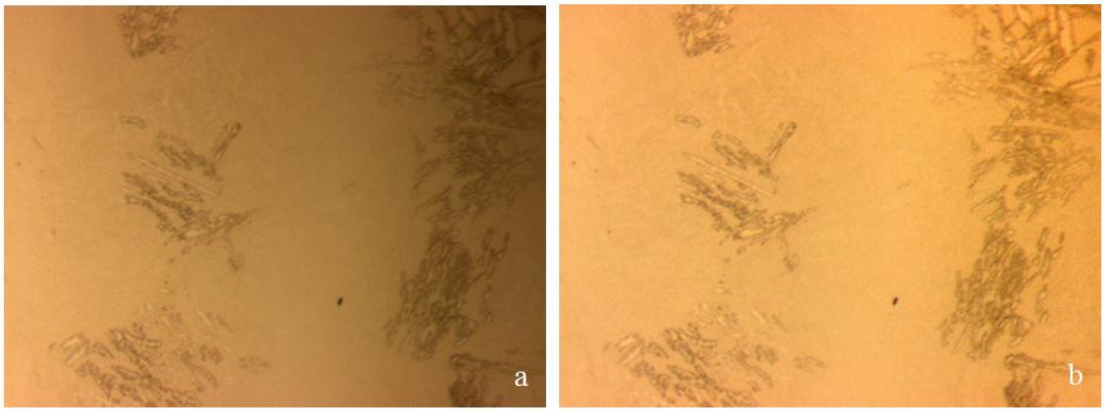

Figure 7- 4 An example image (200x) showing a two phase structure: (a) the initial image; (b) the shade corrected image. The lath with higher contrast is upper bainite and the matrix is martensite.

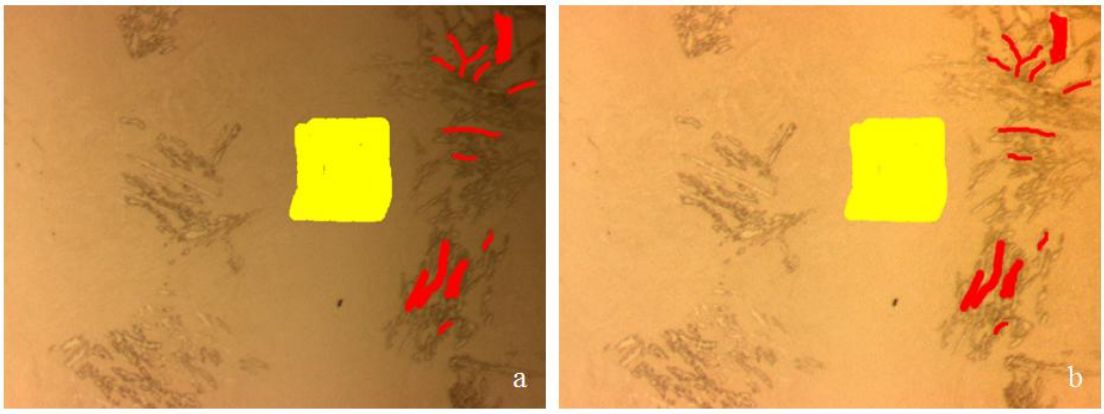

Figure 7- 5 Exactly same region in the initial image (a) and the shade corrected image (b) was used for training. The yellow area is the training region for martensite; the red area is the training region for upper bainite.

The phase fractions obtained for the initial image and shade corrected image by the automatic method were shown in Table 7- 1. Manual classification was also carried out (shown in Figure 7- 7). The table shows that the result obtained automatically from the shade corrected image is closer to the manual classification result than the automatic classification on the initial image.

Table 7- 1 The phase fractions obtained by automatic method (on the initial image and shade corrected image respectively) and the manual method

	Automatic classification on initial image	Automatic classification on shade corrected image	Manual classification
Fraction of upper bainite (%)	12.1	24.4	21.8
Fraction of martensite (%)	87.9	75.6	79.2

The automatically classified images are shown in Figure 7- 6. It can be seen obviously that the classification on the shade corrected image is much better than the initial image in terms of the position of detected phases. On the initial image, some upper bainite area was incorrectly classified as martensite and a number of martensite regions were classified as upper bainite. The classification with the shade corrected image is generally correct.

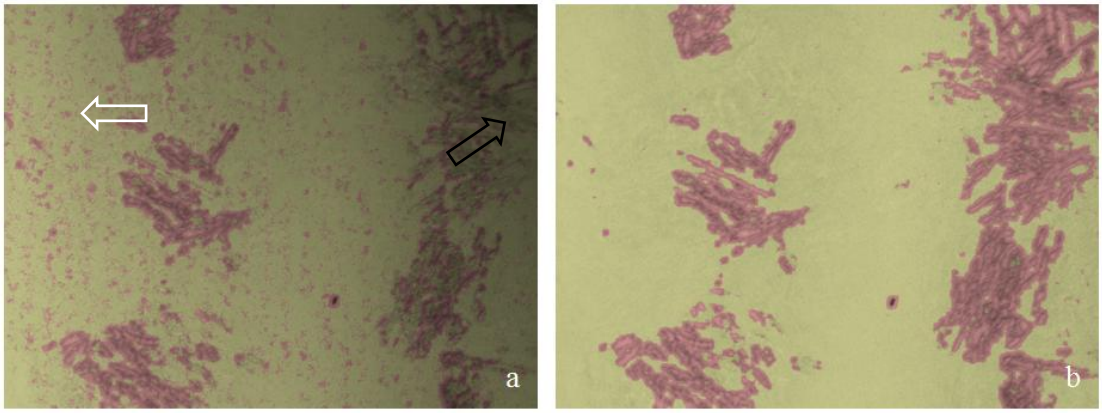

Figure 7- 6 The segmentation results with the initial image (a) and shade corrected image (b). The red area is the automatically classified upper bainite and the yellow area is the automatically classified martensite. The white arrow on image (a) shows the martensite region which was incorrectly classified as upper bainite; the black arrow shows the upper bainite region which was incorrectly classified as martensite.

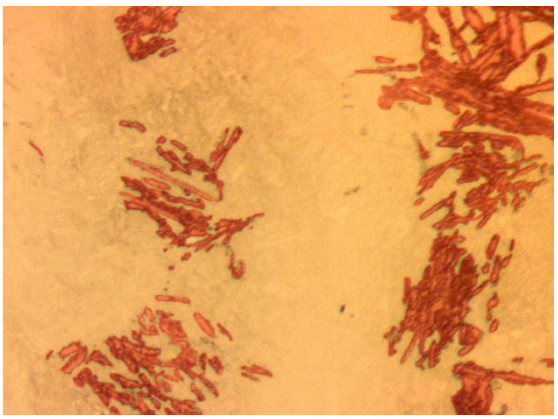

Figure 7- 7 The manual classification on the image. The red area is the manually classified upper bainite and the rest area is martensite.

7.1.3 Conclusion of the Shade Correction Investigation

As an important pre-processing operation, the shade correction can effectively eliminate the influence from the background (everything else from the system but the specimen). This procedure is important for both intensity-based image processing and image texture analysis that was used in this work.

7.2 Pearlitic Colony Characterisation

7.2.1 Optical Observation

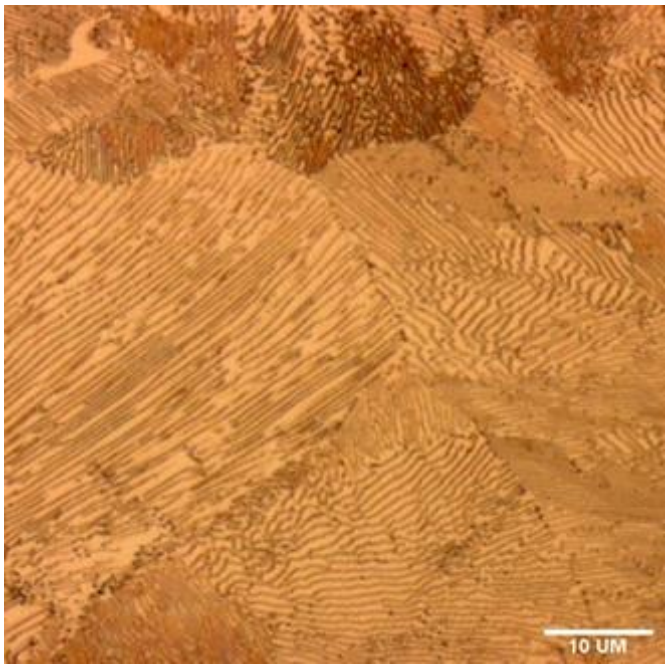

Figure 7- 8 An optical image taken from sample P showing the pearlitic microstructure of R260 (478x478 pixels)

Figure 7- 8 is an optical micrograph showing the microstructures of R260 (sample P). In most areas of the image, there are clear parallel structures called lamellae. The orientation of the lamellae is a most important feature to define pearlitic colonies.

7.2.2 Representation of Every Processing Stage

Figure 7- 8 was used as an example to represent every stage of the aforementioned image processing procedures. Figure 7- 9 shows the orientation angle (ranging from -90 ° to 90 °) map of the example image, while the overlaid image of the orientation map and the initial intensity image is shown in Figure 7- 10. The colours in the images represent orientation angle value. It can be clearly seen that most pearlitic colonies are in same or similar colour.

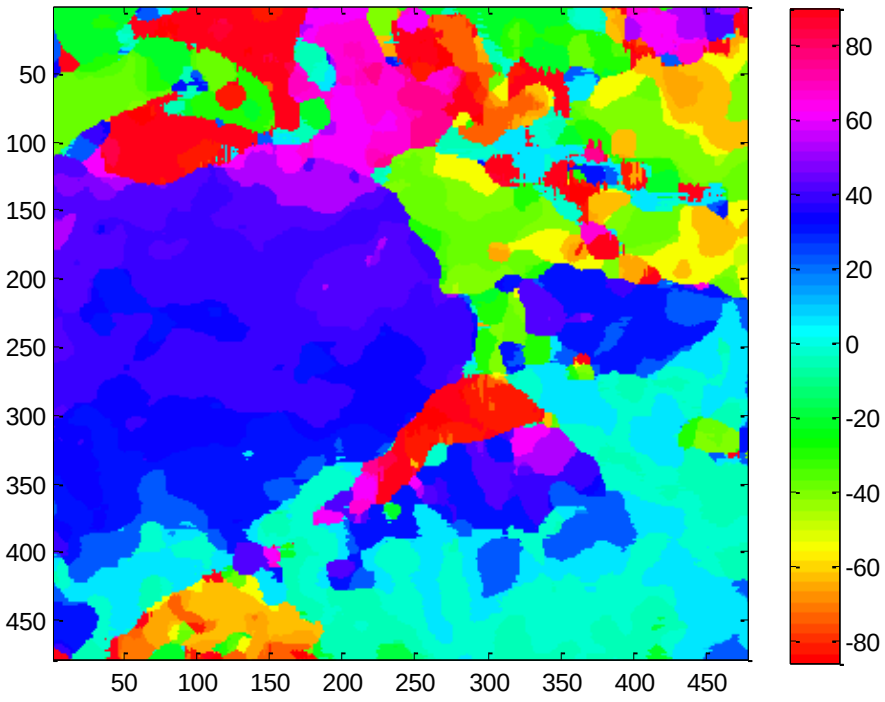

Figure 7- 9 The DFT-measured orientation of the example image. The X-axis and Y-axis correspond to the horizontal and vertical coordinates in the initial image Figure 7- 8. The colour in the image represents the orientation at each point, according to the colour bar on the right.

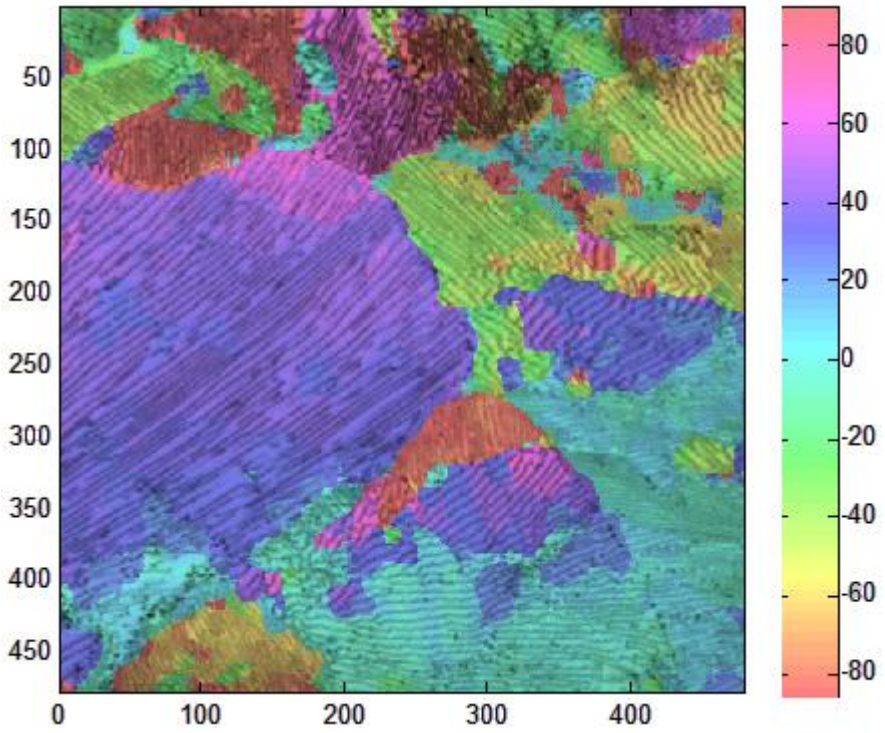

Figure 7- 10 The initial image Figure 7- 8 coloured with the DFT-measured orientation. The X-axis and Y-axis correspond to the horizontal and vertical coordinates. The colour represents the orientation of each point, according to the colour bar shown on the right of the image.

Figure 7- 11 is the KAM map of the example image with the value normalised to [0,1]. Compared with the initial intensity image, most of the pixels with high KAM value are along the colony boundaries.

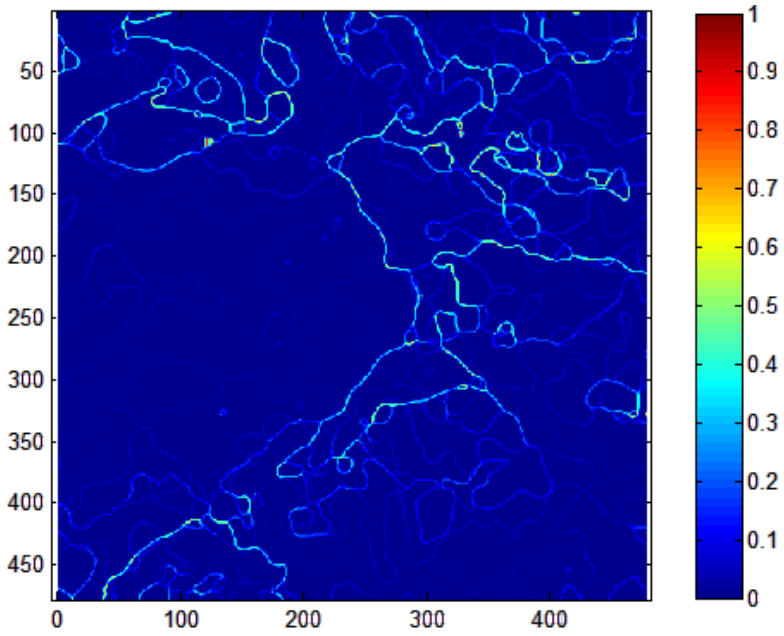

Figure 7- 11 Normalised KAM map based on the orientation graph shown in Figure 7- 9. The colour shows the intensity of the KAM. The X-axis and Y-axis correspond to the horizontal and vertical coordinates in the initial image.

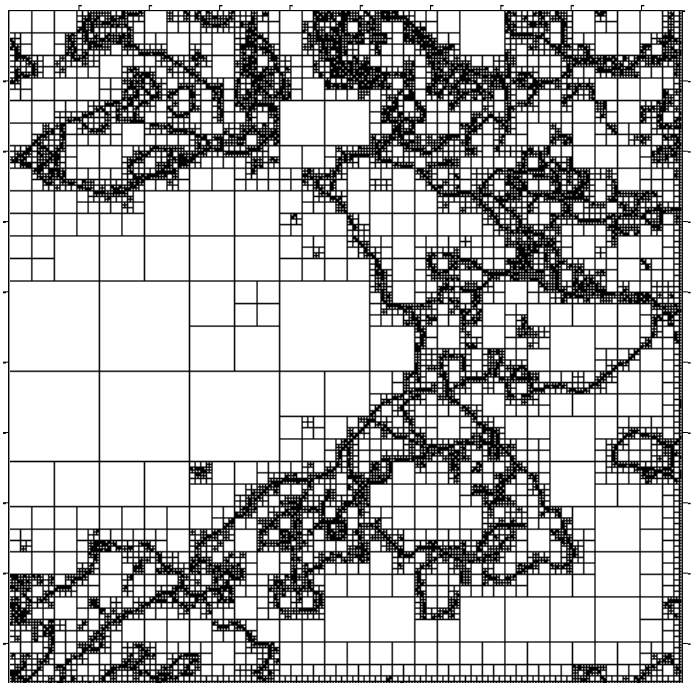

Figure 7- 12 The results after applying a splitting process to the initial image (Figure 7- 8)

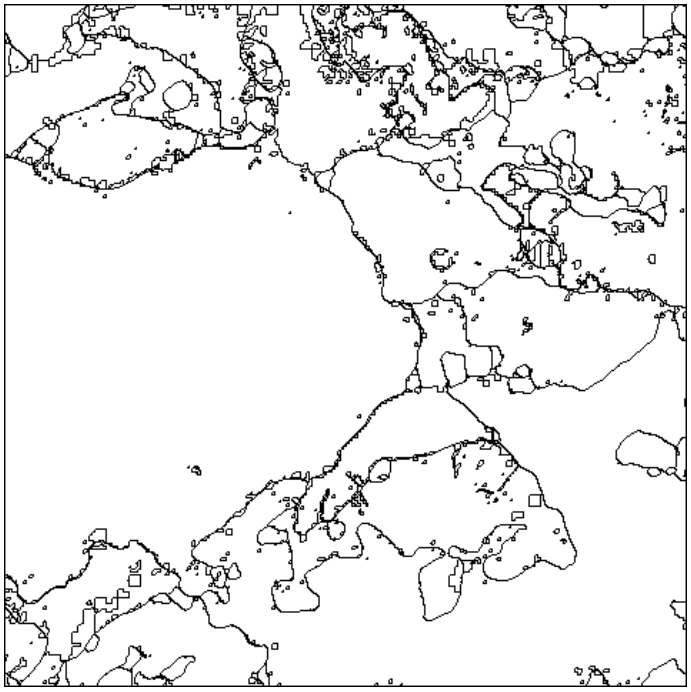

Figure 7- 13 The results after applying a merging process to the split image (Figure 7- 8)

By the algorithm described in section 6.2, the splitting and merging process was carried out. The results are shown in Figure 7- 12 and Figure 7- 13 respectively. In Figure 7- 12 (after splitting) every block is square. Small blocks distribute mainly

along the colony boundaries, where there are rapid spatial changes in orientation and grey level, while inside the grains there are mainly large blocks. By merging the blocks with similar predicate values the colonies are estimated, which are the white regions isolated by black lines in Figure 7- 13. Although some noise-eliminating operations have been carried out both before and during the processing, there are still some small islands appearing in the image, which are not like to be a colony. Therefore post-processing is needed to reduce this phenomenon.

7.2.3 Results Comparison and Discussion

After the aforementioned post-processings, the result is shown in Figure 7- 14. Different colour represents different pearlitic colonies. The same image was also characterised manually by drawing the boundaries, which is shown in Figure 7- 15.

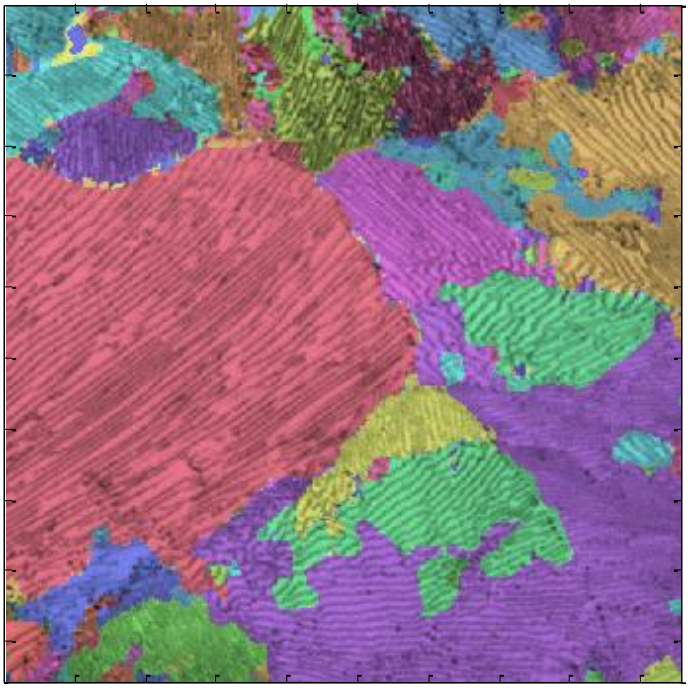

Figure 7- 14 The final segmentation of the initial image (Figure 7- 8). Segmented colonies were shown in different colour.

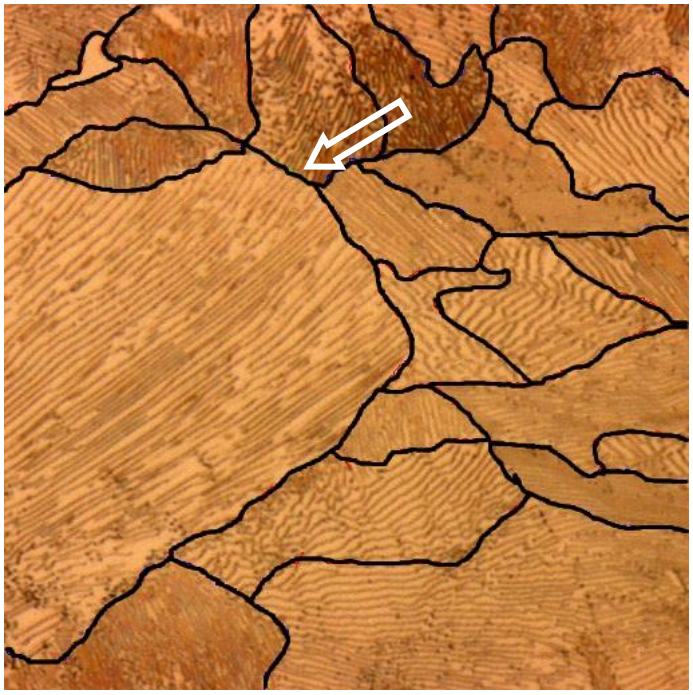

Figure 7- 15 The manually drawn image with colonies separated by the black lines. The white arrow marked colony boundary is segmented by interspacing of lamellae. It is used in section 7.2.9.4.

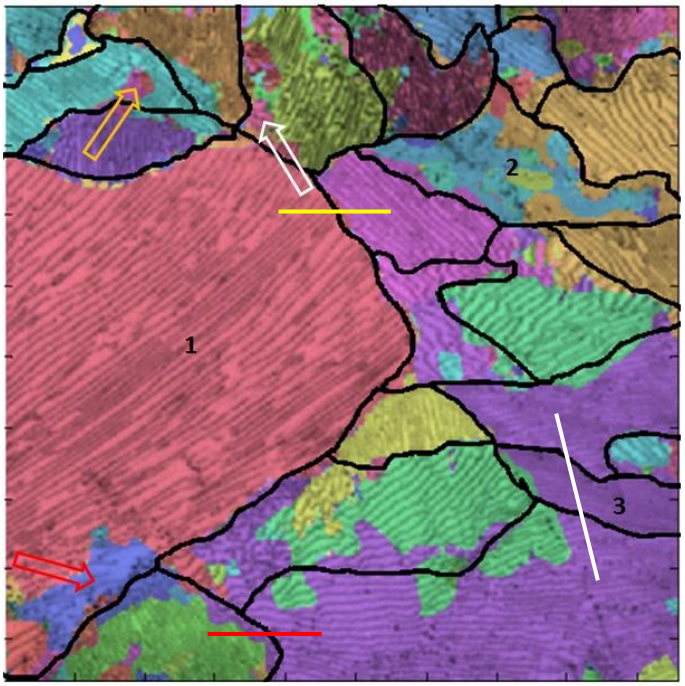

Figure 7- 16 The automatically segmented image with the manually drawn boundaries shown on top in black lines. Region 1, 2, 3 and the arrow and straight line were marked for the discussion in this section and section 7.2.7.

Figure 7- 16 shows the automated result and manual drawing on the same image. Each automatically classified pearlitic colony has a unique colour. The black lines show the colony boundaries drawn manually. From the image it can be seen the automated and manual classification often have a good agreement. However, there are still a few places where these two results are not consistent as follows:

1) The white-arrow marked region was not accurately classified for it contained granular pearlite. Granular pearlite has no orientation or too weak orientation to be detected by the algorithm.
2) The orange-arrow marked region was incorrectly classified as a separate colony. From the original image (Figure 7- 8) it can be seen there is a blurry line across the lamellae at the corresponding position. The blurry line might be sectioning effect or artefacts generated from the sample preparation. Apart from the artefacts, the scratches from sample grinding and polishing could also affect the algorithm for their strong orientation.
3) In the red-arrow marked region, which is in colony 1 near a boundary, the lamellae are not as continuous as in the rest of the colony. The ferrite phase is more dominant here with a few short and disconnected carbide plates distributing within the ferrite. This will affect the classification by mean grey level after low-pass filtering.
4) Region 2 has a similar problem as the orange-arrow marked region: the presence of artefacts. Region 2 has a finer microstructure so that it is more affected by the artefacts. The area inside the region was separated into several random colonies, and the region boundary area was also affected by the adjacent strong-oriented colonies.
5) Region 3 has a similar orientation but smaller spacing than the colonies above and below it in the image. However, in the automated algorithm it was not separated. Since the spacing is characterised by the local average grey level,

the grey levels of these three regions were studied here. The average grey value of a 5x5 neighbourhood centred at each pixel on the line shown in Figure 7- 16 was computed and plotted in Figure 7- 17. It can be seen from the plot that the average grey level difference between region 3 and its neighbouring colony is approximately 10. However, this grey difference between colonies is smaller than that between lamellae within a colony. Therefore, the criteria to characterise lamellar spacing is needed to be reconsidered.

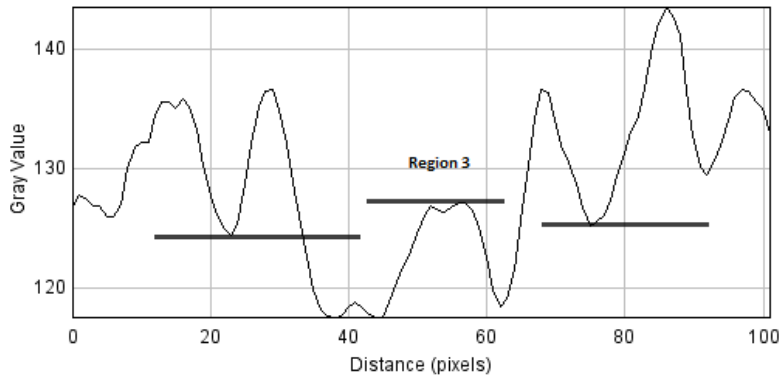

Figure 7- 17 A line plot (white line in Figure 7- 16) showing the grey level of region 3 and its two neighbouring colonies

7.2.4 The Effect of Proposed Orientation Measuring Algorithm

An algorithm was proposed in section 6.2.2 to measure the orientation of a pixel using its neighbourhood. The performance of the algorithm was studied using two ideal patterns shown in Figure 7- 18.

Figure 7- 18 (a) and (b) are two lamellar structures with a horizontal tilt angle of 10 ° and 20 ° respectively. There are two whole cycles in both images. (c) and (d) are their corresponding ASD images. The colours represent the intensity in each position, which can refer to the colour bar in the right hand side of the image. It can be seen that although the initial structures have 10 degree difference in orientation, the pixel

with the highest amplitude spectral intensity is located at the same position in these two corresponding images ((c) and (d)). Consequently same results will be obtained if this position is used solely to work out the orientation. In addition, since there are only 2 or 3 cycles in the initial structures, the peak value in the ASD image will appear at a position where is 2 or 3 pixels away from the centre, which is a small distance for accurate resolution.

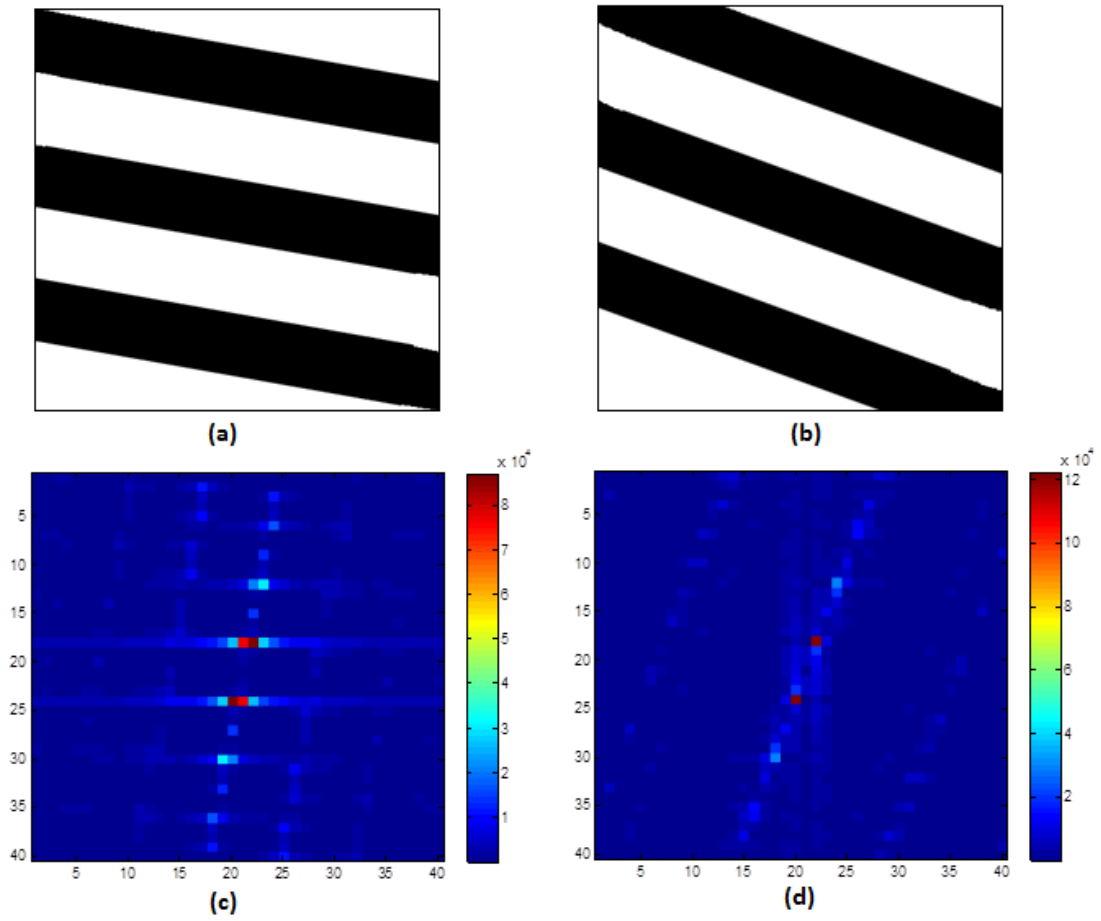

Figure 7- 18 An illustration of the accuracy of the proposed orientation measuring algorithm. (a) and (b): Two lamellae structures (40 x 40 pixels) with a horizontally tilted angle of 10° (a) and 20° (b). (c) and (d): the corresponding ASD images of (a) and (b). The colour in image (c) and (d) represents the ASD intensity with the colour bar showing on the right of each image.

If the orientation of the two images are simply computed by applying the inverse trigonometric function (Eq7.1) to the position of the peak value (the dark red point in

Figure 7- 18 (c) and (d)) in the ASD image, then same value -27 ° is obtained for both images.

$$\varphi = \arctan\left(\frac{dx}{dy}\right) \quad \text{(Eq7.1)}$$

Where dx is the horizontal distance of the peak point from the centre; dy is the vertical distance of the peak point from the centre.

Two methods were proposed to solve the problem:

1) A family of straight lines across the central point on ASD were generated, and the orientation angles of these lines were in linear distribution between 0 ° and 180 °. The number of the lines is determined by the resolution requirement of orientation. For example, 60 lines (180 °/3 °) were needed in order to reach a resolution of 3 °. Since all of the pixels on the same line represent same orientation in the spatial domain but different period, the sum of the intensities of these pixels which are on the line can represent the total energy of their corresponding orientation in the spatial domain. The orientation with maximum energy can be easily obtained by comparing these sums.
2) The lines used for energy computing are 2 pixels in width. The width of the probing line influences the resolution and the accuracy of the method. The reason lies in the discreteness of the image. Any object such as a point, a line or a cube is formed by a certain number of pixels which individually has a non-negligible area. That means the lines in an image are not strictly straight on the pixel-wise scale, which can be shown in Figure 6- 7. The more pixels the line contains, the more representative it is as straight. This ensures the accuracy of the orientation of the lines. However, the resolution is decreased because a wider line takes up a larger proportion of the total area, which reduces the variation between lines. However, it is difficult to determine a

most appropriate width in this case because the precise angle of the pixel with maximum intensity cannot be determined in the pixel-wise scale.

After applying these two methods, the orientation of the Figure 7- 18 (a) and (b) were measured to -9 ° and -21 ° respectively. Both the resolution and accuracy were much improved.

7.2.5 Methods to Avoid Low Frequency Influence

Although shade correction has been applied in the pre-processing stage, the grey value coming from the background might not be same everywhere over the image (see the results in section 7.1.2). It may change gradually and slowly, but performs a strong influence upon the orientation detection.

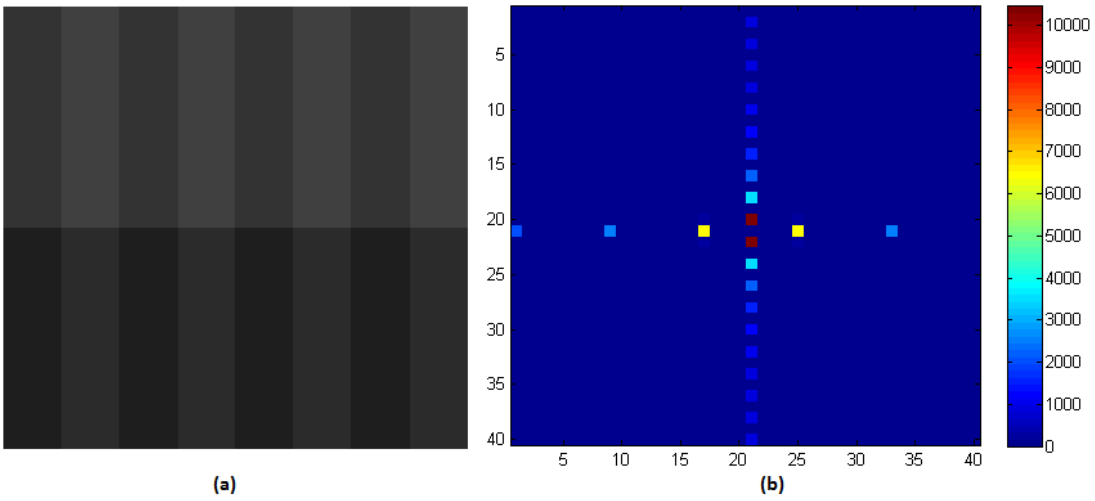

Figure 7- 19 An illustration of the influence from low frequency patterns: (a) a 40x40 pixel image with lamellae structures and uneven background; (b) the corresponding ASD image of (a). The colour in image (b) represents the ASD intensity with the colour bar showing on the right.

Figure 7- 19 is an illustration of the influence from low frequency patterns such as the uneven background. The lamellae in Figure 7- 19(a) represent pearlitic structures, while the grey value of the top half of the image is a few bits higher than the bottom

half, which represents a gradually changing background. Figure 7- 19(b) is the corresponding ASD image of (a), with different colours representing the intensity in that position. The grey level of the lamellar structure changes four times horizontally from dark to bright, so its corresponding Fourier transform will have a local maximum at a position which is 4 pixels horizontally away from the centre, which are the pair of yellow points in Figure (b). The pair of red points (highest intensities in the ASD) comes from the background. Although the orientation of the lamellae structures is needed, it will not be obtained by the aforementioned methods due to the even higher intensity value at the low frequency area caused by the uneven background.

A band pass filter can solve the problem by discarding the low frequency components. High frequency components are also discarded to reduce noise. There are a number of band pass filters such as ideal filter, Butterworth filter and Gaussian filter. Gaussian filter has the same shape in the spatial and Fourier domains and does not incur ringing effect (multiplication in the Fourier domain corresponding to a convolution in the spatial domain. If the filter has multiple peaks in the spatial domain, the filtered image will produce ringing along intensity edges in the spatial domain). Therefore Gaussian filter is used here. The cut-off frequencies are determined by the neighbourhood size and the lamellae width scale, which is discussed as follows.

An example of Gaussian band-pass filter is shown in Figure 7- 20. f_1 and f_2 are the lower and higher cut-off frequency respectively. The filtering process is operated by multiplying the Fourier domain of a local image with an equal-sized Gaussian-shaped coefficient matrix. The filter element with a coefficient ‘1’ or ‘0’ keeps or eliminates the initial value of its counterpart in the Fourier domain. Similarly, other coefficients reduce the frequential signal. For Gaussian band-pass filtering a simplified understanding is that the signal with frequency between f_1 and f_2 is preserved.

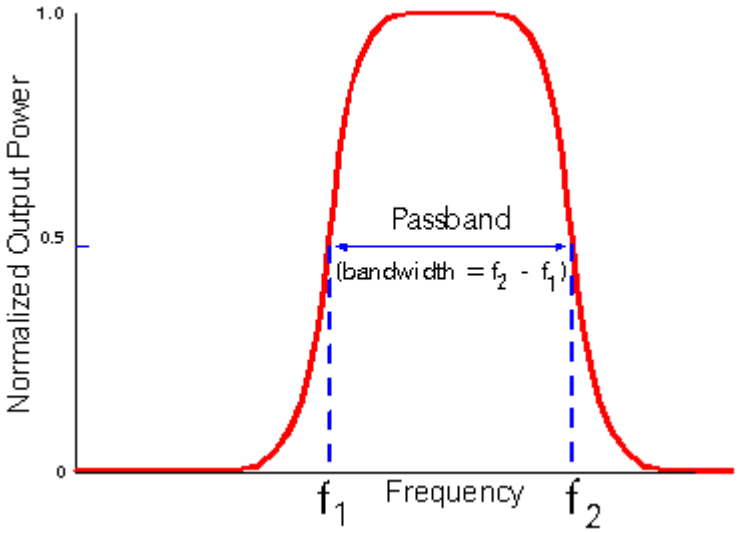

Figure 7- 20 A schematic illustration of Gaussian band pass filter. f_1 and f_2 are the low frequency cut-off and high frequency cut-off respectively.

The two cut-off frequencies are determined by the range of frequency to be studied. In this case the size of local image allows 3 ~ 4 lamellae or cycles, which means the corresponding information is stored in the frequency range of $\left[\frac{1}{4} \quad \frac{1}{3}\right] \times f_s$ where f_s is the sampling frequency. The cut-off frequency could then be selected based on that with an appropriate allowance.

7.2.6 Influence of Neighbourhood Size Selection

The main feature — orientation information — is calculated based on the Fourier analysis, which requires a large local image size (the local image can include more spatial cycles) to increase the accuracy of orientation calculation (the larger the distance between the peak point and the origin is, the more accurate result can be obtained). However, a large local image size will make a pixel affected by pixels that are far from it, which reduce the spatial resolution of algorithm because the orientation information of the pixels within small colonies might get wrong easily. Therefore an appropriate local image size should be determined to balance the resolution and accuracy of the algorithm. The selection is related to the lamellae

spacing (spatial cycles). In the current cases the spacing of most of the lamellae is 7~12 pixels. The local neighbourhood size is defined as 35 pixels which is at least three times the lamellae spacing.

7.2.7 The Influence of Colony Interface

In order to study the influence of the colony interface on the orientation detecting algorithm, one accurately detected boundary and another less accurately detected boundary were selected and the orientation and directionality variation across these boundaries were measured.

The boundary through which a yellow line crosses (in Figure 7- 16) was accurately detected by the automated method compared with the manual results, and the boundary with a red line is less accurately detected. The variation of orientation and directionality of the pixels on these lines were plotted in Figure 7- 21 and Figure 7- 22.

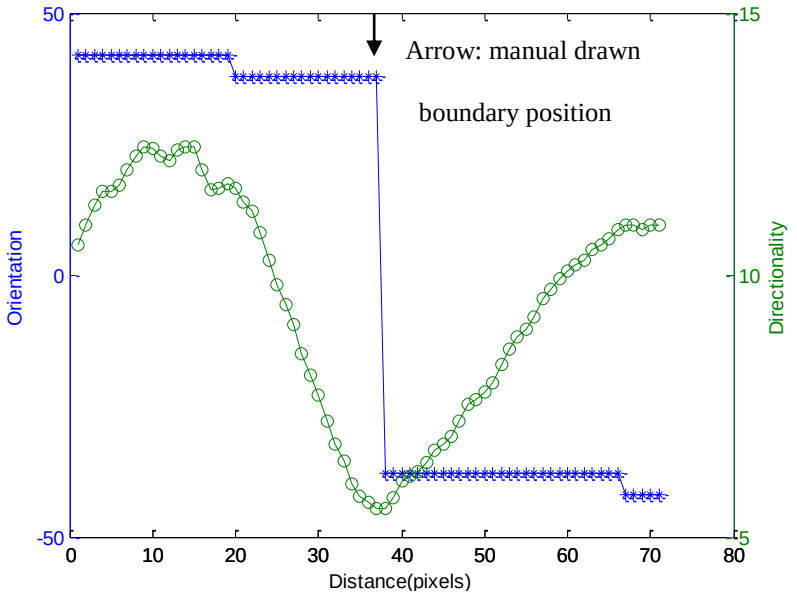

Figure 7- 21 The variation of orientation and directionality of the pixels on the yellow line in Figure 7- 16. The X-axis represents the length of the yellow line in pixel scale. The blue data set and the green data set represents the orientation angle and directionality value of each pixel on the yellow line respectively.

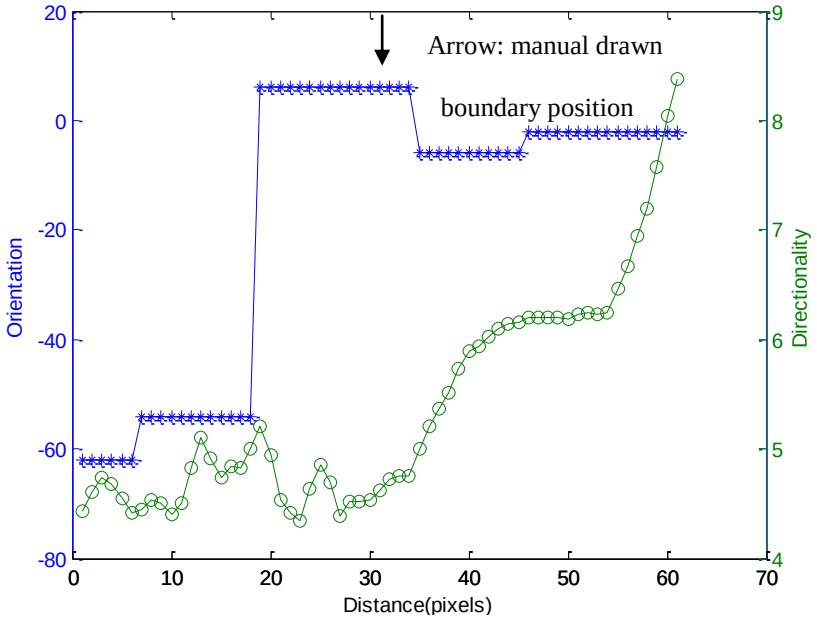

Figure 7- 22 The variation of orientation and directionality of the pixels on the red line in Figure 7- 16. The X-axis represents the length of the red line in pixel scale. The blue data set and the green data set represents the orientation angle and directionality value of each pixel on the red line respectively.

It can be seen from Figure 7- 21 that the orientation changes sharply around the centre of the line, which is consistent with the segmentation image. The directionality strength reaches the minimum value at the orientation changing position. And on both sides of this position, the directionality strength increase to a similar maximum value at a similar rate. However, in Figure 7- 22, the orientation changing position is approximately 19 pixels from the left end, which are about 10 pixels left to the boundary position. The directionality strength to the right of the changing position is greater than that to the left, and this is likely to have lead to the orientation from that region dominating the measurement in the more weakly-oriented region adjacent to it.

It can be concluded that in the orientation segmentation algorithm, the accuracy of estimation of the position of the colony interface is dependent on the directionality strength of both sides of the interface. If they are equal or close, the colony interface

itself does not adversely affect the measurement, and its position can be estimated well.

7.2.8 Necessity and Selection of the Criteria of the Orientation Feature Predicates

Two features including the Orientation difference within a colony and the KAM along the colony boundaries were used to characterise the orientation information. The average orientation angle is used in the splitting process and the KAM is used in merging process. These two orientation features along with average grey levels were used as the predicates for the merging process. The reasons of using them separately in the two processes is because KAM is a characteristic to determine colony boundaries, however, it is not possible to use KAM in the splitting stage (explained in section 6.2.9). Therefore the orientation difference within a colony, which is easy to test, is used as the orientation feature.

The selection of KAM along the colony boundaries is illustrated in Figure 7- 23. It is assumed that the orientation changing from a colony (e.g. region a) to another (e.g. region b) is completed within two pixels (e.g. pixel 1 and pixel 5) in the direction perpendicular to the boundary (but in many cases more than 2 pixels). That means these two pixels share the misorientation. If the boundary is not straight (region a and region c), some irrelevant pixels (pixel 16) will be also detected as boundary pixels. Due to the reasons mentioned above, the KAM of every boundary pixel is no bigger than a half of the total misorientation (10~15 degrees). 5 degrees is used as the criterion here. Therefore, the orientation features are closely related to the physical properties. That makes it easy to determine the critical parameter of the features.

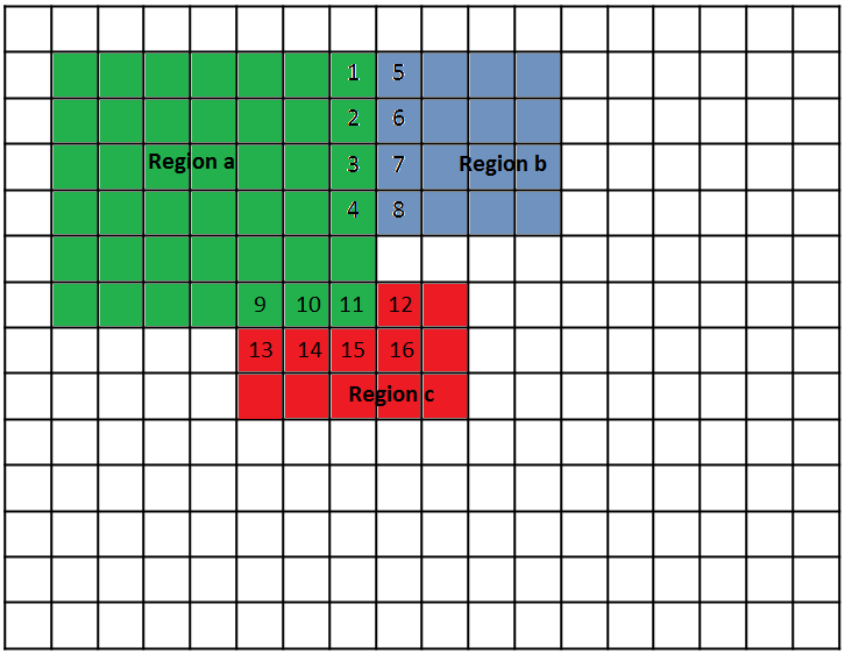

Figure 7- 23 An illustration of interface between blocks. Different colours represent different blocks. The numbered pixels are on the interfaces between blocks.

How different features influence the segmentation of colonies was studied in the following way: segmentation was re-performed using only one feature to observe the results.

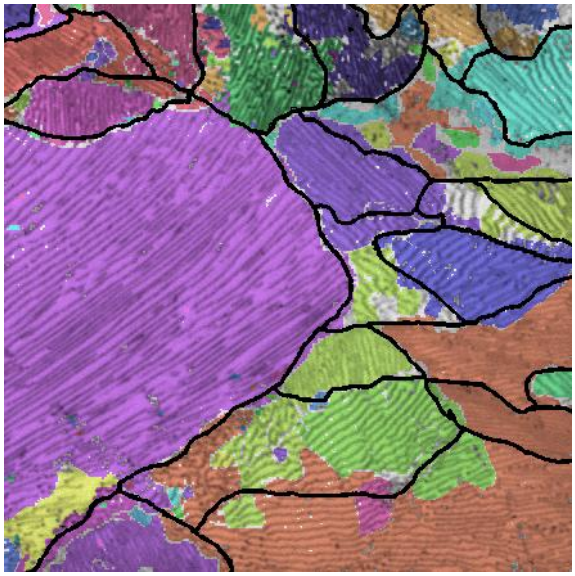

Figure 7- 24 The segmentation results using both KAM and grey level predicates. Same colony is shown in same colour. The black lines represent the manually drawn colony boundaries.

Figure 7- 24 showed the segmentation results using two predicates — the KAM and grey levels. Figure 7- 25(a) and (b) showed the segmentation using only KAM or grey levels respectively. The arrows in (a) represented the boundaries that failed to be detected by KAM predicate only. In (b) it can be seen that the grey level feature is effective in detecting non-orientation-related boundaries, which occupy small amount in this image.

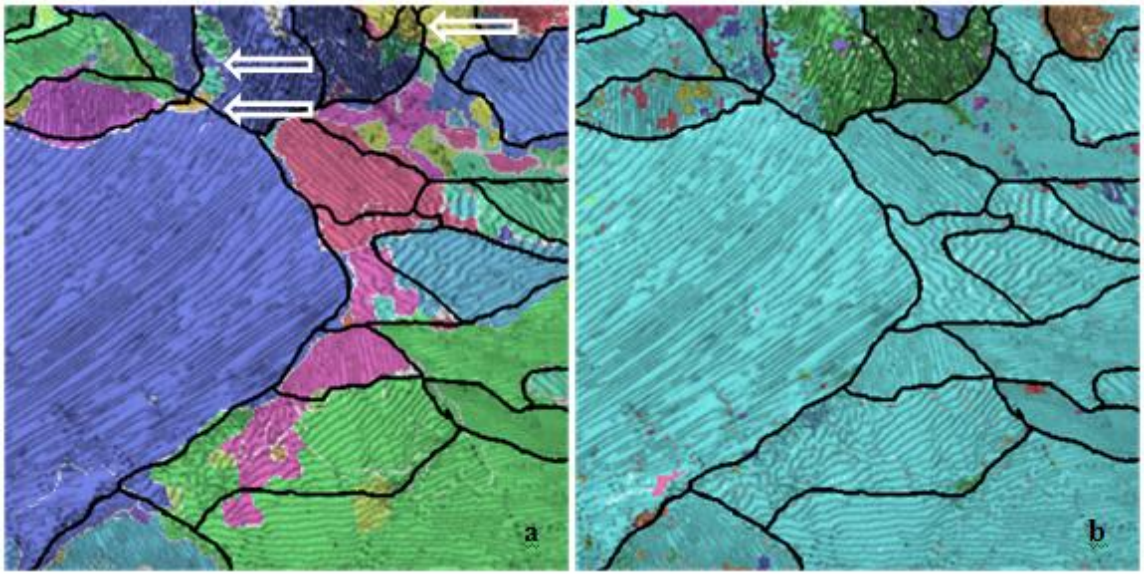

Figure 7- 25 The segmentation results using only KAM predicates only (a) and grey level predicates (b). Same colony is shown in same colour. The black lines represent the manually drawn colony boundaries.

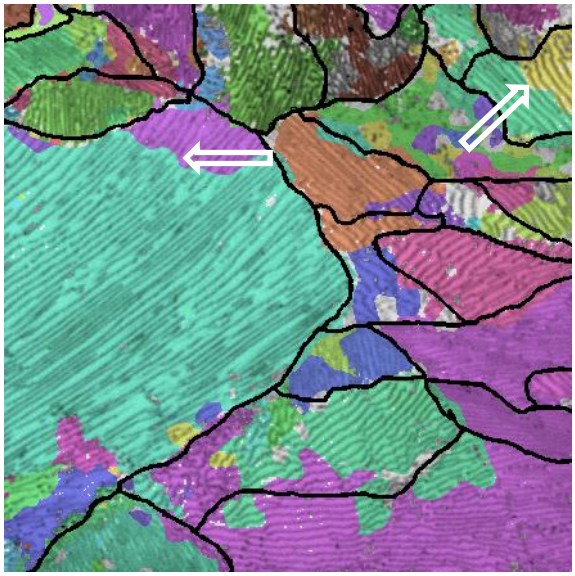

Figure 7- 26 The segmentation results using grey level predicates and average misorientation between colonies instead of KAM. Same colony is shown in same colour. The black lines represent the manually drawn colony boundaries.

Figure 7- 26 showed the segmentation using the average misorientation between colonies instead of KAM. The arrow marked places represented that the algorithm would incorrectly detect the orientation changes within a colony and give oversegmented boundaries. However, since the lamellae in a colony can be curved rather than straight, different parts within a same colony may have a big mean misorientation, or two different colonies may have a small misorientation in average. Therefore, as an edge-detection based method, the KAM along the colony boundaries is a more appropriate orientation feature to detect the colony boundaries. This is because KAM can detect a locally strong change of orientation, whereas mean misorientation does not distinguish between near and far changes in orientation. This also gives evidence that the split-merge algorithm is appropriate in this work for its ability of applying different criteria in splitting and merging.

7.2.9 Quantitative Analysis

7.2.9.1 Test Image

Mosaic function of the AxioVision 4 software was used to obtain images from a continuous region. Then the images were montaged to a 2000-pixel by 1000-pixel image (Figure 7- 27). The image has been applied with shade correction.

7.2.9.2 Automated Segmentation

Followed by the analysing procedures introduced above, the automated segmented image can be obtained as Figure 7- 28. The grey regions in the image are not classified due to their poor directionality. The criteria of the merging predicates were started with 3 degree KAM and 10% of the total grey level range.

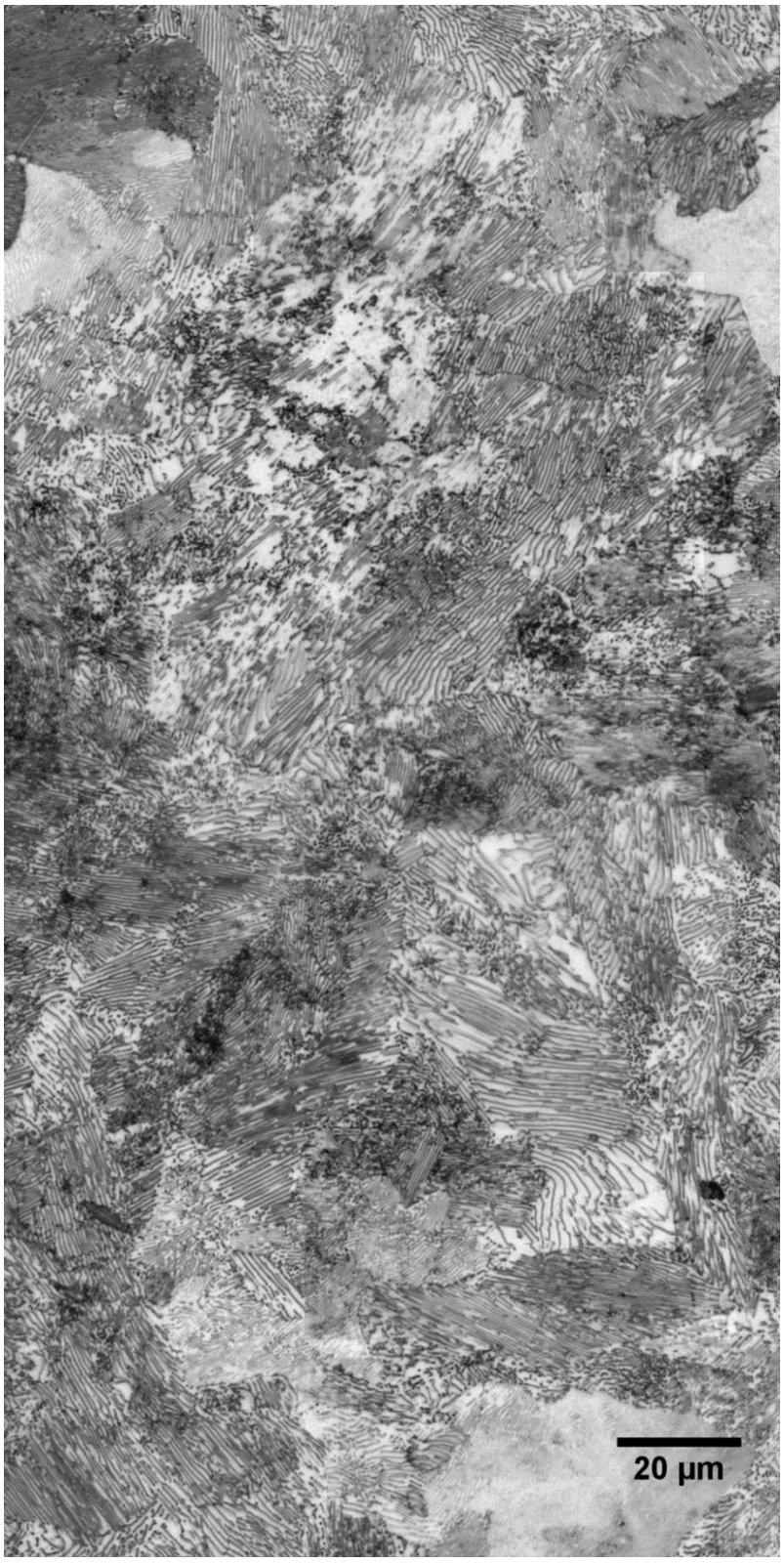

Figure 7- 27 A montage image (2000x1000) of a representative region

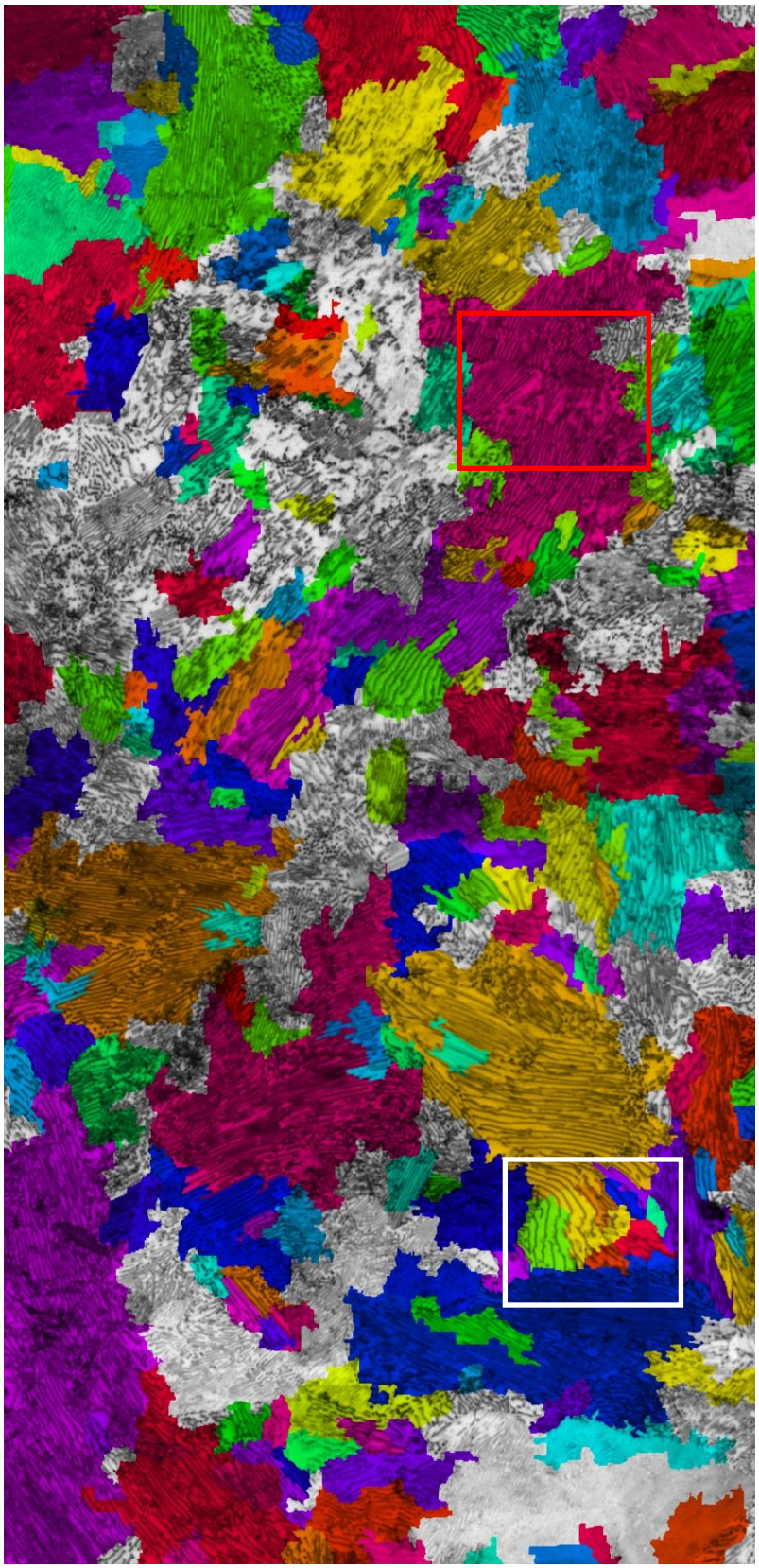

Figure 7- 28 The initial image overlaid with some segmented colonies representing in different colour. 3 degree KAM and 10% of the total grey level range were used as merging predicates. The white and red rectangular marked regions are used for following analysis.

7.2.9.3 Manual Segmentation

The characterisation of pearlite colonies was studied using optical images. Due to the difficulty of microscopic colony size measurement mentioned in the literature review (Walentek et al., 2006, Pickering and Garbarz, 1987), the current characterisation method is by eye by skilled operators. More automatic interpretation of crystallographic orientation information e.g. from EBSD may be equally or more accurate, but research has shown that even EBSD may not be completely accurate (Walentek et al., 2008). It is the author's opinion that the accuracy of EBSD and optical methods should be studied in more detail in future work. However within this PhD only the optical method has been studied due to the much greater speed with which optical images can be obtained for large sample areas, making the optical method more suitable for widespread industrial use. Therefore the automatic characterisation studied in this PhD will aim at duplicating people's criteria to analyse the optical images and manual colony characterisation was carried out by an experienced metallurgist's drawing the colony boundaries (see Figure 7- 29).

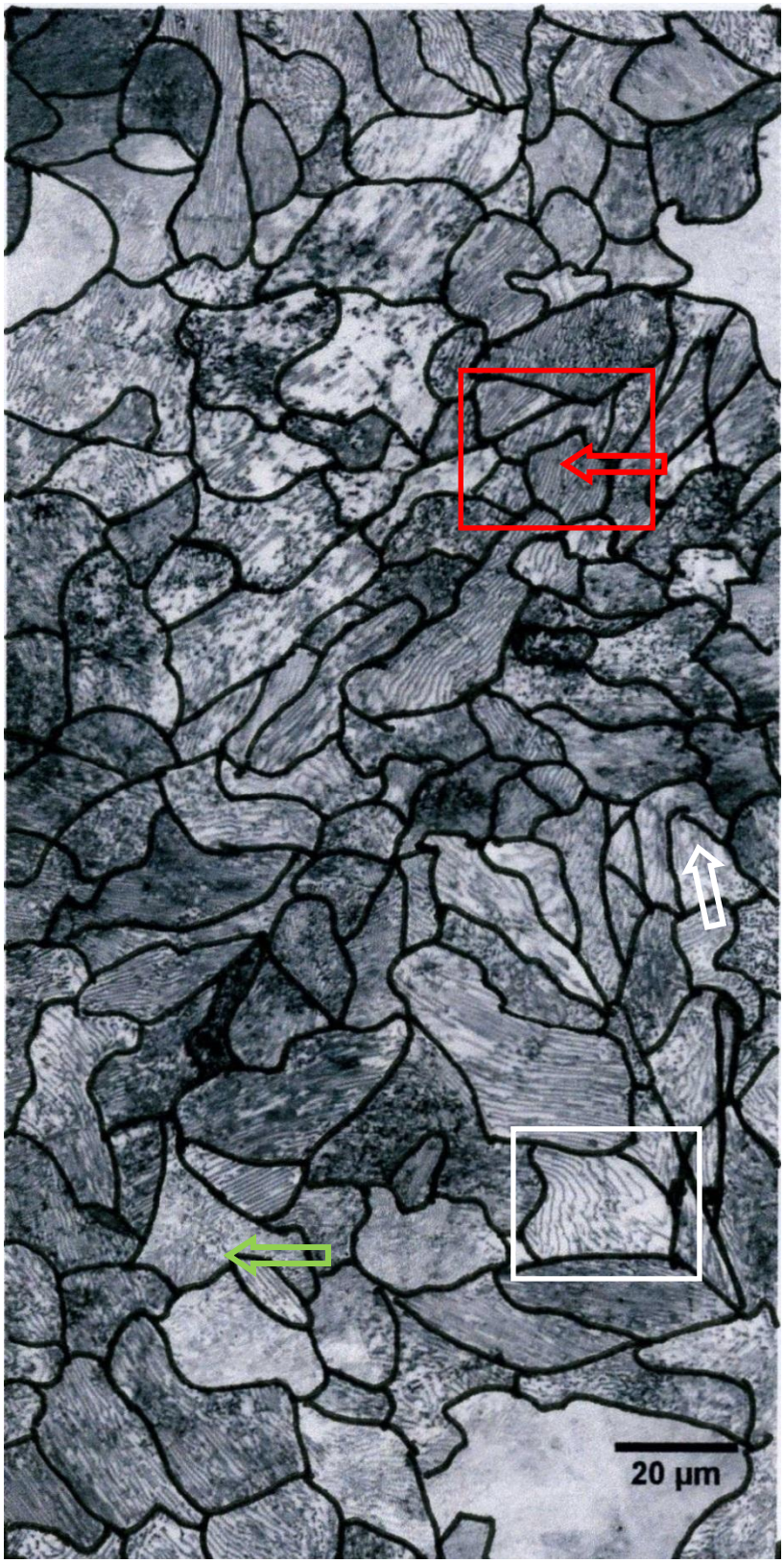

Figure 7- 29 The initial image overlaid with manually drawn boundaries which are shown in black lines. The arrow and rectangular marked regions are used for following analysis.

7.2.9.4 Discussions of the Segmentation Algorithm

From Figure 7- 12, Figure 7- 15 and Figure 7- 16 it can be seen that the splitting stage of the algorithm has worked well. Every region that should have been split, has been. Possibly the splitting could be less aggressive, meaning that the merging process can be quicker, but as long as the merging process operates correctly then the only benefit here should be time and not overall accuracy. Thus the following study was focused on the parameters that were used in the merging process.

From Figure 7- 28 and Figure 7- 29 it can be seen that some colonies are over-segmented and some are under-segmented.

The colony in the white rectangular marked region in Figure 7- 28 and Figure 7- 29 was manually segmented as one colony, however, in the automated segmented results, several small regions were generated. Since the orientation based feature KAM is a main characteristic for colonies and the lamellae in this region are quite curved, then the KAM criterion value should be increased in order to allow them to merge. Figure 7- 30 shows how the segmentation of this region changes with increasing KAM criterion. Figure 7- 30 (a) is the white rectangular marked region in Figure 7- 29. Figure (b) shows the manually drawn boundaries of figure (a). Region 1 is classified as one single colony. Figure (c) – figure (f) are the automatically segmentation of figure (a) with varying KAM criterion from 3 degrees to 20 degrees. The colours in the automatic segmentations represent the segmented regions. In figure (c), region 1 was mainly segmented into 6 sub-regions labelled by 2, 3, 4, 5, 6 and 7. Regions 6 and 7 have very weak directionality, so they are not taken into account for the following analysis. When the KAM criterion was increased to 5 degrees, as shown in figure (d), most of the 4 regions were merged to a big colony, which agrees better with the manual classification. When the KAM criterion was raised to 20 degrees, there was no significant effect on the segmentation.

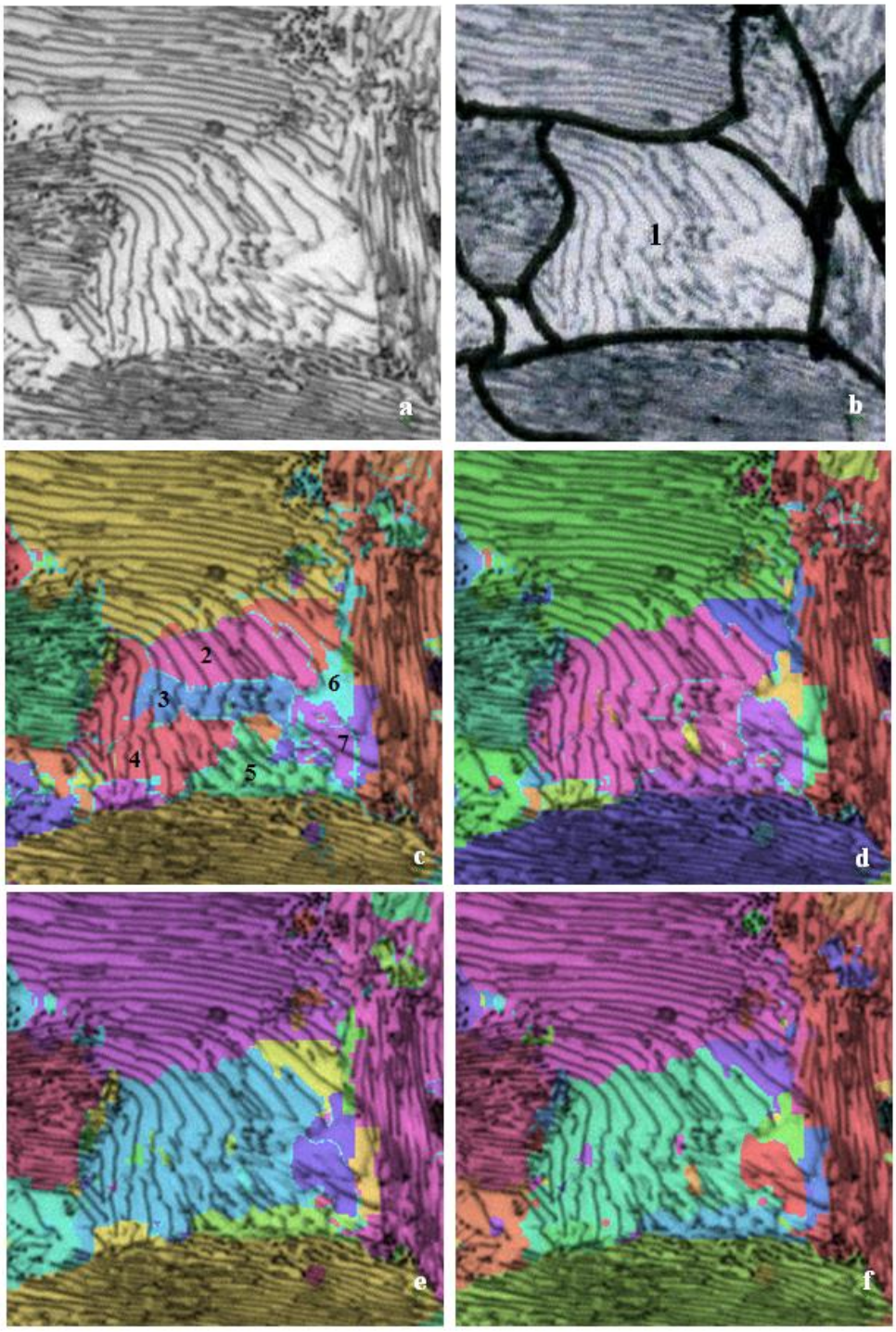

Figure 7- 30 An example region (white rectangular marked region in Figure 7- 28 and Figure 7-29) showing how segmentation changes with increasing KAM criterion: (a) original region; (b) the manually segmented boundaries drawn by an experienced metallurgist; (c) the automatic segmentation result with a KAM criterion of 3°; (d) the automatic segmentation result with a KAM criterion of 5°; (e) the automatic segmentation result with a KAM criterion of 10°; (f) the automatic segmentation result with a KAM criterion of 20°

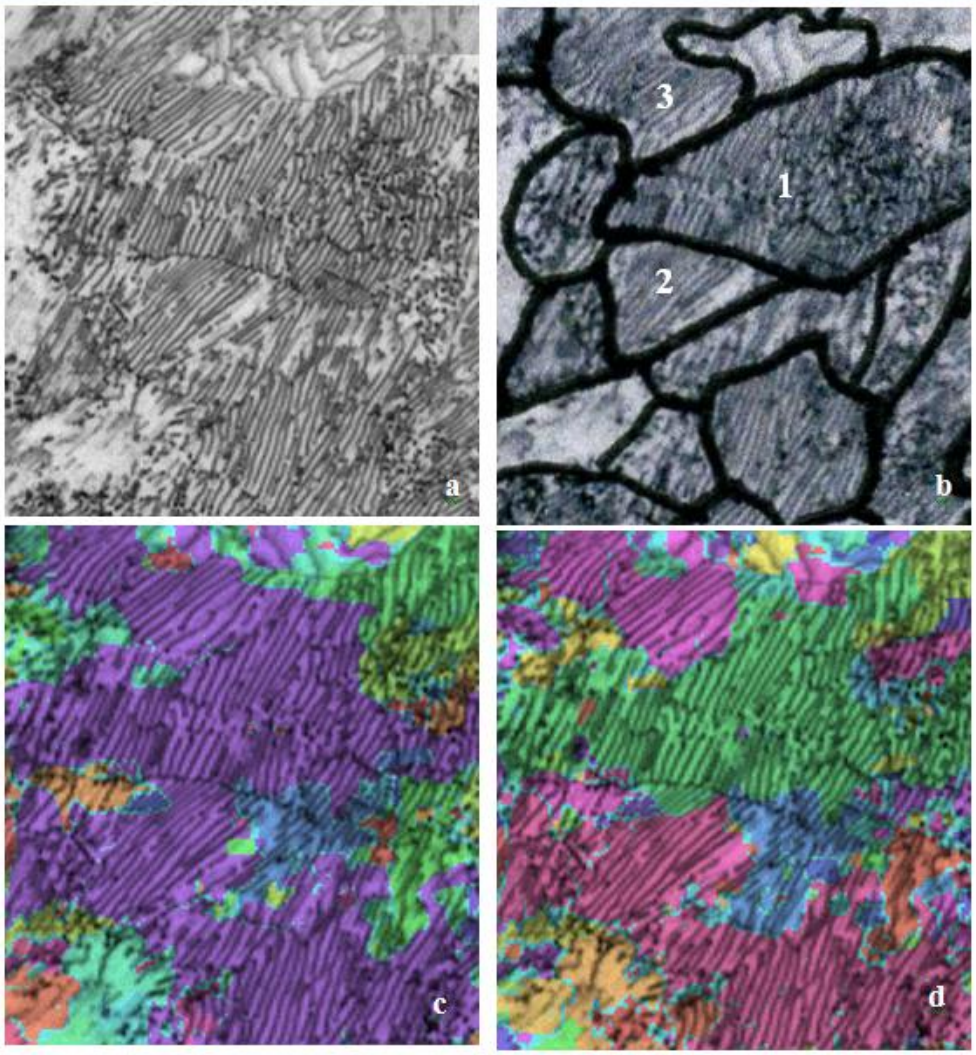

Figure 7- 31 An example region (red rectangular marked region in Figure 7- 28 and Figure 7- 29) showing how segmentation changes with decreasing KAM criterion: (a) original region; (b) the manually segmented boundaries drawn by an experienced metallurgist; (c) the automatic segmentation result with a KAM criterion of 3°; (d) the automatic segmentation result with a KAM criterion of 1.5°

But opposite situations were also found, where the KAM criterion value was too high. Figure 7- 31 is an example showing that the KAM predicate needs to be decreased in order to match the manual segmentation. Figure (a) is the initial image of the red rectangular marked region in Figure 7- 28. Figure (b) shows the manually drawn boundaries of figure (a). The automatic segmentation (figure (c)) shows fewer segmented regions than manual method. When the KAM criterion decreased from 3

to 1.5, the regions 1 2 and 3 were separated.

Regarding the grey level predicate, it is not based directly on the original image but rather on a low pass filtered image. Figure 7- 32 shows the effects of this filtering. Figure (a) is the white rectangular marked region in Figure 7- 29. Figure (b) is the low pass filtered results of figure (a) (cut-off frequency of 10 pixels). Figure (c) is the segmentation based on the grey value of the original image and figure (d) is the segmentation based on the grey value of the low pass filtered image. Criteria of 5 ° KAM and 10% of the total grey level range were used in both segmentations. It can be seen from figure (c) that the region was segmented into many small blocks containing only ferrite or cementite (as the place marked by black arrow). This may result from a combined factor of the bending cementite and grey level contrast between cementite and ferrite. The bending cementite in the colony makes the colony non-uniformly oriented, which subsequently causes that the splitting process might end up at a very fine level (may split into individual pixel). And then due to the grey level differences between cementite and ferrite lamellae, the cementite and ferrite pixels are not possible to be merged together, so that the cementite and ferrite lamellae might be segmented separately. The use of low pass filter to the original image can solve this. The cut-off frequency is selected between the range of interspacing dimension and pearlite colony dimension. Therefore the filtered image would eliminate the contrast between ferrite and cementite lamellae, but preserve the contrast between pearlite colonies (figure (b)). Using the grey level predicate based on the filtered image, the individual segmentation of cementite and ferrite can be solved as shown in figure (d).

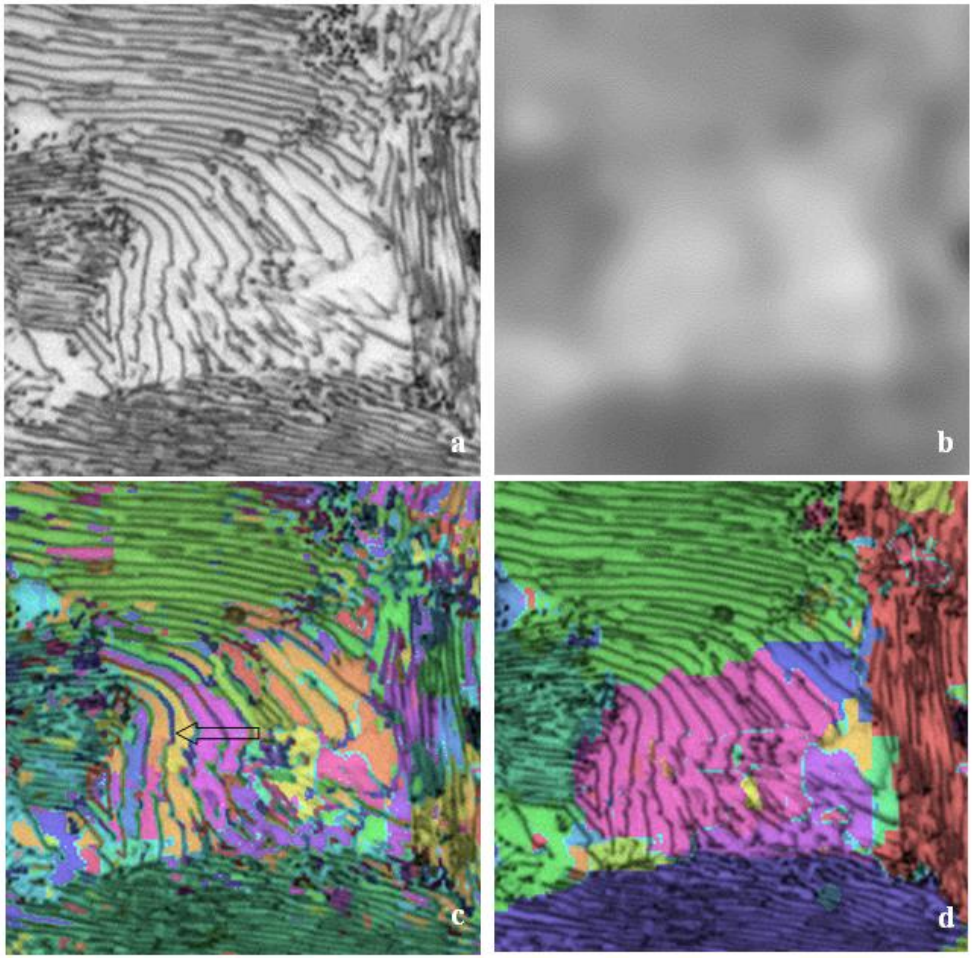

Figure 7- 32 An example (white rectangular marked region in Figure 7- 28 and Figure 7- 29) showing the use of low pass filtered image in the grey level predicate: (a) original region; (b) the Gaussian low pass filtered image of figure (a) (filter cut-off: 10 pixels); (c) the segmented image with the grey value predicate from original image (figure (a)); (d) the segmented image with the grey value predicate from the low pass filtered image (figure (b)) (The predicates of 10° KAM and 10% grey levels were used in both segmentations.)

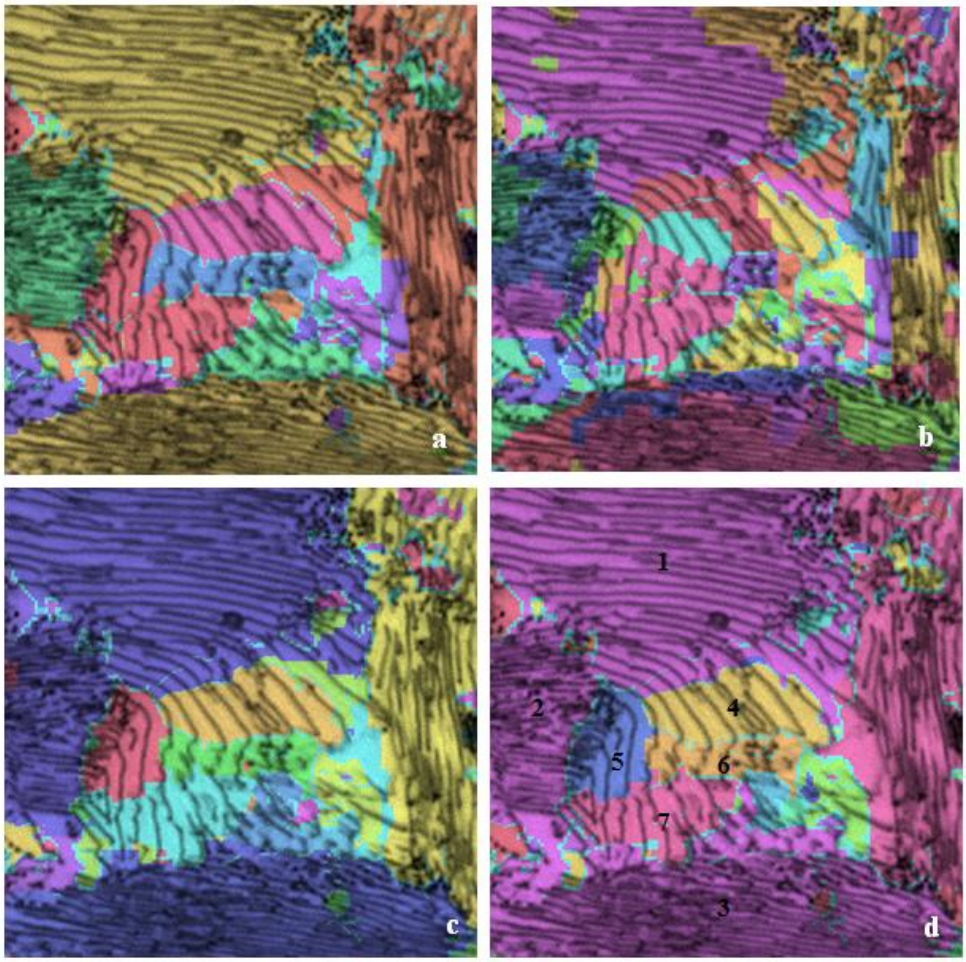

Figure 7- 33 The same example region (white rectangular marked region in Figure 7- 28 and Figure 7- 29) showing how segmentation changes with varying grey value criterion: (a) the automatic segmentation result with grey value criterion of 10% of the total grey levels (255); (b) the automatic segmentation result with grey value criterion of 4% of the total grey levels; (c) the automatic segmentation result with grey value criterion of 16% of the total grey levels; (d) the automatic segmentation result with no grey level predicate. All of the segmentations use a KAM criterion of 5°.

Figure 7- 33 shows the significance of grey level predicate to the segmentation. Figure (a) is the automatic segmentation results using a combined predicates of 3 ° KAM and 10% of the total range of grey levels. When the grey level criterion was restricted to 4%, the automatic segmentation is shown in figure (b). It can be seen that more small regions were generated from previous big colonies. When the grey value

criterion is increasing, some of the colonies that were previously segmented by grey levels start to merge (region 1, 2 and 3 in figure (d)). However, the colonies segmented by KAM predicate still exist (region 4, 5, 6 and 7 in figure (d)).

The above results indicate that the KAM and grey value are independent and significant features to segment pearlitic colonies. Appropriate setting of these predicates can help to segment the pearlite colonies into correct shape and accurate number, which is the main aim of the pearlitic colony characterisation. However, it is difficult to find a specific criteria value suitable everywhere in the image. 5 degree KAM and 10% of the total grey level range were used hereafter to do an overall quantitative analysis.

7.2.9.5 Quantitative Analysis

The segmented image using the optimised parameters (5 degree KAM and 10% of the total grey level range) was shown in Figure 7- 34. The colony equivalent circular diameter distribution was obtained from the automatic methods (two settings) and manual method respectively and shown from Figure 7- 35 to Figure 7- 37. Since the weak oriented area was discarded during the measuring process of automatic method, it was also applied to the measuring process of manual method to keep the results comparable.

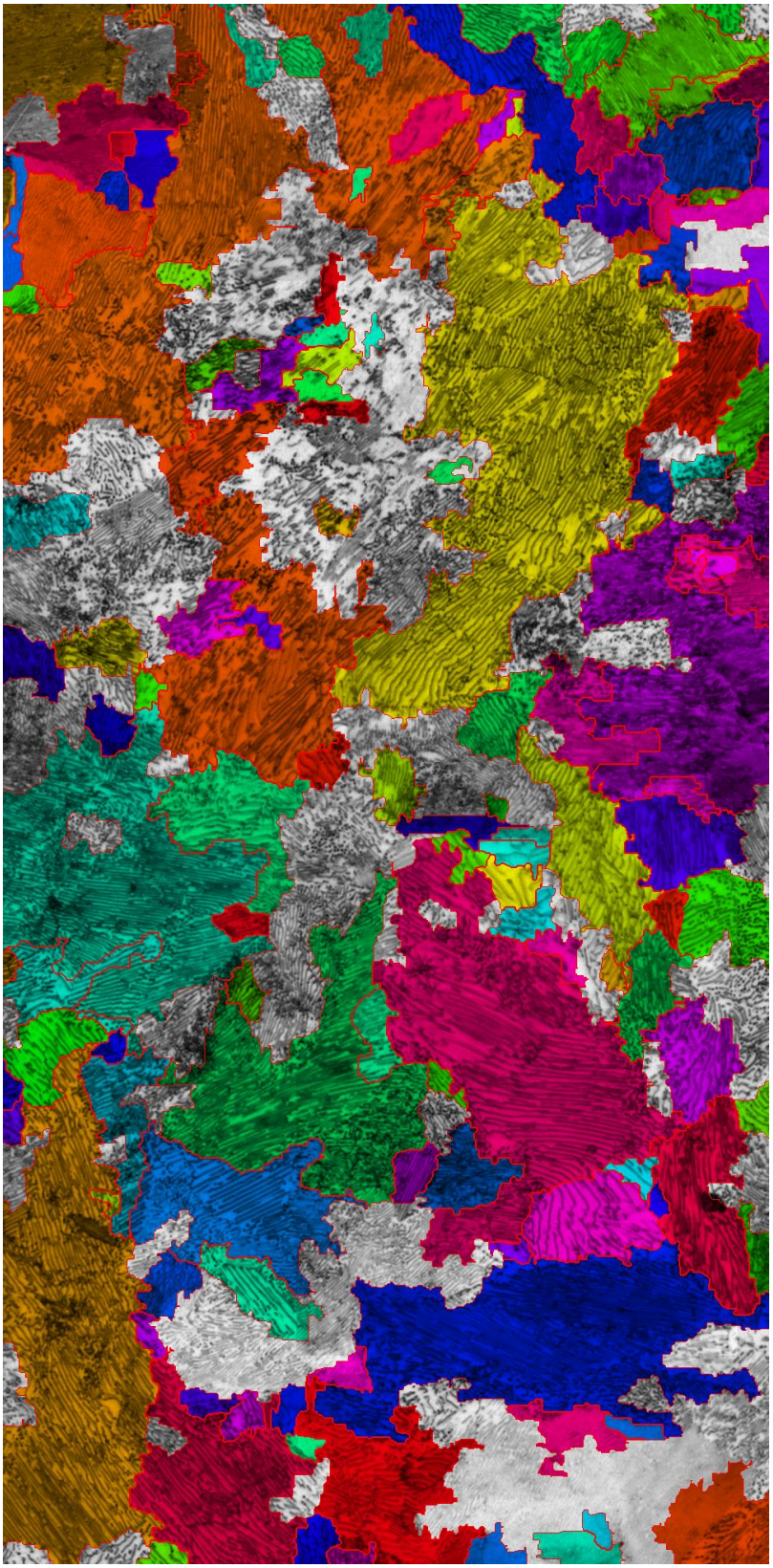

Figure 7- 34 The updated version of segmented image using 5 degree KAM and 10% of the total grey level range: the red line represents the boundaries between the automatically detected colonies.

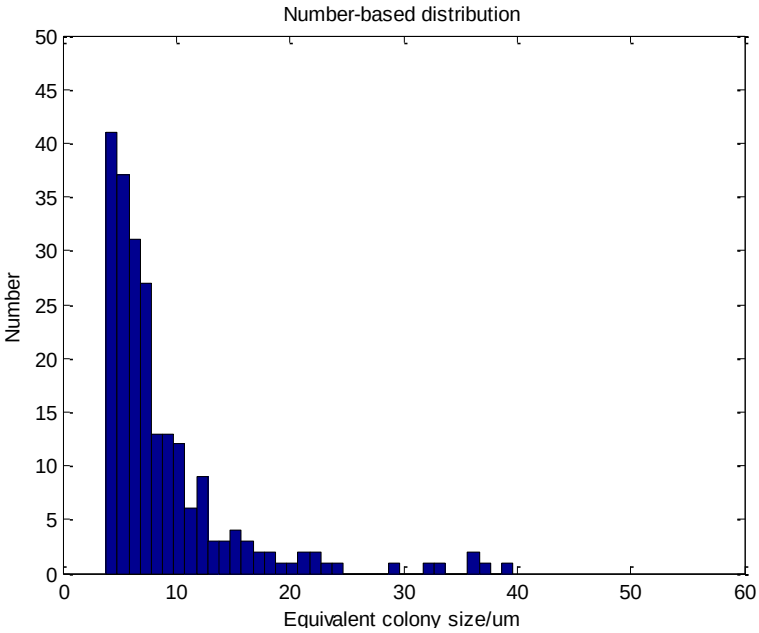

Figure 7- 35 The distribution of the equivalent colony size measured automatically (corresponding to Figure 7- 28, 3 degree KAM and 10% of the total grey level range used)

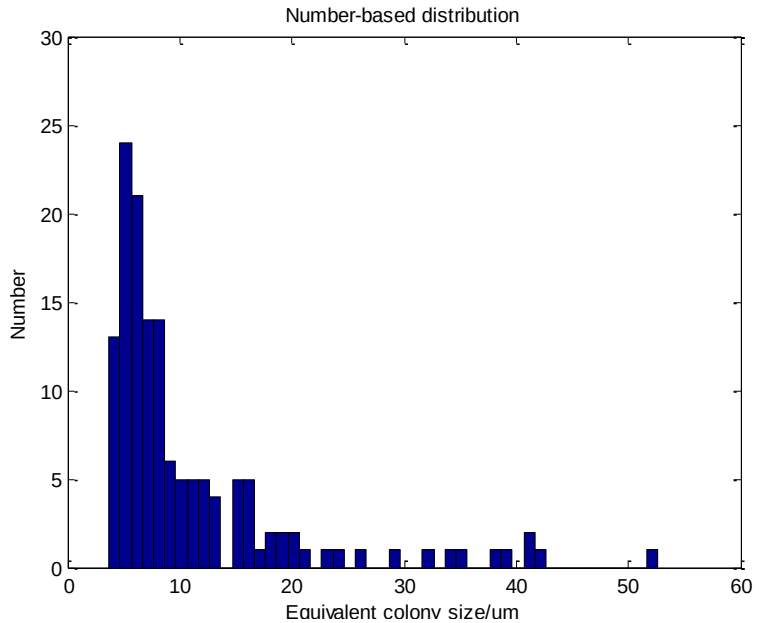

Figure 7- 36 The distribution of the equivalent colony size measured automatically (corresponding to Figure 7- 34, 5 degree KAM and 10% of the total grey level range used)

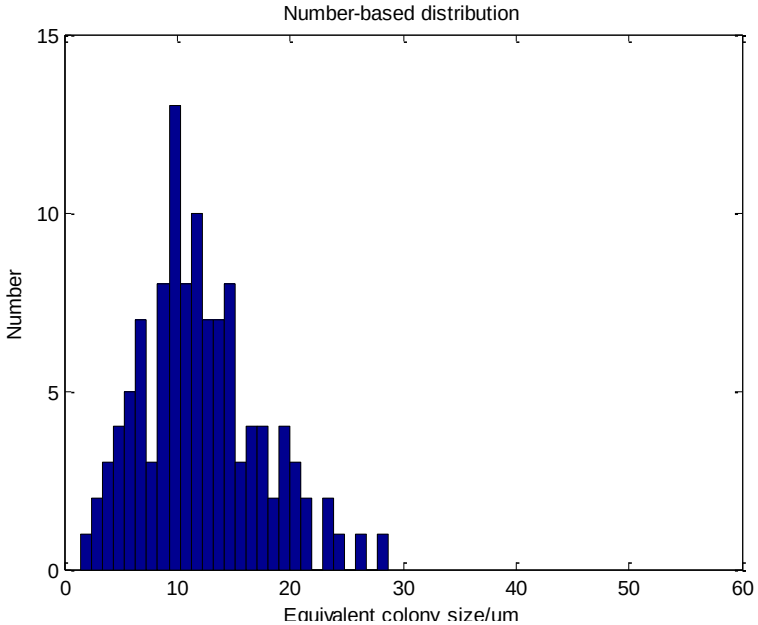

Figure 7- 37 The distribution of the equivalent colony size measured manually (corresponding to Figure 7- 29)

Table 7- 2 The average colony ECD measured using automatic methods and manual method

	Auto method 1 (3° KAM, 10% of the total grey range)	Auto method 2 (5° KAM, 10% of the total grey range)	Manual method
Average colony ECD (μm)	8.9	11.0	12.1

Although Table 7- 2 shows the automatic method can obtain a similar average colony ECD value as the manual method, it does not mean the automatic algorithm is completely successful yet because of the disagreement of the distributions. By increasing the KAM parameter from 3 degree to 5 degree, it can be seen that the number of small colonies decreased (e.g. about 40 colonies with <5 μm size in Figure 7- 35 compared to 13 colonies with <5 μm size in Figure 7- 36) and the number of big colonies increased (e.g. 0 colonies with >40 μm size in Figure 7- 35 compared to about 5 colonies with >40 size in Figure 7- 36). This makes sense because the criteria to determine colonies have been relaxed. By comparing Figure 7- 36 with Figure 7-

37, it shows that the automatically segmented image has more colonies in both small size range (e.g. <10 μm) and large size range (e.g. >30 μm), but fewer colonies in the middle size range (e.g. 10~15 μm). One possible reason is the criterion for defining colonies is not universally appropriate over the entire image: it might be too high for some colony boundaries and too low for some other boundaries. Therefore the colonies might be over-segmented or under-segmented, which subsequently cause the inconsistency of the number distribution.

Although there is no precise rule or standard for manually classifying pearlite colonies found in literature, several features are normally used: an order of several degrees misorientation of the cementite lamellae such as the red arrow marked boundary in Figure 7- 29, the discontinuity of the cementite lamellae such as the green arrow marked boundary in Figure 7- 29 and interspacing change of the ferrite and cementite lamellae such as the white-arrow marked boundary in Figure 7- 15. The discontinuity of the cementite lamellae usually leads to an orientation and a grey level change between adjacent colonies. Therefore, the orientation and grey level criteria used in the automatic method should be appropriate for characterising pearlite colonies.

However, according to Park and Bernstein' finding (1979), the misorientations between adjacent pearlite colonies were dependant on the prior austenite grain size. So the misorientations between colonies vary in a wide range. Moreover, the cementite lamellae in pearlite can be irregularly bent or fragmented under deformation (Fu et al., 2005) and various lamellae growth rate caused by different cooling rate . Therefore, there is likely to be a conflict between detecting the misorientations between colonies and discarding the misorientations of bent cementite lamellae within colonies.

Generally, the problem can be avoided with the manual method operated by an experienced metallurgist. However, it is still a tough issue for the metallurgist to deal

with an image with an amount of imperfections such as Figure 7- 27. The locations with white arrow marks in Figure 7- 29 showed manually a drawn boundary with very big concave angle, which has a very low possibility to be existed in the pearlitic structure.

7.2.10 Results and Analysis Using Synthetic Image

7.2.10.1 The Synthetic Image and Its Ground Truth

The synthetic image used in this study was shown in Figure 6- 18. The ground truth of the segmentation of this image was obtained manually by drawing the boundaries as shown in Figure 7- 38.

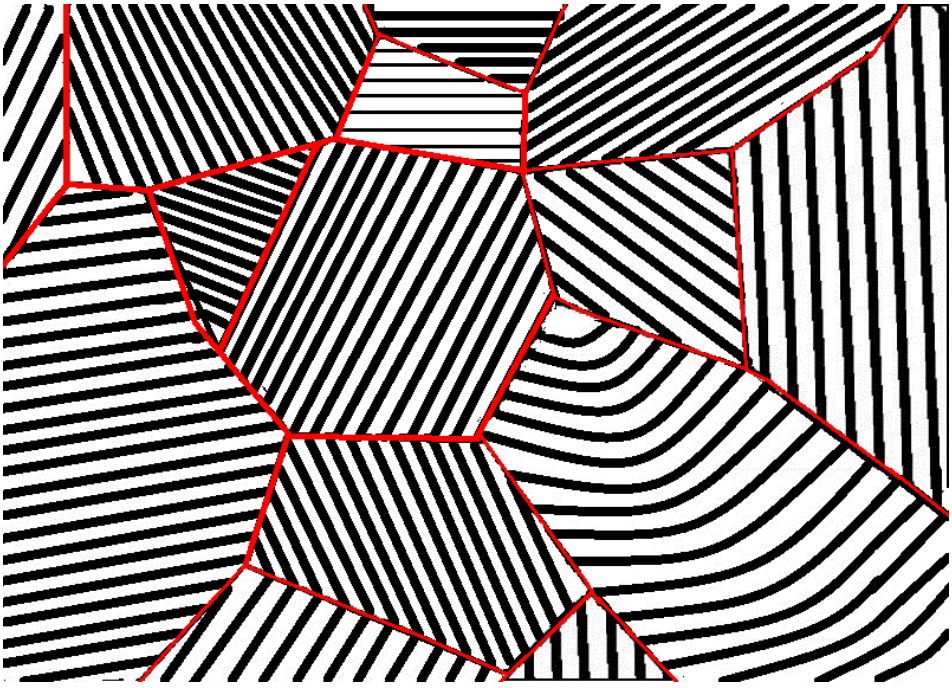

Figure 7- 38 The ground truth of the segmentation of the synthetic image (Figure 6- 18) obtained manually by drawing the boundaries (the boundaries are shown in red)

The three parameters affecting the segmentation results that were investigated in this section are the neighbourhood size of the FFT during the orientation measuring process, and the two predicates (KAM criterion and grey level criterion) used for the

merging process.

7.2.10.2 Changing of Neighbourhood Size Value

The neighbourhood size value was investigated first. It was set to be varying from 15 to 135 pixels with an increment value of 10. During this process, the KAM parameter and the grey value parameter were set constantly to be 2 degree and 20 to make things easier. The segmentation accuracy was measured and shown in Table 7- 3. Three segmented images with the smallest neighbourhood size (15 pixels), the largest neighbourhood size (135 pixels), and the highest segmentation accuracy (using neighbourhood size of 95 pixels) were shown from Figure 7- 39 to Figure 7- 41.

Table 7- 3 The changing value of the used neighbourhood size for orientation measurement by FFT and their corresponding segmentation accuracy

Neighbourhood size parameter used (pixels)	15	25	35	45	55	65	75
Segmentation accuracy (%)	58.5	77.3	74.8	80.2	82.3	83.3	82.6
Neighbourhood size parameter used (pixels)	85	95	105	115	125	135	
Segmentation accuracy (%)	83.7	84.5	83.5	77.6	78.4	75.4	

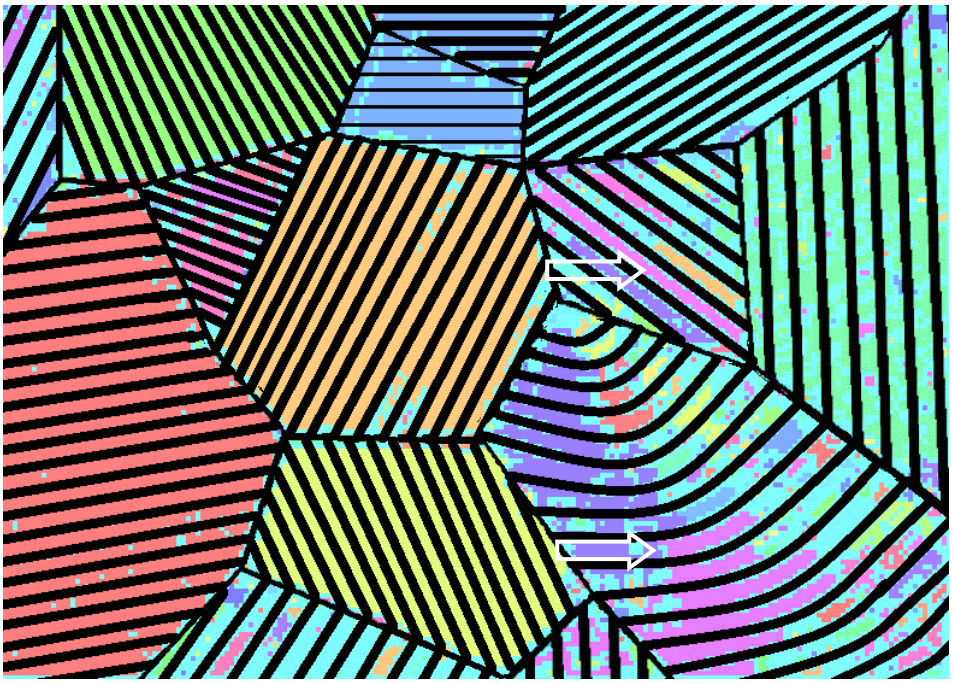

Figure 7- 39 The segmentation results of the initial synthetic image with a FFT neighbourhood size of 15 pixels. Different colours represent different automatically detected colonies. The white arrow marked region represents the area where cementite lamellar and ferrite are separated.

Figure 7- 40 The segmentation results of the initial synthetic image with a FFT neighbourhood size of 95 pixels. Different colours represent different automatically detected colonies.

Figure 7- 41 The segmentation results of the initial synthetic image with a FFT neighbourhood size of 135 pixels. Different colours represent different automatically detected colonies. The white arrow marked area represents the region that is close to colony boundary is affected by its neighbouring colony.

Table 7- 3 shows the general trend of segmentation accuracy when increasing the neighbourhood size from 15 pixels: it increases first to a maximum value (84.5%), and then decreases. If the neighbourhood size is too small (e. g. 15 pixels), the neighbourhood might not contain enough patterns (interlamellar spacing), so that the orientation that extracted from the neighbourhood might be dominantly dependent on an unrepresentative area (such as the area between two cementite lamellae), which causes that different orientation value is measured for the pixels on the cementite lamellae and those between the lamellae. And consequently the cementite and ferrite are separated as shown in Figure 7- 39 (white arrows marked). If the neighbourhood size is very large (e.g. 135 pixels), the neighbourhood for the pixels that are close to colony boundaries would contain area from their neighbouring colonies. Thus the feature extraction of small colonies would be affected because the neighbourhood of their pixels may contain more pixels from other colonies than those from the colony itself. Moreover, the larger neighbourhood size is used, the more area from the edge of the image is needed to be discarded because those pixels do not own enough

neighbouring pixels of required number to do the FFT in order to measure the orientation. The segmentation accuracy from neighbourhood size value of 65 to 105 is very close. The value of 65 is used for the following study (the discarded area is small).

The relationship between the appropriate neighbourhood size and the interlamellar spacing was then studied. The interlamellar spacing of most colonies on the synthetic image is similar. So a local area of the image was randomly selected and the interlamellar spacing was measured on that.

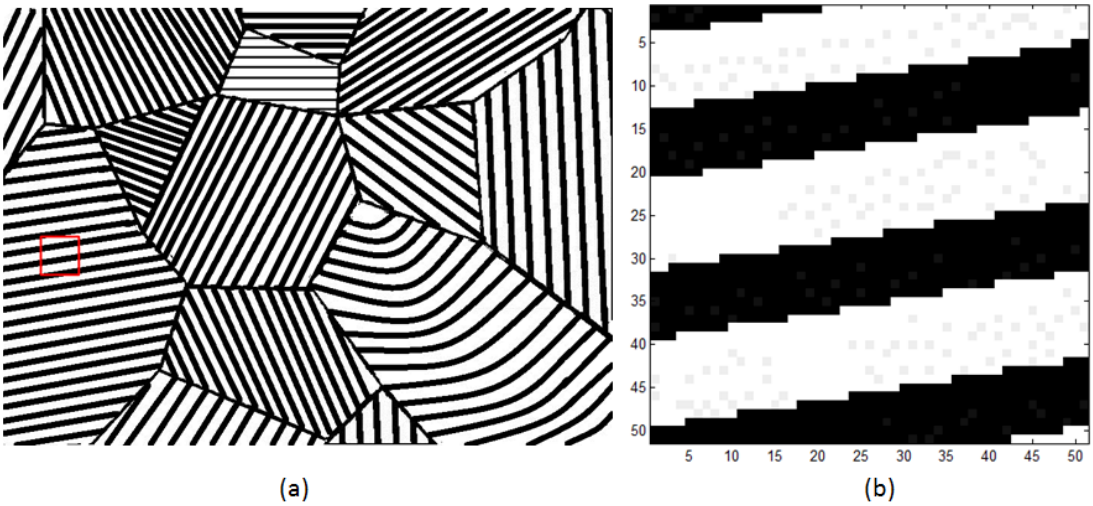

Figure 7- 42 (a) The initial synthetic image with a region (marked in red) selected to study the interlamellar spacing; (b) the selected region in (a) with a higher magnification.

A small region in the initial synthetic image (red line highlighted region in Figure 7-42a) was selected and shown at a higher magnification (Figure 7- 42b). It can be seen that the interlamellar spacing is about 18~20 pixels. The neighbourhood size of 65 pixels is 3~4 times as the interlamellar spacing.

7.2.10.3 Changing of KAM Parameter

The KAM parameter tested ranges from 2 degrees to 6 degrees with an increment

value of 2 each time. The segmentation accuracy was measured and shown in Table 7- 4. The three segmented images were shown from Figure 7- 43 to Figure 7- 45.

Table 7- 4 The segmentation accuracy against its corresponding KAM parameter

KAM predicate value used (degree)	2	4	6
Segmentation accuracy (%)	83.3	91.7	87.4

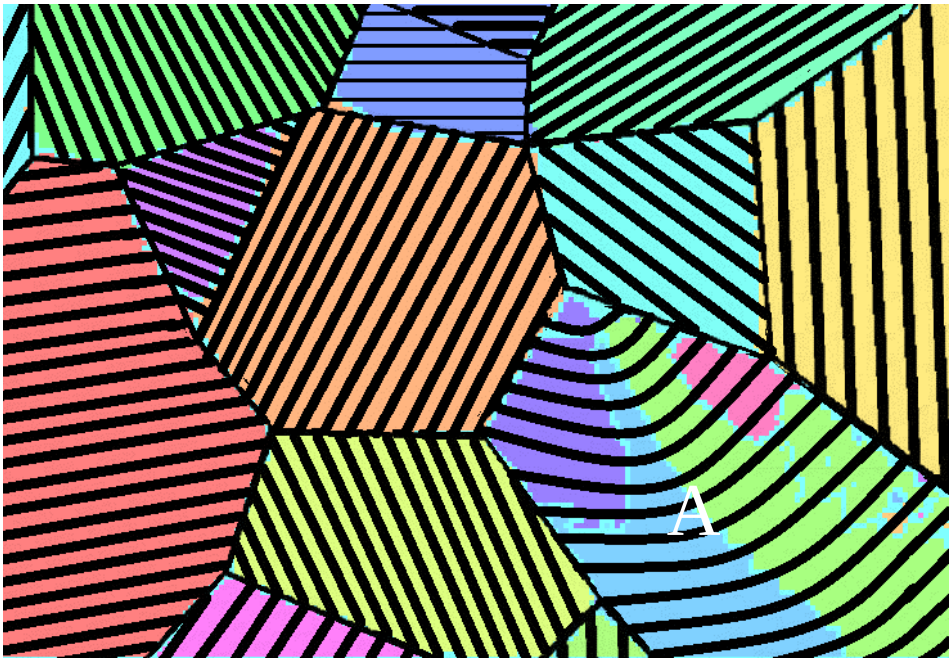

Figure 7- 43 The segmentation results of the initial synthetic image with a KAM predicate value of 2 degree. Different colours represent different automatically detected colonies. Colony A was segmented to separate regions in this case.

Figure 7- 44 The segmentation results of the initial synthetic image with a KAM predicate value of 4 degree. Different colours represent different automatically detected colonies. Colony A was segmented as one single colony in this case.

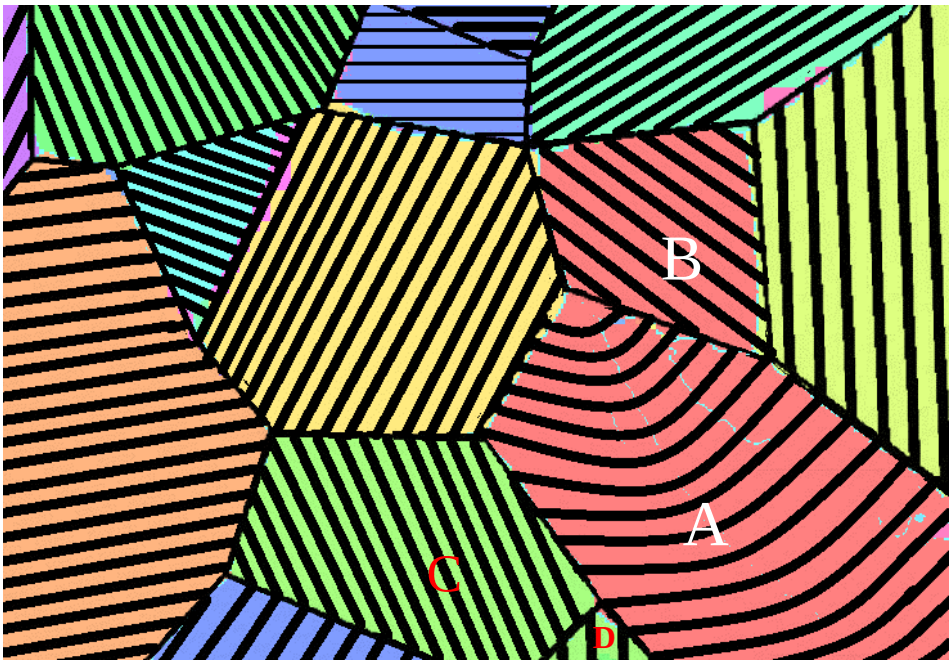

Figure 7- 45 The segmentation results of the initial synthetic image with a KAM predicate value of 6 degree. Different colours represent different automatically detected colonies. Colony A and B were merged as one colony. And so were colony C and D.

It can be seen from Table 7- 4 that as the KAM predicate value is increasing, the

segmentation accuracy increases first to a maximum value (91.7% when KAM is 4 degree) and then starts to decrease. When the KAM predicate value is small, the points within the colony containing curved lamellae are likely to be detected as boundary pixels because at those positions the lamellae orientation changes. This can be seen in Figure 7- 43, region A is a colony containing curved lamellae. With a KAM predicate value of 2 degree, the curvature in colony A was detected and A was over-segmented to several small colonies (around 4). When the KAM predicate value increases to 4 (Figure 7- 44), most of the misorientations can be discarded and A was segmented to a single colony. Although in this case a few pixels where the orientation changes were most still separated from colony A (as the white arrow marked line in Figure 7- 44), they do not greatly affect the size and shape of colony A. If the KAM predicate value keeps increasing, some adjacent colonies those have low misorientation start to merge. In Figure 7- 45, colony A and B were merged as one single colony. And so were colony C and D.

Thus the KAM predicate value of 4 degrees was used for following analysis.

7.2.10.4 Changing of Grey Value Parameter

The grey level predicate value tested ranges from 10 to 100 (the percentage of it to the total grey level range is not used here because in the synthetic image, the grey level ranges from 0 to 255. In real microstructures, it is likely not). The segmentation accuracy was measured and shown in Table 7- 5. Three segmented images were shown from Figure 7- 46 to Figure 7- 48. Table 7- 5 shows that similar as the general trend of the other two studied parameters, the segmentation accuracy increases to a maximum value of (93.8%) as the grey level predicate value increases to 40. Then it keeps constant until the grey level predicate value reaches 60. It finally slightly drops to 93.4% when the grey level predicate value increases to 100.

Table 7- 5 The segmentation accuracy against its corresponding grey level predicate value

Grey level predicate value used (degree)	10	20	30	40	60	80	100
Segmentation accuracy (%)	67.8	91.7	93.1	93.8	93.8	93.4	93.4

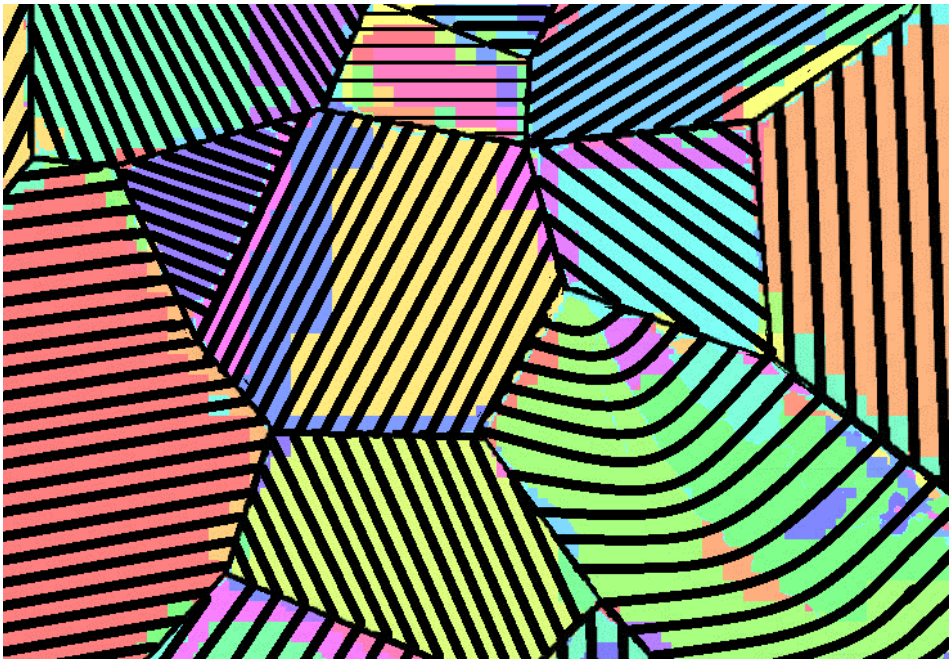

Figure 7- 46 The segmentation results of the initial synthetic image with a grey value criterion of 10

Figure 7- 47 The segmentation results of the initial synthetic image with a grey value criterion of 40

Figure 7- 48 The segmentation results of the initial synthetic image with a grey value criterion of 80

Figure 7- 46 shows that when the grey level predicate value is small, the image is greatly over-segmented. When the grey level predicate value increases to 40 (Figure 7- 47), the over-segmentation is much improved and the colonies (colony A and B in

Figure 7- 47) that have exactly same orientation but different average mean grey levels can be segmented. When the grey level predicate value increases to a value (80) that is greater than the grey level difference between colony A and B, these two colonies could no longer be segmented (Figure 7- 48). Thus the segmentation accuracy in Table 7- 5 drops at grey predicate value of 80, and keep constant hereafter. The segmented image with the grey predicate value of 80 is shown in Figure 7- 48.

Thus the best grey predicate value for the synthetic image turns out to be 40. Using all the three best parameters that were concluded from above results, the segmentation accuracy of the synthetic image can reach 93.8%.

7.2.10.5 Comparison of the Synthetic and Real Microstructure Analysis

The results and analysis of synthetic image provides supportive evidence that the proposed algorithm is appropriate for ideal pearlitic structures. It also gives guidance for selecting the FFT neighbourhood size for the algorithm, which is at least 3 times as the interlamellar spacing. However, a selection principle for the other two important parameters in the algorithm has not been determined yet from the synthetic image work. The optimal parameter values, especially the grey value parameter, slightly differ from the synthetic image to real microstructures. It may be due to the small size of the dataset that was used in this work.

Overall it is not surprising that the algorithm performed better on a synthetic image than on a real microstructure, due to the reasons mentioned in section 7.2.9.5. The main reason might be the overlap between the misorientation of colony boundaries and that of bending lamellae within colonies. This problem did not arise with the synthetic case, possibly as its example of bent lamellae was not properly representative of all real cases. Thus more work (possibly using other features than just KAM and grey value) is needed in the future to complement the algorithm, in order to discriminate the colony boundary misorientations and the bending lamellae

misorientations.

7.2.11 Conclusions of Pearlite Colony Characterisation Study

The orientation information of the pearlitic structures can be well represented to a configurable resolution by the FT based method. Three extracted parameters containing two orientation based and one grey intensity based are raised in the study as the features to segment the pearlitic colonies. Meanwhile, a split-merge algorithm was developed for the image segmentation. These operations as well as some pre-processings and post-processings form the automated pearlitic colony analysis method.

The characterisation of pearlite colonies has two main processes: feature extraction and region segmentation. Based on the physical characteristics of pearlitic colonies, three features were used: average orientation value within regions, KAM value along region boundary and average grey levels within regions. The orientation features were obtained by a Fourier Transform method (detecting the position with the highest intensity in the Fourier domain). A novel split-merge algorithm was developed to segment pearlitic colonies with the computed features. Based on the physical characteristics of pearlite colonies, an edge based feature — KAM was integrated into cooperation with the region based feature — mean grey level of regions — to do the merging process.

There are several factors affecting the pearlite colony segmentation. The strength of directionality of adjacent colonies determines the boundary between these colonies. When the directionality strength of a pearlite colony is higher than one of its neighbouring colony, the boundary between these two colonies will move towards to the neighbouring colony. The predicates used in the split-merge process (primarily the KAM and grey value criteria used in the merging stage) determine the number of segmented colonies. Both of a higher KAM criterion and a higher grey level criterion

can increase the number of segmented colonies. Generally to detect correct number of colonies is of higher priority over to detect the correct position of colony boundaries since the correct number gives the correct average colony size, which greatly affects the properties.

The colony characterisation algorithm works well with images consisting of parallel lamellae. When there is bending or fragmented cementite in colonies, to find appropriate criteria of KAM and grey level predicates become a difficult issue.

The algorithm is also affected by the granular pearlite, the artefacts from sample preparation and the discontinuity of lamellae. So although the algorithm can obtain a similar average colony size as the manual method, the quantitative analysis of pearlitic microstructure is not completely successful yet due to the disagreement of the colony size distribution between the automatic result and the manual result. It is still not clear whether any method based on analysis of a single 2-D image can be completely accurate. More work on the distinguishing of misorientation from colony boundaries and that from bending lamellae within colonies would be possibly helpful in the future.

A synthetic image with idealised pearlitic structures was also generated for the evaluation of the pearlite colony characterisation algorithm. The synthetic image consists of straight lamellae, curved lamellae and lamellae with different spacings. Three influencing parameters (FFT neighbourhood size, KAM predicate and grey level predicate value) were investigated. It is concluded that too big or too small of these parameters all decrease the segmentation accuracy. With appropriate parameters that are derived from the investigation (FFT neighbourhood size: 65; KAM value: 4; Grey level value: 40), the segmentation of the synthetic image can reach 93.8%. In this case, the curved colony was not over-segmented and the neighbouring colonies that have same orientation and different interlamellar spacing were detected and

segmented.

The successful application of the algorithm on synthetic images proves that the developed algorithm including the orientation measuring method, features used to determine colonies (KAM value and grey level after smoothing), and the split-merge segmentation technique is appropriate for this particular pearlite colony characterisation study, although more work is still needed to make it accurate for real micrographs.

7.3 Phase Classification for Complex Steel

7.3.1 Phase Observations and Identifications

Sample A:

Scanning electron microscopy (SEM) was used to accurately identify the phases present. A secondary electron micrograph of heat treated sample A after 5% nital etching is shown in Figure 7- 49. Four phases of ferrite, martensite, upper bainite and lower bainite can be observed. The morphology of four phases with a higher magnification is shown in Figure 7- 50. Figure 7- 50 (a) shows a typical morphology of ferrite in this sample, which is the dark region without textural information; the morphology of martensite is shown in Figure 7- 50 (b), which is also the dark region but with internal structures caused by the boundaries (lath/twin) in martensite. The martensite twin plate is approximately 30 nm ~ 50 nm in width with less contrast than the structures shown in (c) and (d). The reason for the less contrast is that the plate boundaries in martensitic region are not high angle boundaries which are etched most by the nital; upper bainite: coarse-textured regions which are inter-distributed with bright carbide and dark ferrite. The carbide thickness in (c) is about 100 nm ~ 200 nm; lower bainite: fine-textured regions which are also mixture of carbide and ferrite. The carbide plates are of higher number density and have a smaller thickness of about 50

nm compared with those in (c). The uniformly black dots in Figure 7- 49 are contamination either from processing or the etching. The grey dots with black edges are inclusions.

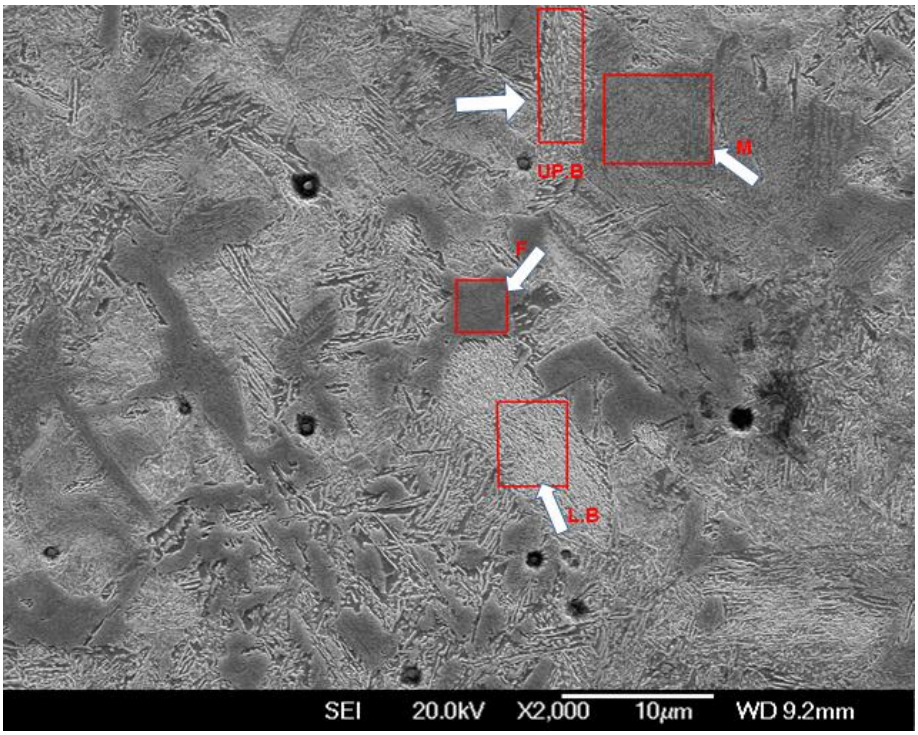

Figure 7- 49 Secondary electron micrograph of heat treated sample A showing martensite (M) upper bainite (UP.B) lower bainite (L.B) and ferrite (F). The rectangular marked regions are magnified in Figure 7- 50.

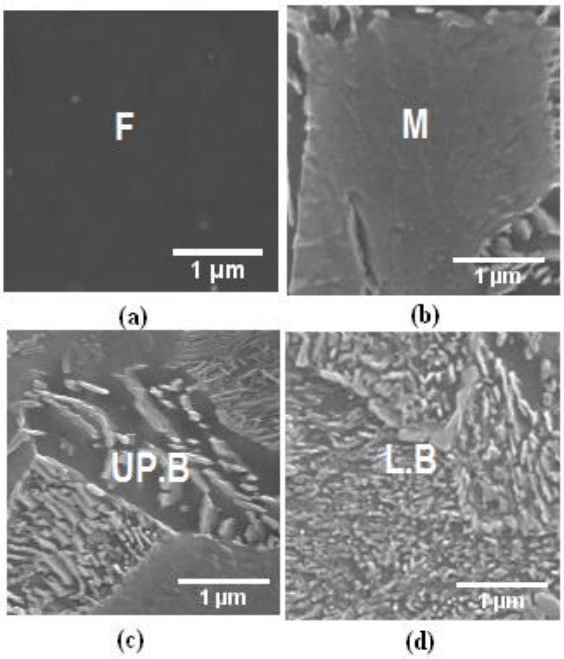

Figure 7- 50 Secondary electron micrograph of four phases (rectangular marked regions) in sample A: (a) ferrite, (b) martensite, (c) upper bainite and (d) lower bainite

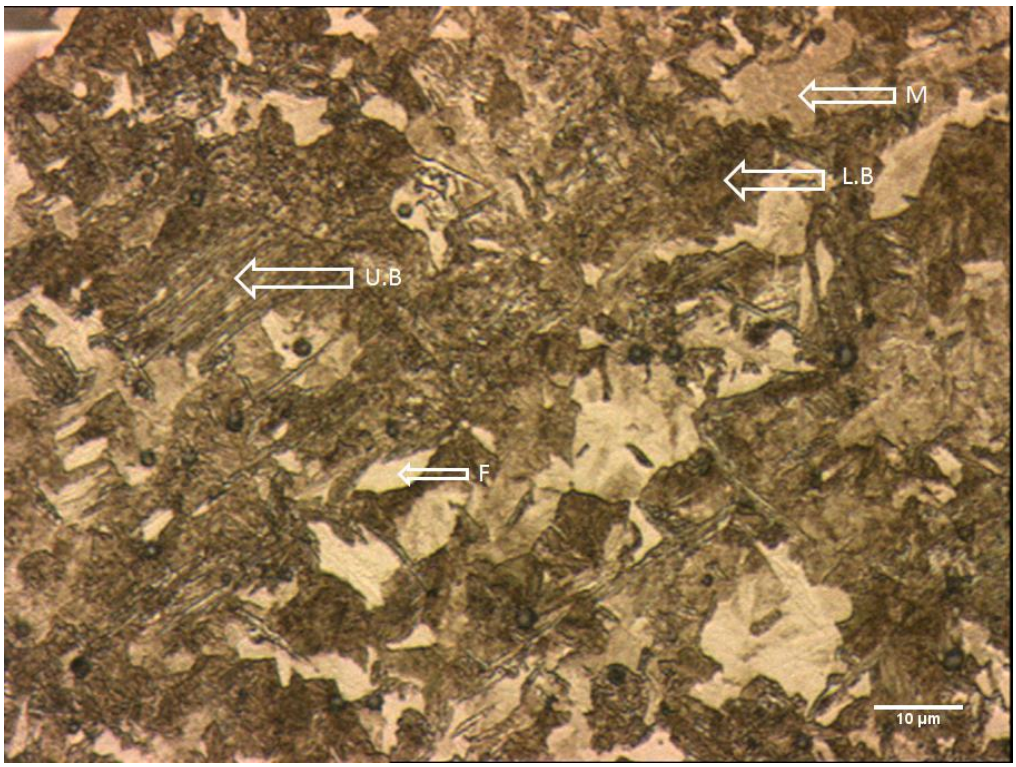

Figure 7- 51 An optical micrograph representing the mixed microstructures of sample A. M: martensite; U.B: upper bainite; L.B: lower bainite; F ferrite.

Figure 7- 51 shows an optical micrograph of sample A after 5% nital etching. Four

phases can be identified: ferrite (uniformly bright regions), martensite (bright regions with internal structures), upper bainite (coarse-textured regions with low average grey levels) and lower bainite (fine-textured regions with low average grey levels). Compared with SE images, the ferrite and martensite regions are brighter than bainite in optical images while those in SE images are darker than bainite.

Sample B and C

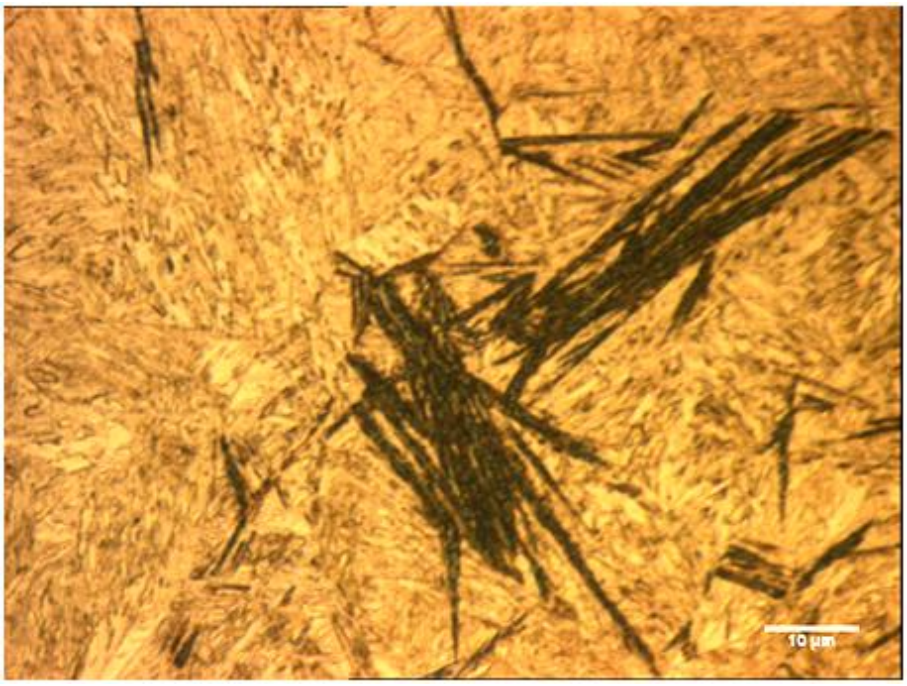

Figure 7- 52 An optical micrograph of sample B showing the mixed microstructure of lower bainite (high contrast darker phase) and martensite (low contrast brighter phase)

From Figure 7- 52 it can be seen that two phases are present in the sample, including a dark lath-like phase and a relatively brighter phase. SEM is carried out in order to accurately identify what these phases are.

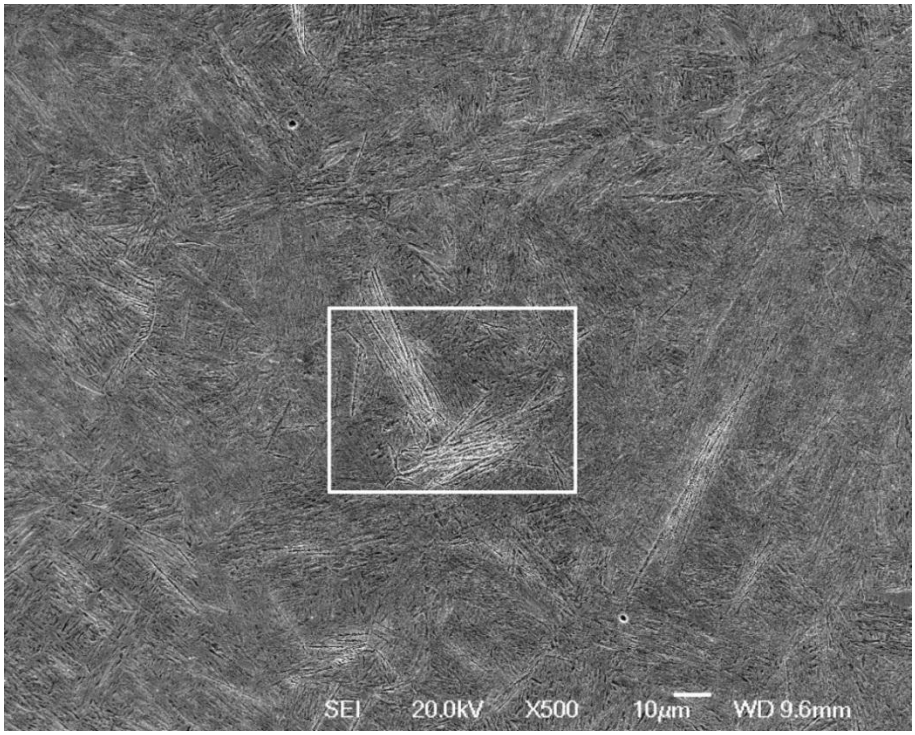

Figure 7- 53 The SE image of the area shown in Figure 7- 52; the rectangular highlighted area is magnified in Figure 7- 54.

Similar as the optical micrograph, there are two phases present in the SE image (Figure 7- 53), although the corresponding grey level of each phase is contrary: the lath-like phase is brighter than the other in the SEI. A magnified image (Figure 7- 54) shows more details of the phases. In Figure 7- 54 bainite sheaves can be clearly seen. There are fine bright particles distributing in the ferrite plates. Therefore the bainite in this image is lower bainite. The other phase shows less contrast and finer lath, thus it is martensite.

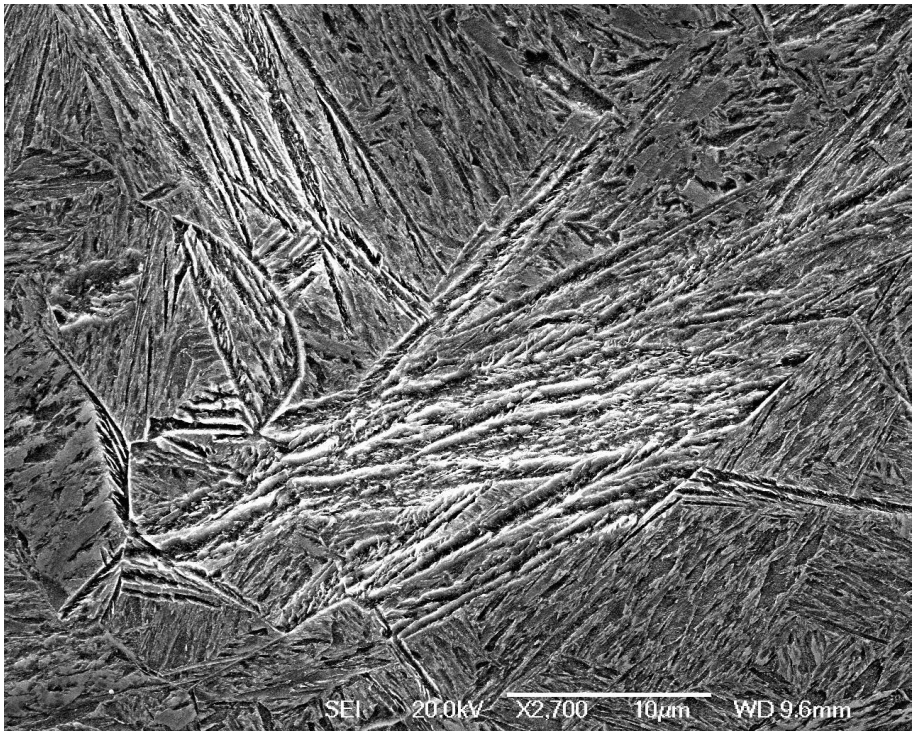

Figure 7- 54 Magnified SE image of the highlighted area in Figure 7- 53

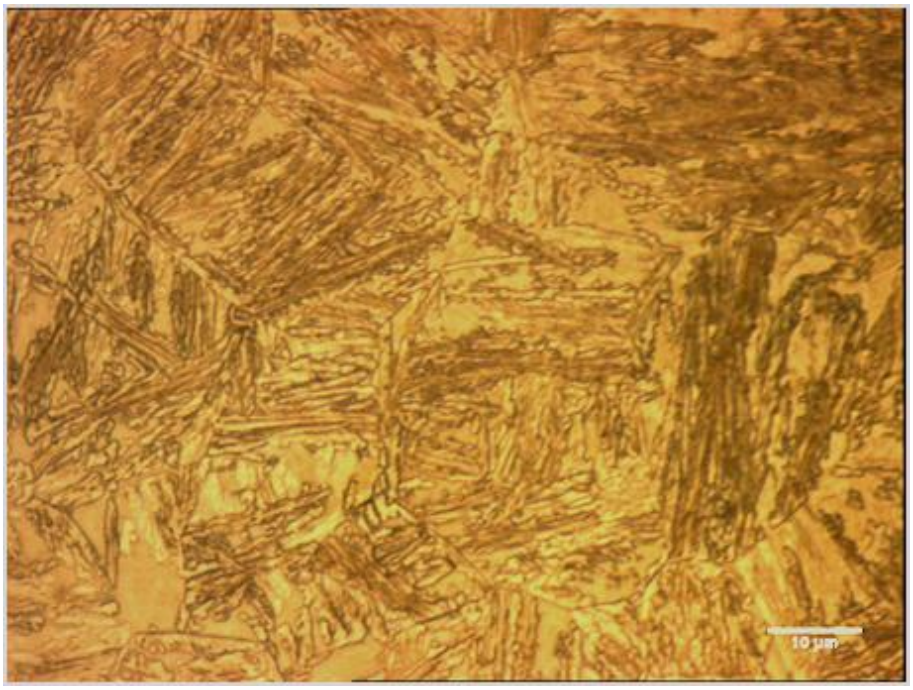

Figure 7- 55 An optical micrograph of sample C showing the mixed microstructure of lower bainite (high contrast darker phase) and martensite (low contrast brighter phase).

Sample C also consists of lower bainite and martensite, which is shown in Figure 7-55.

Sample D, E and F

Figure 7- 56 is an optical micrograph of sample E. Compared with sample B, the laths in E is coarser and has more contrast. The SE image of Figure 7- 57 shows that there are no carbide precipitates within the ferrite plates, which indicates the bainite in the image is upper bainite.

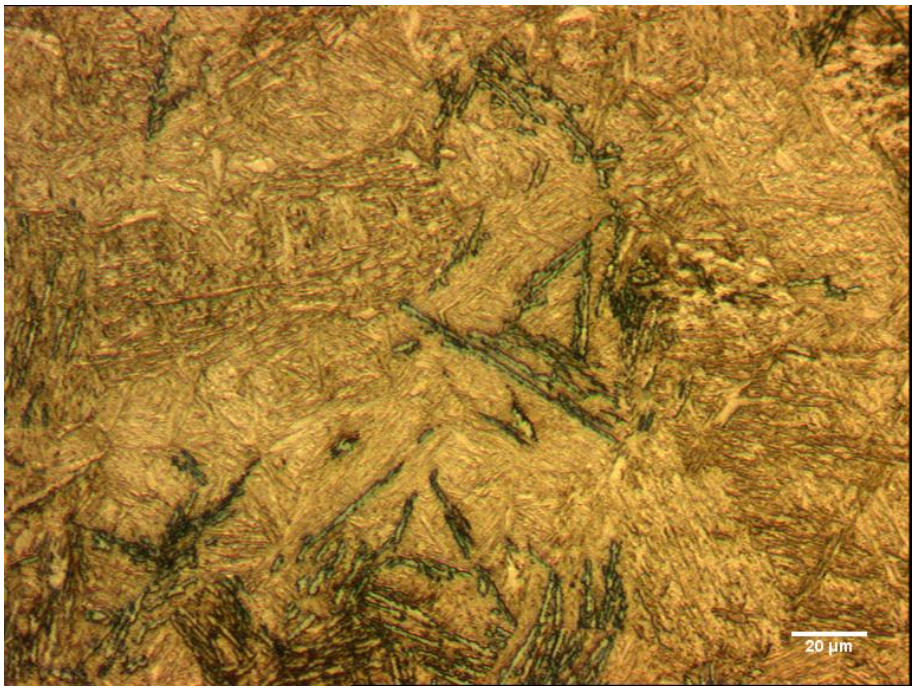

Figure 7- 56 An optical micrograph of sample E showing a mixed microstructure of upper bainite (high contrast darker phase) and martensite (low contrast brighter phase)

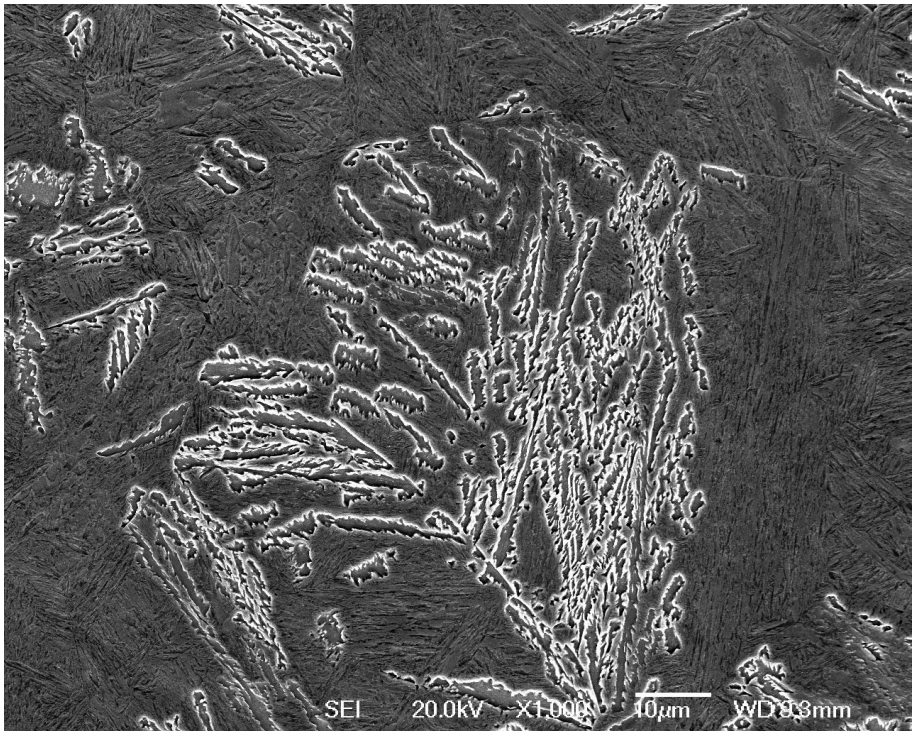

Figure 7- 57 A SE image of sample E

7.3.2 Training Region Selection and GLCM Parameter Determination

Training Regions

Figure 7- 58 is the example image (Figure 7- 51) with the selected training regions shown on it. The red regions represent upper bainite, the green regions represent lower bainite, the yellow regions represent martensite, and the blue region represents ferrite.

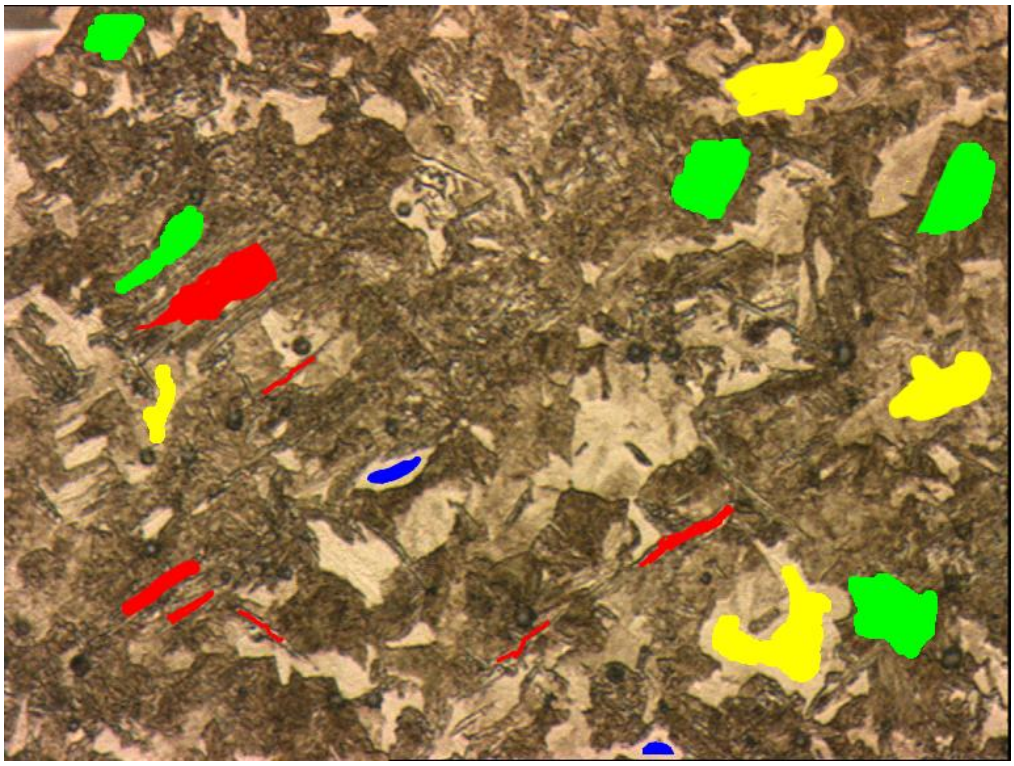

Figure 7- 58 Example image (Figure 7- 51) with the training sets selected. Regions in red: upper bainite; green: lower bainite; yellow: martensite; blue: ferrite.

The determination of α in the GLCM

In order to reduce influencing factors, the pixel pair used in the GLCM in this study is a scalar rather than a vector, which means the angular period of the orientation angle is π. When measuring the GLCM with a distance of 3 pixels and an angle of $0°$ in a region containing pixel *a* and *b* in the example of Figure 7- 59, being considered as a vector, the pixel pair a and b will lead to a count for the measure (1,3). If considered as a scalar, it will lead to a count for both the measure (1,3) and (3,1), which is exactly the same with the situation of measuring from b with a distance of 3 pixels and an angle of $180°$. Therefore a linear combination of the GLCMs for these two directions will represent the properties from not only two directions but also their corresponding opposite directions. Equal weighting factor (0.5) for each direction is used in the combination.

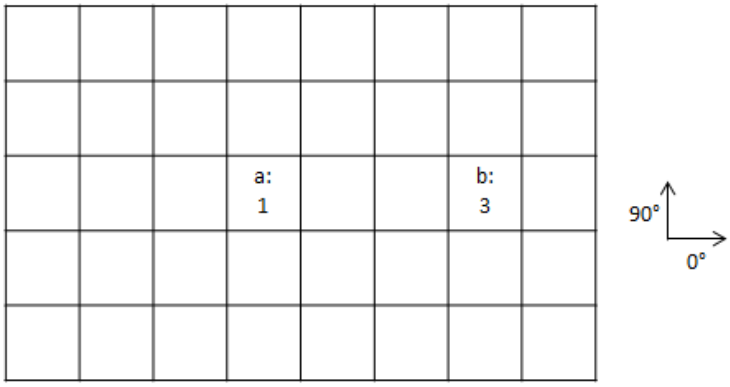

Figure 7- 59 An example of a pixel pair in an image

$$P(i,j,d) = 0.5 * P(i,j,d,0^{\circ}) + 0.5 * P(i,j,d,90^{\circ}) \quad \text{(Eq7.2)}$$

The determination of *d* and *A*

The determination of appropriate parameters for the neighbourhood size *A* and distance *d* is carried out by comparing the classification performance using different combination of the parameters. [9, 13, 17, 21, 25, 29] and [1, 3, 5, 7] are used respectively as the neighbourhood size and the pixel pair distance. Therefore 24 different combinations of these parameters are generated. The average classification accuracy of 3 best features and all of the features are shown respectively in Table 7- 6 and Table 7- 7. Both of the tables show that the classification accuracy becomes higher as the neighbourhood size increase. The classification accuracy with 3 pixel distance between pixel pairs is generally higher than those with other values when their neighbourhood sizes are same. This trend is more evident when more features are studied which is shown in Table 7- 7. In this process, the selected area in Figure 7- 58 was randomly divided into two subsets, one was used for training and the other one was used for the classification accuracy testing. However, the close spatial distances between the training and testing set might improve the classification performance. In order to determine the parameters more accurately, the same procedure was operated

again with testing pixels taken from different regions. Moreover, these testing regions were taken from the interfaces of phases, while the regions for the first time training were taken from non-interface area.

Table 7- 6 The mean classification accuracy of the best 3 features with each parameter setting; training and testing pixels are both subsets taken from the highlighted regions in Figure 7- 58

Distance of pixel Pair (pixels) / Neighou-rhood size (pixels)	1	3	5	7
9	0.879	0.880	0.873	0.856
13	0.910	0.909	0.904	0.892
17	0.912	0.915	0.909	0.913
21	0.926	0.935	0.928	0.931
25	0.946	0.950	0.946	0.942
29	0.941	0.949	0.946	0.949

Table 7- 7 The mean classification accuracy of all features with each parameter setting; training and testing pixels are both subsets taken from the highlighted regions in Figure 7- 58

Distance of pixel Pair (pixels) / Neighou-rhood size (pixels)	1	3	5	7
9	0.525	0.532	0.515	0.471
13	0.567	0.577	0.568	0.548
17	0.588	0.608	0.594	0.560
21	0.615	0.633	0.629	0.615
25	0.635	0.656	0.646	0.641
29	0.641	0.663	0.661	0.657

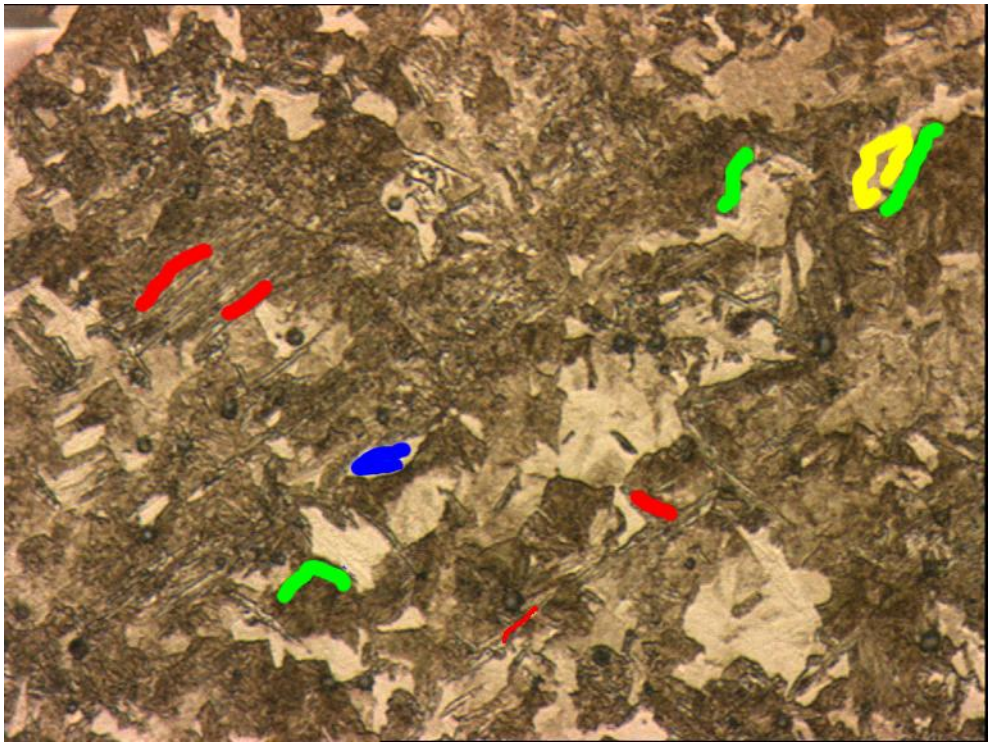

Figure 7- 60 the second testing regions for the parameter determination process

Figure 7- 60 shows the testing regions used for the second time. The classification accuracy including the average of 3 best features and all features were shown in Table 7- 8 and Table 7- 9.

Table 7- 8 The mean classification accuracy of the best 3 features with each parameter setting; training set is the highlighted regions in Figure 7- 58, and testing set is the highlighted regions in Figure 7- 60

Distance of pixel pairs (pixels) / Neighour-hood size (pixels)	1	3	5	7
9	0.746	0.745	0.719	0.688
13	0.737	0.741	0.737	0.719
17	0.725	0.720	0.722	0.717
21	0.712	0.713	0.715	0.710
25	0.724	0.728	0.724	0.720
29	0.709	0.716	0.716	0.717

Table 7- 9 The mean classification accuracy of all features with each parameter setting; training set is the highlighted regions in Figure 7- 58, and testing set is the highlighted regions in Figure 7- 60

Distance of pixel pairs (pixels) / Neighour-hood size (pixels)	1	3	5	7
9	0.415	0.430	0.414	0.377
13	0.438	0.446	0.439	0.429
17	0.430	0.434	0.428	0.422
21	0.428	0.434	0.422	0.416
25	0.429	0.435	0.424	0.424
29	0.422	0.432	0.422	0.420

From the tables it can be seen that, with the same neighbourhood size, the classification accuracy using 3-pixel-distance pixel pairs is generally higher than those using other distances. The relationship between this parameter and the

microstructure is investigated in the pixel scale. Two exampling regions were taken from upper bainite and martensite region, which were marked with red arrow and yellow arrow respectively in Figure 7- 61.

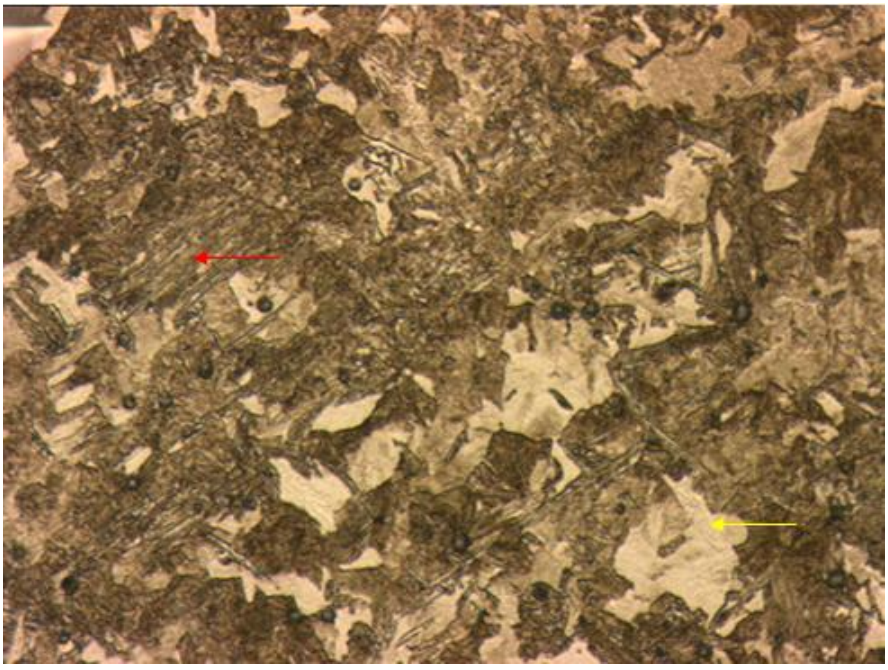

Figure 7- 61 The example image with two arrow marked location to be studied in the pixel scale

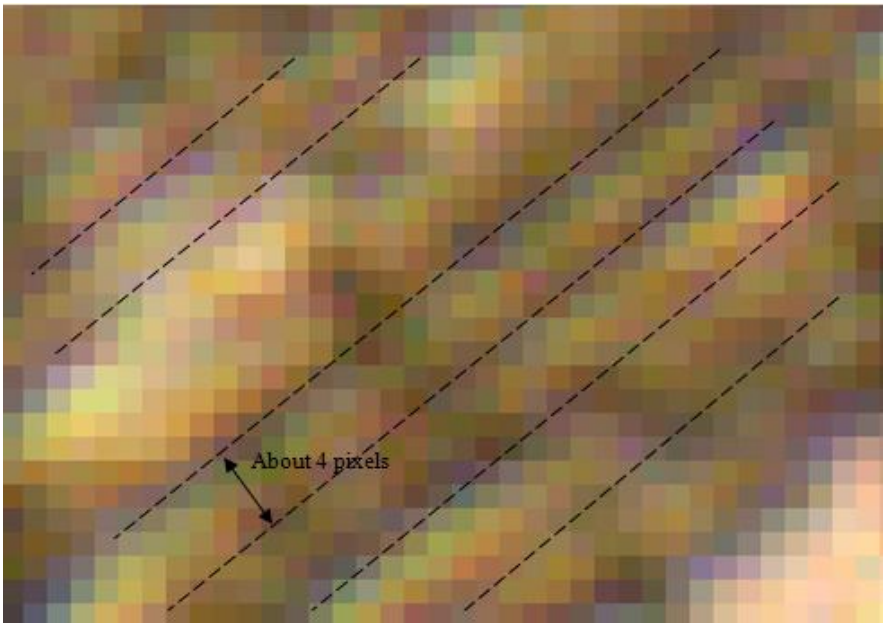

Figure 7- 62 The microstructure of the upper bainite (red arrow marked region in Figure 7- 61) in pixel scale. The dotted lines represent the sheaves of upper bainite. The distance between sheaves is down to about 4 pixels.

Figure 7- 62 shows the magnified upper bainite microstructure which is marked with red arrow in Figure 7- 61. The dotted lines represent the sheaves of upper bainite. The distances between the lines vary. Most of them are down to about 4 pixels. Figure 7- 63 shows the magnified martensite microstructure. Since the etchant has less attacking effect to twin boundaries than to high angle boundaries, the contrast in martensite is much lower than that in upper bainite. However it can still be seen that there are some lines in the microstructure and the distances between the lines can be as small to 4 pixels.

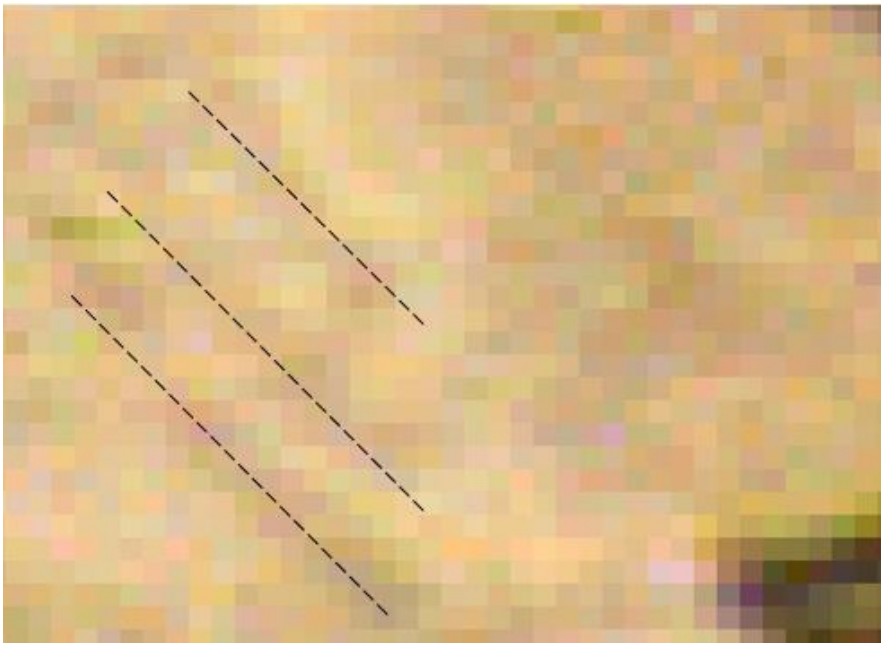

Figure 7- 63 The microstructure of the martensite (yellow arrow marked region in Figure 7- 61) in pixel scale. The dotted lines represent the plate of martensite. The distance between sheaves is also down to about 4 pixels.

Compared with the upper bainite and martensite, lower bainite and ferrite have less oriented microstructure. Therefore the scale of the characteristics is to be a minimum of 4 pixels. Hence important information would be very likely to be missed if the pixel pairs with a distance bigger than 4 pixels were chosen for the GLCM.

Meanwhile, the neighbourhood size should be greater than this value in order to cover the characteristics of interest within the neighbourhood of every pixel.

From Table 7- 6 and Table 7- 7 it can be seen that the classification accuracy keeps increasing probably to an extreme value as the neighbourhood size goes up in the situation that the testing regions were taken from non-interface area. It may because within a pattern, the larger the neighbourhood size is, the more pixel pairs there were, which improves classification performance.

The classification performance is not easy to evaluate when the testing regions are taken from interface area. It might be related to the dimensions of each phase. However, from Table 7- 8 and Table 7- 9, it can be seen that a neighbourhood size of 9 or 13 might be suitable for this case.

The determination of N_g in the GLCM

There are two steps in feature extraction process from intensity images, which are GLCM generation and statistics computation based on the GLCM. A small N_g leads to a poor resolution in the new intensity system, while a large N_g results in a heavy computation load in the statistics computation process. In order to determine an appropriate value of N_g, the classification accuracy were computed using a same idea as in the determination of *d* and *A*.

The classification accuracy using different combination of pixel pair distance and number of grey levels is shown in Table 7- 10, and the data was obtained using exactly same training and testing sets. It can be seen that best performance is reached when N_g is 16.

Table 7- 10 The classification accuracy against pixel pair distance and number of grey levels in new intensity system (local neighbourhood size = 9 pixels)

N_g / Dist (pixels)	8	16	32	64
3	0.877	0.908	0.878	0.872
5	0.888	0.894	0.886	0.865
7	0.878	0.902	0.871	0.872

7.3.3 The KNN Classifier

After the training stage, a combination of 3 features is selected automatically by the algorithm as the most distinguishing features of these images. These three features are: Contrast, Homogeneity and Sum Average. The training values can be plotted in a 3 dimension space, which is shown in Figure 7- 64. Although the majority of each class is clustered separately from that of another class, there are still some overlapping pixels between adjacent classes such as upper bainite and lower bainite, which might result in classification error.

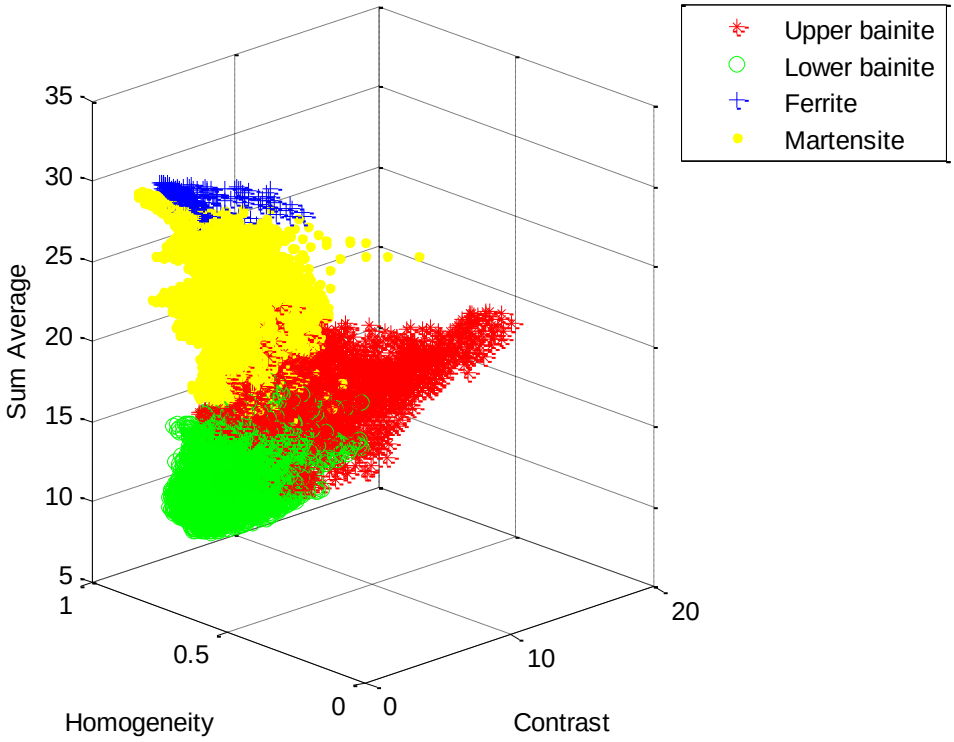

Figure 7- 64 The values of the selected features for each class plotted in a 3-dimensional feature space

From Figure 7- 64, it can be seen that although there are overlaps between adjacent classes, the different classes are generally clustered at different locations in the feature space, which is suitable for the applying of KNN classifier.

7.3.4 Values of K in the KNN Method

As an influencing factor of the accuracy of classification, the selection of K value in the KNN method depends greatly on the size of the training data. A very small K value (to a minimum of 1) leads to the new data being classified as the geometrically closest vector every time, which would be affected greatly by the noise of the training data. A large K value means that the result will always equal to the most frequent class in the training date, which would be affected largely by the size of the different classes in the training data.

7.3.5 The Position of Training Regions

The effect from shape of training regions was studied by selecting regions which are close to the interface between phases and plotting their statistical parameters into a feature space.

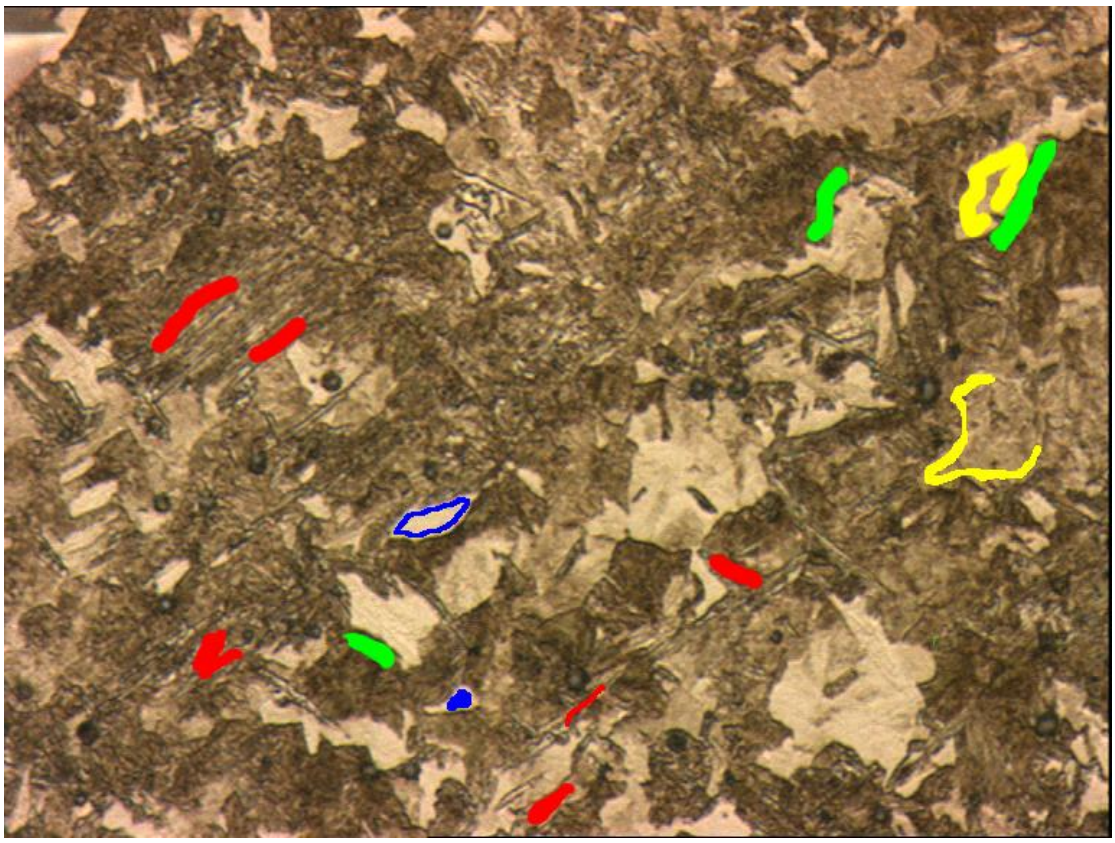

Figure 7- 65 The selected regions for studying the affect from the shape of training regions. Interfaces between phases were selected. Red: upper bainite; green: lower bainite; blue: ferrite; yellow: martensite.

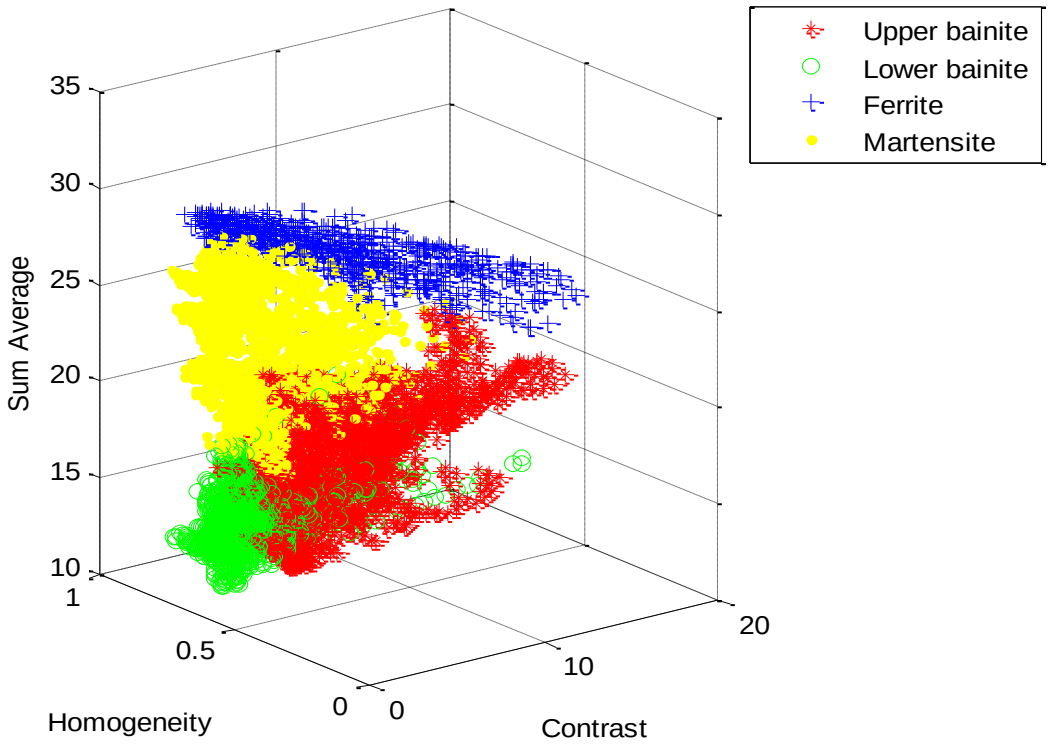

Figure 7- 66 The values of the selected features for each class (selected from Figure 7- 65) plotted in a 3-dimenional feature space

Compared to Figure 7- 64, in Figure 7- 66 most of the upper bainite points have been overlapped with martensite or lower bainite and some upper bainite points start to overlap with ferrite point. Meanwhile, a part of martensite and lower bainite points were overlapped. Therefore the regions close to the interface between classes do not have statistical parameters as distinguishable as the regions which are not close to the interfaces and should be avoided when selecting the training regions.

7.3.6 The Size of Training Regions

The effect of the size of training regions on the classification performance was studied by measuring the classification accuracy with varying size of training regions. The selected regions in Figure 7- 58 were used as a training pixel library and the selected regions in Figure 7- 60 were used as the testing set. A certain percentage of the total pixels were selected randomly from the training library for the training. In order to

eliminate the stochastic error, the testing operation was performed 20 times in each percentage varying case and the average classification accuracy was measured. Since all the training pixels used for each trial are randomly taken from a same library, and all the testing pixels are exactly same, the error caused by the varying locations can be greatly reduced.

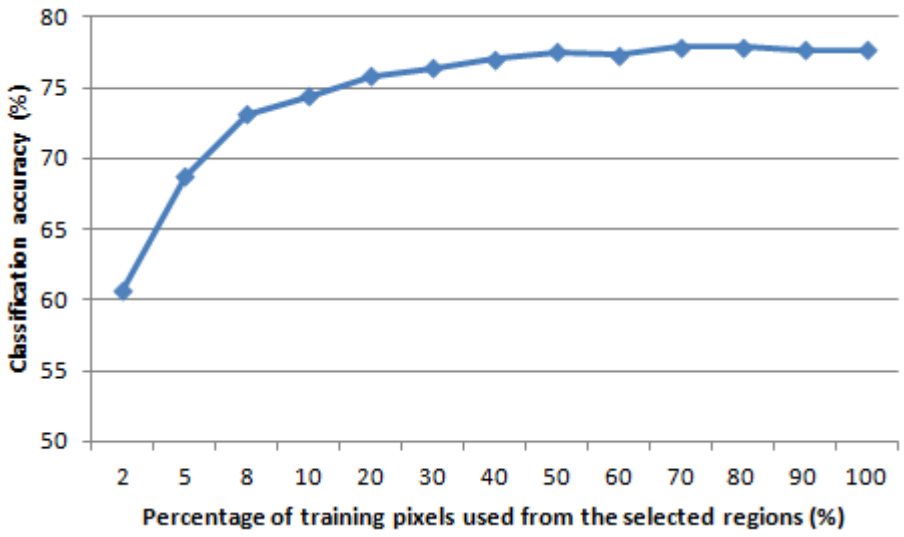

Figure 7- 67 The classification accuracy computed against the percentage of the training pixels used

Figure 7- 67 shows the classification accuracy against the size of training pixels used. It can be seen that generally the classification accuracy increases as the number of training pixels grows. However, as the size of training set gets larger, its effect on the classification performance becomes less because the classification accuracy growth rate decreases to zero.

7.3.7 The Shape of Training Regions

The shape of the training regions plays less important role in this study compared with the location and size of training regions as long as the selected neighbourhood size is big enough to cover the scale of the characteristics of each class (refer to section

7.3.2).

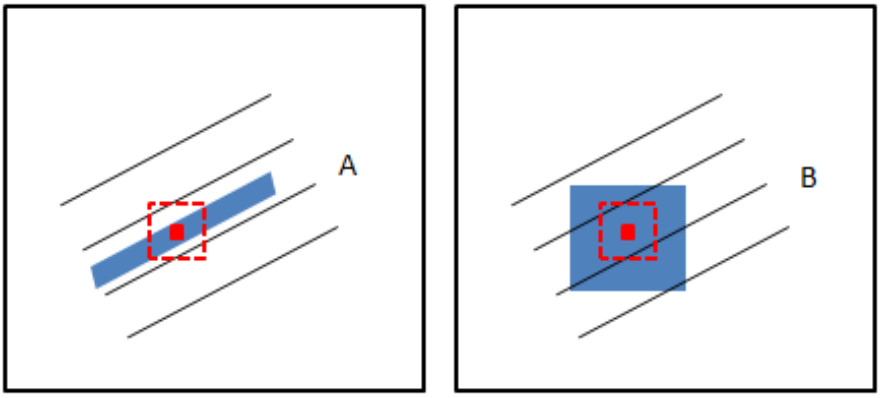

Figure 7- 68 Two different shapes of training region. Region A: line-like shape with a large aspect ratio; Region B: square shape with a small aspect ratio. The red point represents one element in training region A and B.

Figure 7- 68 represents two different training region shapes. Region A is a line-like shape. Although all the training pixels in region A are located between two laths, they get spatial information and create features from an neighbouring area which is big enough to across two laths. So the training sets still get the orientation characteristic of the structure as training region B. Specifically for the red pixel, it gives same numerical values in either region A or region B.

7.3.8 The Justification of SBS

SBS selection method was used in the study to for the feature optimization. The algorithm starts from the full set of the features and sequentially removes a feature that gives least contribution to the classification depending on the performance of the feature combinations. The plot showing the best classification performance against the number of features used was shown in Figure 7- 69. It is shown that the classification performance is gradually increasing when the number of features starts to decrease from full set. Then the accuracy does not vary greatly from 10 features to

3 features, and then it dropped sharply when the number goes down to 1.

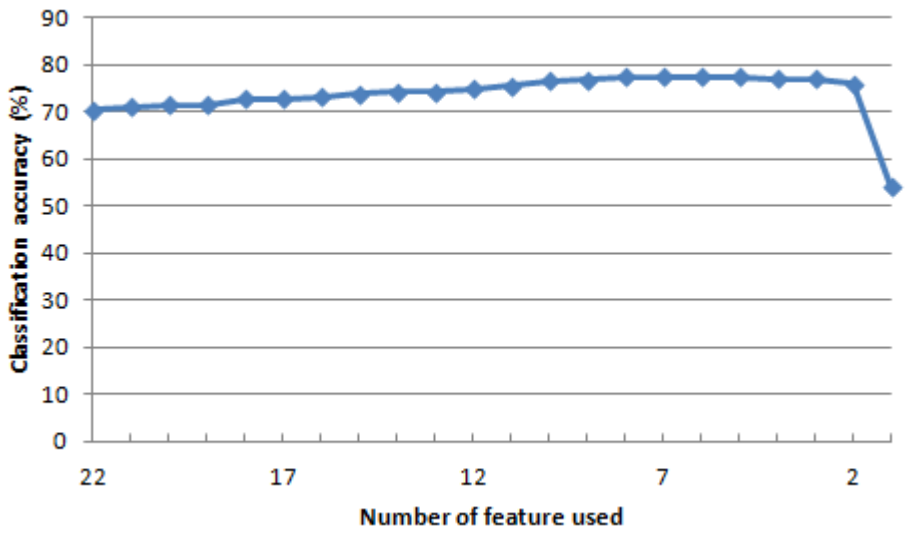

Figure 7- 69 The best classification performance against the number of features used

The justification of SBS was studied by comparing the classification performance using the combination of best 3 features selected by SBS to those selected by other methods. A Sequential Forward Selection (SFS) method (starting from one feature, determine a new feature each time based on the performance of combined features) and a direct combination of three features that individually perform best (measure the classification performance of features individually, and select the best three features) were used as a comparison. The training and testing regions used the selected regions in Figure 7- 58 and Figure 7- 60. The classification accuracy of these three methods was shown in Table 7- 11.

Table 7- 11 The classification accuracy using different feature selection methods (3 features were selected by each method)

	Selected by Individual Performance	SFS	SBS
Classification Accuracy (%)	67.4	74.9	77.7

From Table 7- 11 it can be seen that SBS method performed slightly better than SFS in this study. However, both of them significantly improved the performance compared than the selection by individual performance of features.

7.3.9 Mathematical Features and Physical Microstructure

After the training stage, a combination of 3 features is selected automatically by the algorithm as the most distinguishing features of these images. These three features are: Contrast, Homogeneity and Sum Average. In order to schematically illustrate why these parameters distinguish upper bainite, lower bainite, ferrite and martensite, four synthetic structures (Figure 7- 70) were generated to represent four phases and the relationship between the three parameters and the structures was studied.

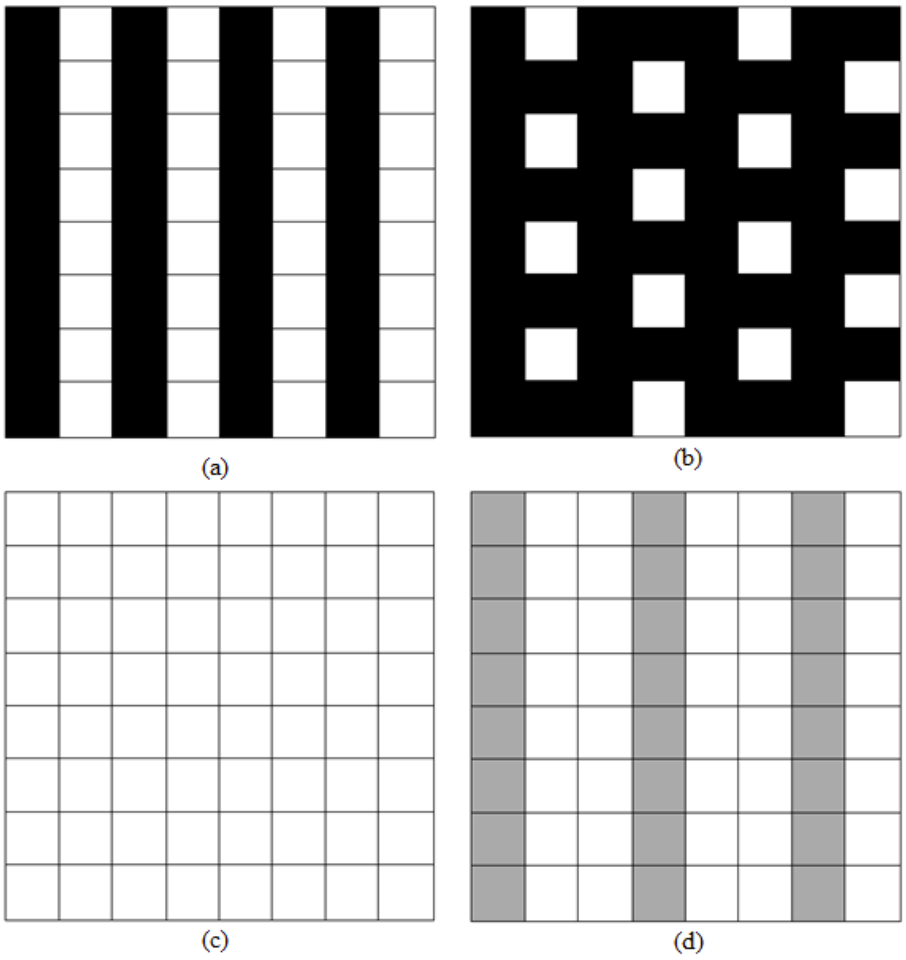

Figure 7- 70 The synthetic structures (8x8 pixels) representing (a) upper bainite; (b) lower bainite; (c) ferrite; (d) martensite. The grey intensities are defined with 4 levels: 0,1, 2 and 3. The grey level of the white pixels in all 4 figures is 3; the grey level of the black pixels in (a) and (b) is 0; the grey level of the grey pixels in (d) is 2.

The grey intensities in Figure 7- 70 are defined with 4 levels: 0, 1, 2 and 3. The grey level of the white pixels in all 4 figures is 3; the grey level of the black pixels in (a) and (b) is 0; the grey level of the grey pixels in (d) is 2. Figure (a) consists of black and white lath representing cementite and ferrite in the upper bainite; figure (b) represents lower bainite which has cementite within the ferrite lath; figure (c) represents ferrite and figure (d) consists of grey lath representing the martensite twin boundaries which was less attached during etching compared with the cementite/ferrite boundaries.

The GLCM was generated with 1-pixel distance in the horizontal direction. From the GLCMs shown in Figure 7- 70, it can be seen that the probabilities of the synthetic ferrite (Figure 7- 70 (c)) are concentrated in the bottom right element, while the probability distribution of synthetic martensite (Figure 7- 70 (d)) is similar to it but have a little spread into the neighbouring elements of the bottom right position due to the existence of grey laths. The probability of synthetic upper bainite (figure (a)) is concentrated distributed in the positions representing high grey level difference between pixel pairs ((1,4) and (4,1) in this example); the structure of synthetic lower bainite (figure (b)) also has probabilities distributed in those positions, and in the positions representing smaller grey level difference as well ((1,1) in this example).

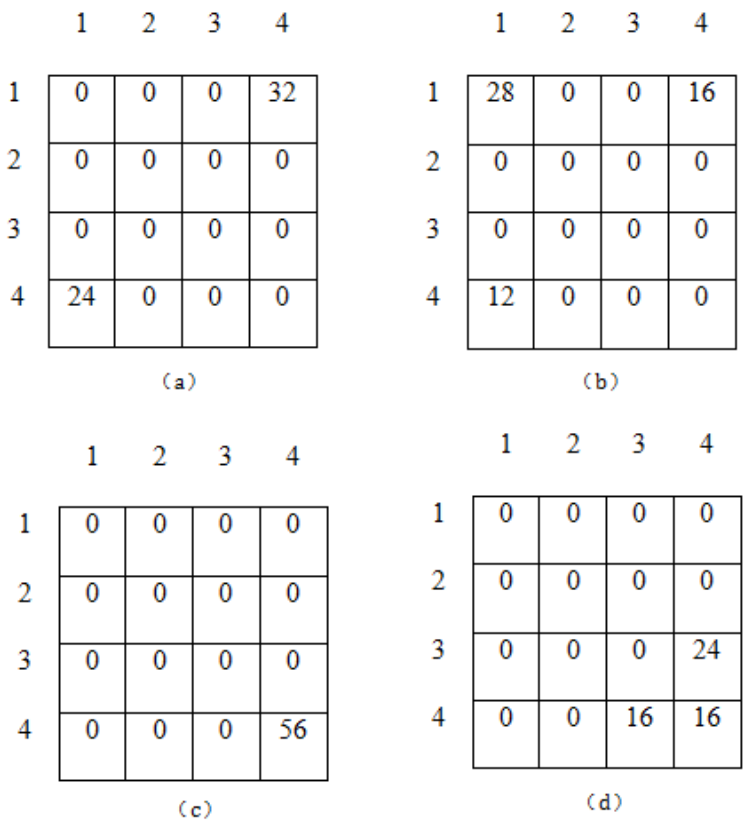

	1	2	3	4
1	0	0	0	32
2	0	0	0	0
3	0	0	0	0
4	24	0	0	0

(a)

	1	2	3	4
1	28	0	0	16
2	0	0	0	0
3	0	0	0	0
4	12	0	0	0

(b)

	1	2	3	4
1	0	0	0	0
2	0	0	0	0
3	0	0	0	0
4	0	0	0	56

(c)

	1	2	3	4
1	0	0	0	0
2	0	0	0	0
3	0	0	0	24
4	0	0	16	16

(d)

Figure 7- 71 The GLCMs generated from the four structures shown in Figure 7- 70

Contrast

The equation of Contrast is:

$$Contrast = \sum_{n=0}^{N_g-1} n^2 \left[\sum_{i=1}^{N_g} \sum_{j=1}^{N_g} p(i,j) \right]_{|i-j|=n} \quad \text{(Eq 7.2)}$$

The measure of Contrast is a calculation related to the distance from GLCM diagonal. The pixel pair corresponding to the GLCM diagonal has same grey level. So contrast parameter is determined by two aspects: the value of the probability and the distance between its position and the GLCM diagonal. The values of Contrast parameter for the four GLCMs in Figure 7- 71 are shown in Table 7- 12.

Table 7- 12 The values of Contrast parameter for the four GLCMs in Figure 7- 71

	Synthetic upper bainite	Synthetic lower bainite	Synthetic ferrite	Synthetic martensite
Contrast	9	4.5	0	0.7

Homogeneity

The equation of Homogeneity is expressed as:

$$Homogeneity = \sum_i \sum_j \frac{p(i,j)}{1+|i-j|} \quad \text{(Eq 7.3)}$$

The measure of Homogeneity is also related to the value of the element in GLCM and the distance between it and the GLCM diagonal. A smaller distance leads to a higher homogeneity value. The values of Homogeneity parameter for the four GLCMs in Figure 7- 71 are shown in Table 7- 13.

Table 7- 13 The values of Homogeneity parameter for the four GLCMs in Figure 7- 71

	Synthetic upper bainite	Synthetic lower bainite	Synthetic ferrite	Synthetic martensite
Homogeneity	0.25	0.625	1	0.643

Sum average

The equation of Sum Average is expressed as:

$$Sum\ Average = \sum_{i=2}^{2N_g} i \cdot p_{x+y}(i) \qquad \text{(Eq 7.4)}$$

The measure of Sum Average uses weights related to the distance between the anti-diagonal from the top left of the GLCM. The pixel pairs on a same GLCM anti-diagonal line have the same sum value. Hence it is a statistic measure derived from the GLCM. A higher mean grey level of the original image (martensite) results in a higher probability that a grey-level co-occurrence pair locate in the bottom right part of the GLCM, and consequently leads to a higher value of the Sum Average measure. The values of Sum Average parameter for the four GLCMs in Figure 7- 71 are shown in Table 7- 14.

Table 7- 14 The values of Sum Average parameter for the four GLCMs in Figure 7- 71

	Synthetic upper bainite	Synthetic lower bainite	Synthetic ferrite	Synthetic martensite
Sum Average	5	3.5	8	7.3

Then the average value of these measures for the training sets of each class in Figure 7- 58 is measured and shown in Table 7- 15. The trend of the values is consistent with the results and discussions shown above.

Table 7- 15 The average values of the selected measures for the training sets of each class

	Upper bainite	Lower bainite	Ferrite	Martensite
Contrast	4.6	2.1	1.0	1.9
Homogeneity	0.49	0. 59	0.71	0.62
Sum Average	17.9	13.8	30.3	25.0

7.3.10 Comparison of the Classification and Manual Results

Three images were classified automatically and manually drawn by three postgraduates who did research on steel. One of the images was shown from Figure 7- 72 to Figure 7- 76. Figure 7- 72 is the initial image containing four phases: upper bainite, lower bainite, ferrite and martensite. Figure 7- 73 shows the classification of the initial image by automatic analysis. The three manual classifications are shown from Figure 7- 74 to Figure 7- 76.

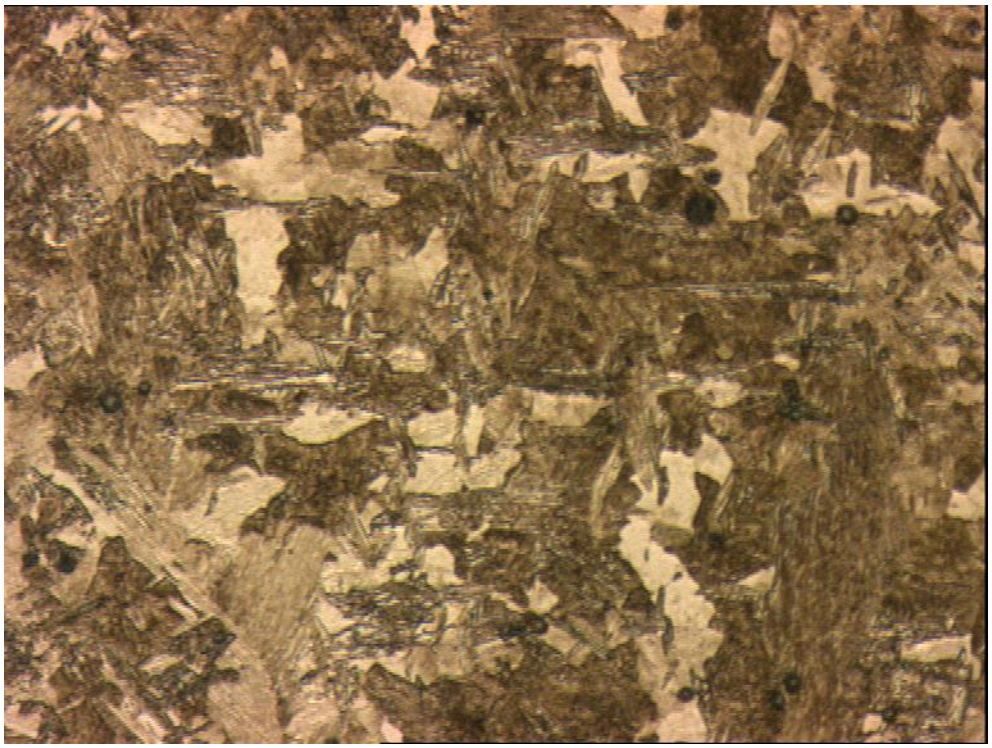

Figure 7- 72 An example image (500x) used for phase classification containing four phases: upper bainite, lower bainite, ferrite and martensite.

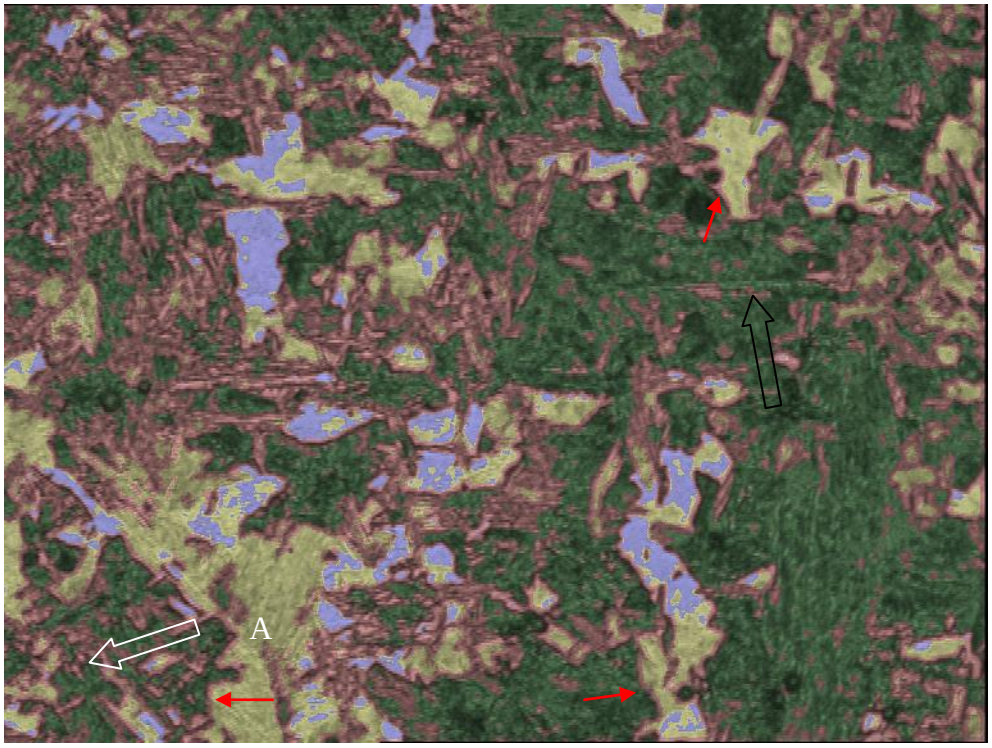

Figure 7- 73 The automatic classification of the initial image (Figure 7- 72) (red region: upper bainite; green region: lower bainite; blue region: ferrite; yellow region: martensite)

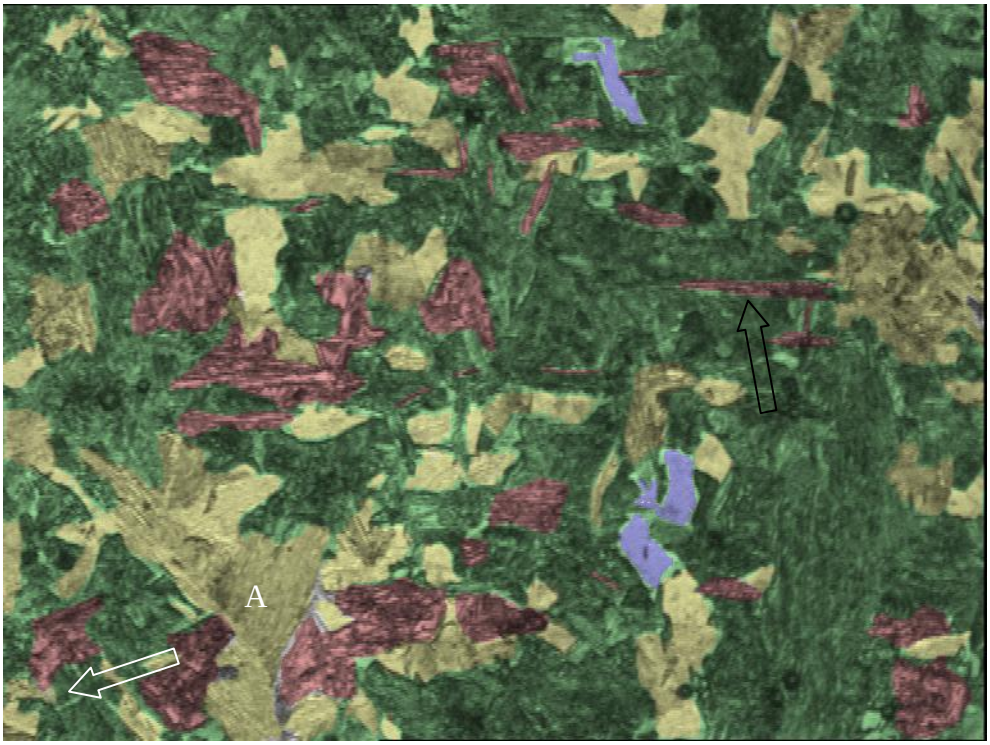

Figure 7- 74 The first manual classification of the initial image (Figure 7- 72) (red region: upper bainite; green region: lower bainite; blue region: ferrite; yellow region: martensite)

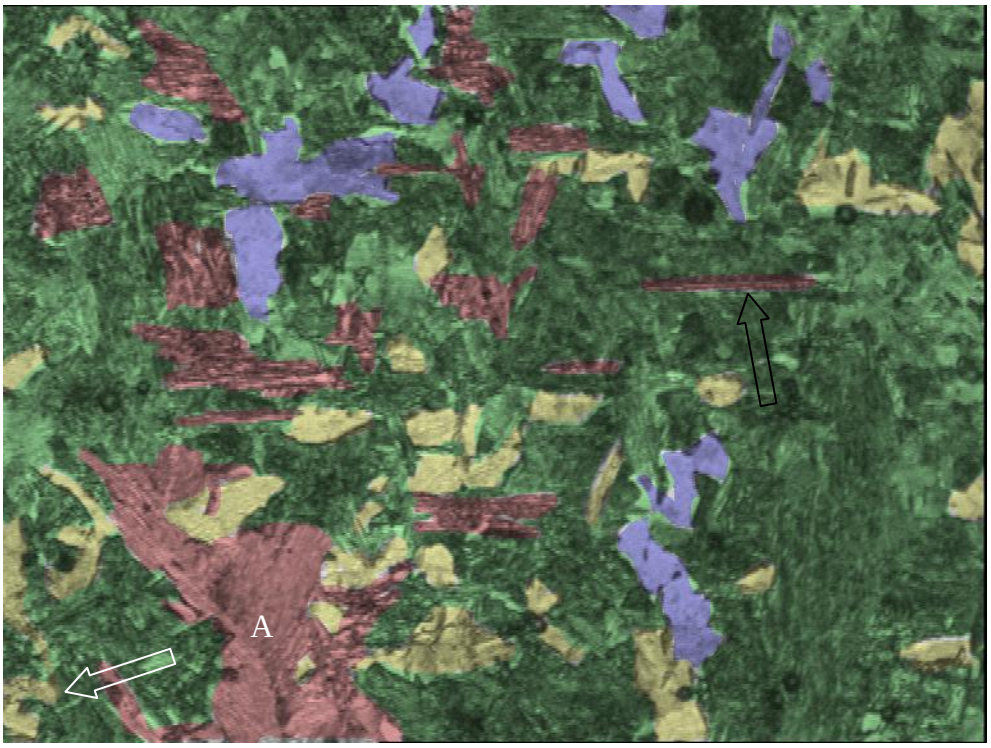

Figure 7- 75 The second manual classification of the initial image (Figure 7- 72) (red region: upper bainite; green region: lower bainite; blue region: ferrite; yellow region: martensite)

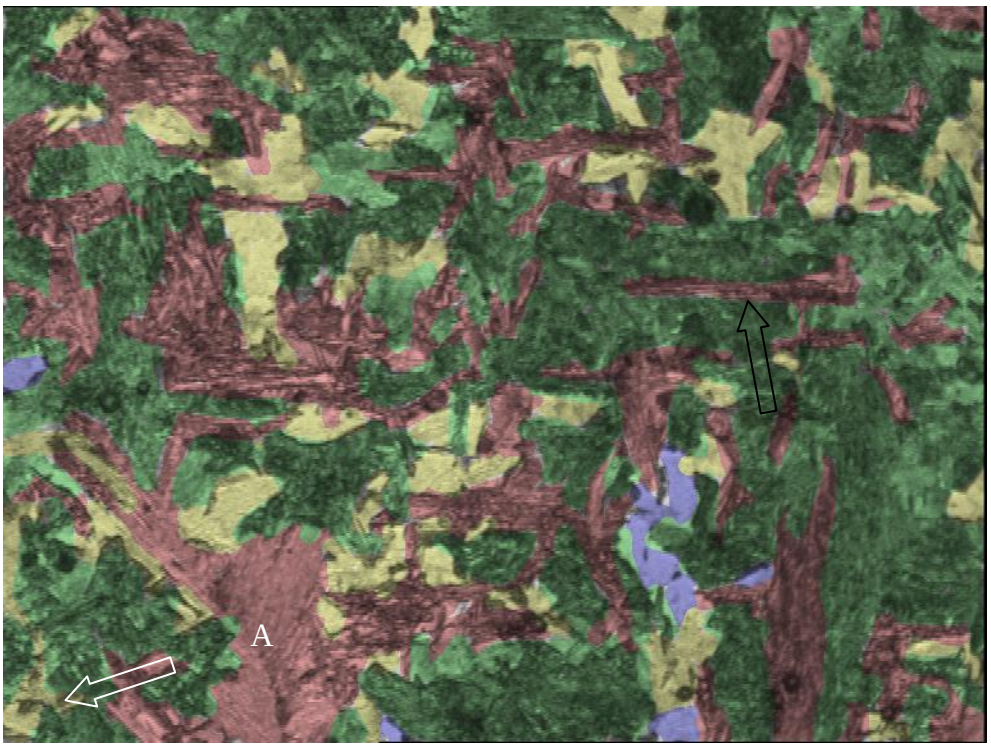

Figure 7- 76 The third manual classification of the initial image (Figure 7- 72) (red region: upper bainite; green region: lower bainite; blue region: ferrite; yellow region: martensite)

From the image shown above, it can be seen that the automatic classification method is able to detect correct present phases at a local position even if the phase is a small amount (the white arrow marked upper bainite in the images), but in some detected phases have shifted boundary problem such as the black arrow marked region in the images. The interface of two phases might be incorrectly classified if there is another phase located between these two phases in the feature space (the interface of martensite and lower bainite was classified as upper bainite as shown in the red arrow marked region in Figure 7- 73). However, there is some inconsistency among the manual classifications such as region A and most ferrite/martensite regions in the classification images. Region A has intra-phase lower contrast and finer microstructure than the upper bainite in this sample, so it is probably martensite, which agrees with the algorithm's decision.

The quantitative statistics of the analysis are shown in Table 7- 16.

Table 7- 16 The quantitative statistics of the automatic algorithm and manual classifications

	Upper bainite	Lower bainite	(Total bainite)	Ferrite	Martensite
Auto method	33.9%	47.9%	(81.8%)	4.7%	13.5%
Manual 1	11.4%	63.9%	(75.3%)	0.8%	23.9%
Manual 2	12.7%	69.8%	(82.5%)	5.6%	11.9%
Manual 3	29.3%	52.5%	(81.8%)	1.4%	16.8%

From Table 7- 16 it can be seen that the fractions of ferrite, martensite and total bainite (upper bainite + lower bainite) obtained automatically are all within the range of manual result. The automatic result of upper bainite is slightly higher than the upper limit of the manual result. By referring to the images and above discussions, a certain source of the extra upper bainite is the interface between martensite and lower

bainite. The statistical parameter of the interface pixels are likely to be in-between those values of the two phases. In the feature space shown in Figure 7- 66, upper bainite is clustered between martensite and lower bainite. Therefore, any value which is in-between the martensite feature cluster and lower bainite cluster is more likely to be labelled as upper bainite pixel.

Due to the greatly different contribution that they give to the properties of the steels as reviewed in chapter 2, it is important to accurately discriminate upper and lower bainite. Because of the difficulties of manually classifying the phases (e.g. show great scattering), the manual results shown in this study is just regarded as references rather than ground truth. So in this work only a certain factor that causes the errors was analysed, which is the incorrect classification of boundaries between phases. The ground truth of these images requires a manual classification on the secondary electron images with a much higher magnification. It needs a large amount of time but the project has a time limitation. Therefore, the evaluation by secondary electron images was not carried out with this sample and is addressed as a part of future work. The validation of the algorithm was performed instead using two phase microstructures which can be easier classified by people but still difficult for machine due to the inter-phase contrast.

7.3.11 Quantitative Results of Sample B to F

Samples B, C, D, E and F were used to do quantitative analysis. 36 768x576 optical micrographs were obtained from each sample, with a total area of 1.56 mm^2.

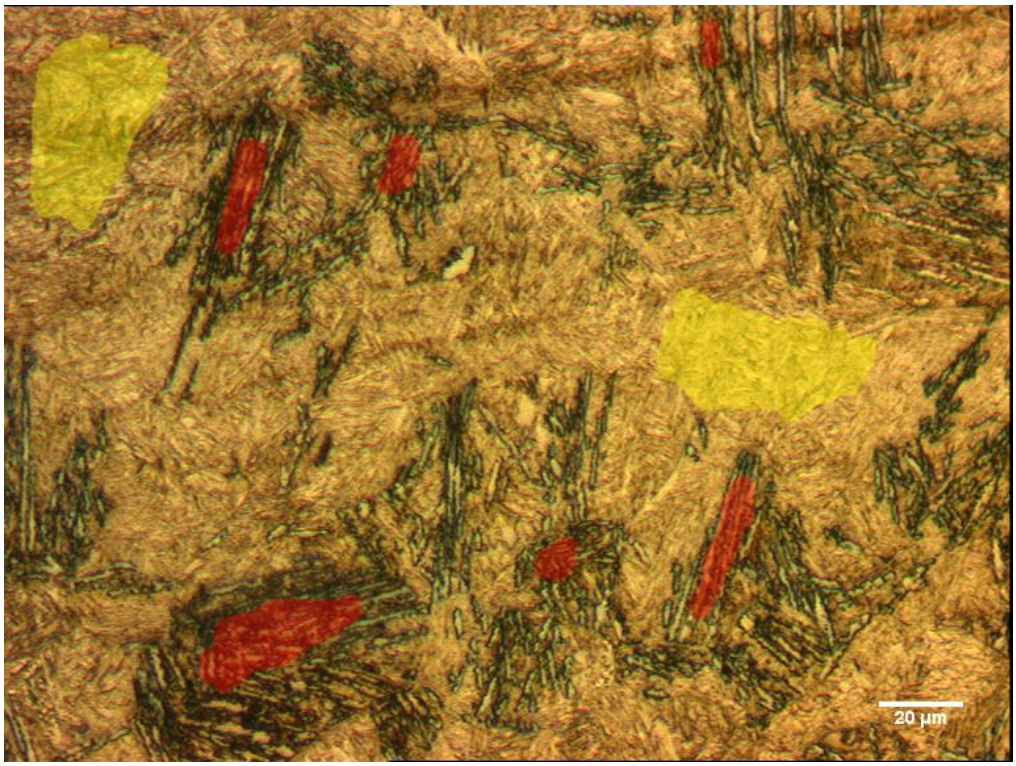

Figure 7- 77 An optical micrograph of sample E (image E-1) with the training regions (yellow: Martensite; red: upper bainite)

Figure 7- 77 shows an optical micrograph (image E-1) of sample E. The training areas are painted with light red (upper bainite) and light yellow (martensite). The classification result of the entire image is shown in Figure 7- 78 (light red: upper bainite; light yellow: martensite). The algorithm was also applied to another image (Figure 7- 79) from a different area of the same sample and the classification is shown in Figure 7- 80.

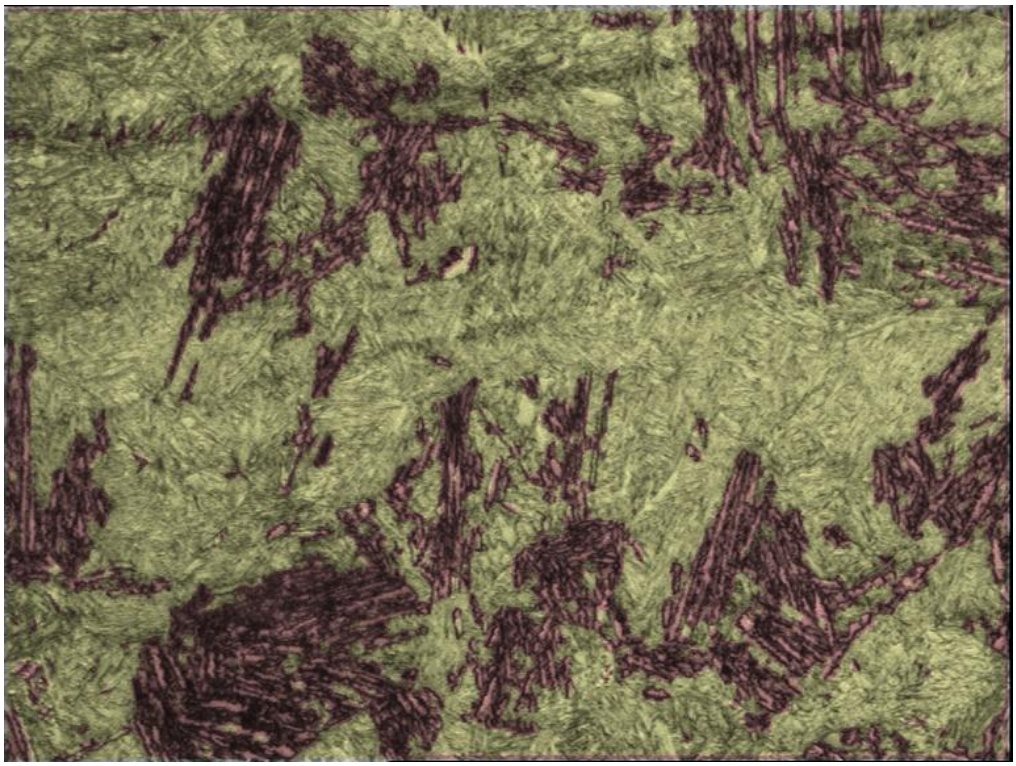

Figure 7- 78 Image E-1 (Figure 7- 77) with automated classification results showing in different colour (yellow: martensite; red: upper bainite)

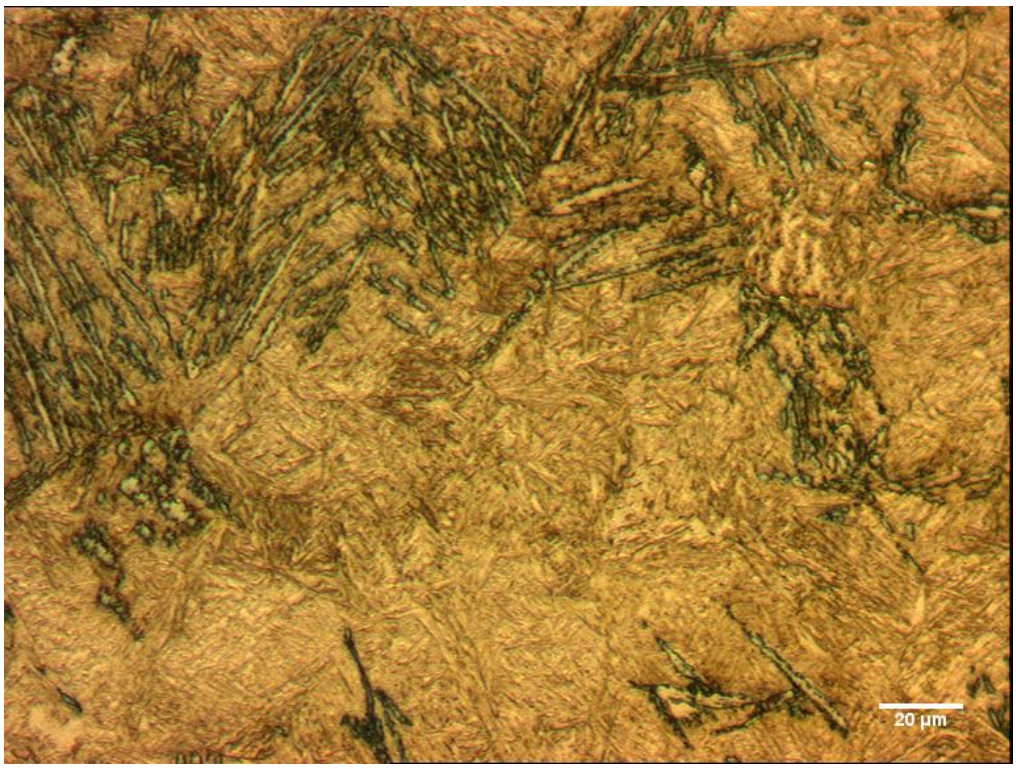

Figure 7- 79 Another optical micrograph of sample E (image E-2)

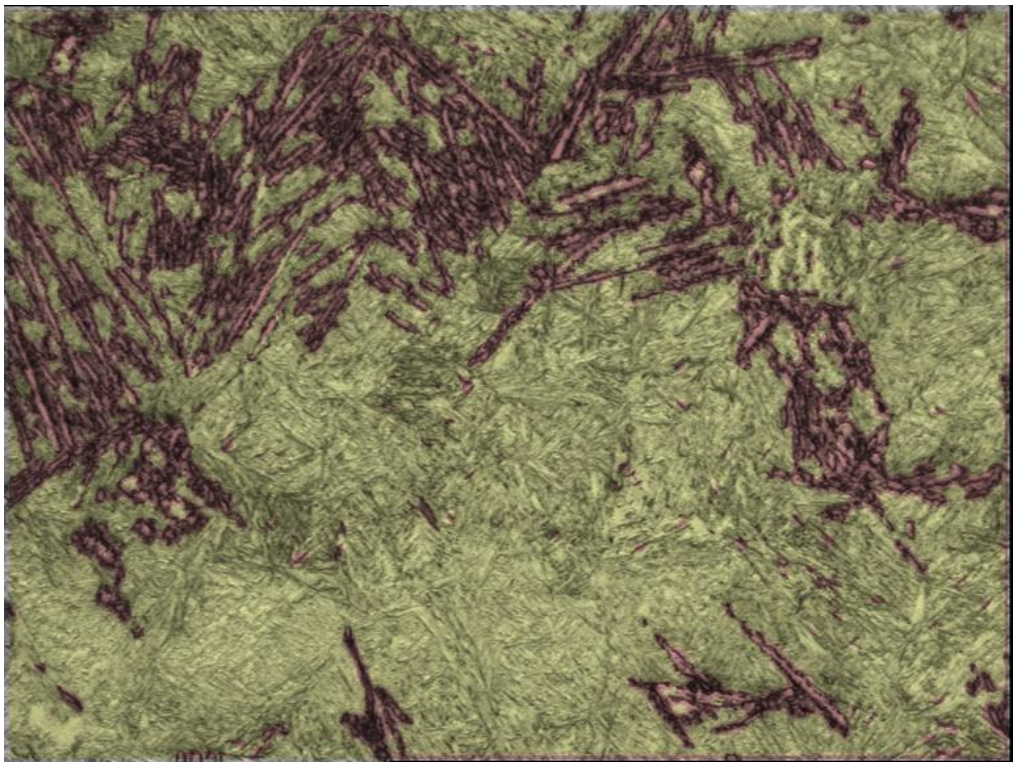

Figure 7- 80 Image E-2 (Figure 7- 79) with classification results showing in different colour (yellow: martensite; red: upper bainite) using the automated classification method developed in this study

In order to verify the accuracy of the automated method, the images were classified manually.

The manual quantification was carried out with the software GIMP 2.6.10 (GNU Image Manipulation Program), which allows retouching, editing, free-form drawing and basic processing on the image. A layer image with equivalent size with the original image was created and phases were drawn on the layer image. Then the drawn layer image with was transformed in to a binary image and quantified using Matlab software.

Same features were used to train and classify the images of sample F, which has a similar microstructure with sample E. The example image, the automatic processed

and manually drawn images are shown from Figure 7- 81 to Figure 7- 83. Figure 7- 81 shows an optical micrograph of sample F, which also contains upper bainite and martensite. Training regions were selected and painted red or yellow for the two phases. Figure 7- 82 and Figure 7- 83 show respectively the classification results of automated method and manual method. Table 7- 17 and Table 7- 18 illustrates the phase fraction values of the samples B to F obtained by the automated and manual image analysis method.

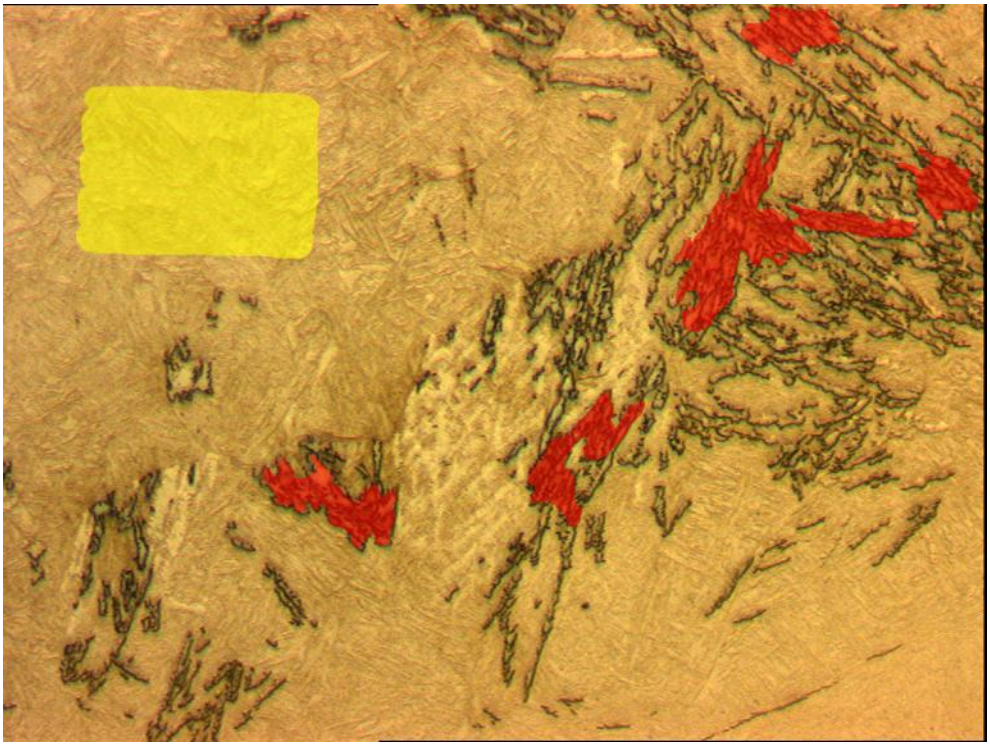

Figure 7- 81 The training regions for the images from sample F (red: the training regions for upper bainite; yellow: martensite)

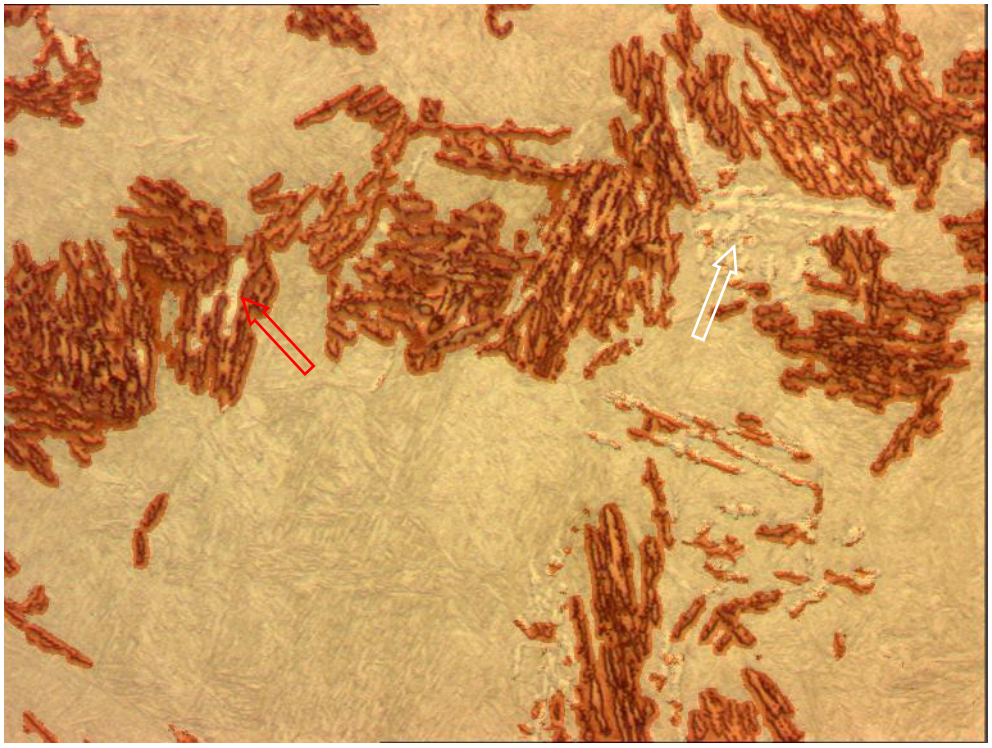

Figure 7- 82 An example image from Sample F showing the automatic classification results (the detected upper bainite region is shown in red)

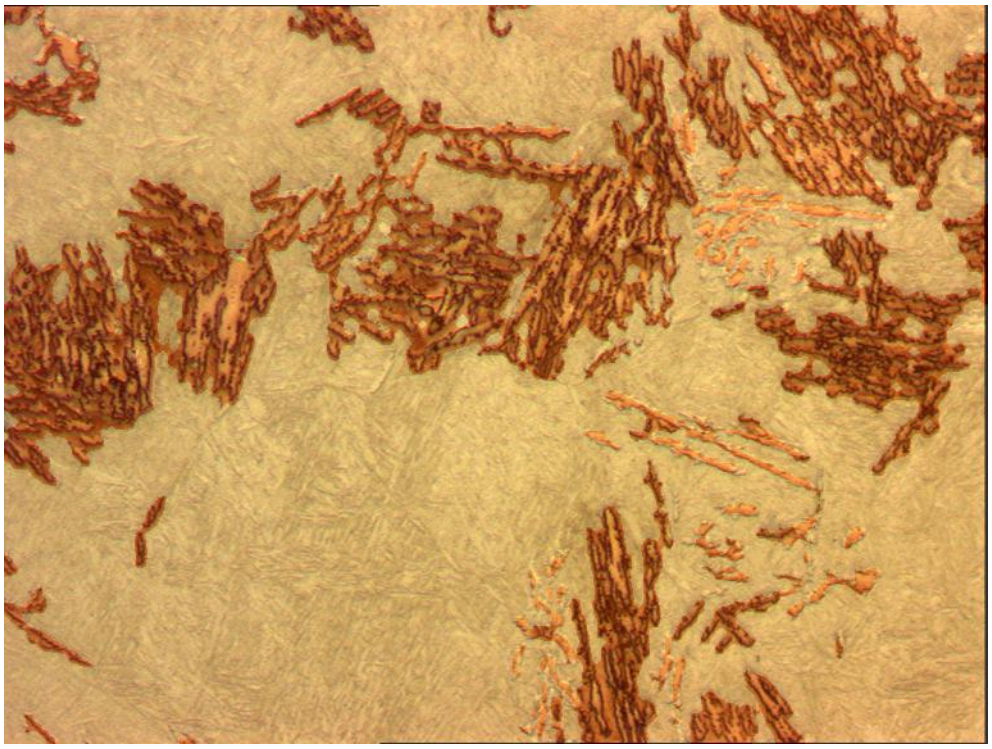

Figure 7- 83 Manual classification results of Figure 7- 82 (the upper bainite is shown in red)

Table 7- 17 Phase fractions of the samples obtained by automated image analysis method

	Bainite	Martensite
Sample B	1.4% (lower bainite)	98.6%
Sample C	93.9%(lower bainite)	6.1%
Sample D	6.9%(upper bainite)	93.1%
Sample E	27.0%(upper bainite)	73.0%
Sample F	38.5%(upper bainite)	61.5%

Table 7- 18 Phase fractions of the samples obtained by manual method

	Bainite	Martensite
Sample B	1.1% (lower bainite)	98.9%
Sample C	93.1%(lower bainite)	6.9%
Sample D	6.4%(upper bainite)	93.6%
Sample E	26.4%(upper bainite)	73.6%
Sample F	38.1%(upper bainite)	61.9%

It can be seen that the bainite fraction increases from sample B to sample C and from sample D to sample F. The bainite fraction increases for sample F compared to sample E is much smaller than that for sample E compared to sample D, despite that holding time in 425℃ of sample F is a lot longer than that of D and E. The reason is bainite transformation is still to some degree diffusive process, in which the reaction rate decreases as the time increases until the chemical balance is reached.

By comparison there are three main differences between the automated and manual methods:

1. Similar phase fractions for same sample were obtained by automated and manual method. The automated values are slightly bigger than the manual ones mainly because the martensitic area that is closely along the interface between bainite and

martensite is classified as bainite as highlighted with black arrow in the images. An example (Figure 7- 84) was used to illustrate the classification of the interface area.

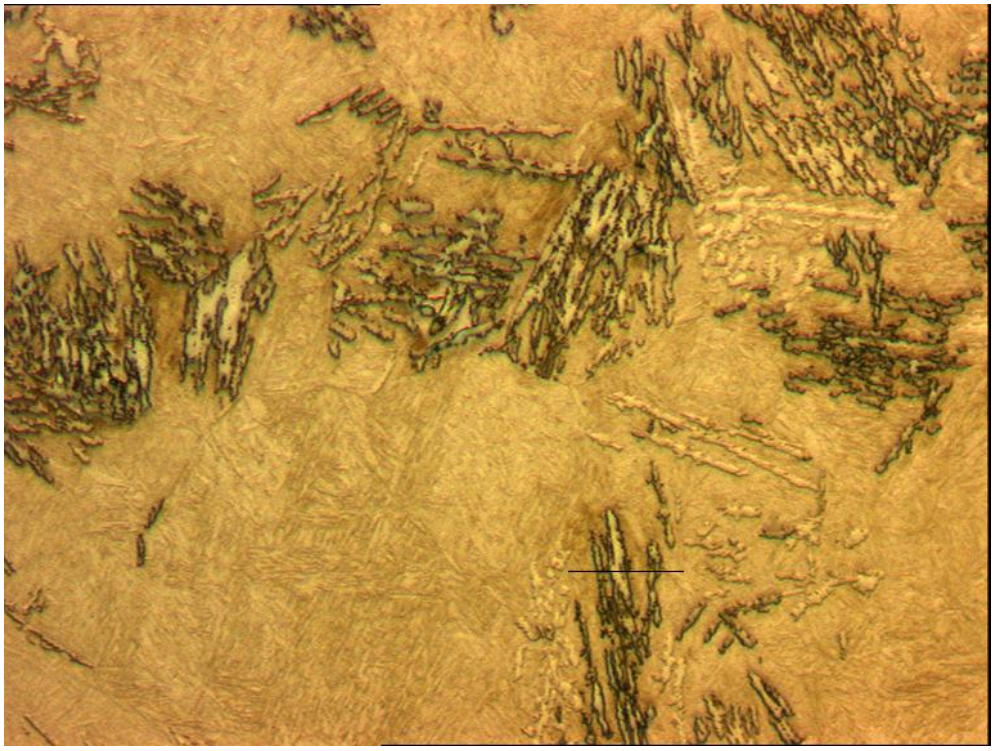

Figure 7- 84 The example to illustrate the classification of the interface area. The black line (the bottom right) across martensitic and bainitic regions was studied.

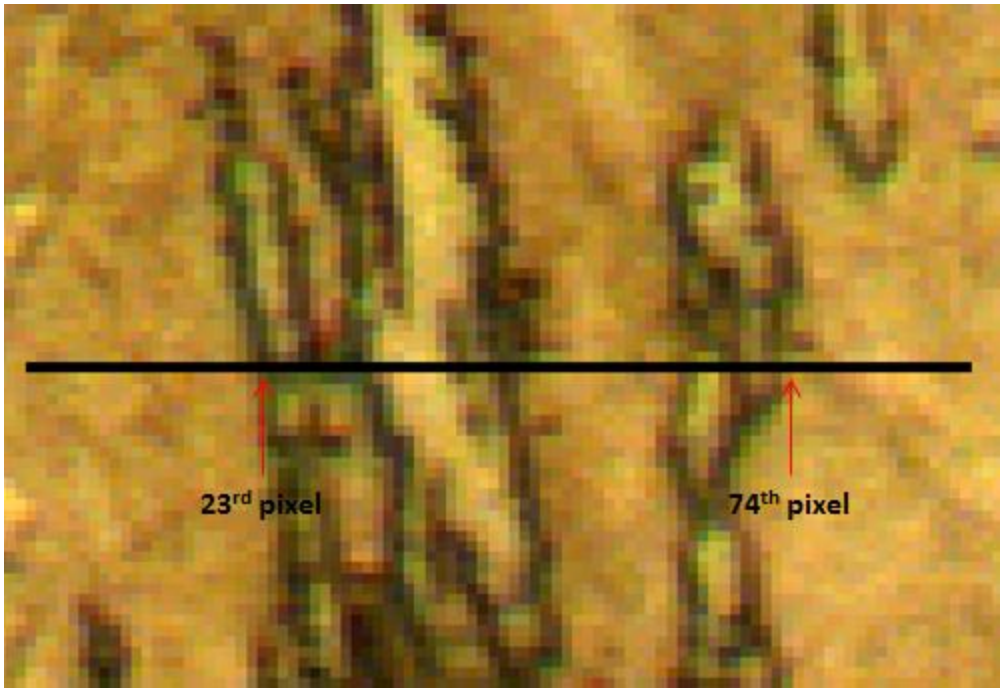

Figure 7- 85 The studied line in Figure 7- 84 with higher magnification

After the training stage, a combination of 3 features was selected automatically by the algorithm as the most distinguishing features of these images. These three features are: Sum Average, Difference Variance and Mean Grey Level. These features can form a 3-dimensional feature space. Each pixel in the original image corresponds to a point in the feature space, which has three coordinates whose value represents the three features. So the pixels with similar features locate closely in the feature space.

The average distances in the feature space between each pixel on the black line in Figure 7- 85 and all the training pixels of each class were computed and plotted in Figure 7- 86.

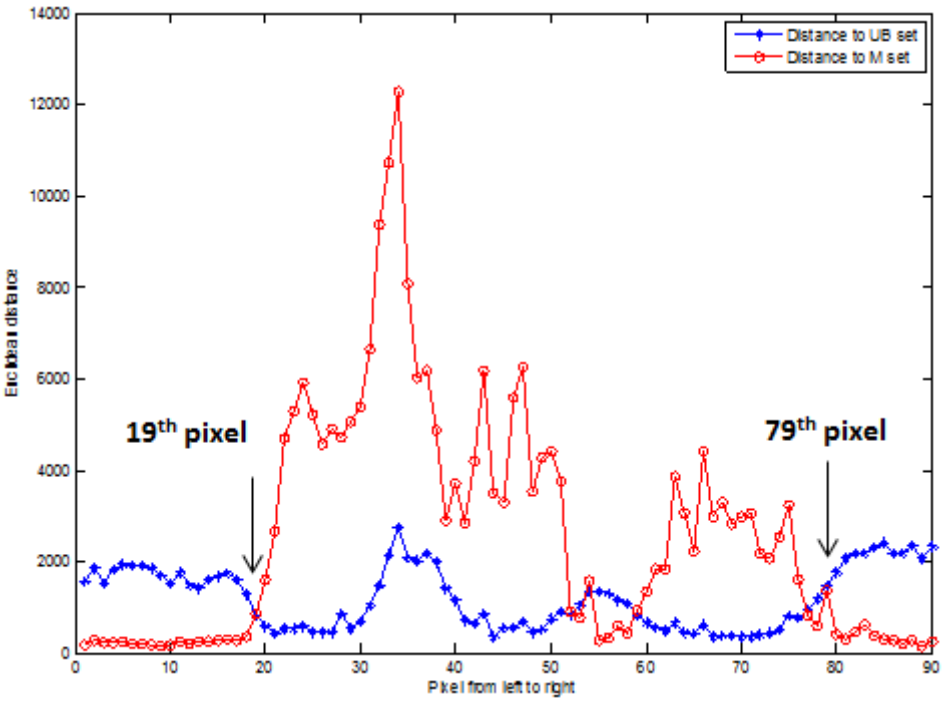

Figure 7- 86 The average distances in the feature space between each pixel on the black line in Figure 7- 85 and all the training pixels of each class

From Figure 7- 86 it can be seen that the distances between every pixel in the left end until the 19th pixel and the martensite training points are greater than those of bainite training points, which means that these 18 pixels are classified as upper bainite.

However, in Figure 7- 85, the interface between martensite and bainite regions appears at the 23rd pixel from the left end. The same situation also occurs at the right end.

The reason should lie in the feature extraction method. The features used to classify every individual pixel are determined not only by the pixel itself but also by a certain number of its neighbouring pixels. In this study, the features of a pixel are extracted from a 9x9 neighbourhood, making them affected by the elements within 4 pixels distance. This makes the automatically classified bainite region about up to 4 pixels larger than the manual result.

2. The central part of some relatively big bainitic ferrite plates are not detected as bainite. The reason lies in the different scales of the training structure and testing structure. The width of the bainitic plate being highlighted by red arrow in Figure 7- 82 is apparently bigger than the training bainitic structures , which makes it fail to be correctly classified in the central.

3. Some upper bainite as white arrow highlighted in Figure 7- 82 is not detected by the automated method. These regions have different morphology (similar shape but less contrast) as the other bainitic regions. They are not detected with automated method because no such microstructures were trained in Figure 7- 81. These two type of upper bainite have both coarse texture but different contrast. The trained upper bainite has much higher contrast than the other type of upper bainite. Grey level plays a most important role in the algorithm as the features used in this study are based on the grey level co-occurrence. It might be difficult to detect the upper bainite which has a different contrast level with the trained upper bainite area. It indicates that a fundamental flaw of most supervised classification methods: if some training sets are excluded from training then there might be failures in the classification.

The excluded untrained bainitic morphology was implemented to the training set and the training and classifying process was re-performed. An image (Figure 7- 87) containing both bainitic structures was selected and trained. Another classified image using the new training sets is shown in Figure 7- 88. It can be seen that both two bainitic morphologies were classified (black arrows marked area), which indicates that in the process of training, all different types of microstructure in each class should be selected for training.

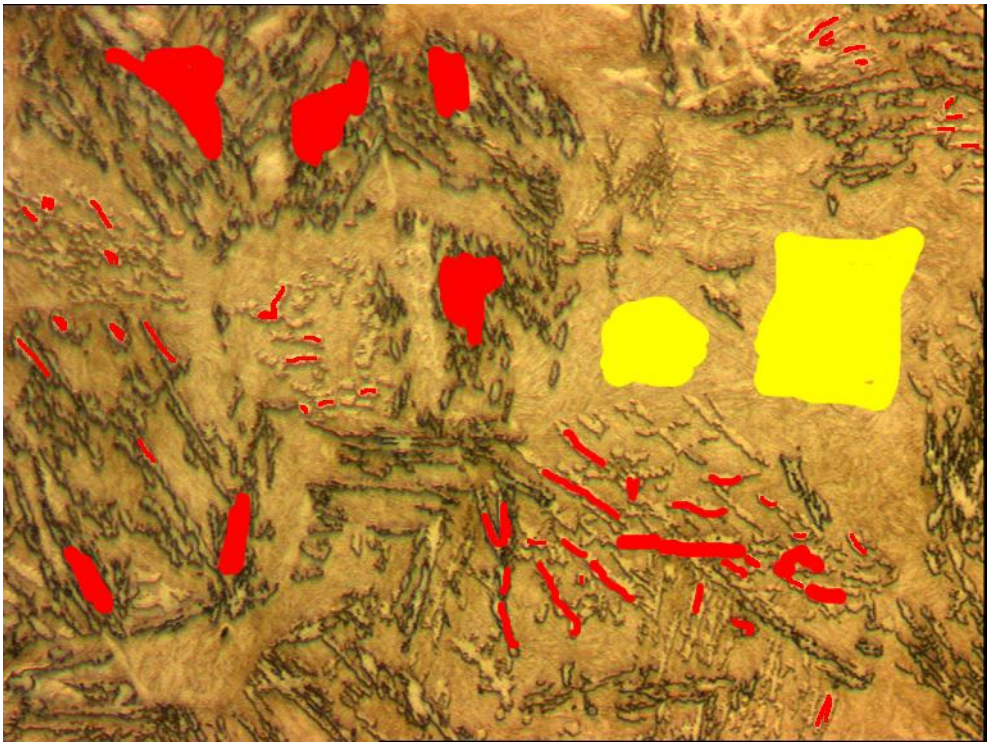

Figure 7- 87 An image taken from sample F used for re-training and re-classification. Two types of bainitic morphology were contained in the image and both were selected for training. Red: training regions for bainite; yellow: training regions for martensite.

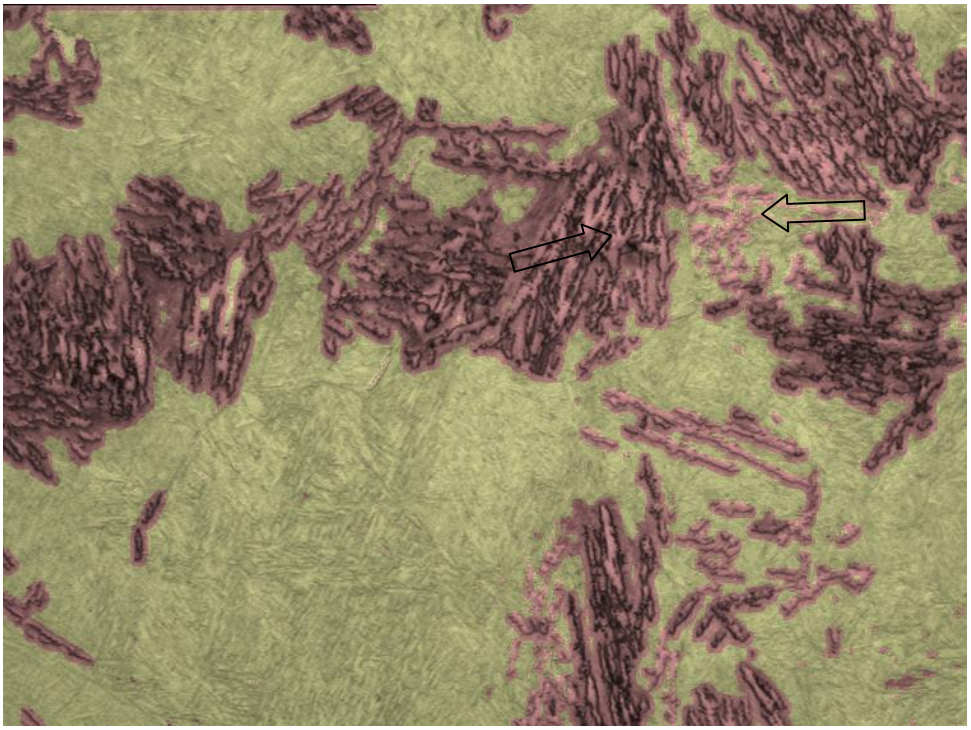

Figure 7- 88 A re-classified result for the example image in Figure 7- 82. The training was done with Figure 7- 87.

7.3.12 Time Required

The computation time for the automated method consists of two parts: feature selection process and image classification process. Feature selection process is with high computational load for its multi-dimension. It takes about 3 hours with an Intel i7 3.5GHz CPU. However, this process is only necessary to operate once for a set of images with similar microstructure. For the image classification, it takes about 15 minutes for each image.

For the manual method, the drawing time for each image may vary from 20 minute to 30 minutes or even more depending on the content and distribution of phases.

7.3.13 Conclusions of the Phase Classification Study

The aim of this study is to develop a generalised classifier of complex steel

microstructures at an appropriate resolution that can properly reveal the optical features of phase constituents of the microstructure. Varying resolutions would be considered in the future rather than this work.

A whole process of phase characterisation approach was developed. The feature library includes a number of second order statistics based on the GLCM. A feature reduction algorithm was used to determine a combination of most distinguishable features. During the testing stage in the supervised classification, a k-NN classifier was used.

Many factors that affect image classification were studied. It was found that the larger training set was selected, the more accurate the classification can get. However, as the number of training set is increasing, its contribution to the classification performance improvement is decreasing.

The location and shape of training sets were also studied. The training set that is taken from the interface area between two phases is not as separable as the training set that is taken from the non-interface area within phases. The shape of training set has no significant influence on the classification due to the neighbourhood operation based feature extraction method.

Two materials were used to testify the phase classification algorithm. One material was heat treated to generate a mixed microstructure including upper bainite, lower bainite, ferrite and martensite. Manual classification by hand drawing was also performed by three postgraduates who did research on steel. The manual results show large fluctuation due to the very similar microstructure of the phases and low resolution of the optical image. Thus precise phase fraction measurement was not available in this study, however, the automatic classification results is within the fluctuation of manual results, and show its capability or potential in replacing manual

work or at least saving a large amount of labour time in the complex phase classification.

The second material was used to generate a series of microstructures containing bainite and martensite. These structures are simpler than the other material which has four phases. But they still contain two phases which have overlapped grey levels and cannot be classified using the conventional intensity histogram based classification methods. Manual classification was also carried out. It is shown good agreement in term of the phase fraction between the automatic classification and manual method. And for samples having same phase constituents and phase morphology, the best feature combination was obtained based on the images from one sample using the feature selection algorithm and applied to another. This could significantly improve this technique's applicability to industry.

7.4 The Effect of Etching Degree on Image Analysis

7.4.1 Microstructure and Optical Observations

Figure 7- 89, Figure 7- 90, Figure 7- 91 and Figure 7- 92 show images from 1 identical location with different degree of etching varying from 5 seconds to 20 seconds. It can be seen that the sample was under-etched after 5 second etching since the contrast of upper bainite is not much and the internal structure of martensite is hardly revealed (see Figure 7- 89). 20 second etching leads to over-etched microstructure (see Figure 7- 92) as the martensite shows similar contrast as the upper bainite does.

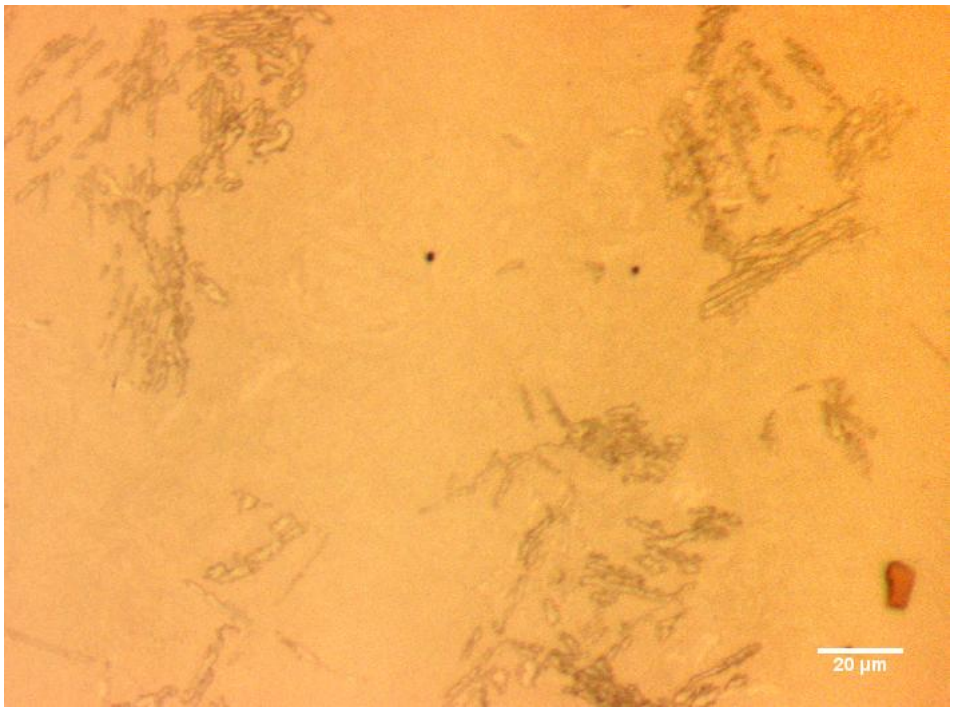

Figure 7- 89 The optical image of location 1 of sample being etched for 5 seconds

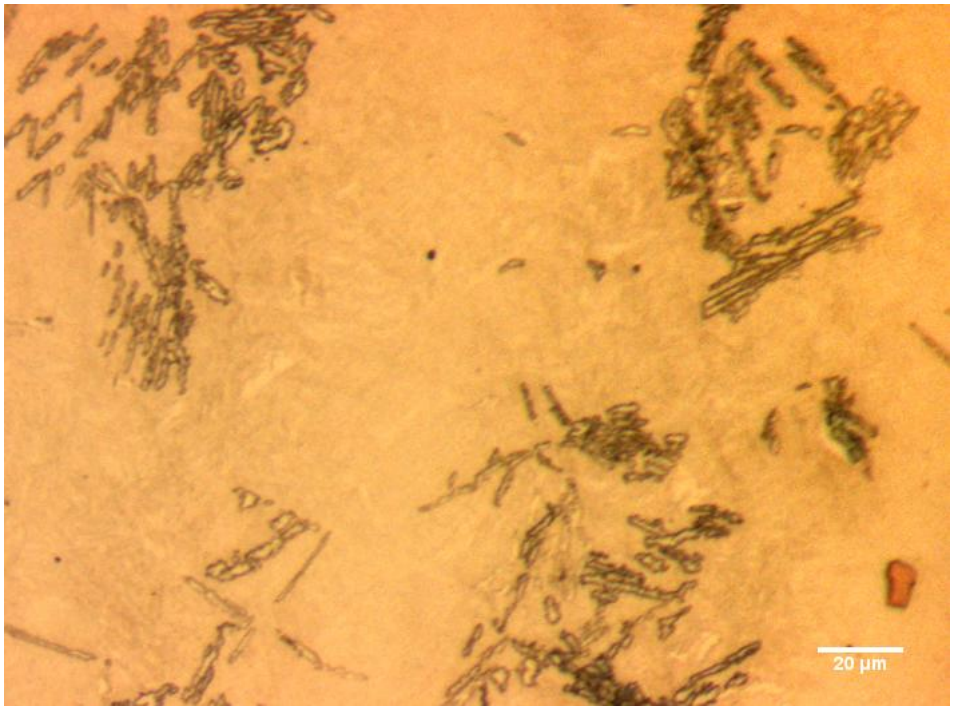

Figure 7- 90 The optical image of location 1 of sample being etched for 10 seconds

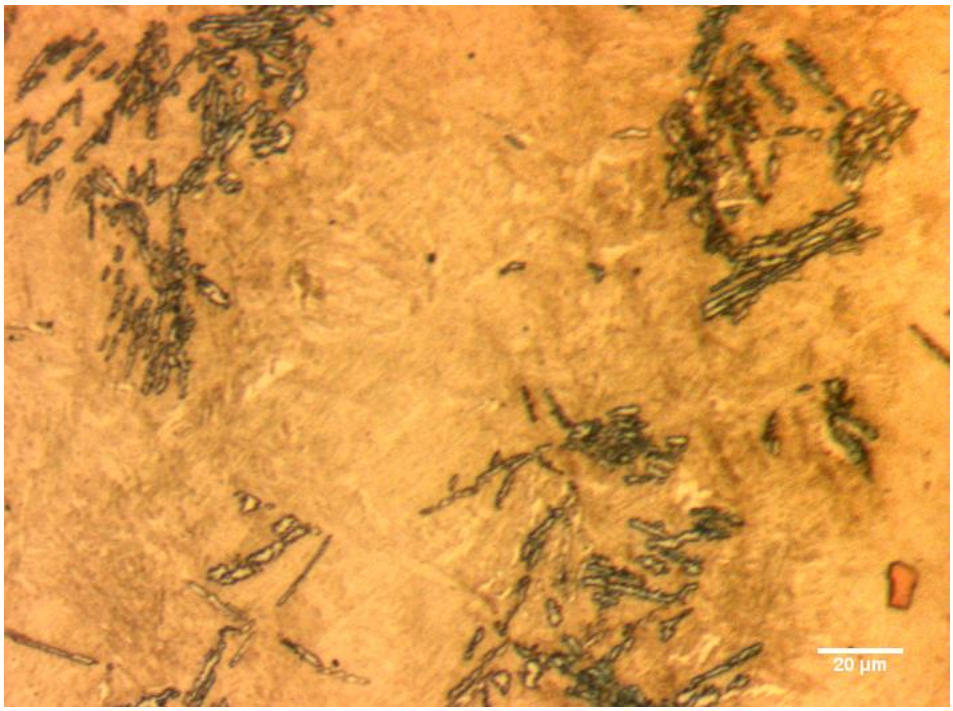

Figure 7- 91 The optical image of location 1 of sample being etched for 15 seconds

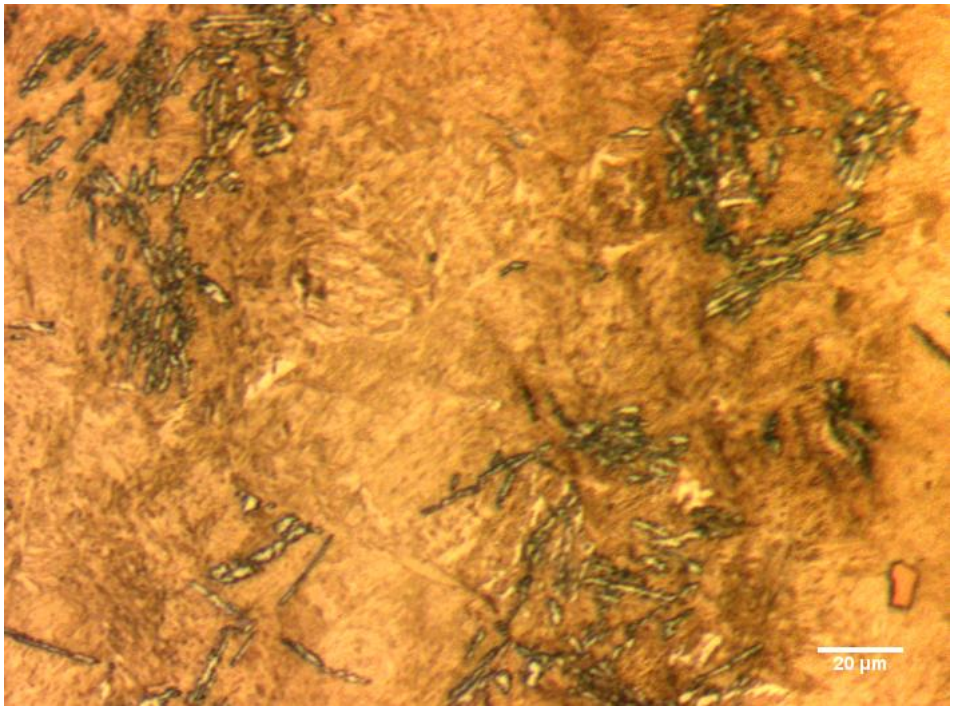

Figure 7- 92 The optical image of location 1 of sample being etched for 20 seconds

The training set was selected separately from another image of each etching degree. The location of the training set on that image is shown in Figure 7- 93. The training set for each etching degree was at same locations.

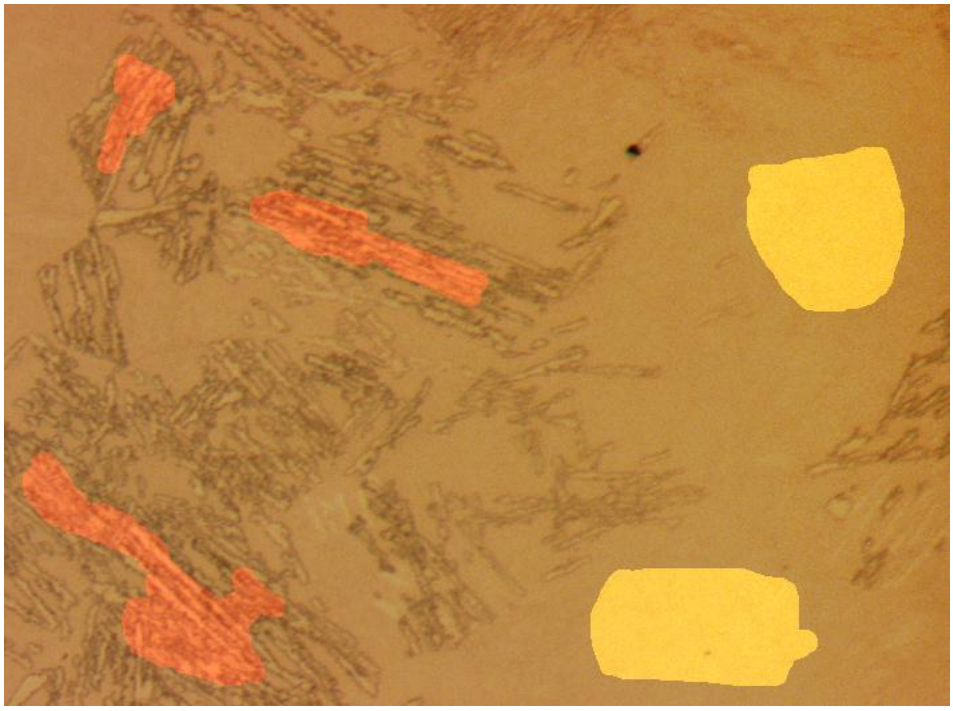

Figure 7- 93 The location of the training set on the image (red region: training area for upper bainite; yellow region: training area for martensite)

7.4.2 Classification Results and Discussions

7.4.2.1 Training and Testing Images Having Same Etching Degree

The classification results of the images of the same location from samples with different etching durations are shown from Figure 7- 94 to Figure 7- 97. Exactly same training regions from same location of the 4 sets were used to classify each image set, in order to eliminate the influence from the variance of training data.

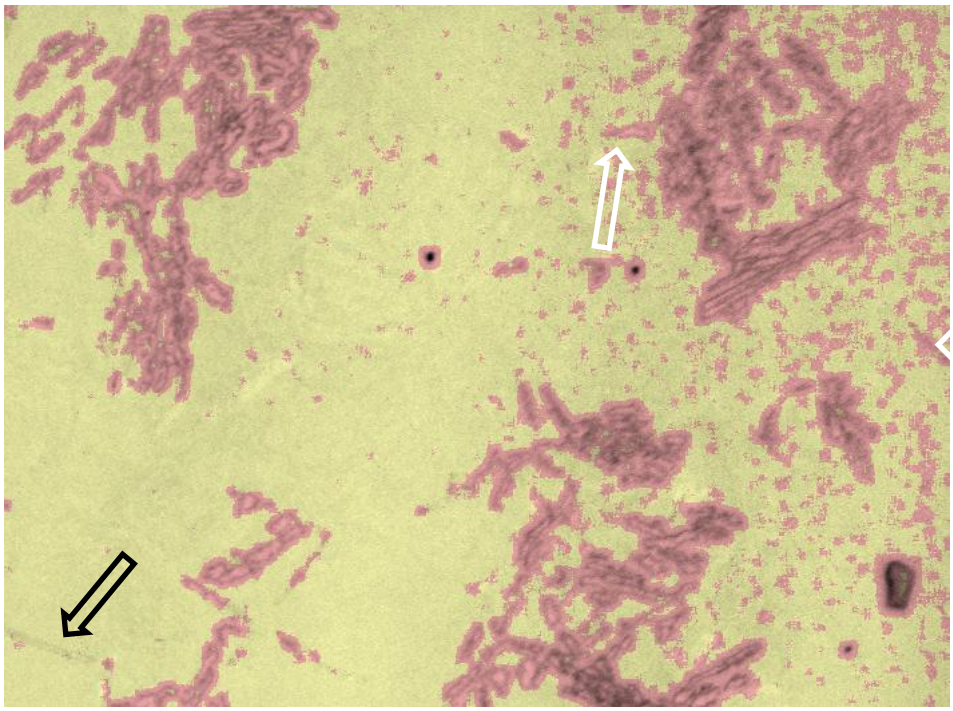

Figure 7- 94 The classification results of an image from the sample being etched for 5 seconds. The regions shown in red represent the detected upper bainite. The matrix is detected martensite. The white arrows are showing the misclassified upper bainite regions. The black arrow shows the unclassified upper bainite region.

It can be seen clearly from Figure 7- 94 a few upper bainite was failed to be classified (highlighted with a black arrow) because of its lack of contrast resulting from the light etching. Meanwhile there are quite a few martensitic regions wrongly being classified as upper bainite.

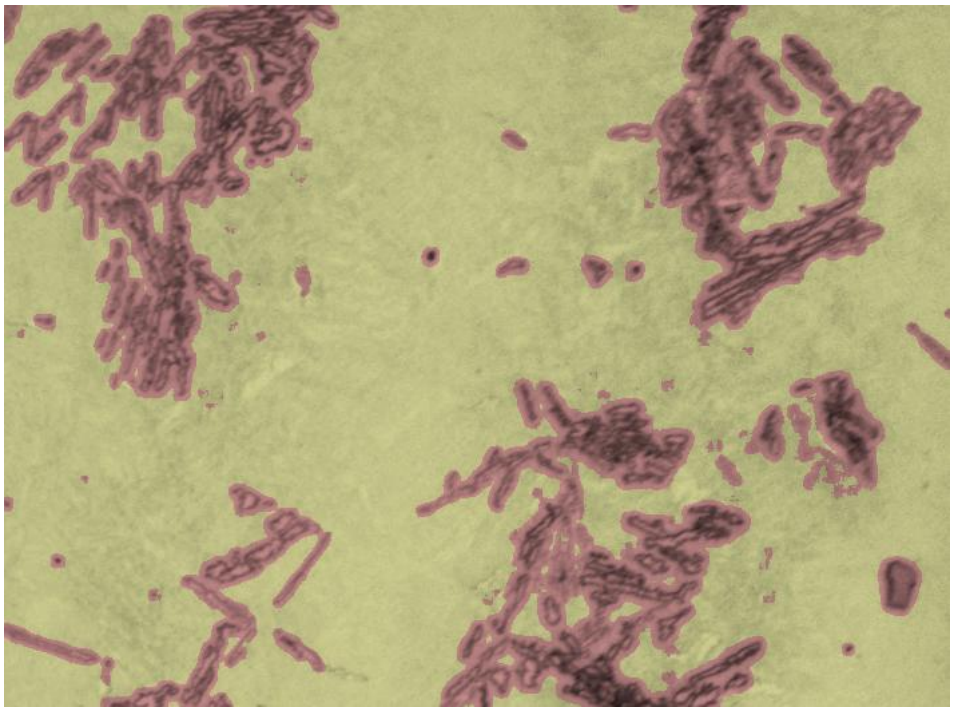

Figure 7- 95 The classification results of an image from the sample being etched for 10 seconds. The regions shown in red represent the detected upper bainite. The matrix is detected martensite.

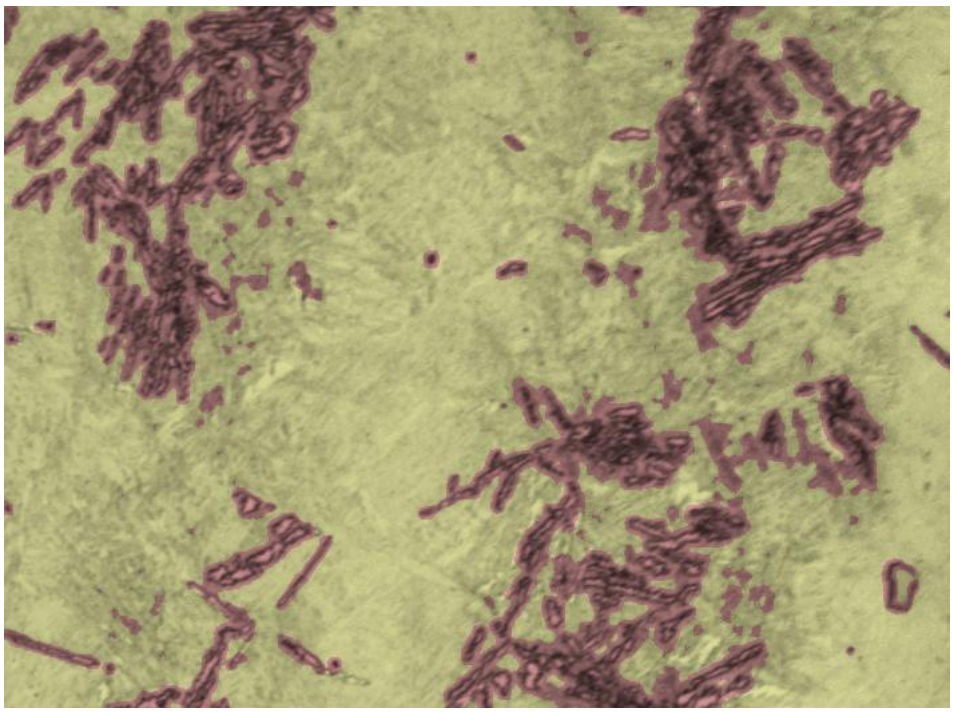

Figure 7- 96 The classification results of an image from the sample being etched for 15 seconds. The regions shown in red represent the detected upper bainite. The matrix is detected martensite.

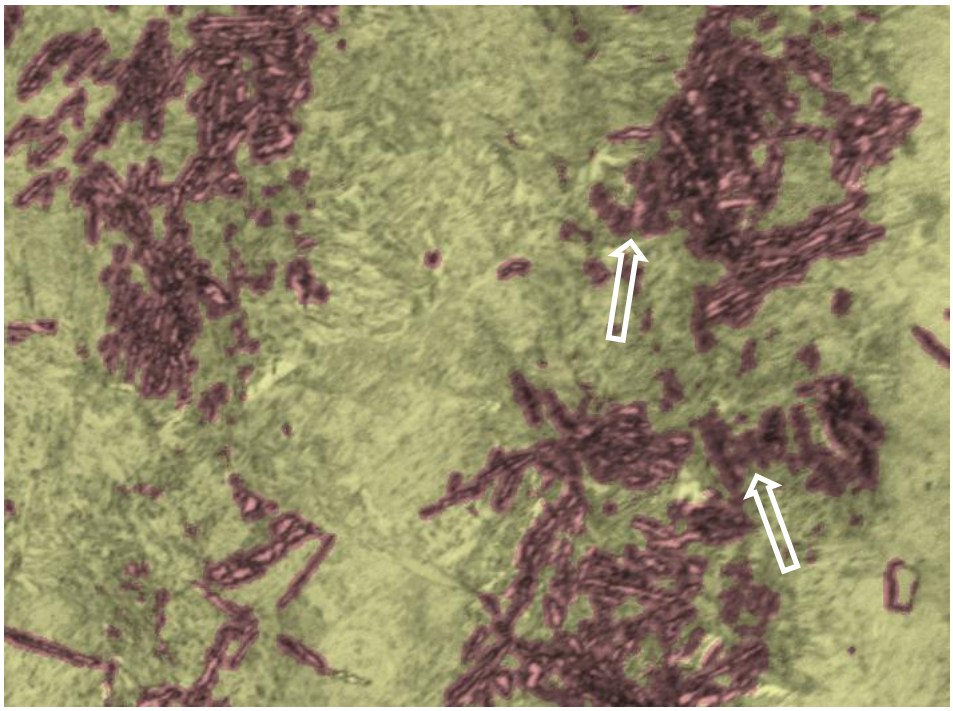

Figure 7- 97 The classification results of an image from the sample being etched for 20 seconds. The regions shown in red represent the detected upper bainite. The matrix is detected martensite. The white arrow marked regions were incorrectly classified as upper bainite.

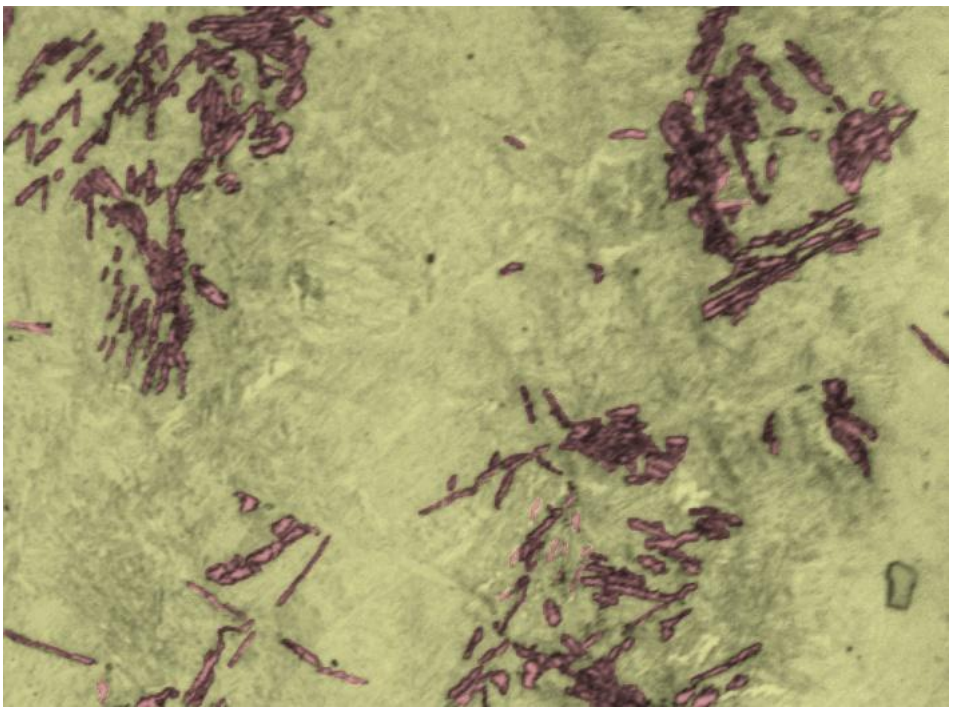

Figure 7- 98 The manual classification results of the image from the same location as Figure 7- 94 to Figure 7- 97. The regions shown in red represent the detected upper bainite. The matrix is detected martensite.

In the image (Figure 7- 97) with the longest etching a few martensitic regions that located closely between upper bainite regions (white arrow marked) were incorrectly classified as upper bainite. Both Figure 7- 95 and Figure 7- 96 have a better classification performance over Figure 7- 94 and Figure 7- 97. But it is hard to compare these two visually. Figure 7- 98 shows the manual classification results of the image from the same location as Figure 7- 94 to Figure 7- 97. Compared to the automatic classifications, the interfaces between martensite and bainite areas on the manual results are more correctly classified. It is well agreed with the results obtained in section 7.3.11.

The separability measures, which were introduced in section 6.4, were computed from the total area of the images with the same etching degree (Table 7- 19).

Table 7- 19 The separability measures computed from the total area of the images with the same etching duration

Separability measures / Etching Duration (sec)	J1	J2	J3
5	3.9	79.2	18.3
10	14.0	6552.4	95.4
15	13.4	1849.1	50.2
20	4.6	453.4	27.0

Table 7- 19 shows the trend that the data from the images with 10 second etching have the highest separability and the images with 15 second etching are the second best. The separability of the images with 5 second etching duration is the lowest. The

separability measures agree well with the classification results shown from Figure 7-94 to Figure 7- 97.

Table 7- 20 The phase fractions computed from the images with the same etching duration (the images of each etching duration were trained separately)

	Phase fraction by auto method after 5s etching (%)	Phase fraction by auto method after 10s etching (%)	Phase fraction by auto method after 15s etching (%)	Phase fraction by auto method after 20s etching (%)	Phase fraction by manual method (%)
Upper bainite	51.4	38.6	37.3	45.3	32.2%
Marte-nsite	48.6	61.4	62.7	54.7	67.8%

The quantitative analysis was applied to all the images and the phase fractions with each etching degree were shown in Table 7- 20. The result obtained from the sample with 15 seconds etching is closest to the manual results (32.2% for upper bainite and 67.8% for martensite). The differences mainly come from the incorrect classification of the interface between bainite and martensite area, which is well agreed with the results shown in section 7.3.11. The results of the sample with 10 seconds etching is close to the 15 second one with a small difference. The data (upper bainite fraction) from both the 5 second etching sample and the 20 second etching one are both much higher than those two samples with 10 seconds and 15 seconds etching.

It can be seen from the above results (images, separability measures and quantitative analysis) that the etching degree does have an influence on the phase classification algorithm. However, the error of the results from the etching degree within a certain range (e.g. 10 seconds to 15 seconds in this study) can be smaller than the error from

the classification algorithm itself. So the algorithm is fairly insensitive to the etching degree.

7.4.2.2 Training and Testing Images Having Different Etching Degree

A tougher task was given to the algorithm, which is to classify all of the images regardless of the difference of etching degree using same training data. An image (Figure 7- 91) from 15 second etching set was used as the training image. Figure 7- 89, Figure 7- 90 and Figure 7- 92 were used here to qualitatively show the results, so that comparison can be made easily between them and those in 7.4.2.1.

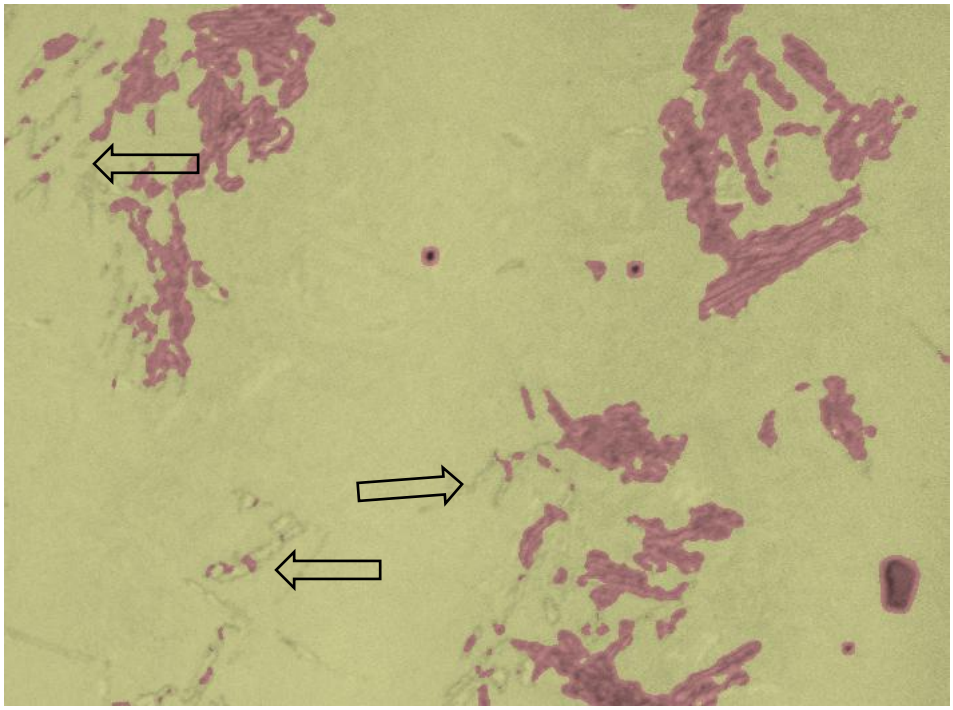

Figure 7- 99 The classification results of Figure 7- 89 using the training data selected in Figure 7- 91 (red colour represents bainite; yellow colour represents martensite)

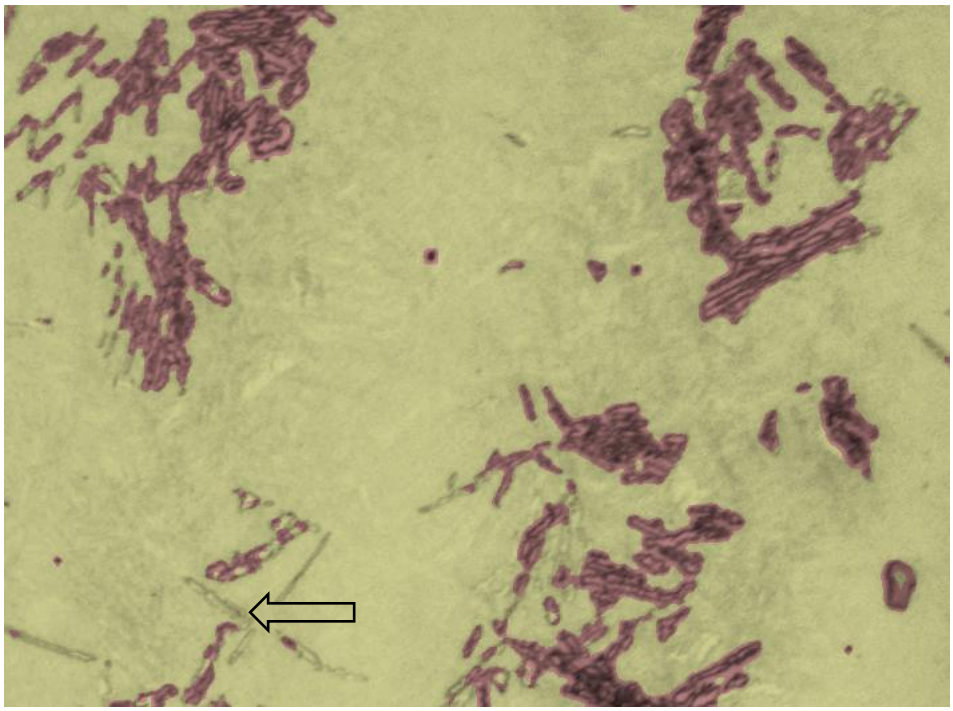

Figure 7- 100 The classification results of Figure 7- 90 using the training data selected in Figure 7- 91. Red colour represents bainite; yellow colour represents martensite. The arrow represents the upper bainite region that is not classified.

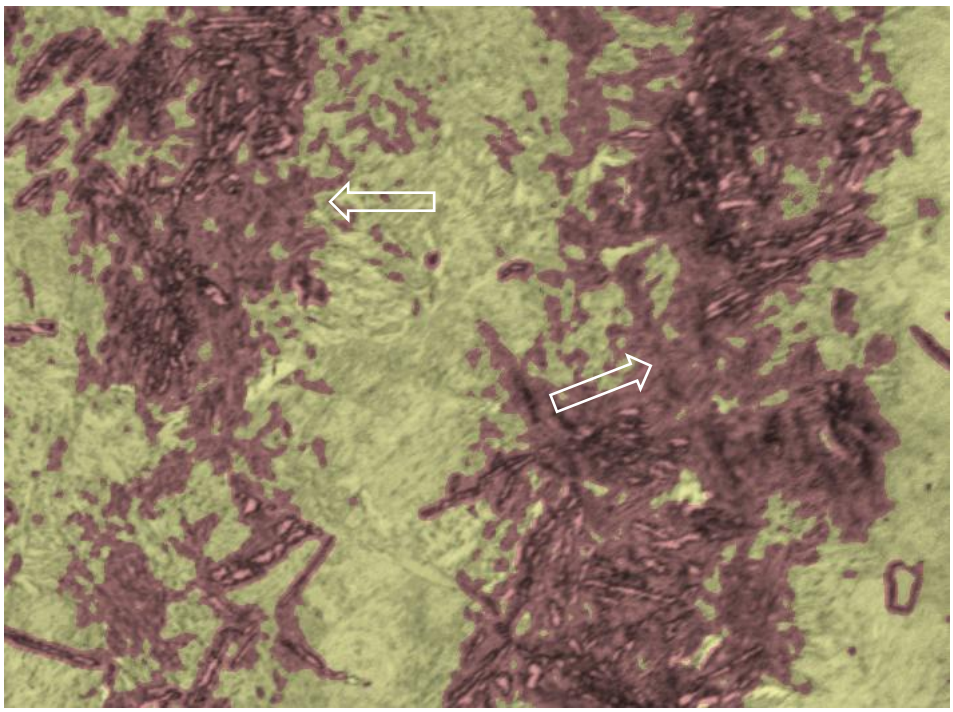

Figure 7- 101 The classification results of Figure 7- 92 using the training data selected in Figure 7- 91. Red colour represents bainite; yellow colour represents martensite. The arrow represents the martensite regions that are not classified.

Table 7- 21 The phase fractions computed from the images with the same etching duration (all of the images were trained by an image from 15 second etching)

	Phase fraction by auto method after 5s etching (%)	Phase fraction by auto method after 10s etching (%)	Phase fraction by auto method after 15s etching (%)	Phase fraction by auto method after 20s etching (%)	Phase fraction by manual method (%)
Upper bainite	20.3	28.4	37.3	52.6	32.2
Marten site	79.7	71.6	62.7	47.4	67.8

Table 7- 21 shows that if all the images are trained by the data from one etching degree (15 seconds), the upper bainite fraction obtained increase as the etching degree increase. It is evident that the classification result from same training set is not as good as that from separate training sets. Both Figure 7- 89 and Figure 7- 90 have a lighter etching degree than the training image (Figure 7- 91), hence they have less contrast and consequently some bainitic regions failed to be detected (Since Figure 7- 89 has the lightest etching degree, a large amount of bainite in it is not detected). Compared with Figure 7- 97, even more martensitic regions were misclassified into bainite in Figure 7- 101. It also showed that the classification accuracy with training data coming from different etching sets is lower than that with training data from the same etching set. The purpose of etching is to give contrast to the various constituents present in the microstructure. Appropriate etching can give highest contrast. Either under-etching or over-etching gives less contrast, which hence causes the inaccuracy of the image analysis.

7.4.3 Conclusion of the Etching Degree Study

The influence of degree of etching to image analysis was studied in this chapter. Through the quantitative analysis of images from the samples with 5 second, 10 second, 15 second and 20 second etching, it has been found that the both under-etching and over-etching decrease the contrast of image, which will probably increase the fraction of high-contrasted phase (bainite in this case). The etching degree does have an influence on the phase classification algorithm. However, the error of the results from the etching degree within a certain range (e.g. 10 seconds to 15 seconds in this study) can be smaller than the error from the classification algorithm itself. So the algorithm is fairly insensitive to the etching degree.

Also, if there are same types of phases in different set of images, and the same phase has the same morphology, it still need to train them set by set as long as the sets have different etching degree.

Chapter 8. Conclusions and Future Work

8.1 Conclusions

As has been discussed, the properties of steels are significantly determined by their microstructures. For pearlitic steels, the pearlite colony size as well as two other factors — pearlite nodule size and interlamellar spacing — primarily determine the strength and toughness. In multiple phase steels containing ferrite, bainite and martensite, the phase fractions of each constituent primarily affect the properties of the materials. Therefore, it is important to measure the pearlite colony size in pearlitic steels and the phase fractions in multiple phase steels, in order to predicate the properties of materials.

Characterisation of steel using image analysis methods based on optical micrographs has been undertaken in this project, including pearlite colony size measurement in a eutectoid steel and phase classification in complex steel. The effect of etching during the sample preparation stage on the image analysis results was also investigated.

Image pre-processing such as shade correction is an important technique to improve image quality and image analysis accuracy. The investigation of shade correction in this study proved that it leads to great improvement for both intensity based image analysis and the texture based image analysis algorithm that this study used.

The characterisation of pearlite colonies has two main processes: feature extraction and region segmentation. The orientation features were obtained by a Fourier Transform method (detecting the positions with the highest intensity in the Fourier domain). This novel combination of features was used with a split-merge algorithm to segment pearlitic colonies. Based on the physical characteristics of pearlite colonies,

two region based features — mean orientation value and mean grey level of regions were used as predicates in the merging process; an edge based feature — KAM - was integrated into cooperation with a region based feature — mean grey level of regions — to do the merging process.

There are several factors affecting the pearlite colony segmentation. The strength of directionality of adjacent colonies (based on the clarity, size, spacing and shape of the lamellae) determines the boundary between these colonies. When the directionality strength of one pearlite colony is higher than that of a neighbouring colony, the estimated size of the colony with higher directionality will expand and the boundary between these two colonies will move towards the neighbouring colony. The predicates used in the merging stage of the split-merge process (the KAM and grey value criteria) mostly determine the number of segmented colonies. Increasing the KAM parameter and/or the grey level parameter required for merging will increase the number of segmented colonies.

The colony characterisation algorithm was found to work well with images consisting of parallel lamellae. However when there was bending or fragmentation of the cementite in colonies, the misorientation of colony boundaries and that of bending lamellae within colonies was overlapped. Thus it is not likely to find appropriate parameters for KAM. Consequently more small colonies as well as more big colonies were generated than the manual segmentation because of over-segmentation and under-segmentation respectively. The accuracy of the algorithm was also affected by granular pearlite and artefacts from sample preparation. So although the algorithm developed in this study was capable of obtaining a roughly similar result of average colony size as the manual method in the tests done here, the manually- and automatically-measured distributions of colony size were different, showing that the quantitative analysis of pearlitic microstructure is not completely successful yet.

To help understand the performance on actual images, a synthetic image with idealised pearlitic structures was also generated for the evaluation of the pearlite colony characterisation algorithm. The synthetic image consists of straight lamellae, curved lamellae and lamellae with different spacings. Three influencing parameters (FFT neighbourhood size, KAM predicate and grey level predicate value) were investigated. It is concluded that optimal values of these parameters all increase the segmentation accuracy. With the best values of parameters found for the synthetic image in this work (FFT neighbourhood size: 65; KAM value: 4; Grey level value: 40), the accuracy of segmentation of the synthetic image reached 93.8% (using one particular measure of quality based on correctly segmented region area). In this case, the colony with curved lamellae was not over-segmented and the neighbouring colonies that had the same orientation but different interlamellar spacing were correctly detected and segmented.

The successful application of the algorithm on a synthetic image proves that the developed algorithm, including the orientation measuring method the features used to determine colonies, and the split-merge segmentation technique are tentatively likely to be appropriate for pearlite colony characterisation in general. However more work is still needed to quantitatively characterise the features of real micrographs that lead to problems (such as the overlapping between the misorientation from colony boundaries and that from the bending lamellae within colonies), and to assess whether the algorithms can be modified to cope with these.

The phase classification of complex steels had three stages: feature selection, training (studying) and testing. A library containing a number of 2-point statistical features was set up to solve general problems. Only a few features might be the most effective in any individual case; the feature determination stage was to choose the best combination of features using a sequential backward selection method. Then a k-NN classifier was used to classify the images.

Many factors that affect image classification were studied. It was found that the larger the training set that was selected, the more accurate the classification became. However, the rate of increase in performance reduced comparatively as the training set continued to increase in size.

The location and shape of training sets were also studied. In the feature space, the distributions of the training set that is taken from the interface area between two phases is more overlapped than that is taken from the non-interface area within phases, making it inappropriate for training purpose. The shape of the training set was found to have no significant influence on the accuracy of classification due to the neighbourhood operation based feature extraction method (the features of a pixel is extracted from a number of its neighbours. So as long as the size of its defined neighbourhood is big enough to cover the textural patterns, the shape of the training region would have little effect).

Two materials were used to test the phase classification algorithm. One material was heat treated to generate a mixed microstructure including upper bainite, lower bainite, ferrite and martensite. Manual classification by hand drawing was also performed by three postgraduates who did research on steel. The manual results show large fluctuation due to the very similar optical appearance of the microstructure of some of the phases. Thus precise phase fraction measurements for comparison were not available in this study; however, the automatic classification results were within the range of manual results. This shows its capability or potential in replacing manual work or at least saving a large amount of labour in complex phase classification.

The second material was used to generate a series of microstructures containing bainite and martensite. These structures are simpler than the other material which has four phases. But they still contain two phases which have overlapped grey levels and

cannot be successfully classified using the conventional intensity histogram based classification methods. Manual classification was also carried out. Good agreement was found in terms of the phase fractions between the automatic classification and manual method. For two samples having same phase constituents and phase morphology, the best features obtained using the feature selection algorithm based on one sample is also appropriate to the other sample. This could significantly save the computation time of this technique and improve its applicability to industry.

Although both of the pearlite colony characterisation and the phase classification have similar processing routines which contain feature extraction and region classification stages, there are some differences between them. Most significantly, the phase classification algorithm is supervised classification as a training stage is possible here due to the known number and morphology of phases. For a supervised classification, to find out proper and distinguishable features within the classes is more important than the classification stage in this study because the classification is simply to label each point to a known class based on the measurements of the features. However, supervised classification is not applicable in the pearlitic colony size measurement since the number of data classes (colonies) is large and each class does not necessarily own unique feature sets (colonies are determined by the differences in orientation (KAM) and grey levels between adjacent regions rather than an absolute value). Therefore apart from determining distinguishable features, it is also important to develop an effective and efficient segmentation method to detect and separate colonies based on the features. The segmentation algorithm developed in this work achieved this goal to a high degree, at least for a synthetic image.

As an important external factor to image analysis, the etching degree of sample was also studied. It turned out that although the etching degree does have an influence on the phase classification algorithm, the error of the results from the etching degree within a certain range (e.g. 10 seconds to 15 seconds in this study) can be smaller than

the error from the classification algorithm itself. So the algorithm is fairly insensitive to the etching degree (within typical industrial limits) and can be widely applied with confidence.

8.2 Future Work

The further implementation of these techniques will require:

a) An algorithm to better distinguish the difference between misorientation of bending or fragmented cementite within a colony, and the misorientation between that colony and an adjacent colony. This is in order to avoid the oversegmentation of colonies due to the misorientation within colonies.
b) An expansion of the feature library for multi-phase steels based on the evaluation of the effectiveness of other texture measures on the studied microstructures.
c) Evaluate the accuracy of the pearlite colony characterisation and phase classification algorithm using low error characterisation methods such as EBSD and manual classification on secondary electron images respectively.
d) To try other segmentation techniques (such as region growing) and classification methods (such as neural networks) to see whether the colony segmentation and phase classification performance can be improved.
e) Investigate the algorithm at various magnifications, to study the relationship between the algorithm itself and the pixel size, although the results in this study were obtained at a high resolution as might be used commonly in industry.
f) Investigate calculating higher-level statistics on the phase classification data, and link this with property prediction. For example, the size of individual phase regions and their spatial distribution (clustered vs randomly-spaced vs ordered) might be important.
g) Exploring the possibilities of transplanting the algorithms to other image

analysis applications. For instance the code can be documented and uploaded to internet, and open for public use to researchers from any field. The algorithm can also be implemented and improved through this.

References

ABBASZADEH, K., SAGHAFIAN, H. & KHEIRANDISH, S. 2012. Effect of Bainite Morphology on Mechanical Properties of the Mixed Bainite-martensite Microstructure in D6AC Steel. *Journal of Materials Science & Technology,* 28**,** 336-342.

ABDELLAH, M. 2012. *High performance Fourier volume rendering on graphics processing units(GPUS).* Master, Cairo University.

AL-JANOBI, A. 2001. Performance evaluation of cross-diagonal texture matrix method of texture analysis. *Pattern Recognition,* 34**,** 171-180.

ANDERSON, J. A., PELLIONISZ, A. & ROSENFELD, E. 1990. *Neurocomputing 2: Directions for Research,* Cambridge Mass, MIT Press.

ANYS, H. & DONG-CHEN, H. 1995. Evaluation of textural and multipolarization radar features for crop classification. *Geoscience and Remote Sensing, IEEE Transactions on,* 33**,** 1170-1181.

ARDIZZONI, S., BARTOLINI, I. & PATELLA, M. Windsurf: region-based image retrieval using wavelets. Database and Expert Systems Applications, 1999. Proceedings. Tenth International Workshop on, 1999 1999. 167-173.

AREBEY, M., HANNAN, M. A., BEGUM, R. A. & BASRI, H. 2012. Solid waste bin level detection using gray level co-occurrence matrix feature extraction approach. *Journal of Environmental Management,* 104**,** 9-18.

ARIVAZHAGAN, S. & GANESAN, L. 2003. Texture classification using wavelet transform. *Pattern Recognition Letters,* 24**,** 1513-1521.

ASM 1977. *Atlas of Isothermal Transformation and Cooling Transformation Diagrams,* Ohio, American Society for Metals.

ASTM 2004. Standard test methods for determining average grain size. Pennsylvania, U.S.A: ASTM International.

AUGUSTEIJN, M. F., CLEMENS, L. E. & SHAW, K. A. 1995. Performance evaluation of texture measures for ground cover identification in satellite images by means of a neural network classifier. *Geoscience and Remote Sensing, IEEE Transactions on,* 33**,** 616-626.

AZENCOTT, R., JIA-PING, W. & YOUNES, L. 1997. Texture classification using windowed Fourier filters. *Pattern Analysis and Machine Intelligence, IEEE Transactions on,* 19**,** 148-153.

BACKES, A. R., CASANOVA, D. & BRUNO, O. M. 2013. Texture analysis and classification: A complex network-based approach. *Information Sciences,* 219**,** 168-180.

BAIN, E. C. 1939. *Functions of The Alloying Elements in Steel,* Cleveland, Ohio, American Society for Metals.

BARBACKI, A. 1995. The role of bainite in shaping mechanical properties of steels. *Journal of Materials Processing Technology,* 53**,** 57-63.

BAZEN, A. M. & GEREZ, S. H. 2002. Systematic Methods for the Computation of the Directional Fields and Singular Points of Fingerprints. *Ieee Transactions on Pattern Analysis and Machine Intelligence,* 24**,** 905-919.

BAZEN, A. M., VERWAAIJEN, G. T. B., GEREZ, S. H., VEELENTURF, L. P. J. & ZWAAG, B. J. V. D. 2000. A Correlation-Based Fingerprint Verification System. *Workshop on Circuits, System and Signal Processing.* Veldhoven, The Netherlands.

BERGMAN, T. L., LAVINE, A. S., INCROPERA, F. P. & DEWITT, D. P. 2011. *Fundamentals of Heat and Mass Transfer,* Danvers, U.S.A, John Wiley & Sons.

BERGONNIER, S., HILD, F. & ROUX, S. 2007. Local anisotropy analysis for non-smooth images. *Pattern Recognition,* 40**,** 544-556.

BEYER, M. H.-. 2000. Special Transformations: Band Ratioing, Principal Components Analysis, Vegetation Indices, and Texture Transformations. Available: http://www.r-s-c-c.org/node/221 [Accessed 02/10/2013].

BHADESHIA, H. K. D. H. 2001. *Bainite in Steels,* London, Institute of Materials.

BHADESHIA, H. K. D. H. & HONEYCOMBE, R. W. K. 2006. *Steels -- Microstructure and Properties*, Butterworth-Heinemann.

BLUM, W., LI, Y. J., CHEN, J., ZENG, X. H. & LU, K. 2006. On the Hall-Petch relation between flow stress and grain size. *International Journal of Materials Research,* 97**,** 1661-1666.

BOHLOOLI, H. & NAKHAEI, M. 2013. Comparison of mechanical properties of bainite/ferrite dual phase 4340 steels with different percents of ferrite. *World of Science Journal,* 3**,** 161-169.

BOLTON, P. J. & CLAYTON, P. 1984. Rolling—sliding wear damage in rail and tyre steels. *Wear,* 93**,** 145-165.

BORGENSTAM, A. & HILLERT, M. 1996. Bainite in the light of rapid continuous cooling information. *Metallurgical and Materials Transactions A,* 27**,** 1501-1512.

BOSWELL, P. G. & CHADWICK, G. A. 1977. Eutectoid decomposition of Zn-Al splat-quenched and bulk specimens. *Acta Metallurgica,* 25**,** 779-792.

BOWEN, P., DRUCE, S. G. & KNOTT, J. F. 1986. Effects of microstructure on cleavage fracture in pressure vessel steel. *Acta Metallurgica,* 34**,** 1121-1131.

BRAMFIT, B. L., STEELE, R. K. & MARTENS, J. H. Rail Steels for the 21st Cnetury. *In:* BRAMFIT, B. L., STEELE, R. K. & MARTENS, J. H., eds. ISS, 1995 Warrendale, PA. IOM3.

BRAMFITT, B. L. 1998. Structure/Property Relationships in Irons and Steels. *In:* DAVIS, J. R. (ed.) *Metals Handbook Desk Edition.* 2 ed.: ASM International.

BRAMFITT, B. L. & MARDER, A. R. 1973a. Effect of cooling rate and alloying on the transformation of austenite. *Metallurgical Transactions,* 4**,** 2291-2301.

BRAMFITT, B. L. & MARDER, A. R. 1973b. A transmission-electron-microscopy study of the substructure of high-purity pearlite. *Metallography,* 6**,** 483-495.

BURIKOVA, K. & ROSENBERG, G. Quantification of Microstructural Parameter Ferritic-Martensite Dual Phase Steel by Image Analysis. Metal 2009, 19-21/05/2009 2009 Hradec nad Moravici. 185-189

CALLISTER, W. D. 2007. *Materials Science and Engineering, An Introduction*, John Wiley & Sons, Inc.

CANNY, J. 1986. A Computational Approach to Edge Detection. *Pattern Analysis and Machine Intelligence, IEEE Transactions on,* PAMI-8**,** 679-698.

CHAUDHURI, B. B. & SARKAR, N. 1995. Texture segmentation using fractal dimension. *Pattern Analysis and Machine Intelligence, IEEE Transactions on,* 17**,** 72-77.

CHEN, J. K. & CHEN, S. F. 2011. *Thermal Conductivity of an in-Situ Metal Matrix Composite - Cast Iron*.

CHEN, L., LU, G. & ZHANG, D. Effects of different Gabor filters parameters on image retrieval by texture. Multimedia Modelling Conference, 2004. Proceedings. 10th International, 5-7 Jan. 2004 2004. 273-278.

CHEN, Y.-K., CHENG, F.-C. & TSAI, P. 2011. A gray-level clustering reduction algorithm with the least

PSNR. *Expert Systems with Applications,* 38**,** 10183-10187.

CHENG, Q. 1999. The gliding box method for multifractal modeling. *Computers & Geosciences,* 25**,** 1073-1079.

CHI-HO, C. & PANG, G. K. H. 2000. Fabric defect detection by Fourier analysis. *Industry Applications, IEEE Transactions on,* 36**,** 1267-1276.

CHMIELA, J., SŁOTA, D. & SZALA, J. 2009. Multiscale description of the inhomogeneity of multiphase materials. *Materials Characterization,* 60**,** 1145-1150.

CINCOTTI, G., GIOVANNA, L. & PAPPALARDO, M. 2001. Frequency decomposition and compounding of ultrasound medical images with wavelet packets. *Medical Imaging, IEEE Transactions on,* 20**,** 764-771.

CLAUSI, D. A. 2002. An analysis of co-occurrence texture statistics as a function of grey level quantization. *Canadian Journal of Remote Sensing,* 28**,** 45-62.

CLAUSI, D. A. & DENG, H. 2005. Design-based texture feature fusion using Gabor filters and co-occurrence probabilities. *IEEE Trans. Image Process,* 14**,** 925-936.

COHEN, J. 1960. A Coefficient of Agreement for Nominal Scales. *Educational and Psychological Measurement,* 20**,** 37-46.

COHEN, M. 1962. Strengthening of Steel. *Transactions of the Metallurgical Society of Aime,* 224**,** 638-&.

COMANICIU, D. & MEER, P. 2002. Mean shift: a robust approach toward feature space analysis. *Pattern Analysis and Machine Intelligence, IEEE Transactions on,* 24**,** 603-619.

CONNERS, R. W. & HARLOW, C. A. 1980. A Theoretical Comparison of Texture Algorithms. *Pattern Analysis and Machine Intelligence, IEEE Transactions on,* PAMI-2**,** 204-222.

COSTE, A. 2012. *Histograms - Image processing report* [Online]. University of Utah. Available: http://www.sci.utah.edu/~acoste/uou/Image/project1/Arthur_COSTE_Project_1_report.html [Accessed 01/10 2013].

CUN LU, X. & YAN QIU, C. Statistical landscape features for texture classification. Pattern Recognition, 2004. ICPR 2004. Proceedings of the 17th International Conference on, 23-26 Aug. 2004 2004. 676-679 Vol.1.

DAVIS, L. S. 1975. A survey of edge detection techniques. *Computer Graphics and Image Processing,* 4**,** 248-270.

DENG, Y. & MANJUNATH, B. S. 2001. Unsupervised segmentation of color-texture regions in images and video. *Pattern Analysis and Machine Intelligence, IEEE Transactions on,* 23**,** 800-810.

DENGIZ, O., SMITH, A. E. & NETTLESHIP, I. 2005. Grain boundary detection in microstructure images using computational intelligence. *Computers in Industry,* 56**,** 854-866.

DERIN, H. & ELLIOTT, H. 1987. Modeling and Segmentation of Noisy and Textured Images Using Gibbs Random Fields. *Pattern Analysis and Machine Intelligence, IEEE Transactions on,* PAMI-9**,** 39-55.

DIETER, G. E. 1988. *Mechanical Metallurgy,* London, McGraw-Hill Book Co.

DU BUF, J. M. H., KARDAN, M. & SPANN, M. 1990. Texture feature performance for image segmentation. *Pattern Recognition,* 23**,** 291-309.

DUNNE, D. P. & WAYMAN, C. M. 1971. CRYSTALLOGRAPHY OF FERROUS MARTENSITES. *Metallurgical Transactions,* 2**,** 2327-&.

DUTTA, S., BARAT, K., DAS, A., DAS, S. K., SHUKLA, A. K. & ROY, H. 2014. Characterization of micrographs and fractographs of Cu-strengthened HSLA steel using image texture analysis.

Measurement, 47**,** 130-144.

DUTTA, S., DAS, A., BARAT, K. & ROY, H. 2012. Automatic characterization of fracture surfaces of AISI 304LN stainless steel using image texture analysis. *Measurement,* 45**,** 1140-1150.

EFFORD, N. 2000. *Digital Image Processing -- A Practical Introduction Using Java,* Essex, Pearson Education Limited.

EL OIRRAK, A., DAOUDI, M. & ABOUTAJDINE, D. 2002. Affine invariant descriptors using Fourier series. *Pattern Recognition Letters,* 23**,** 1109-1118.

EL OIRRAK, A., DAOUDI, M. & ABOUTAJDINE, D. 2003. Affine invariant descriptors for color images using Fourier series. *Pattern Recognition Letters,* 24**,** 1339-1348.

ELWAZRI, A. M., WANJARA, P. & YUE, S. 2005. The effect of microstructural characteristics of pearlite on the mechanical properties of hypereutectoid steel. *Materials Science and Engineering: A,* 404**,** 91-98.

ENGELBRECHT, J. R. & WAHL, F. M. 1988. Polyhedral object recognition using Hough-space features. *Pattern Recognition,* 21**,** 155-167.

ERDOGAN, M. & TEKELI, S. 2002. The effect of martensite volume fraction and particle size on the tensile properties of a surface-carburized AISI 8620 steel with a dual-phase core microstructure. *Materials Characterization,* 49**,** 445-454.

FAN-CHEI, C., YU-KUMG, C. & KUAN-TING, L. An Efficient Gray-level Clustering Algorithm for Image Segmentation. Informatics in Control, Automation and Robotics, 2009. CAR '09. International Asia Conference on, 1-2 Feb. 2009 2009. 259-262.

FEICHTINGER, H. G. & STROHMER, T. 1998. *Gabor Analysis and Algorithms: Theory and Applications,* Boston, U. S. A, Birkhauser.

FESSLER, J. A. & SUTTON, B. P. 2003. Nonuniform fast Fourier transforms using min-max interpolation. *Signal Processing, IEEE Transactions on,* 51**,** 560-574.

FILICE, C. & PRITCHARD, J. E. 1998. Advanced Ausbay Quenching. *Advanced Materials & Processes,* 154**,** 191-196.

FOWLKES, E. B. & MALLOWS, C. L. 1983. A Method for Comparing Two Hierarchical Clusterings. *Journal of the American Statistical Association,* 78**,** 553-569.

FREITAS, V. L. D. A., ALBUQUERQUE, V. H. C. D., SILVA, E. D. M., SILVA, A. A. & TAVARES, J. M. R. S. 2010. Nondestructive characterization of microstructures and determination of elastic properties in plain carbon steel using ultrasonic measurements. *Materials Science and Engineering: A,* 527**,** 4431-4437.

FREIXENET, J., MUÑOZ, X., RABA, D., MARTÍ, J. & CUFÍ, X. 2002. Yet Another Survey on Image Segmentation: Region and Boundary Information Integration. *In:* HEYDEN, A., SPARR, G., NIELSEN, M. & JOHANSEN, P. (eds.) *Computer Vision — ECCV 2002.* Springer Berlin Heidelberg.

FROM, A. & SANDSTRÖM, R. 1998. Assessment of Banding in Steels by Using Advanced Image Analysis. *Materials Characterization,* 41**,** 11-26.

FU, W., XIONG, Y., ZHAO, J., LI, Y., FURUHARA, T. & MAKI, T. 2005. Microstructural Evolution of Pearlite in Eutectoid Fe-C Alloys during Severe Cold Rolling. *J. Mater. Sci. Technol.,* 21**,** 25-27.

FUCHS, A. 2005. *Applicaiton of Microstructural Texture Parameters to Diffusional and Didplacive Transformation Products.* Doctor of Philosophy, The University of Birmingham.

GARBARZ, B. & PICKERING, F. B. 1988. Effect of pearlite morphology on impact toughness of eutectoid steel containing vanadium. *Materials Science and Technology,* 4**,** 328-334.

GARNHAM, J. E. & DAVIS, C. L. 2011. Very early stage rolling contact fatigue crack growth in pearlitic rail steels. *Wear,* 271**,** 100-112.

GIBSON, D. & GAYDECKI, P. A. 1995. Definition and application of a Fourier domain texture measure: Applications to histological image segmentation. *Computers in Biology and Medicine,* 25**,** 551-557.

GLADMAN, T., MCIVOR, I. D. & PICKERIN.FB 1972. SOME ASPECTS OF STRUCTURE-PROPERTY RELATIONSHIPS IN HIGH-CARBON FERRITE-PEARLITE STEELS. *Journal of the Iron and Steel Institute,* 210**,** 916-930.

GLASBEY, C. A. & HORGAN, G. W. 2000. Encyclopaedia of Environmetrics: Image Analysis. [Accessed 2001].

GODAVARTHY, S. S., ROBINSON JR, R. L. & GASEM, K. A. M. 2008. Improved structure–property relationship models for prediction of critical properties. *Fluid Phase Equilibria,* 264**,** 122-136.

GONZALEZ, R. C. & WOODS, R. E. 2007. *Digital Image Processing,* Beijing, Publishing House of Electronics Industry.

GRANGE, R., HRIBAL, C. & PORTER, L. 1977. Hardness of tempered martensite in carbon and low-alloy steels. *Metallurgical and Materials Transactions A,* 8**,** 1775-1785.

GREGORY, S. W. & GALLAGHER, T. J. 2002. Spectral analysis of candidates' nonverbal vocal communication: Predicting US presidential election outcomes. *Social Psychology Quarterly,* 65**,** 298-308.

GU, J., ZHOU, J. & ZHANG, D. 2004. A combination model for orientation field of fingerprints. *Pattern Recognition,* 37**,** 543-553.

GUO, Z. & ZHANG, D. 2010. A Completed Modeling of Local Binary Pattern Operator for Texture Classification. *Image Processing, IEEE Transactions on,* 19**,** 1657-1663.

GUO, Z., ZHANG, L. & ZHANG, D. 2010. Rotation invariant texture classification using LBP variance (LBPV) with global matching. *Pattern Recognition,* 43**,** 706-719.

GUY, A. G. & HREN, J. J. 1974. *Elements of physical metallurgy,* Reading, Massachusetts, U. S. A, Addison-Wesley

HALL, E. O. 1951. THE DEFORMATION AND AGEING OF MILD STEEL .3. DISCUSSION OF RESULTS. *Proceedings of the Physical Society of London Section B,* 64**,** 747-753.

HARALICK, R. M. 1979. Statistical and structural approaches to texture. *Proceedings of the IEEE,* 67**,** 786-804.

HARALICK, R. M., SHANMUGA.K & DINSTEIN, I. 1973. TEXTURAL FEATURES FOR IMAGE CLASSIFICATION. *Ieee Transactions on Systems Man and Cybernetics,* SMC3**,** 610-621.

HECHT, E. 2002. *Optics*, Addison Wesley.

HERIAN, J. & ANIOTEK, K. 2008. The structure and properties of steel with different pearlite morphology and its resistance to abrasive wear. *Archives of Materials Science and Engineering,* 31**,** 83-86.

HOROWITZ, S. L. & PAVLIDIS, T. 1976. Picture segmentation by a tree traversal algorithm. *Journal of the Association for Computing Machinery,* 23**,** 368-388.

HUANG, Q. & DOM, B. Quantitative methods of evaluating image segmentation. Image Processing, 1995. Proceedings., International Conference on, 23-26 Oct 1995 1995. 53-56 vol.3.

HUBER, T. P. & CASLER, K. E. 1990. Initial analysis of Landsat TM data for elk habitat mapping. *International Journal of Remote Sensing,* 11**,** 907-912.

HULL, F. C. & MEHL, R. F. 1942. The structure of pearlite. *Trans. ASM,* 30**,** 381-424.

HYZAK, J. M. & BERNSTEIN, I. M. 1976. The role of microstructure on the strength and toughness of fully pearlitic steels. *Metallurgical Transactions A,* 7**,** 1217-1224.

IDRISSA, M. & ACHEROY, M. 2002. Texture classification using Gabor filters. *Pattern Recognition Letters,* 23**,** 1095-1102.

ILONEN, J., KAMARAINEN, J. K. & KALVIAINEN, H. 2005. Efficient computation of Gabor features. Lappeenranta, Finland: Lappeenranta University of Technology.

IRVINE, K. J., PICKERING, F. B., HESELWOOD, W. C. & ATKINS, M. 1957. The physical metallurgy of low-C low-alloy steels containing boron. *Journal of the Iron and Steel Institute***,** 54-57.

JACQUES, P., DELANNAY, F. & LADRIÈRE, J. 2001. On the influence of interactions between phases on the mechanical stability of retained austenite in transformation-induced plasticity multiphase steels. *Metallurgical and Materials Transactions A,* 32**,** 2759-2768.

JAIN, A. K., DUIN, R. P. W. & MAO, J. C. 2000. Statistical pattern recognition: A review. *Ieee Transactions on Pattern Analysis and Machine Intelligence,* 22**,** 4-37.

JAIN, A. K. & FARROKHNIA, F. Unsupervised texture segmentation using Gabor filters. Systems, Man and Cybernetics, 1990. Conference Proceedings., IEEE International Conference on, 4-7 Nov 1990 1990. 14-19.

JAIN, A. K., RATHA, N. K. & LAKSHMANAN, S. 1997. Object detection using gabor filters. *Pattern Recognition,* 30**,** 295-309.

JINGYI, S., SERGIO, T. & ERIK VAN DER, G. 2011. Analysis of banded morphology in multiphase steels based on a discrete dislocation–transformation model. *Modelling and Simulation in Materials Science and Engineering,* 19**,** 074006.

JONKMAN, J. E. N., SWOGER, J., KRESS, H., ROHRBACH, A. & STELZER, E. H. K. 2003. Resolution in optical microscopy. *In:* GERARD MARRIOTT, I. P. (ed.) *Methods in Enzymology.* Academic Press.

KANOPOULOS, N., VASANTHAVADA, N. & BAKER, R. L. 1988. Design of an image edge detection filter using the Sobel operator. *Solid-State Circuits, IEEE Journal of,* 23**,** 358-367.

KAPLAN, L. M. & KUO, C. C. J. 1995. Texture roughness analysis and synthesis via extended self-similar (ESS) model. *Pattern Analysis and Machine Intelligence, IEEE Transactions on,* 17**,** 1043-1056.

KAUR, M., KUMAR, D., WALIA, E. & SANDHU, M. 2011. Periodic noise removal in strain and natural images using 2-D Fast Fourier Transform. *International Journal of Computer & Communication Technology,* 2**,** 1-5.

KAVITHA, A. R. & CHELLAMUTHU, C. 2010. Implementation of gray-level clustering algorithm for image segmentation. *Procedia Computer Science,* 2**,** 314-320.

KELLEY, P. M. & NUTTING, J. 1961. The Morphology of Martensite. *Journal Iron and Steel Institute,* 197**,** 199.

KIM, C. 1988. *Processing Microstructure and Properties of HSLA Steels,* Warrendale, PA, TMS.

KIM, D., LIU, J. J. & HAN, C. 2011. Determination of steel quality based on discriminating textural feature selection. *Chemical Engineering Science,* 66**,** 6264-6271.

KIMBALL, S. & MATTIS, P. 1996. GNU Image Manipulation Program. 2.8.8 ed.: The GIMP Development Team.

KLEBER, X., HUG-AMALRIC, A. & MERLIN, J. 2008. Evaluation of the Proportion of Phases and Mechanical Strength of Two-Phase Steels Using Barkhausen Noise Measurements: Application to Commercial Dual-Phase Steel. *Metallurgical and Materials Transactions A,* 39**,** 1308-1318.

KOMENDA, J. 2001. Automatic recognition of complex microstructures using the Image Classifier. *Materials Characterization,* 46**,** 87-92.

KOTRECHKO, S. A., MESHKOV, Y. Y. & TELEVICH, R. V. 2006. Effect of the size of martensite laths and carbide particles on the “brittle” strength of low-carbon martensitic steels. *Metal Science and Heat Treatment,* 48**,** 405-411.

KRAUSS, G. 2005. *Steels--Processing, Structure, and Performance*, ASM International.

KREBS, B., HAZOTTE, A., GERMAIN, L. & GOUNÉ, M. 2011. *QUANTITATIVE ANALYSIS OF BANDED STRUCTURES IN DUAL-PHASE STEELS*.

KRISHNAMACHARI, S. & CHELLAPPA, R. 1997. Multiresolution Gauss-Markov random field models for texture segmentation. *Image Processing, IEEE Transactions on,* 6**,** 251-267.

KRUIZINGA, P. & PETKOV, N. 1999. Nonlinear operator for oriented texture. *Image Processing, IEEE Transactions on,* 8**,** 1395-1407.

KUMAR, T. & SAHOO, G. 2010. A Noval Method Of Edge Detection Using Cellular Automata. *International Journal of Computer Applications,* 9**,** 38-44.

KUMARV, M. & SUMITHRA, M. G. 2012. Performance comparisonof different medical image segmentation algorithms for normal and abnormal brain MRI. *International Journal of Lastest Research in Science and Technology,* 1**,** 369-372.

KUTSOV, A., TARAN, Y., UZLOV, K., KRIMMEL, A. & EVSYUKOV, M. 1999. Formation of bainite in ductile iron. *Materials Science and Engineering: A,* 273**–**275**,** 480-484.

KUZIAK, R., KAWALLA, R. & WAENGLER, S. 2008. Advanced high strength steels for automotive industry: a review. *Archives of Civil and Mechanical Engineering,* 8**,** 103-117.

LAM, W. K. & LI, C. K. 1997. Rotated texture classification by improved iterative morphological decomposition. *Vision, Image and Signal Processing, IEE Proceedings -,* 144**,** 171-179.

LAPRADE, R. H. 1988. Split-and-merge segmentation of aerial photographs. *Computer Vision, Graphics, and Image Processing,* 44**,** 77-86.

LATALA, Z. & WOJNAR, L. 2001. Computer-aided versus manual grain size assessment in a single phase material. *Materials Characterization,* 46**,** 227-233.

LEE, C. Y. & HAN, J.-H. Selective noise removal method in low frequency region for fiber bundle-based endoscopy. Systems, Man, and Cybernetics (SMC), 2012 IEEE International Conference on, 14-17 Oct. 2012 2012. 1109-1111.

LEE, H.-C., JIN, Y.-G., LEE, Y.-H., SON, I.-H., LEE, D.-L. & IM, Y.-T. 2010. Process design of high-strength bolt of fully pearlitic high-carbon steel. *Journal of Materials Processing Technology,* 210**,** 1870-1875.

LEE, S.-J., PARK, Y.-M. & LEE, Y.-K. 2009. Reverse transformation mechanism of martensite to austenite in a metastable austenitic alloy. *Materials Science and Engineering: A,* 515**,** 32-37.

LEMKIN, P. 1979. An approach to region splitting. *Computer Graphics and Image Processing,* 10**,** 281-288.

LESUER, D. R., SYN, C. K., SHERBY, O. D. & KIM, D. K. Processing and Mechanical Behavior of Hypereutectoid Steel Wires. *In:* PARIS, H. G. & KIM, D. K., eds. Metallurgy, Processing and Applications of Metal Wires, 1996 Warrendale, PA, US. TMS, 109-121.

LI, S. & SHAWE-TAYLOR, J. 2005. Comparison and fusion of multiresolution features for texture classification. *Pattern Recognition Letters,* 26**,** 633-638.

LI, X.-F., LANGENBERG, P., MUNSTERMANN, S. & BLECK, W. 2005. Recent developments of modern rail steels. *Kang T'ieh/Iron and Steel (Peking),* 40**,** 775-781.

LIFENG, L. & SCLAROFF, S. Deformable shape detection and description via model-based region grouping. Computer Vision and Pattern Recognition, 1999. IEEE Computer Society Conference on., 1999 1999. 27 Vol. 2.

LIU, L. & SCLAROFF, S. 2004. Deformable model-guided region split and merge of image regions. *Image and Vision Computing,* 22**,** 343-354.

LIU, R. Y. & SINGH, K. 1992. Ordering Directional Data: Concepts of Data Depth on Circles and Spheres. *The Annals of Statistics,* 20**,** 1468-1484.

MAN, O., PANTĚLEJEV, L. & PEŠINA, Z. 2009. EBSD Analysis of Phase Compositions of TRIP Steel on Various Strain Levels *Materials Engineering,* 16**,** 15-21.

MANIVANNAN, K., AGGARWAL, P., DEVABHAKTUNI, V., KUMAR, A., NIMS, D. & BHATTACHARYA, P. 2012. Particulate matter characterization by gray level co-occurrence matrix based support vector machines. *Journal of Hazardous Materials,* 223–224**,** 94-103.

MANJUNATH, B. S. & CHELLAPPA, R. 1991. Unsupervised texture segmentation using Markov random field models. *Pattern Analysis and Machine Intelligence, IEEE Transactions on,* 13**,** 478-482.

MANJUNATH, B. S. & MA, W. Y. 1996. Texture features for browsing and retrieval of image data. *Pattern Analysis and Machine Intelligence, IEEE Transactions on,* 18**,** 837-842.

MARCEAU, D. J., HOWARTH, P. J., DUBOIS, J. M. & GRATTON, D. J. 1990. Evaluation Of The Grey-level Co-occurrence Matrix Method For Land-cover Classification Using Spot Imagery. *Geoscience and Remote Sensing, IEEE Transactions on,* 28**,** 513-519.

MARTINST, A. C. G. & RANGAYYAN, R. M. 1997. Complex cepstral filtering of images and echo removal in the radon domain. *Pattern Recognition,* 30**,** 1931-1938.

MARUTA, H., NAKAMURA, A., YAMAMICHI, T. & KUROKAWA, F. Image based smoke detection with local Hurst exponent. Image Processing (ICIP), 2010 17th IEEE International Conference on, 26-29 Sept. 2010 2010. 4653-4656.

MATERKA, A. & STRZELECKI, M. 1998. Texture analysis methods - a review. Brussels: Technical University of Lodz.

MATLAB 2012. *Matlab help documentation version 7.14 (R2012a),* Natick, Massachusetts, The MathWorks Inc.

MEHL, R. F. 1939. *Hardenability of alloy steels,* Cleveland, OH, ASM.

MEHL, R. F. & HAGEL, W. C. 1956. The austenite: Pearlite reaction. *Progress in Metal Physics,* 6**,** 74-134.

MEILĂ, M. 2003. Comparing Clusterings by the Variation of Information. *In:* SCHÖLKOPF, B. & WARMUTH, M. (eds.) *Learning Theory and Kernel Machines.* Springer Berlin Heidelberg.

MEYER, F. G. & COIFMAN, R. R. 1997. Brushlets: A tool for directional image analysis and image compression. *Applied and Computational Harmonic Analysis,* 4**,** 147-187.

MOORTHY, V., VAIDYANATHAN, S., JAYAKUMAR, T. & RAJ, B. 1997. Microstructural characterization of quenched and tempered 0.2% carbon steel using magnetic Barkhausen noise analysis. *Journal of Magnetism and Magnetic Materials,* 171**,** 179-189.

MURPHY, D. B. 2001. *Fundamentals of Light Microscopy and Electronic Imaging,* New York, John Wiley & Sons, Inc.

NADERNEJAD, E., SHARIFZADEH, S. & HASSANPOUR, H. 2008. Edge Detection Techniques: Evaluations and Comparisons. *Applied Mathematical Science,* 2**,** 1507-1520.

NAKKALIL, R., HORNADAY JR, J. R. & NABIL BASSIM, M. 1991. Characterization of the compression properties of rail steels at high temperatures and strain rates. *Materials Science and*

Engineering: A, 141**,** 247-260.

NANYAM, Y., CHOUDHARY, R., GUPTA, L. & PALIWAL, J. 2012. A decision-fusion strategy for fruit quality inspection using hyperspectral imaging. *Biosystems Engineering,* 111**,** 118-125.

NG, I., TAN, T. & KITTLER, J. On local linear transform and Gabor filter representation of texture. Pattern Recognition, 1992. Vol.III. Conference C: Image, Speech and Signal Analysis, Proceedings., 11th IAPR International Conference on, 30 Aug-3 Sep 1992 1992. 627-631.

NIEH, T. G. & WADSWORTH, J. 1991. Hall-petch relation in nanocrystalline solids. *Scripta Metallurgica Et Materialia,* 25**,** 955-958.

NIKOLAIDIS, N. & PITAS, I. 1998. Nonlinear processing and analysis of angular signals. *Signal Processing, IEEE Transactions on,* 46**,** 3181-3194.

O'FLAHERTY, S. & EDWARDS, J. 2011. Digital Imaging: A Powerful Quality Tool for Materials Analysis. *Advanced Materials & Processes,* 169**,** 19-22.

OHANIAN, P. P. & DUBES, R. C. 1992. Performance evaluation for four classes of textural features. *Pattern Recognition,* 25**,** 819-833.

OROWAN, E., KOEHLER, J. S., SEITZ, F., READ, W. T. & SHOCKLEY, W. 1954. *Dislocations in Metals,* New York, The American Institute of Mining and Metallurgical Engineers, INC.

OSICKA, T. 2008. *Wavelet-based Pulmonary Nodules Features Characterization on Computed Tomography (CT) Scans.* Doctor of Philosophy, The Catholic University of America.

PAN, J., TONG, J. & TIAN, M. 1998. *Fundamentals of Materials Science,* Beijing, Tsinghua University Press.

PARASHER, M., SHARMA, S., SHARMA, A. K. & GUPTA, J. P. 2011. Anatomy on Pattern Recognition. *Indian Journal of Computer Science and Engineering,* 2**,** 371-378.

PARIKH, J. 1977. A comparative study of cloud classification techniques. *Remote Sensing of Environment,* 6**,** 67-81.

PARK, Y. J. & BERNSTEIN, I. M. 1978. Mechanisms of Cleavage Fracture in Fully Pearlitic 1080 Rail Steel. *In:* STONE, D. H. & KNUPP, G. G. (eds.) *Rail Steels - Developments, Processing, and Use, ASTM STP 644.* American Society for Testing and Materials.

PARK, Y. J. & BERNSTEIN, I. M. 1979. The process of crack initiation and effective grain size for cleavage fracture in pearlitic eutectoid steel. *Metallurgical Transactions A,* 10**,** 1653-1664.

PEARSON, K. 1901. On Lines and Planes of Closest Fit to Systems of Points in Space. *Philosophical Magazine,* 2**,** 559-572.

PELLEQUER, J., CHEN, Y. J. & CHEN, S. W. Removal of Non-uniform Stripe Noises from AFM Images. Biomedical Engineering and Biotechnology (iCBEB), 2012 International Conference on, 28-30 May 2012 2012. 876-879.

PEREGRINA-BARRETO, H., TEROL-VILLALOBOS, I. R., RANGEL-MAGDALENO, J. J., HERRERA-NAVARRO, A. M., MORALES-HERNÁNDEZ, L. A. & MANRÍQUEZ-GUERRERO, F. 2013. Automatic grain size determination in microstructures using image processing. *Measurement,* 46**,** 249-258.

PETCH, N. J. 1953. The cleavage strength of polycrystals. *Journal of the Iron and Steel Institute,* 174**,** 24.

PHOTOS, E. 1989. The Question of Meteoritic versus Smelted Nickel-Rich Iron: Archaeological Evidence and Experimental Results. *World Archaeology,* 20**,** 403-421.

PICKERING, F. B. & GARBARZ, B. 1987. The effect of transformation temperature and prior austenite grain size on the pearlite colony size in vanadium treated pearlitic steels. *Scripta Metallurgica,* 21**,** 249-253.

PREWITT, J. M. S. 1970. Object enhancement and extraction. *In:* LIPKIN, B. S. & ROSENFELD, A. (eds.) *Picture Processing andPsychopictorics.* New York: Academic Press.

R.E.SMALLMAN & A.H.W.NGAN 2007. *Physical Metallurgy and Advanced Materials,* Oxford, Butterworth-Heinemann.

RAHEJA, J. L., KUMAR, S. & CHAUDHARY, A. 2013. Fabric defect detection based on GLCM and Gabor filter: A comparison. *Optik - International Journal for Light and Electron Optics,* 124**,** 6469-6474.

RAJKUMAR, P., WANG, N., EIMASRY, G., RAGHAVAN, G. S. V. & GARIEPY, Y. 2012. Studies on banana fruit quality and maturity stages using hyperspectral imaging. *Journal of Food Engineering,* 108**,** 194-200.

RANDEN, T. & HUSOY, J. H. 1999. Filtering for texture classification: a comparative study. *Pattern Analysis and Machine Intelligence, IEEE Transactions on,* 21**,** 291-310.

RAO, A. R. 1990. *A Texonomy for Texture Description and Identification,* Berlin, Springer.

RAVIRAJ, P., LYDIA, A. & SANAVULLAH, M. Y. 2011. An Accurate Image Segmentation Using Region Splitting Technique. *GESJ: Computer Science and Telecommunications,* 2**,** 12-21.

REED, T. R. & DUBUF, J. M. H. 1993. A Review of Recent Texture Segmentation and Feature Extraction Techniques. *CVGIP: Image Understanding,* 57**,** 359-372.

REUZE, P., BRUNO, A. & LE RUMEUR, E. Performance evaluation of some textural features for muscle tissue classification. Engineering in Medicine and Biology Society, 1994. Engineering Advances: New Opportunities for Biomedical Engineers. Proceedings of the 16th Annual International Conference of the IEEE, 3-6 Nov 1994 1994. 645-646 vol.1.

RIDLEY, N. 1984. A Review of the Data on the Interlamellar Spacing of Pearlite. *Metallurgical Transactions A,* 15**,** 1019-1036.

RIPLEY, B. 1993. *Statistical Aspects of Neural Networks*, Chapman and Hall.

ROBERTS, L. G. 1963. *Machine perception of three-dimensional solids.* PhD, Massachusetts Institute of Technology.

ROCHOW, T. G. & TUCKER, P. A. 1994. *Introduction to microscopy by means of light, electrons, X rays, or acoustics,* New York, Plenum Press.

ROMERO, P., OTERO, N., CABRERA, J. M. & MASAGUÉ, D. 2010. Laser assisted conical spin forming of dual phase automotive steel. Experimental demonstration of work hardening reduction and forming limit extension. *Physics Procedia,* 5, Part B**,** 215-225.

ROSENFELD, A. 1972. Edge and Curve Detection: Further Experiments. *IEEE Transactions on Computers,* 21**,** 677-715.

ROSENFELD, A., THOMAS, R. B. & LEE, Y. H. 1969. *Edge and curve enhancement in digital pictures*, University of Maryland Tech.

RUSS, J. C. 2011. *The Image Processing Handbook,* Boca Raton, FL, US, Taylor & Francis Group.

SAEIDI, N. & EKRAMI, A. 2009. Comparison of mechanical properties of martensite/ferrite and bainite/ferrite dual phase 4340 steels. *Materials Science and Engineering: A,* 523**,** 125-129.

SAMUEL, L. E. 1999. *Light Microscopy of Carbon Steels,* Materials Park, OH, ASM International.

SANDVIK, B. P. J. 1982. THE BAINITE REACTION IN FE-SI-C ALLOYS - THE PRIMARY STAGE. *Metallurgical Transactions a-Physical Metallurgy and Materials Science,* 13**,** 777-787.

SCHULGASSER, K. 1977. Bounds on the conductivity of statistically isotropic polycrystals. *Journal of Physics C: Solid State Physics,* 10**,** 407.

SCHWARTZ, A. J., KUMAR, M. & ADAMS, B. L. 2009. *Electron Backscatter Diffraction in Materials*

Science, New York, Springer Science and Business Media.

SHAH, K. P. 2013. *The Hand Book on Mechanical Maintenance* [Online]. [Accessed Nov 21 2013].

SHAPIRO, L. & STOCKMAN, G. 2001. *Computer Vision,* Upper Saddle River, Prentice Hall.

SHARMA, M. 2001. *Performance evaluation of image segmentation and texture extraction methods in scene analysis.* Master of Philosophy, University of Exeter.

SHARMA, M. & SINGH, S. Evaluation of texture methods for image analysis. Intelligent Information Systems Conference, The Seventh Australian and New Zealand 2001, 18-21 Nov 2001. 117-121.

SHARMA, N., RAY, A. K., SHARMA, S., SHUKLA, K. K., PRADHAN, S. & AGGARWAL, L. M. 2008. Segmentation and classification of medical images using texture-primitive features: Application of BAM-type artificial neural network. *Journal of Medical Physics,* 33**,** 119-126.

SINGH, K. K. & SINGH, A. 2010. A Study of Image Segmentation Algorithms For Different Types of Images. *UCSI International Journal of Computer Science Issues,* 7**,** 414-417.

SINGH, S. B. & BHADESHIA, H. K. D. H. 1998. Estimation of bainite plate-thickness in low-alloy steels. *Materials Science and Engineering: A,* 245**,** 72-79.

SMITH, S. & BRADY, J. M. 1997. SUSAN—A New Approach to Low Level Image Processing. *International Journal of Computer Vision,* 23**,** 45-78.

SNEDDON, I. N. 1995. *Fourier transforms,* Mineola, N. Y. , Dover Publications.

SODJIT, S. & UTHAISANGSUK, V. 2012. Microstructure based prediction of strain hardening behavior of dual phase steels. *Materials & Design,* 41**,** 370-379.

SOH, L. K. & TSATSOULIS, C. 1999. Texture analysis of SAR sea ice imagery using gray level co-occurrence matrices. *Geoscience and Remote Sensing, IEEE Transactions on,* 37**,** 780-795.

SONKA, M., HLAVAC, V. & BOYELE, R. 1998. *Image Processing, Analysis, and Machine Vision,* Toronto, Thomson.

SPANN, M. & WILSON, R. 1985. A quad-tree approach to image segmentation which combines statistical and spatial information. *Pattern Recognition,* 18**,** 257-269.

SPYCHALSKI, W. L., KURZYDLOWSKI, K. J. & RALPH, B. 2002. Computer study of inter- and intraangular surface cracks in brittle polycrystals. *Materials Characterization,* 49(9).

SRINIVASAN, G. R. & WAYMAN, C. M. 1968. Transmission electron microscope study of the bainite transformation in iron-chromium-carbon alloys. *Acta Metallurgica,* 16**,** 609-620.

STONE, D. H. & KNUPP, G. G. Rail Steels - Developments, Processing, and Use. *In:* STONE, D. H. & KNUPP, G. G., eds. STP 644, 1978. ASTM.

STRINGFELLOW, R. G., PARKS, D. M. & OLSON, G. B. 1992. A constitutive model for transformation plasticity accompanying strain-induced martensitic transformations in metastable austenitic steels. *Acta Metallurgica et Materialia,* 40**,** 1703-1716.

SU, X. & CHEN, W. 2001. Fourier transform profilometry: a review. *Optics and Lasers in Engineering,* 35**,** 263-284.

SUGUNA, N. & THANUSHKODI, K. 2010. An Improved k-Nearest Neighbor Classification Using Genetic Algorithm. *International Journal of Computer Science Issues,* 7**,** 18-21.

SURULIANDI, A., SRINIVASAN, E. M. & RAMAR, K. 2011. Texture analysis using local texture patterns: a fuzzy logic approach. *International Journal of Pattern Recognition and Artificial Intelligence,* 25**,** 741-762.

SWALLOW, E. & BHADESHIA, H. 1996. High resolution observations of displacements caused by bainitic transformation. *Materials Science and Technology,* 12**,** 121-125.

SZENASI, S. 2013. Medical Image Segmentation with Split-and-Merge Method. *5th International Symposium on Logistics and Industrial Informatics (LINDI2013).* Technical University of Applied Sciences Wildau Bahnhofstr Wildau, Germany.

TAN, X. & TRIGGS, B. 2010. Enhanced Local Texture Feature Sets for Face Recognition Under Difficult Lighting Conditions. *Image Processing, IEEE Transactions on,* 19**,** 1635-1650.

TARPANI, J. R., BRAZ, M. H. P., BOSE FILHO, W. W. & SPINELLI, D. 2002. Microstructural and Fractographic Characterization of a Thermally Embrittled Nuclear Grade Steel: Part II - Quenching and Tempering. *Materials Research,* 5**,** 365-371.

TARUI, T., TAKAHASHI, T., TASHIRO, H. & NISHIDA, S. Metallurgical Design of Ultra High Strength Steel Wires for Bridge Cable and Tire Cord. *In:* PARIS, H. G. & KIM, D. K., eds. Metallurgy, Processing and Applications of Metal Wires, 1996 Warrendale, PA, US. TMS, 87-96.

THEODORIDIS, S. & KOUTROUMBAS, K. 2009. *Pattern Recognition,* Oxford, UK, Elsevier.

TOMITA, Y. & OKABAYASHI, K. 1983. Heat treatment for improvement in lower temperature mechanical properties of 0.40 pct C-Cr-Mo ultrahigh strength steel. *Metallurgical Transactions A,* 14**,** 2387-2393.

TOMITA, Y. & OKABAYASHI, K. 1985. Mechanical-Properties of 0.40 Pct C-Ni-Cr-Mo High-Strength Steel Having a Mixed Structure of Martensite and Bainite. *Metallurgical Transactions a-Physical Metallurgy and Materials Science,* 16**,** 73-82.

TUCEYRAN, M. & JAIN, A. K. 1998. Texture analysis. *In:* CHEN, C. H., PAU, L. F. & WANG, P. S. P. (eds.) *The Handbook of Pattern Recognition and Computer Vision.* World Scientific.

TURNER, M. R. 1986. Texture discrimination by Gabor functions. *Biological Cybernetics,* 55**,** 71-82.

UNNIKRISHNAN, R., PANTOFARU, C. & HEBERT, M. A Measure for Objective Evaluation of Image Segmentation Algorithms. Computer Vision and Pattern Recognition - Workshops, 2005. CVPR Workshops. IEEE Computer Society Conference on, 25-25 June 2005 2005. 34-34.

VAN BOXEL, S., SEEFELDT, M., VERLINDEN, B. & VAN HOUTTE, P. 2005. Visualization of grain subdivision by analysing the misorientations within a grain using electron backscatter diffraction. *Journal of Microscopy,* 218**,** 104-114.

VAN DEN DOEL, L. R., KLEIN, A. D., ELLENBERGER, S. L., NETTEN, H., BODDEKE, F. R., VAN VLIET, L. J. & YOUNG, I. T. 1998. Quantitative evaluation of light microscopes based on image processing techniques. *Bioimaging,* 6**,** 138-149.

VERHOEVEN, J. D. 2007. *Steel metullurgy for the non-metallurgist,* Materials Park, OH, ASM International.

WALENTEK, A., SEEFELDT, M., VERLINDEN, B., AERNOUDT, E. & HOUTTE, P. V. 2006. Electron backscatter diffraction on pearlite structures in steel *Journal of Microscopy,* 224**,** 256-263.

WALENTEK, A., SEEFELDT, M., VERLINDEN, B., AERNOUDT, E. & VAN HOUTTE, P. 2008. Investigation of pearlite structure by means of electron backscatter diffraction and image analysis of SEM micrographs with an application of the Hough transform. *Materials Science and Engineering: A,* 483–484**,** 716-718.

WANG, C. Y., SHI, J., CAO, W. Q. & DONG, H. 2010. Characterization of microstructure obtained by quenching and partitioning process in low alloy martensitic steel. *Materials Science and Engineering: A,* 527**,** 3442-3449.

WANG, F. 2006. *Advanced methods for testing and analysing of materials,* Beijing, Beijing Institute of Technology Press.

WANG, J. & LIU, D. C. 2-D FFT for Periodic Noise Removal on Strain Image. Bioinformatics and

Biomedical Engineering (iCBBE), 2010 4th International Conference on, 18-20 June 2010 2010. 1-4.

WANG, X. D., HUANG, B. X., RONG, Y. H. & WANG, L. 2006. Microstructures and stability of retained austenite in TRIP steels. *Materials Science and Engineering a-Structural Materials Properties Microstructure and Processing,* 438**,** 300-305.

WEBB, A. R. & COPSEY, K. D. 2011. *Statistical Pattern Recognition,* Chichester, West Sussex, UK, John Wiley & Sons, Ltd.

WEI, D. Y., GU, J. L., FANG, H. S., BAI, B. Z. & YANG, Z. G. 2004. Fatigue behavior of 1500 MPa bainite/martensite duplex-phase high strength steel. *International Journal of Fatigue,* 26**,** 437-442.

WESZKA, J. S., DYER, C. R. & ROSENFELD, A. 1976. A Comparative Study of Texture Measures for Terrain Classification. *Systems, Man and Cybernetics, IEEE Transactions on,* SMC-6**,** 269-285.

WORDSTEELASSOCIATION 2012. World Steel in Figures 2012.

WU, J., POEHLMAN, S., NOSEWORTHY, M. D. & KAMATH, M. V. 2009. Texture feature based automated seeded region growing in abdominal MRI segmentation. *J. Biomedical Science and Engineering,* 2**,** 1-8.

XIA, W., LEWITT, R. M. & EDHOLM, P. R. 1995. Fourier correction for spatially variant collimator blurring in SPECT. *Medical Imaging, IEEE Transactions on,* 14**,** 100-115.

XIAN, G.-M. 2010. An identification method of malignant and benign liver tumors from ultrasonography based on GLCM texture features and fuzzy SVM. *Expert Systems with Applications,* 37**,** 6737-6741.

XIN, L., YAO, L. & YAN, W. Segmentation of fiber image based on GVF snake model with clustering method. *In:* ZHOU, M. & TAN, H., eds. International Conference, CSE 2011, 2011 Qingdao, China.

YAN, J., LI, J. & GAO, X. 2011. Chinese text location under complex background using Gabor filter and SVM. *Neurocomputing,* 74**,** 2998-3008.

YANG, Z.-G. & FANG, H.-S. 2005. An overview on bainite formation in steels. *Current Opinion in Solid State and Materials Science,* 9**,** 277-286.

YAU, W. Y., JIANG, X. & SER, W. Enhancing Oriented Pattern Using Adaptive Directional FFT Filter IEEE 2nd International Conference on Information, Communication & Signal Processing, 1999 Singapore.

YOUNG, C. H. & BHADESHIA, H. K. D. H. 1994. Strength of mixtures of bainite and martensite. *Materials Science and Technology,* 10**,** 209-214.

YOUNG, I. T. 2000. Shading Correction: Compensation for Illumination and Sensor Inhomogeneities. Delft, The Netherlands: Delft University of Technology.

YU, W., SOMMER, G. & DANIILIDIS, K. Using skew Gabor filter in source signal separation and local spectral multi-orientation analysis. Computer Vision and Pattern Recognition, 2004. CVPR 2004. Proceedings of the 2004 IEEE Computer Society Conference on, 27 June-2 July 2004 2004. I-462-I-469 Vol.1.

ZARE, A. & EKRAMI, A. 2011. Effect of martensite volume fraction on work hardening behavior of triple phase (TP) steels. *Materials Science and Engineering: A,* 528**,** 4422-4426.

ZHA, L., LIU, Z., LUO, S. & SHEN, L. A novel region merging based image segmentation approach for automatic object extraction. Circuits and Systems (ISCAS), 2013 IEEE International Symposium on, 19-23 May 2013 2013. 970-973.

ZHENG, C. 2005. Propagation of elliptical flat-topped beam in spatial-frequency domain. *Optik - International Journal for Light and Electron Optics,* 116**,** 563-567.

ZHOU, F., FENG, J.-F. & SHI, Q.-Y. Texture feature based on local Fourier transform. Image Processing, 2001. Proceedings. 2001 International Conference on, 7-10 Oct 2001 2001. 610-613 vol.2.

ZRNIK, J., MAMUZIC, I. & DOBATKIN, S. V. 2006. Recent progress in high strength low carbon steels. *Metalurgija,* 45**,** 323-331.

ZUCKER, S. W. 1976. Region growing: Childhood and adolescence. *Computer Graphics and Image Processing,* 5**,** 382-399.